UNIVERSITY OF SOUTHAMPTON

FACULTY OF SOCIAL AND HUMAN SCIENCES

Geography and Environment

Bank Erosion Processes along the Lower Mekong River

by

Hai Quang Trieu

Thesis for the degree of Doctor of Philosophy

April 2012

UNIVERSITY OF SOUTHAMPTON

ABSTRACT

FACULTY OF SOCIAL AND HUMAN SCIENCES
GEOGRAPHY AND ENVIRONMENT

Doctor of Philosophy

BANK EROSION PROCESSES ALONG THE LOWER MEKONG RIVER

by Hai Quang Trieu

This project conducts an analysis of bank erosion processes on a large, monsoon-affected river, the Lower Mekong River in Laos. The methodological approach taken was to build integrated models of bank erosion processes at three study sites on the Lower Mekong River in Laos (Friendship Bridge, Ang Nyay and Pakse) to simulate processes of (i) groundwater seepage and pore water pressure evolution, (ii) the effect of this on mass-wasting (using the Geo-slope model) and, (iii) fluvial erosion (using a model adapted from Kean and Smith, 2006ab). In all cases the models were parameterised using measured bank geotechnical properties. Across the study sites, a total of 42 simulations were undertaken to represent a wide range of observed flow events. Specifically, 14 selected flow hydrographs (comprising three types: single peak, multiple peak and rapid fall) were evaluated at each of the study sites, such that the influence on bank erosion of the hydrological properties of different monsoon floods could be evaluated.

The main findings indicate that although the Mekong is a big river, its dominant bank erosion process is one of slow, gradual, fluvial erosion. This research forms a partial contribution to understanding bank erosion processes operating in the Mekong. It was found that bank stability on the Mekong responses to variations in flood magnitude in ways that are similar to other rivers located within humid temperate areas. However, the Mekong has had the greater stability than these rivers due to its greater bank heights and more consolidated bank materials.

List of Contents

List of Figures

List of Tables

List of Accompanying Material

A CD-Rom that contains the animation files for simulation of:

Ang Nyay	1966 flow event, scenario 1, 2, 3;
Friendship Bridge	1966 flow event; scenario 1, 3; and
Pakse	2000 flow event; scenario 1, 3.

DECLARATION OF AUTHORSHIP

I, **Hai Quang Trieu**,

declare that the thesis entitled

Bank Erosion Processes along the Lower Mekong River

and the work presented in the thesis are both my own, and have been generated by me as the result of my own original research. I confirm that:

- this work was done wholly or mainly while in candidature for a research degree at this University;
- where any part of this thesis has previously been submitted for a degree or any other qualification at this University or any other institution, this has been clearly stated;
- where I have consulted the published work of others, this is always clearly attributed;
- where I have quoted from the work of others, the source is always given. With the exception of such quotations, this thesis is entirely my own work;
- I have acknowledged all main sources of help;
- where the thesis is based on work done by myself jointly with others, I have made clear exactly what was done by others and what I have contributed myself;
- parts of this work have been published as: Darby, S.E., Trieu, H.Q., Carling, P.A., Sarkkula, J., Koponen, J., Kummu, M., Conlan, I. and Leyland, J., 2010, A physically based model to predict hydraulic erosion of Fine-Grained River Banks: The Role of Form Roughness in Limiting Erosion, Journal of Geophysical Research, 115.

Signed: ……

Date:……

Acknowledgements

I would like to thank all the people who have helped me complete this research. However, I take the opportunity here to give special mention to a few of the people and organisations who have offered help or support during the production of this thesis.

First, I wish to acknowledge the support of the Mekong River Commission (MRC) and the University of Southampton (Geography and Environment) provided through studentship funding and to support the overseas components of my fieldwork.

On a professional note, I have been fortunate enough to work alongside two highly dedicated professors, Steve Darby and Paul Carling. They have suggested the original topic for the research; provided sound advice, guidance, and ongoing support throughout my study.

Special thanks go to Iwona Conlan (University of Melbourne) for providing the aDCP data at Ang Nyay and Pakse; to Matti Kummu (Helsinki University of Technology) for sharing his hydrodynamic model at Friendship Bridge; and to Massimo Rinaldi (University of Florence) for providing supporting data from the Sieve and Cecina Rivers.

I would like to extend my warm thanks to staff at the MRC in Laos who helped make my fieldwork possible: to Juha Sarkkula (Finnish Environment Institute); to Peter Adamson (MRC) for providing supporting hydrological data; and Prasith Deemaneevong (Hydrology Department) for helping with fieldwork measurements.

In terms of support of a more social nature, there are numerous people to thank at the University of Southampton. Thanks to all the administration staff in Geography and Enviroment for their willingness to assist in my PhD period. I also wish to thank my peers, Sergey, who gave a suggestion of building my model geometry and discussed my work; Luba and Tri who helped me to collect samples at the fieldwork sites.

Finally, I would like to thank my family, especially my parents, wife and son for their support and encouragement during my PhD.

Chapter 1 Introduction

River bank erosion, sediment transport and land loss hazards are aspects of a problem with global implications (Darby et al., 2000). Specifically, bank erosion phenomena can cause several problems relating to (Alonso and Combs, 1990; Lawler et al., 1997; Rinaldi and Casagli, 1999):

- Loss of agricultural land,
- Damage to structures which are located next to the river channel,
- Accumulation of bank-derived sediments in downstream reaches, which can promote flooding there,
- Channel instability
- Ecological impacts coming from changes in sediments.

To effectively manage these problems, it is necessary to understand bank erosion processes. There are two main sets of these processes, namely fluvial erosion and mass failure (Rinaldi and Darby, 2008). With respect to mass failure, recent studies have focused on two main topics: (1) accounting for the effects of positive and negative pore water pressures and confining river pressures (Casagli et al., 1999; Simon et al., 2000; Rinaldi et al., 2004); and (2) quantifying the effects of riparian vegetation on bank stability (Simon and Collison, 2002; Pollen and Simon, 2005; Pollen, 2006; Van de Wiel and Darby, 2007). In contrast to mass wasting, our current understanding of the process of fluvial erosion has, until now, been limited by an inability to parameterise available models of the process sufficiently accurately.

Around a quarter of the world's total population live in the basins of the 10 largest rivers of the monsoonal Asia Pacific region: Indus, Ganges-Brahmaputra-Meghna (GBM), Irrawaddy, Salween, Chao Phraya, Mekong, Red River, Pearl River, Yangtze and Yellow River (Varis et al., 2012). Because of industrialisation and urbanisation, the population is growing fast in these areas, especially in South Asia. With the high density of people, the World Bank (2008) identifies the major problems occurring within these river basins as poverty, malnutrition and uncontrolled urbanisation. Most of these rivers and their basins have changed dramatically over the years and no doubt they will be modified in the future too. Of these rivers the Mekong is perhaps the only large Asian river remaining approximately in pristine condition (except in the delta area), but even the Mekong is under pressure from plans for hydropower development (Kummu et al., 2010).

Most of the Asian mega-rivers have to face natural hazards, with nine out of ten of the world's horrible disasters taking place in these countries (Hough, 2004). Some disasters just occurred recently with massive damage to human lives and properties such as disastrous floods of the Indus in 2010 and 2011, the cyclone Nargis that hit the Irrawaddy delta in 2008, and the Sichuan earthquake within the Yangtze basin in 2008.

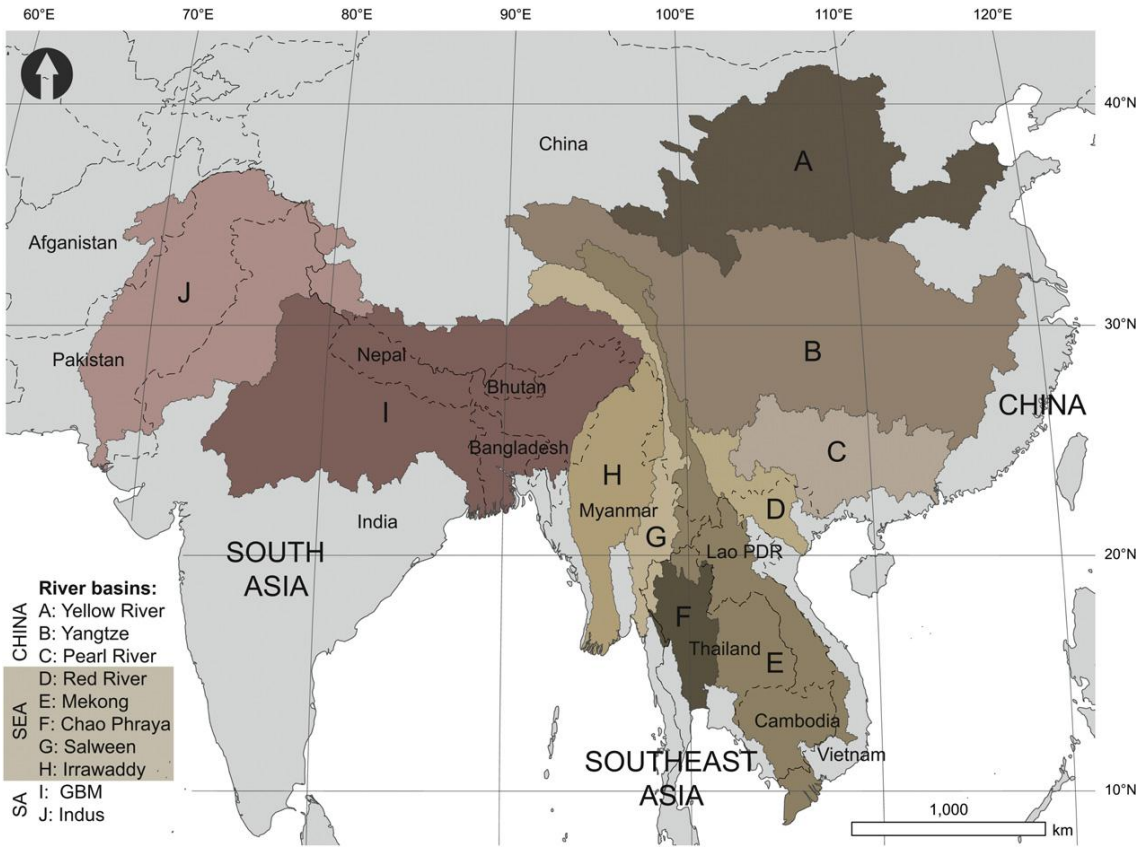

Figure 1.1. The ten river basins with the division of the three geographical areas (Varis et al., 2012).

Of the Asian mega-rivers, each is vulnerable to different issues. For example the Red River, Pearl River, Yangtze and Yellow River have problems with environmental factors. According to the Environmental Systems Indicator (Esty ey al., 2005), the South Asian basins have most problems with the quality of their environmental systems, followed by the Chinese ones. The Irrawaddy and Salween Rivers are facing to hazard and economic development, these two basins are undergoing rapid urbanization and the number of people that should be able to enter the modern economic system is growing very fast. The Indus and Yellow River are combating with water scarcity as their both annual precipitation is below 500 mm. Very little runoff is produced by the Yellow River and the Indus is not much more affluent with water (GWSP Digital Water Atlas, 2008).

	Basin	Area (x 10^3 km^2)	Shared by Number of countries	Population (millions)
China	Yellow River	1022.3	1	185.3
	Yangtze	1717.6	1	378.4
	Pearl	419.0	3	92.5
SE Asia	Red	156.7	3	27.8
	Mekong	811.5	6	69.1
	Chao Phraya	167.5	3	25.0
	Salween	262.7	3	7.8
SA	Irrawaddy	412.6	3	37.2
	GBM	1630.9	6	623.8
	Indus	1141.3	5	236.5
Total		7742	12	1683
World total		130,677		6441

Table 1.1. The ten river basins: land surface area, number of countries sharing the river basin and population in year 2005 (Varis et al., 2012)

In all ten large Asian rivers, bank erosion is a problem. On the Yangtze river in China, serious bank erosion occurred in the middle reaches during the last two decades (Jia et al., 2010). The rate of bank retreat in this section has been measured at a maximum of 88.4 m/year. On the Red River in Vietnam, controlling rapid erosion is one of the most prominent issues (Akkerman et al., 2006). The Bangladeshi government highlighted bank erosion on the Ganges, Brahmaputra and Meghna rivers the national adaptation programme of action (NAPA, 2005) with its strategic goals and objectives being to reduce the adverse effects of climate change. Maximum bank erosion on the Ganges river in the period 1984-93 was 665 m/year, while along the right and left bank of the Ganges, erosion rates are 56m and 20m per year, respectively. On the Upper Megna river, average bank erosion rates along the right and left banks of the river were found to be 9 m and 7 m per year, respectively. On the Mekong river, very high erosion rates in occur in the delta (Le et al., 2006) causing sediment deposition in the water line, the obstruction of navigation, enhancing peak flood level, as well as causing a wide range of serious damage for habitant's life. On the Indus river in Pakistan, extensive works have been constructed to control flooding and erosion (NHC, 2006). These works include about 5,000 km of flood dikes or levees, spurs with riprapped ends to protect the levees.

The Asian mega-rivers, in terms of river bank erosion research, are therefore most interesting as they are very big and they are very dynamic. However, research on bank

erosion on these rivers is limited. Most of the erosion rate data has been extracted from satellite images or is only observed where large rates of erosion occur. There are very few data that describe bank sediment, pore water pressure or the bank strength on these rivers. Bank erosion is important, but most recent works have been undertaken on different systems (temperate, small scale system). As noted above, the recent research done by Casagli et al., 1999; Simon et al., 2000; Rinaldi et al., 2004; Darby et al., 2007; Rinaldi and Darby, 2008; Luppi et al., 2009 have been conducted on temperate, relatively small rivers.

The Mekong River is a globally significant river, with a hydrological regime driven by the Asian monsoon. There are many sediment-related issues associated with the Mekong River, particularly bank erosion. Farm and residential lands near the riverbank have been damaged by bank erosion. A population of more than 50 million are living within the Lower Mekong Basin, which includes Laos, Thailand, Cambodia, and Vietnam. The population density along the riverbank is much greater than in other parts of these countries, excluding the coastal zones. The riverbank zone in the basin provides important economic goods and services for production and consumption, as well as areas for population settlement, and social and cultural arenas. Along the river, there are several sites where the river banks are eroding. However, there is a little knowledge about bank erosion processes in this type of physiographic setting (tropical, monsoonal).

For these reasons, this thesis focuses on undertaking a detailed investigation of bank erosion processes on the Mekong, as an example of a monsoonal mega river. The thesis aims to:

(1) Develop existing approaches to undertaking integrated analysis of bank erosion, focusing in particular on the quality of individual sub-models, especially in relation to fluvial erosion.

In fluvial erosion calculation in recent research, near bank shear stress is converted mostly from mean boundary shear stress using Leutheusser's method (1963). However, there are over predictions in estimating mean boundary shear stress using this approach, leading to potentially large errors in fluvial erosion then factor of safety, computations. Therefore, this research will focus on employing a novel method which brings greater accuracy in fluvial erosion modeling.

(2) Identify the key factors which are responsible for bank erosion in large, monsoonal rivers; thereby extending recent process based bank erosion research to a new physiographic setting.

There are several factors affecting river bank stability such as bank geometry, hydraulic and hydrological parameters, and geological characteristics. However, in a monsoonal river like the Mekong, some factors have different magnitudes than others in different climate regions (i.e. hydrograph; in the large river, the flow hydrograph has a much longer duration, which in the case of the Mekong is a matter of several months). Some factors like vegetation have a strong effect on low banked rivers, but have less effect on high banks along rivers like the Mekong. Other factors might have not any effect (i.e. freeze-thaw weakening is not taken into account in the Mekong, but is a crucial factor in many temperate zone rivers). Therefore, this research will identify the dominant factors controlling bank stability in large tropical monsoonal river, as well as considering these factors in relation to bank erosion on other rivers.

Chapter 2 Literature Review

This chapter provides a detailed review of the literature concerning bank erosion processes, in order to identify existing technical limitations in bank erosion modelling, which can then be addressed in the research. The review is structured in three sections. The first two parts discuss bank erosion processes. In the final section, the key controlling factors influencing bank erosion are discussed to determine how these factors are likely to affect the river banks of large, monsoonal rivers such as the Mekong.

2.1 Bank erosion processes and mechanisms

Bank erosion is a phenomenon which occurs when material from the side of a river channel is eroded, not only by fluvial processes, but also potentially by frost heave, drying, groundwater sapping, surface wash, and slope failure. The processes and mechanisms of bank erosion have been reviewed by numerous authors (e.g. Wolman, 1959; Twidale, 1964; Knighton, 1973). Further research has been undertaken in more recent years, focusing in particular on the mechanisms of mass failure (e.g Hooke, 1979; Thorne and Tovey, 1981; Thorne, 1982; Lawler, 1986, 1992, Darby and Thorne, 1996a; ASCE, 1998), the role of pore water pressure (Rinaldi and Casagli, 1999; Darby et al., 2000, Dapporto, 2001; Dapporto et al., 2003; Rinaldi et al., 2004), and in developing models that link the effects of fluvial erosion and mass failure (Darby et al., 2007; Rinaldi and Darby, 2008; Luppi et al., 2009).

In general, bank erosion can be classified according to the different bank erosion processes and mechanisms that contribute to net retreat and determine the controlling factors which affect bank stability (Figure 2.1). Bank erosion involves the entrainment of bank material that is subsequently removed downstream by the river. Thorne (1982) defined the processes of bank erosion as comprising (1) weakening and weathering processes, and (2) fluvial entrainment processes, while (3) bank failures under gravity occur through several types of specific failure mechanisms.

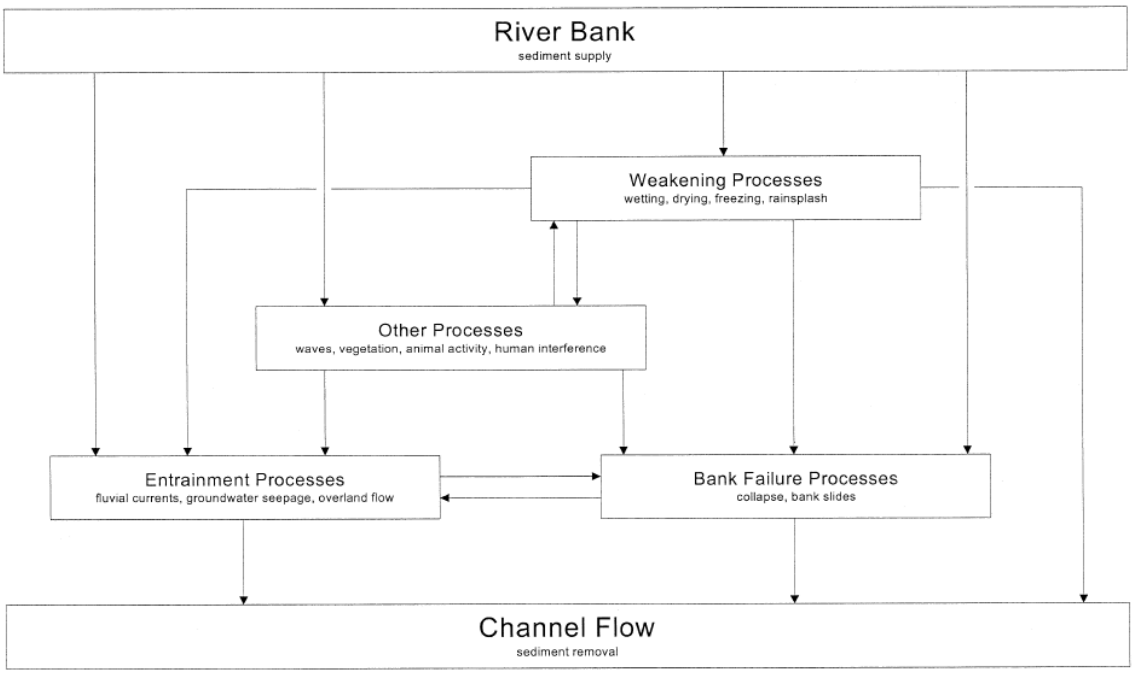

Figure 2.1. Relationship between bank erosion processes (Van de Wiel, 2003)

There are several kinds of bank mass failure, the basic types having been defined by Thorne (1982) as (i) rotational slip, (ii) shallow slip, (iii) plane slip failure. The specific forms of failure normally are influenced by bank material composition. For example, plane slip and shallow slip failures tend to occur in cohesionless materials while rotational failures tend to dominate cohesive banks (Hemphil and Bramley, 1989). Another basic type of mass failure is the cantilever failure mechanism, which is associated with composite banks which mostly are formed of relatively coarse-grained (non-cohesive) materials at the toe and fine-grained materials higher up.

Some other failure types were defined by Dapporto et al. (2001) as alcove-shaped failures, which were observed to occur in the middle part of the bank, leading to cantilever failure in moderate flow events. This type of bank consists of clay at the basal layer, silty sand in the middle layers and silt or sand at the top of the bank profile.

Figure 2.2 illustrates the main mechanisms of bank collapse, showing the morphological status of the river bank before and after failure. High, steep, nature banks are likely to generate planar or rotational type failures.

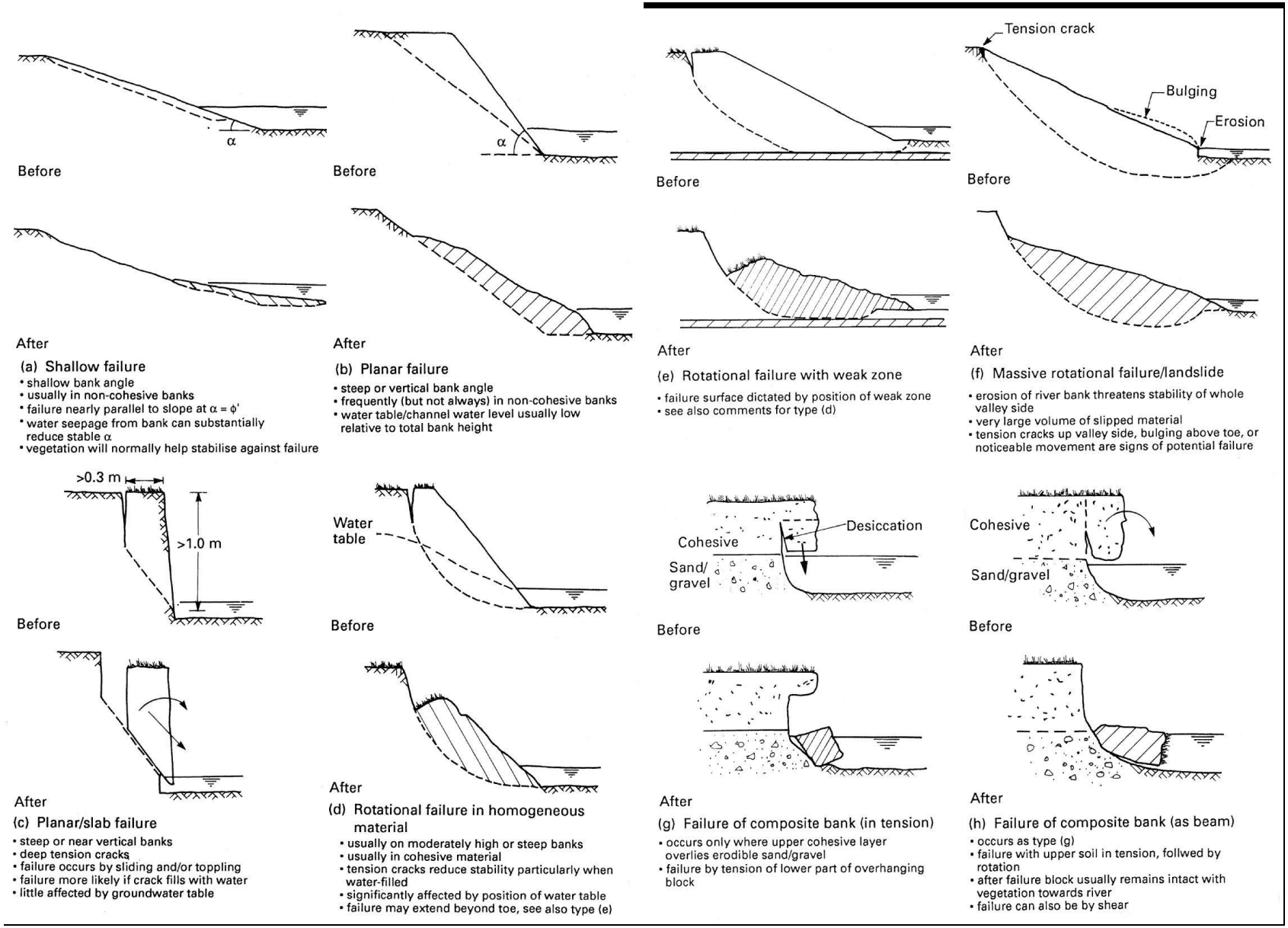

Figure 2.2. Types of mass failure of banks (Hemphil and Bramley, 1989)

Bank mass failure can be considered as a special case of a slope failure and therefore can be assessed using the principles of geotechnical engineering. In this approach, the stability of the bank usually is defined by calculating the ratio between the resisting forces and driving forces, expressed as a factor of safety (FS). When FS<1, the resisting forces are less than the driving forces, causing bank instability and collapse. In contrast, when FS>1, the bank is stable.

The specific methods employed to analyse these forces has developed gradually through time. The first method was the Culmann method (1866), which employed only a very simple failure block geometry and a limited description of the imposed forces (Figure 2.3).

2.1.1 Plane slip failure

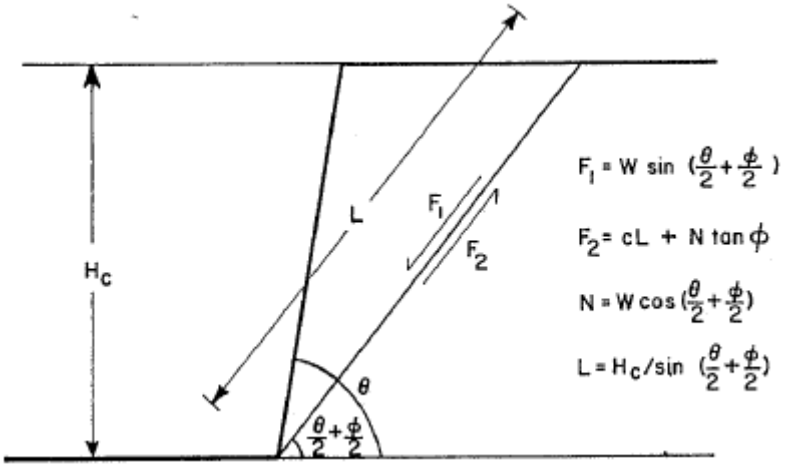

Figure 2.3. Culmann analysis for plane slip failure (Thorne, 1982): F_1- driving force, F_2- resisting force, H_c- critical bank height, L- length of failure plane, N- component of the weight W (normal to failure surface), c- effective cohesion, γ- material unit weight, θ- bank angle and ϕ- internal friction angle.

The Culmann method calculates the critical bank height using the simple fomula:

$$H_c = \frac{4c}{\gamma} \frac{\sin\theta\cos\phi}{\left[1-\cos(\theta-\phi)\right]} \tag{2.1}$$

For nearly vertical slopes, the bank stability predictions estimated by the Culmann method are similar to those derived from the circular arc analysis method (Thorne, 1982). However, when the bank angle decreases and bank height increases, the Culmann method overestimates the bank stability and plane slip failure happens rarely, meaning that the validity of the Culmann method is strictly limited to very steep slopes.

Lohnes and Handy (1968), Thorne et al. (1981), Huang (1983) and Simon et al. (1991) used a relatively simple, idealised geometry to analyse the stability of steep, cohesive, eroding banks which fail along planar surfaces. When applied at the field scale with real data, the limitations of these approaches are revealed (Darby and Thorne, 1996a; Millar and Quick, 1997):

- The idealised and simple geometry is inadequate to describe the bank profile of natural, eroding riverbanks in reality, especially when there is an occurrence of a tension crack (Osman and Thorne, 1988). Figure 2.4 shows a modified bank profile which is deformed by a combination of near-bank bed degradation and bank-toe erosion.
- The failure plane is forced to go through the bank toe (Simon et al., 1991), which is not always realistic.

- The effects of pore water pressure and hydrostatic confining pressure are ignored, leading to inaccuracy in calculate bank stability (Simon et al., 1991).
- As noted above, the planar failure analysis is valid only for very steep banks (Taylor, 1948; Millar and Quick, 1997).

To address these limitations, Darby and Thorne (1996a), Osman and Thorne (1988) and Darby et al. (2000) developed stability analyses that account for a more natural bank geometry that results from the deformation of the bank by a combination of bed aggradation or degradation with direct lateral fluvial erosion (Figure 2.4).

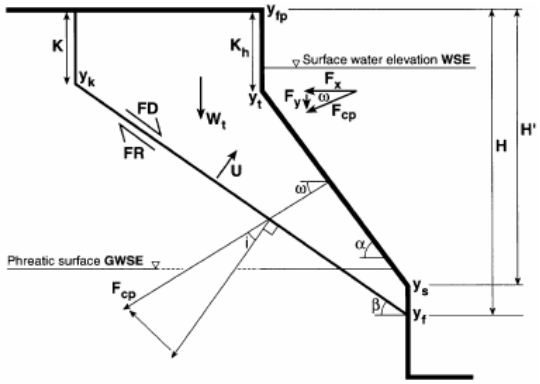

Figure 2.4. Definition diagram for the bank stability analysis. K- tension crack depth, K_h- relic tension crack depth, i- angle between resultant of hydrostatic confining force and normal to failure plane, β- failure plane angle, U- hydrostatic uplift force, F_{cp}- hydrostatic confining force, ω- angle at which the resultant of the hydrostatic confining force is directed, α- uneroded bank angle, GWSE- groundwater surface elevation, WSE- surface water elevation, W_t- failure block weight, FD- driving force, FR- resisting force, y_{fp}- floodplain elevation, y_t- base of `vertical face', $y_s$- elevation of base of uneroded bank slope (base of `upper bank'), y_f- elevation of base of failure plane, y_k- elevation of base of tension crack, H- total bank height, H'- uneroded bank height, L- length of failure plane (Darby et al., 2000).

Therefore, in addressing the above limitations, a more natural bank geometry is applied (Darby et al., 2000), reflecting the effect of fluvial erosion combined with bed aggradation or degradation (Figure 2.4). In recent years further advances have led to the widespread use of commercial stability models (e.g. Geo-slope) in which arbitrary bank geometry can be specified (Dapporto, 2001; Dapporto et al., 2003; Rinaldi et al., 2004; Darby et al., 2007).

2.1.2 Plane failure

Using the position of the intersection between the failure arc and the ground surface as a defining criterion, three types of rotational slip failures can be defined: base failure, toe failure and slope failure (Thorne, 1982). The "Swedish slices method" is so called due to the pioneering work of Swedish engineers. Taylor (1948) used only a simple circular arc because similar results are obtained using circular arc or log-spiral failures. By using the most common assumption that the inter-slices forces act horizontally, Bishop (1955) estimated the factor of safety for unit length along the bank using:

$$F_s = \sum_B^A \left\{ \frac{\left[c'b + (W - ub)\tan\phi'\right]\sec\theta_F}{1 + \frac{\tan\theta_F \tan\phi'}{F_s}} \frac{1}{W\sin\theta_F} \right\} \tag{2.2}$$

in which u - pore water pressure, is taken into account because this equation is showed in terms of effective stress, c'- effective cohesion, ϕ- friction angle, F_s- factor of safety with respect to rotational slip, W- weight of the bank material within the failure arc, θ_F- local angle of the failure plane and

$$\sec\theta_F = \sqrt{\tan^2\theta_F + 1} \tag{2.3}$$

Equation 2.3 has a limit which is identifying the critical slip circle, thus a number of likely locations must be examined iteratively (Thorne, 1982), leading to a large computational burden. Therefore, Taylor (1948), Bishop and Morgenstern (1960), Morgenstern (1963) and then Ponce (1978) built stability charts to help predict the worst case. However, there is still a limitation in that applications of the method are limited to cases where there are circular failure surfaces and critical undrained conditions, which rarely coincide in natural river banks (Thorne and Tovey, 1979). Eventually, with the aid of computer modelling, these limitations are no longer an issue because many failure surfaces can be explored iteratively.

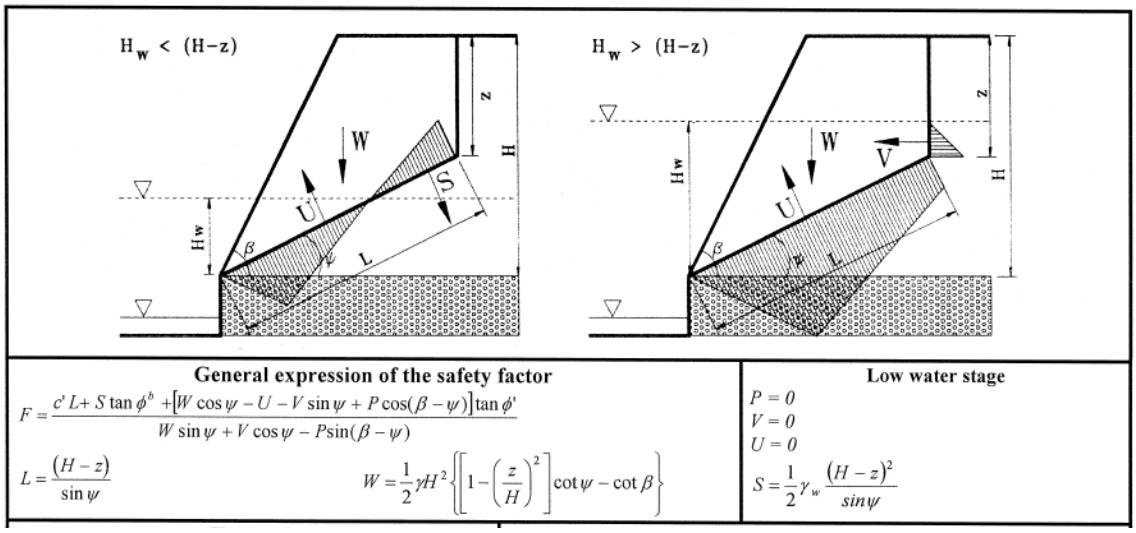

Figure 2.5. Bank stability analysis and pore water pressure distribution (Rinaldi and Casagli, 1999).

For river bank stability analyses, positive pore water pressures are typically applied for saturated soil, neglecting the stabilizing effects of negative pore pressures in the unsaturated portion of the bank (Lohnes and Handy, 1968; Selby, 1982; Huang, 1983; Simon et al., 1991; Osman and Thorne, 1988; Darby and Thorne, 1996a). Therefore an advantage of the work by Rinaldi and Casagli (1999) is that they account for both positive and negative pore water pressures when calculating the factor of safety (Figure 2.5). By using a combination of two different failure criteria which are applied to the unsaturated and saturated portions of the bank, the factor of safety is calculated using the expression:

$$F_s = \frac{c' L + S\tan\phi^b + [W\cos\varphi - U + P\cos\theta]\tan\phi'}{W\sin\varphi - P\sin\theta} \tag{2.4}$$

where W - weight of failing material, U - hydrostatic uplift force on the saturated portion of the failure surface, S - suction force on the unsaturated portion of the failure surface, P - resultant of the hydrostatic confining force due to the external water level, φ - failure plane inclination and θ - angle formed by the resultant of the hydrostatic confining force with the failure surface.

Later on, Simon et al. (2000) and Rinaldi et al. (2004) included the effects of hydrostatic confining river pressures as well as the effects of negative pore water pressure. The effects of matric suction on shear strength are reflected in the apparent or total cohesion using an equation of Fredlund and Rahardjo (1993):

$$c_a = c' + (u_a - u_w)\tan\phi^b = c' + \Psi\tan\phi^b \tag{2.5}$$

In Equation 2.5 the negative pore water pressures (positive matric suction, Ψ) in the unsaturated zone provide an apparent cohesion over and above the effective cohesion,

and thus, greater shearing resistance; this is often manifested in steeper bank slopes than would be indicated by ϕ'.

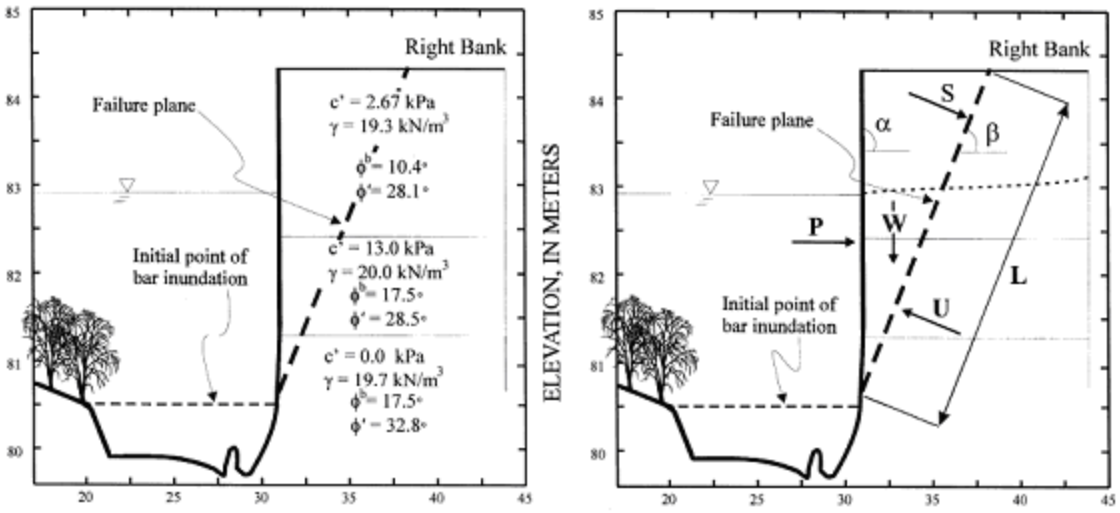

Figure 2.6. Geometry of the Goodwin Creek stream showing failure plane and parameter values which are considered in Equation **2.6** (Simon et al., 2000)

In more realistic applications, Simon et al. (2000) used the above model for multiple layers (Figure 2.6) in which each layer's weight is affected by its moisture content using:

$$F_s = \frac{\sum c_i' L_i + \left(S_i \tan\phi_i^b\right) + \left[W_i \cos\beta - U_i + P_i \cos(\alpha-\beta)\tan\phi_i'\right]}{\sum W_i \sin\beta - P_i \sin(\alpha-\beta)} \qquad (2.6)$$

where L_i- the length of the failure plane incorporated within the ith layer, S - the force produced by matric suction on the unsaturated part of the failure surface (kN/m), U - hydrostatic-uplift force on the saturated portion of the failure surface (kN/m) and P is the hydrostatic-confining force due to external water level (kN/m). Equation 2.6 represents the continued refinement of bank-failure analyses by incorporating additional forces and soil variability (Osman and Thorne, 1988; Simon et al., 1991; Darby and Thorne 1994; Casagli et al., 1997, 1999).

Dapporto et al. (2001, 2003) and Rinaldi et al. (2004) used Geo-Office v.4 software to analyse bank stability. Saturated and unsaturated flows are modelled by two-dimensional, finite element seepage analysis (seep/w) using the equations of motion and mass conservation, while bank stability analyses are modelled by slope/w using the Morgenstern-Price method (Morgenstern, 1963). There are some advantages in applying this software relative to the previous studies reviewed above, namely:
- The river bank geometry is freely defined without any limitation to its shape,

- All kinds of river bank failure such as planar, rotational and composite sliding surfaces are included in the software,
- By defining the water stage, the river confining pressure is calculated in the model,
- The effects of both positive and negative pore water pressures are taken into account.

However, the most recent literature has two significant limitations: the lack of information on fluvial erosion, and all the factors which act upon the bank are not taken into account completely. Therefore, Darby et al. (2007) have presented a simulation modelling approach in which hydraulic erosion, finite element seepage (Figure 2.7), and limit equilibrium stability analyses are, for the first time, linked together into a fully-integrated analysis. This integration will be the approach adopted in this study.

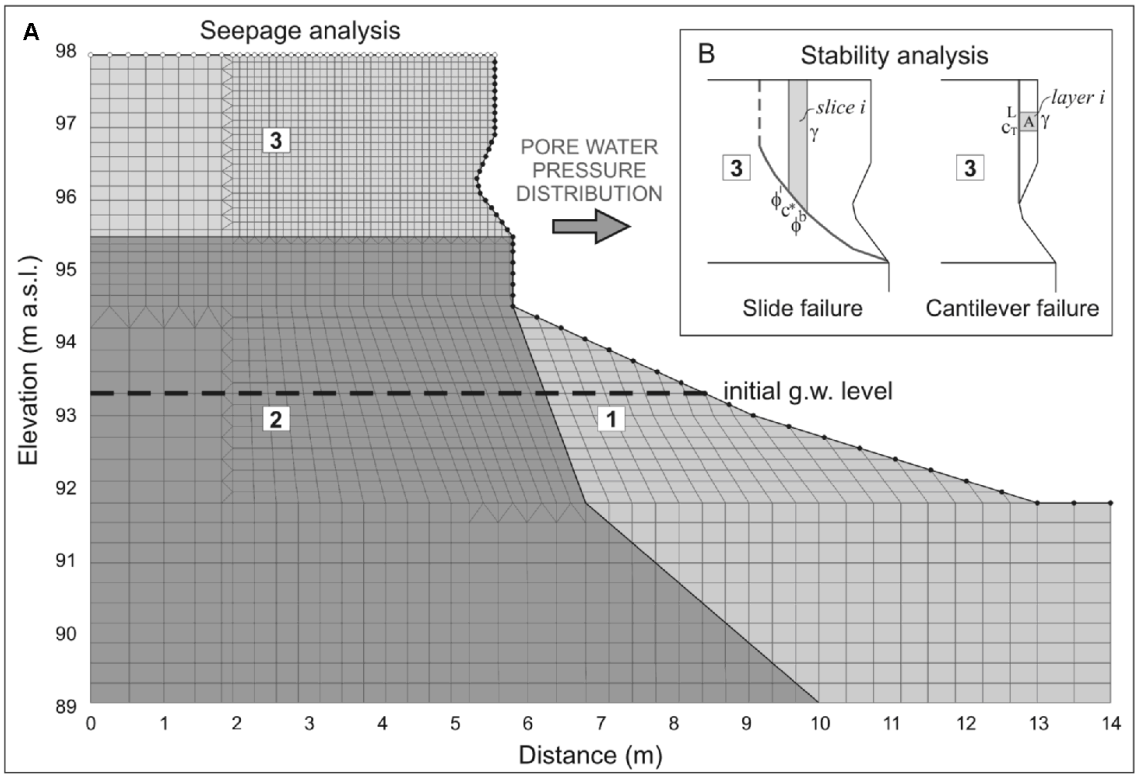

Figure 2.7. (A) Geometry of the finite element seepage analysis, indicating the different types of assigned boundary conditions, (B) slide- and cantilever-failure mass wasting analyses applied to the upper cohesive part of the river bank (Darby et al., 2007).

2.1.3 Tension crack

Tension cracks are created when the horizontal tensile stress in the upper layer of a river bank exceeds the tensile strength of the soil (Darby and Thorne, 1994). Identifying the presence of a tension crack is important in the analysis of the stability of cohesive river banks (Thorne, 1982). There are two kinds of forces which produce tensile stresses: (a) forces created from desiccation due to shrinkage and (b) forces associated with the weight of the failure block (Darby and Thorne, 1994). A method developed by Darby and Thorne (1994) predicts the location of a tension crack in order to calculate the geometry of the riverbank failure block and estimate the land loss and bank sediment yield along the channel.

Taylor (1948) identified the depth of the tension crack from the Mohr diagram as follows:

$$Z_c = \frac{2c}{\gamma}\tan\left(45 + \frac{\phi}{2}\right) \tag{2.7}$$

where: Z_c- maximum depth of tension (m), c - soil cohesion (kPa), γ- soil unit weight (kNm^{-3}) and ϕ- friction angle (degrees). Then Thorne (1982) gave the equation to calculate the critical height of a vertical bank with a tension crack:

$$H_{cr}^{'} = H_{cr} - z_0 = \frac{2c}{\gamma}\tan\left(45 + \frac{\phi}{2}\right) \tag{2.8}$$

2.1.4 Cantilever failure

This type of failure often occurs when the river bank is a composite bank, which consists of cohesive and non-cohesive material. The most frequent case comprises a non-cohesive layer underneath the cohesive layer (Richard and Lorriman, 1987; Thorne and Tovey, 1981). Because of the difference in erosion resistance of these two kinds of material, the non-cohesive material is usually eroded preferentially by fluvial entrainment (Thorne, 1982). Thorne (1982) also classified three kinds of cantilever failure: shear failure, beam failure and tensile failure (Figure 2.8). To calculate the stability of cantilever failures, Thorne and Tovey (1981) combined the static equilibrium of forces and bending beam theory. They also presented stability charts which apply for each kind of failure to estimate the factor of safety.

Shear failure occurs when the overhanging block slides along a surface. The reason simply is that the weight of the block exceeds the shear strength of the soil (Thorne and Tovey, 1981). However, beam failures, the most common cantilever failure, occur when the moment of the weight of the block overcomes the moment of the soil's

strength in tension. The failure block rotates about the neutral axis towards and inwards to the river. For tensile failure, the lower section is detached from the overhang block due to its weight. Therefore, because of its detaching mechanism, it is rarely observed in the field (Darby et al., 2007).

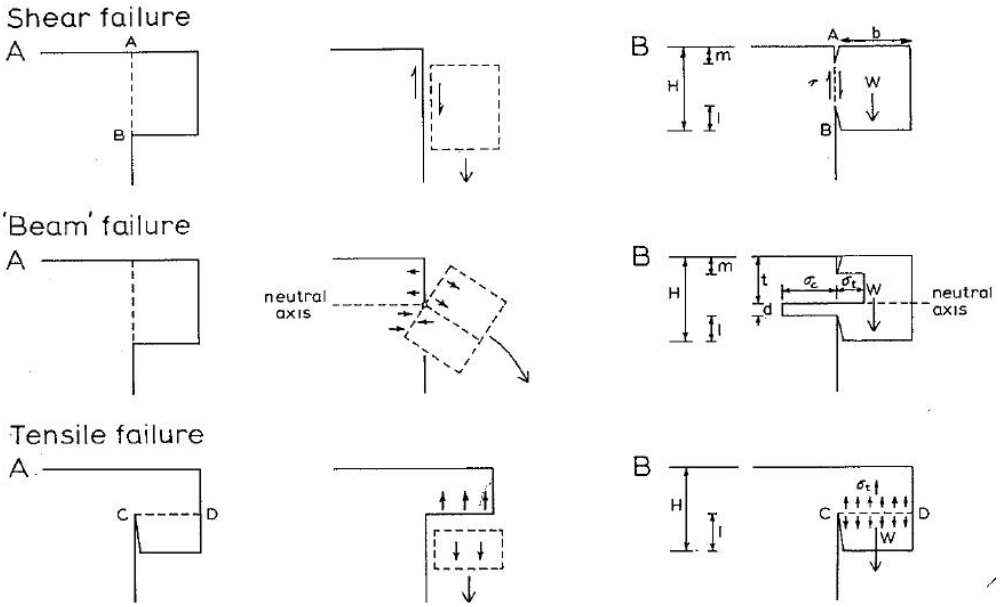

Figure 2.8. Definition diagram for shear, beam and tensile failure of cantilever overhangs formed by basal undercutting (Richard and Lorriman, 1987)

The factor of safety is calculated for each of the mechanisms using:
for shear failure:

$$\frac{F_{ss}}{A} = \frac{(\beta - \chi)}{\beta}\frac{\beta}{2r} \tag{2.9}$$

for beam failure,

$$\frac{F_{sb}}{A} = \frac{\beta^2}{(1+r)B'} \tag{2.10}$$

for tensile failure,

$$\frac{F_{st}}{A} = \frac{B}{1-\beta} \tag{2.11}$$

where,

$$A = \frac{\sigma_t}{\gamma b} \tag{2.12}$$

σ_t - is the tensile strength of the soil, γ- the unit weight of the soil, b - the overhang width, β, χ, B, B' - dimensionless numbers that depend only on the geometry of the cantilever overhang, r - ratio of the tensile strength to the compressive strength of the soil.

2.1.5 Vegetation

There are many effects of vegetation on river bank processes and, as such, the influence of individual factors is quite difficult to isolate (Rinaldi and Darby, 2008). Vegetation has a dual effect on bank stability. In some cases, it increases the stability by limiting the effectiveness of bank erosion, protecting the soil surface directly and reinforcing the soil as well as producing extra cohesion through roots and rhizomes. Indeed increasing the soil strength is the most important effect of vegetation on bank stability (Gray, 1978; Wu et al., 1979; Gray and Baker, 2004) due to the changes in bank geotechnical properties induced by the roots (Abernethy and Rutherfurd, 1998; 2000). By adding overburden (in some cases), vegetation reduces bank stability by decreasing the shear strength of the soil (Nanson and Hickin, 1986). Thorne and Osman (1988) classified some major properties of both bank and vegetation, which both increase and decrease the bank stability: (1) type of vegetation as some types have roots reinforcing the soil, some not, (2) bank geometry, that is the relationship between bank height and rooting depth. If the height of bank is less than rooting depth, roots certainly cut the incipient plane, leading to reinforcement. In contrast, when the failure surface is below the rooting depth, there is a switch from enhancing to reducing bank stability, (3) density of vegetation, single plants or small groups of vegetation being less effective in reinforcing banks than a continuous band of vegetation, and (4) age and health of vegetation, if vegetation has died, the bank has relic roots in it, leading to pathways for seepage, that promote piping type failures.

Vegetation position and root shape play an important role in affecting bank stability (Van de Wiel, 2003). However, in the case of the Mekong, the role of vegetation may be less than other rivers that have formed the focus of much of the reviewed literature. This is because very large bank heights (typically more than 10 m) means that the presence of roots is limited to a relatively small area of the top of the bank, leading to little stabilising effect of vegetation to the bank. Therefore, in this research, the appearance of vegetation in the stability model is ignored, although it is recognised that this might be considered as a limitation.

2.2 Fluvial entrainment and fluvial erosion model

The bank surface interacts with the hydraulics of flow close to the surface (Grissinger, 1982), thus soil particles or aggregates have the potential to be removed directly from the bank surface or at the bank toe when the driving forces of fluid drag and lift are greater than the resisting forces of friction, erosion and gravity (Thorne, 1982; ASCE, 1998). If the opposite is true, the sediment particles remain in place. The strength of

the driving and resisting forces are estimated based on the characteristics of the flowing water and bank properties, respectively.

For cohesionless materials, soil particles are detached and entrained separately, grain by grain. The stability of an individual partical is based on the balance of all forces acting on it. On the other hand, for cohesive soil, the individual particles often are combined into small aggregates. It is very complex to understand clearly how the interparticle forces work together because they relate to a variety of soil properties, but Grissinger (1982) gave a detailed view about the properties which relate to the stability of cohesive materials (see section 2.2.1.2).

Fluvial bank erosion rates can be estimated using an excess shear stress formula such as that of Partheniades (1965), Arulanandan et al. (1980), Darby et al. (2007) or Rinaldi and Darby (2008):

$$\varepsilon = k_d \left(\tau_b - \tau_c\right)^a \tag{2.13}$$

where ε (m/s) is the fluvial bank-erosion rate per unit time and unit bank area, τ_b (Pa) is the boundary shear stress applied by the flow, k_d (m^3/Ns) and τ_c (Pa) are erodibility parameters (erodibility coefficient, k_d, and critical shear stress, τ_c) and a (dimensionless) is an empirically-derived exponent, generally assumed to equal 1.0. The erodibility parameters and boundary shear stress all are highly variable, therefore, this explains why observed rates of fluvial erosion range over several orders of magnitude (Hooke, 1980).

This model (Equation 2.13) has the advantage of simplicity, but in practice difficulties in estimating the values of the erodibility (k_d, τ_c) and shear stress parameters inhibit its predictive accuracy. Therefore, in the next section, the state of the science is reviewed in terms of our current ability to estimate the parameters in Equation 2.2.13.

2.2.1 Estimating critical shear stress

2.2.1.1 Non-cohesive material

For non-cohesive materials, individual particles are entrained into the river by rolling or sliding (Thorne, 1982). The two forces which act to affect particle stability are the net motivating force and net resisting force. The resisting force depends on grain size and grain size distribution (ASCE, 1998). River flow exerts fluid forces which drag and lift the grains from the river bank. The drag force is calculated by determining the boundary shear stress when analysing the stability of the non-cohesive grains.

An equation that has been used to calculate the entrainment of non-cohesive particles is given by ASCE (1966):

$$\tan\phi = \frac{F_1}{F_2} = \left[\frac{C_2^2 \tau_c^2 d_s^4 + W_s \sin^2\theta + 2c_2 \tau_2 d_s^2 W_s \sin\theta \sin\alpha}{w_s \cos\theta} \right]^{0.5} \tag{2.14}$$

where: F_1 - disturbing force and F_2 - restoring force illustrated by Figure 2.9 using field data, d_s - grain size, W_s - submerged weight of grain, c_2 - empirical coefficient, θ - bank angle, α - flow angle to longstream direction, φ-friction angle, τ_c - critical boundary shear stress.

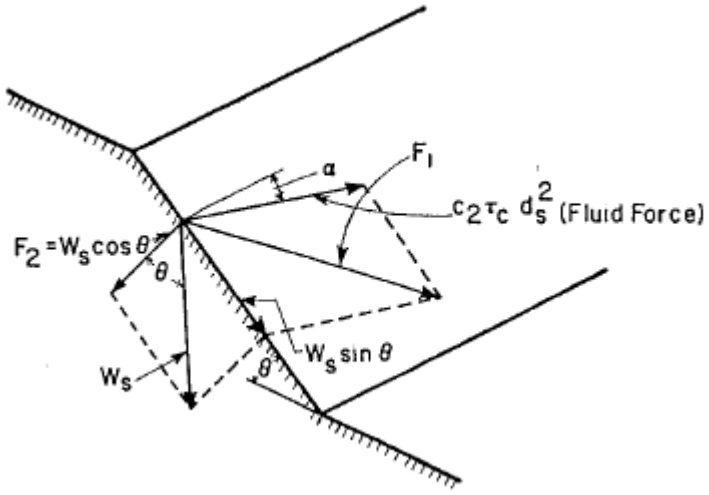

Figure 2.9. Forces on particle at the surface of a submerged non-cohesive bank (Thorne, 1982)

Equation 2.14 ignores the fluid lift force, which can be as large as 80% of the fluid shear force (Thorne, 1982). However, the effects of the fluid lift force can still be taken into account by adjusting the empirical coefficients, which amongst other things represent the effects of shape and packing density of grains and the magnitude of instantaneous peak stresses relative to their mean value (ASCE, 1966).

In non-cohesive river banks, the resisting force is produced mainly by the submerged weight of the particles (ASCE, 1998) and surface roughness (Simon et al., 2003). A Shields-type entrainment function is usually applied to estimate the mobility of non-cohesive bank material (Ashworth and Ferguson, 1989; Ferguson, 1994):

$$\tau_c^* = \frac{\tau_c}{(\rho_s - \rho) g D} \tag{2.15}$$

where: τ^*_c - critical dimensionless shear stress, τ_c - dimensional critical shear stress, D - particle diameter, ρ_s, ρ - density of sediment and water, γ - gravity acceleration. For steady uniform flow, the mean boundary shear stress is given by (Chow, 1959):

$$\tau = \rho g d S \tag{2.16}$$

where: d - mean water depth (more precisely, d should be the hydraulic radius) and S - water surface slope. However, as discussed in Section 2.2.2 the validity of Equation 2.16 is discussed further.

2.2.1.2 Cohesive material

The physical properties of cohesive and non-cohesive material are quite different, thus the processes of fluvial entrainment associated with these materials differs too. The resistance force for fine grain sediments depends on a range of soil properties, especially the magnitude of the inter-particle forces of cohesion (Grissinger, 1982). However, the cohesive material of the bank surface often consists of desiccated aggregates or crumbs, as a result, fluvial erosion may occur by their entrainment rather than entrainment of the constituent particles (Thorne, 1982).

It is more complex to determine the critical shear stress of cohesive materials than non-cohesive materials. Several factors which complicate this estimation are the clay content, organic content and the variable composition of interstitial fluids (Arulanandan et al., 1980; Grissinger, 1982). Arulanandan et al. (1980) and Osman and Thorne (1988) estimated critical shear stress based on soil sodium adsorption ratio (SAR), pore fluid concentration (CONC) and dielectric dispersion ($\Delta\varepsilon$) (Figure 2.10)

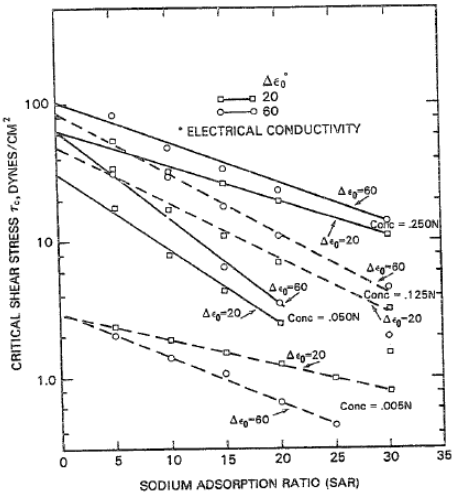

Figure 2.10. Critical shear stress τ_c versus SAR for different soil salt concentrations and different dielectric dispersion values (Arulanandan et al., 1980).

Given the difficulty of predicting critical shear stress values, a number of authors have developed measurement techniques instead. Hanson (1990, 1991) measured critical shear stress of cohesive materials on a variety of bank and bank toe materials using a non-vertical submerged jet-testing device. The device applies an impinging, submerged jet on the bank materials and measures the applied shear stress and erosion rate. This

relationship is used to calculate the critical shear stress (at zero applied stress) and erodibility coefficient (k; the slope of the erosion rate vs. applied stress curve):

$$\tau_c = \tau_0 \left(\frac{H_p}{H_e} \right)^2 \tag{2.17}$$

where: H_p- potential core length from the origin of the jet, H_e- distance from the jet nozzle to the equilibrium depth of scour, τ_0- maximum applied bed shear stress within the potential core. The erodibility coefficient k_d is then calculated by curve-fitting measured values of H versus time t (H - the distance from the jet nozzle to the maximum depth of scour at time t).

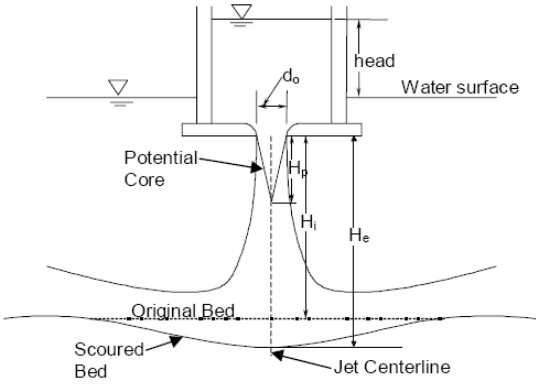

Figure 2.11. Schematic of jet scour parameters (Hanson and Simon, 2001)

By undertaking many in situ tests, Hanson and Simon (2001) showed that there is an inverse relationship between τ_c and k_d. These results have a similar trend to the findings of a flume study conducted by Arulanandan et al. (1980). Hanson and Simon (2001) expressed k_d as a function of τ_c (r^2=0.64) as:

$$k_d = 0.2\tau_c^{-0.5} \tag{2.18}$$

A fact to be kept in mind that the choice of units of k_d in Equation 2.18 must be consistent with their definition in Equation 2.2.13. If erosion rate is expressed in unit of metres per second, the critical shear stress is in units of Newtons per square metre, and then it is necessary to employ the conversion:

$$k_d = \frac{0.2\tau_c^{-0.5}}{1000000} \tag{2.19}$$

In addition, to estimate the critical shear stress, Julian and Torres (2006) used the silt-clay percentage (SC%) (Vanoni, 1977) combined with observations by Dunn (1959) in order to develop a rating curve for τ_c based on SC% as a function below:

$$\tau_c = 0.1 + 0.1779(SC\%) + 0.0028(SC\%)^2 - 2.43E - 5(SC\%)^3$$

Figure 2.12. Cohesive Strength Meter (CSM) (Tolhurst et al., 1999)

Of particular relevance to this study is a recent development in which critical shear stress can be estimated directly in the field using a novel instrument called the Cohesive Strength Meter (CSM) (Tolhurst et al., 1999). The CSM is a jet-testing device that has been used to study cohesive sediments on inter-tidal flats, but which has not been employed previously in river bank investigations. This device (Figure 2.12) is based upon the principle of a vertically impinging jet of water firing at varying pressures on the sediment surface within an enclosed sampling chamber. It uses attenuation of an infra-red light path to detect the onset of sediment erosion. Compared to conventional jet-testing devices, the portability and small size of the CSM's sampling chamber, together with the high speed of individual tests, mean that it is feasible to undertake replicate sampling within discrete sedimentary horizons, such that the variability of the bank materials can be defined. The critical stress is then related to k_d using Equation 2.18 (Hanson & Simon, 2001).

2.2.2 Estimating near-bank shear stress

To estimate near-bank shear stress, it is necessary to transform the reach averaged boundary shear stress to a more realistic value. For an infinitely wide, straight channel exhibiting two-dimensional uniform unidirectional flow, the mean boundary shear stress is given by:

$$\tau = \gamma RS \tag{2.20}$$

where γ is the specific of water, R is the hydraulic radius and S is the water surface slope (or bed slope in uniform flow). The water surface slope is generally fixed by topographical controls; consequently, it does not change with discharge. Therefore mean boundary shear stress varies with flow depth and reaches a maximum value at the peak flow discharge.

In a wide, open channel Chow (1959, p.169) calculated boundary shear stress on the basal area of the bank as follows:

$$\tau_b = 0.75\tau \tag{2.21}$$

where τ_b- shear stress on the bank and, τ- mean boundary shear stress in the cross section.

These equations are used to calculate mean boundary and bank shear stresses during the flow events that produce bank toe erosion. However, Equation 2.21 can only be used to provide very crude approximations of bank shear stress because of its simplified assumption about chanel shape.

There are many functions describing the distribution of boundary shear stress around the wetted perimeter. For a trapezoidal cross section with gentle bank slope, the distribution is shown in Figure 2.13 (Lane, 1955; Osman and Thorne, 1988; Raudkivi, 1998).

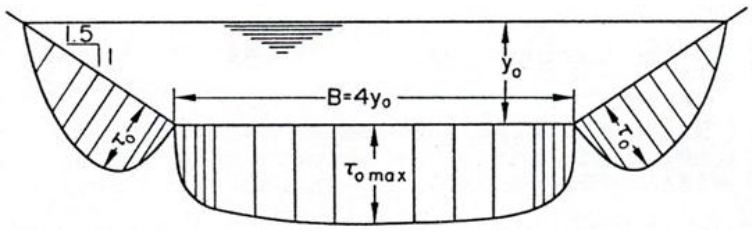

Figure 2.13. Shear stress distribution over the periphery of the trapezoidal channel (Lane, 1955)

Lane (1955) showed that $\tau_{0\ (max)}$ equals 0.89; 0.97 and 0.99 times $\gamma y_0 S$ for B equals 2; 4 and 8 times y_0, respectively. The maximum value on the side, τ_0, equals 0.735; 0.750 and 0.76 times $\gamma y_0 S$, respectively and occurs at 0.1 to 0.2 of the depth and varies slightly with the slope of the side.

Yuen (1989) obtained data from tests on channels with side slopes of 1:1 that indicated a maximum value of 0.82ydS for wide channels and Chow (1959) quoted the commonly used maximum value of 0.76ydS.

It should be kept in mind that differences in the roughness of the channel bed and banks have further effects on the boundary shear stress distribution. The effect of the channel sides being rougher or smoother than the bed is, respectively, to increase or decrease the shear force on the side (Yuen, 1989). Although it is not possible to

predict the shear distribution theoretically, assumptions can be used to take this effect into account (see Section 2.2.2.1).

2.2.2.1 Flintham and Carling (1988)

Flintham and Carling (1988) proposed a method to estimate the distribution of boundary shear stress that is based on the method of Knight (1981) and Knight et al. (1984). The shear force acting on a boundary, per unit length of channel, is equal to the mean boundary shear stress $\bar{\tau}$ multiplied by the boundary cross section length. The shear force acting on a channel's side walls (SF_{bank}) and bed (SF_{bed}) are therefore equal to:

$$SF_{bank} = \bar{\tau}_{bank} P_{bank} \tag{2.22}$$

$$SF_{bed} = \bar{\tau}_{bed} P_{bed} \tag{2.23}$$

The total is therefore obtained by summation:

$$SF_{total} = SF_{bank} + SF_{bed} \tag{2.24}$$

$$\bar{\tau} P = \bar{\tau}_{bank} P_{bank} + \bar{\tau}_{bed} P_{bed} \tag{2.25}$$

The shear force carried by the side-walls or bed can be expressed as a percentage of the total shear force (%SF) such that:

$$\%SF_{bank} = \frac{\bar{\tau}_{bank} P_{bank}}{\bar{\tau} P} \times 100 \tag{2.26}$$

Kinght's work was restricted to rectangular channels. Flintham and Carling (1988) extended the analysis to include trapezoidal channels. The percentage of the shear force being carried by the bank of a channel with uniform bed and bank roughness $\%SF_{bank}$ was given as

$$\log \%SF_{bank} = -1.4026 \log\left(\frac{P_{bed}}{P_{bank}} + 1.5 \right) + 2.247 \tag{2.27}$$

The mean bank and bed shear stress are obtained for symmetrical trapezoidal ($\theta > 45°$) and rectangular channels using:

$$\frac{\bar{\tau}_{bank}}{\gamma H S_f} = 0.01\%SF_{bank} \left[\frac{(B + P_{bank}) \sin\theta}{4H} \right] \tag{2.28}$$

$$\frac{\bar{\tau}_{bed}}{\gamma H S_f} = 1 - 0.01\%SF_{bed} \left[\frac{B}{2P_b} + 0.5 \right] \tag{2.29}$$

where SF_{bank} - the proportion of the total cross sectional shear force acting on the bank, P_{bed} and P_{bank} - wetted perimeters of the bed and banks, respectively, B -water surface width, τ- cross sectional shear stress.

Flintham and Carling (1988) have provided a quick and simple method of determining the bed and bank shear stress in straight, symmetrical trapezoidal and rectangular channel ($45° < \theta < 90°$) in which the bed roughness is equal to or greater than the bank roughness. This method has been applied by Millar and Quick (1993); and Julian and Torres (2006) to estimate bank erosion rate.

2.2.2.2 Kean and Smith's (2006ab) stress partitioning method

To estimate the near-bank boundary shear stress, Kean and Smith (2006ab) produced a new method to determine the form drag exerted on small-scale topographic bank features and thus quantify the near-bank flow field. They found that small-scale topographic features on the river bank surface affect river flow. These features primarily consist of undulations produced by erosion and slumping of bank material (Figure 2.14). Flow over or past these small-scale topographic features produces form drag, which can substantially affect the overall flow resistance of the channel. Therefore, accurate quantitative treatment of the form roughness is essential for determining overall and local flow resistance in fully predictive river flow models. Consequently, this present research uses the Kean and Smith (2006ab) approach to calculate fluvial erosion; therefore, the details of this method are described in the methodology chapter.

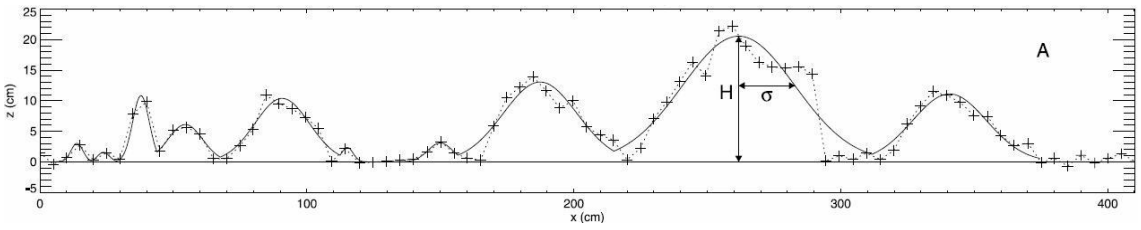

Figure 2.14. Measurements of plan view bank topographic profile near USGS streamflow gauging station, Lost Creek near Anaconda, Montana (Kean and Smith, 2006a)

2.3 Controlling factors

The previous review has shown that a range of controlling factors is important in determining rates of bank erosion. However, it is interesting to note that the literature is biased by studies of relatively small rivers in humid-temperate zones. For example, Hooke's (1979, 1980) study sites are in a Devon river; Thorne and Tovey (1981) and Thorne (1982) considered the River Severn; Lawler (1986, 1992) considered the Bollin-Dean River; Darby and Thorne (1996b): Goodwin Creek; Darby et al. (2000), Simon et al. (2002): Missouri river; most research of Rinaldi and Casagli (1999), Darpporto (2001), Dapporto et al. (2003), Rinaldi et al. (2004), Darby et al. (2007), Rinaldi and Darby (2008), Luppi et al. (2009) are about the Sieve, Cecina and Arno Rivers. Because the physiographic controls on the controlling factors are very different for a large, monsoonal river, it can be hypothesised that the dominant factors controlling erosion on large tropical river may differ from the current conceptual model.

This research tries to classify the differences between these two types of rivers: small rivers in humid-temperate areas and large rivers in monsoonal, tropical regions. Some of the controlling factors (Figure 2.15), which are discussed below, affect the erosion processes of large, tropical rivers, but some do not.

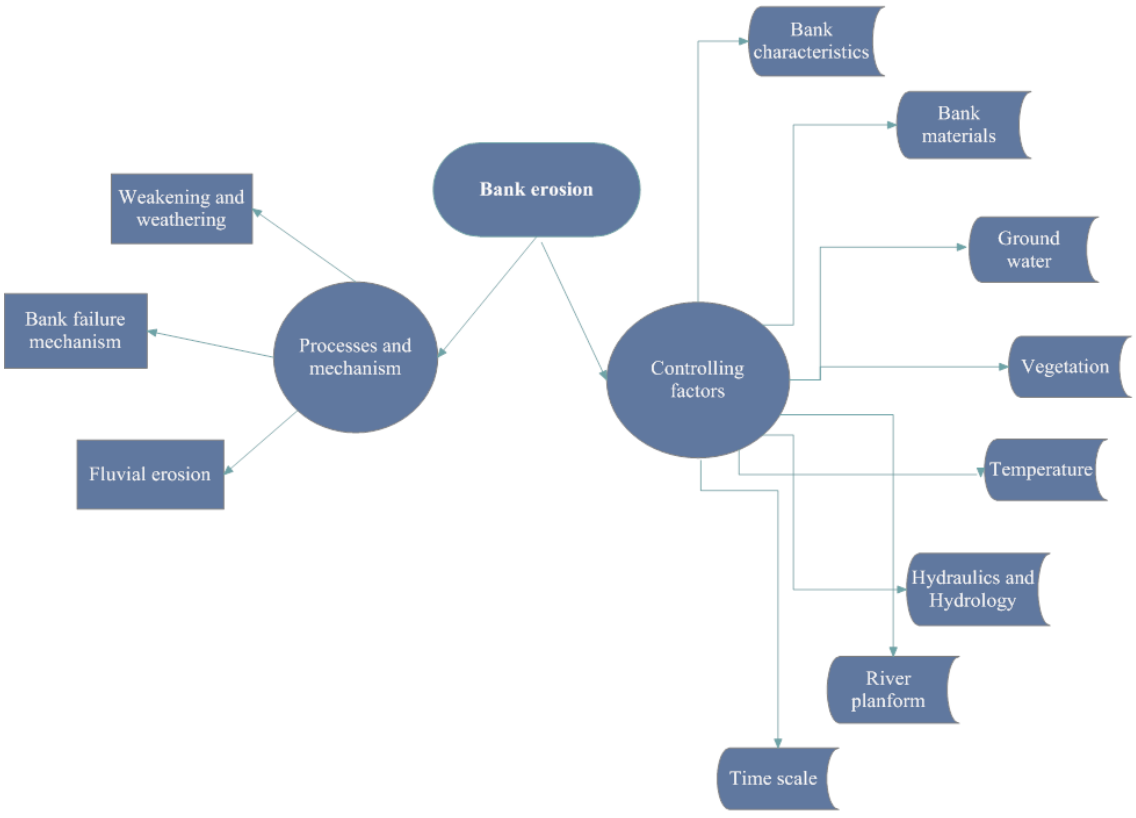

Figure 2.15. Bank erosion processes and controlling factors

Papers	River name	River type	Hydro climatic regime	Bank material characteristic	Methods used
Simon et al. (2000a)	Goodwin Creek	Sinuous channel	Climate is warm and humid.	Cohesive brown clayed silt over grey blocky silt	Limit Equilibrium Method
Simon et al. (2000b)	Missouri River	Sinuous, severe bends	Continental climate with warm, wet summer and harsh coild winter	Upper layer of clay and sandy silt basal layer	Fluvial erosion model and Seep/w, BSTEM
Dapporto et al. (2001)	Arno River	Low degree of sinousity	Temparate climate zone with a dry in the summer, a minimum rainfall in July, maximum rainfall in early and late winter.	3.6m bank height, mean slope 71°; clay, sand and silt sand bank materials.	Seep/w and Slope/w
Dapporto et al. (2003)	Arno River	Low degree of sinousity	Temparate climate zone with a dry in the summer, a minimum rainfall in July, maximum rainfall in early and late winter.	Six main types: fine-grained bank; sand, gravel and cobble bank; composite bank, silty sand and clay and silt bank, coarse basal layer bank; sandy and silty clayed bank.	Seep/w and Slope/w

Rinaldi et al. (2004)	Sieve River	Single thread, sinuous pattern	Climate is temperate, dry in the summer	Mostly cohesive sediment, cobbles included. Non-cohesive material at bank toe	Seep/w and Slope/w
Darby et al. (2007)	Sieve River	Single thread, sinuous pattern	Climate is temperate, dry in the summer	Mostly cohesive sediment, cobbles included. Non-cohesive material at bank toe	Seep/w, Slope/w couple with fluvial erosion model
Chu-Agor et al (2008)	Little Topashaw Creek	Sinuous channel	Temporal climate	Silt loam upper layer, loamy sand middle layer and clay loam lower layer	Seep/s and Slope/w
Parker et al. (2008)	Goodwin Creek	Sinuous channel	Climate is warm and humid.	Cohesive brown clayed silt over grey blocky silt	BSTEM, Seep/w, Sigma/w
Luppi et al. (2009)	Cecina River	Predominantly sinuous and locally meandering	Temparate climatic zone with a dry in the summer	Cohesive upper portion, gravel toe	DELFT3D, Seep/w and Slope/w
Nardi et al. (2010)	Cecina River	Sinuous river and locally meandering	Climate is temperate, dry in the summer	Cohesive upper layers, coase gravel/cobble bank toe	BSTEM, River 2D, HEC-RAS

Table 2.1 Bank erosion studies and simulation approaches

Table 2.1 shows some bank erosion studies which have adopted similar simulation approaches with this study. More details about the methodology will be described in the next chapter.

2.3.1 Bank characteristics and properties

Bank height is one of the most important factors affecting critical failure surfaces. Combined with the bank material type, it can cause different kinds of bank collapse; the mechanism of bank failure is related to the properties of the individual material stratigraphy that make up the bank (Grissinger, 1982). For low, steep banks, the mode of bank collapse often is planar, slab or block slides moving outwards and downwards to the channel. In contrast, for high, shallow angle banks, rotational slips often occur, and the failure block tends to rotate backwards as its toe slides outwards to the river.

Another important difference is bank sediment composition. The large scale of the Mekong river means that there is little coarse material in the lower basin, thus fine grain size sediments are present all the way down to the bank toe (Figure 2.17). It is very different from somewhere like the River Severn or River Cecina or Goodwin Creek where there is gravel at the bank toe (Figure 2.16).

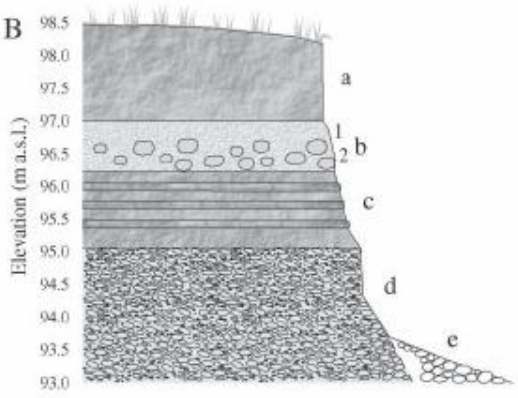

Figure 2.16. Bank stratigraphy of Sieve river (Italy): a, massive silty fine sand; b, sand (b1) with cobbles included in the lower portion (b2); c, silty sand, with regular sublayers of silt; d, packed and imbricated sand, gravel and cobbles; e, loosely packed gravel and cobbles (Rinaldi et al., 2004)

Figure 2.17. River bank stratigraphy at Ang Nyay (18°3'15.9"N 102°19'5.5"E) (photo taken in 10.2008), sand is the upper layer, clay is middle layer and mottle clay is the lower layer.

2.3.2 Channel gradient

In terms of river morphology, slope also is a big difference between the two types of river. Because slopes control shear stress, the fluvial erosion processes are different too. The slope in the upstream area is relatively high in low stream order rivers; while it is less in large, high stream order rivers such as the Mekong (Figure 2.18). Gracia et

al. (2010) shows that slope of some tropical rivers in America such as Parana is 0.00024, Grande is 0.00069, Iguazu is 0.00010 while the overall slope in the Mekong is 0.0002 for the whole system.

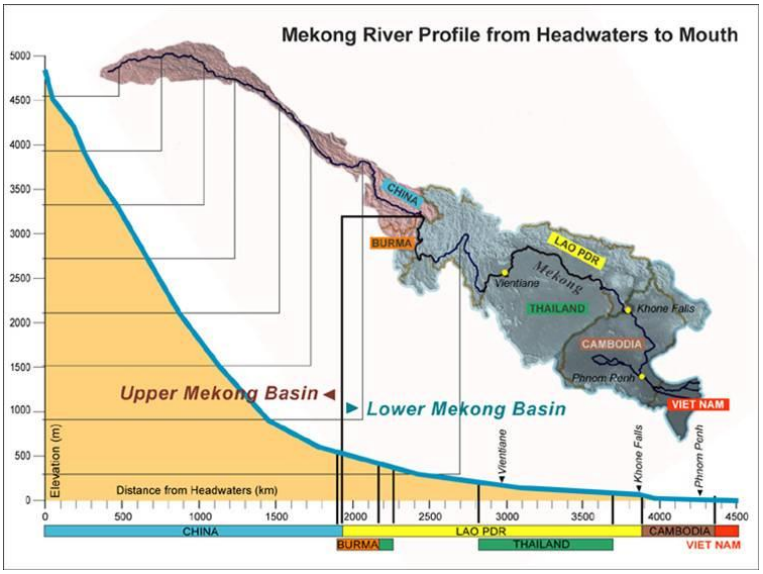

Figure 2.18. Mekong river profile from Headwaters to Mouth (MRC, 2005)

2.3.3 River planform

The shape of the river might influence the tendency for bank erosion or not. As we investigated the Mekong river (Figure 2.19), there are some places in which bank erosion occurs. In the literature, mostly the erosion occur at a straight reach or the outer bend of the river (Hooke, 1980; Rinaldi et al., 2004; Julian and Torres, 2006) but in the Mekong, the wide variety of wide planforms with erosion styles show that there are some other controlling factors which are not known from previous studies.

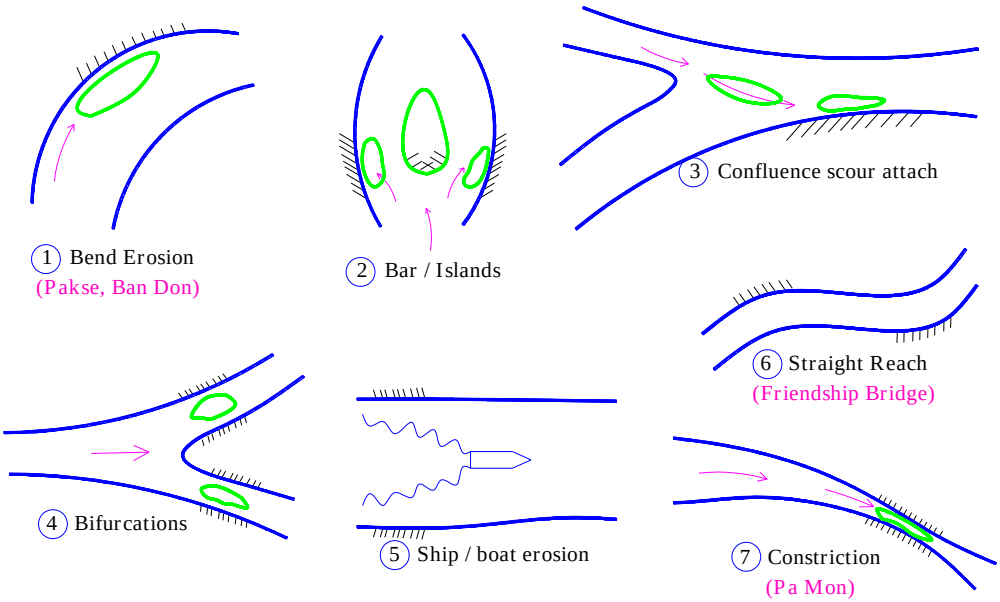

Figure 2.19. Erosion style in the Mekong Delta

The note above has reviewed the bank erosion processes and mechanism, as well as developments of bank erosion calculation and modelling of bank erosion. In mass wasting, several methods have been upgraded from a simple geometry to complex finite element bank geometry (Geo-slope software). In fluvial erosion modelling, quantifying the erodibility parameters is still difficult but a novel device (CSM) is now helping to estimate the critical shear stress more accurately. Determining the near bank shear stress may be undertaken by very crude approximation (Chow, 1959; Lane 1955) or using assumptions about the channel shape (Flintham and Carling, 1988). Several controlling factors affecting bank erosion are named such as the pore water pressure, bank characteristics or hydraulic and hydrology conditions and all based on research conducted in humid-temperate areas. Therefore, in the next chapter, a method to model bank erosion processes at the Mekong river study sites will be described.

Chapter 3 The Methodology

To address the aims and objectives of this thesis, a series of methods were employed and these are described in this chapter. From the preceding literature review, the overall approach is to employ an integrated model of bank erosion, following the approach of Darby et al. (2007). However, this approach will be extended to include Kean and Smith's (2006ab) model, which parameterises the boundary shear stress exerted on the river bank. This hydraulic model accounts for the influence of form roughness imparted by natural topographic features (slumps, embayments, etc) that are characteristic of the Mekong's river banks. By repeating the integrated analysis at a number of selected study sites which encompass a range of bank material characteristics, and across a range of monsoonal flow regimes, the outputs of the model can be used to build a large database of simulated bank erosion events that can be analysed to investigate what are the key controlling factors on the Mekong.

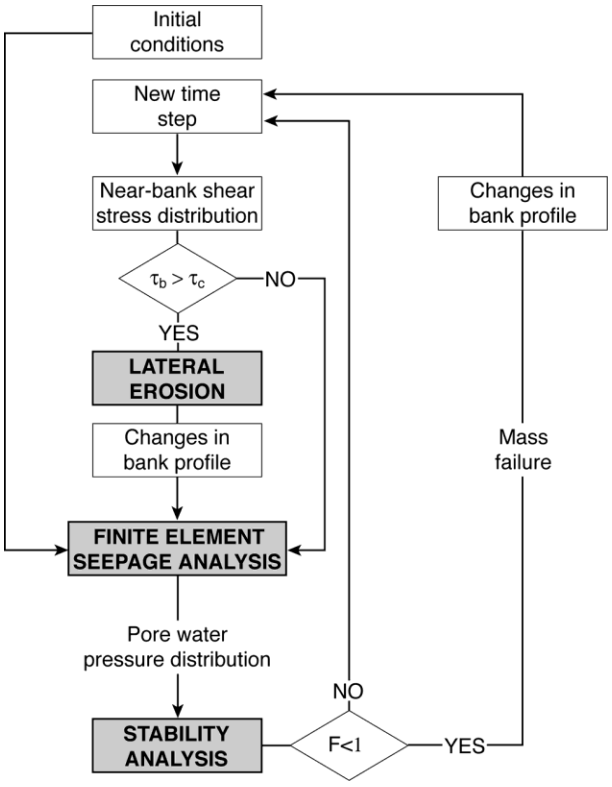

Figure 3.1. Computational algorithm of Darby et al. (2007) employed in the bank erosion simulations conducted herein. The shaded boxes represent the three sub-models (lateral fluvial erosion, finite element seepage analysis, and bank slope stability analysis) described in more detail in the text.

Figure 3.1 illustrates the logic diagram used in the analysis of Darby et al. (2007). There are three sub-models for modelling saturated and unsaturated flow, bank stability and fluvial erosion. A number of models are capable of simulating seepage

flow, but Seep/w was selected here based on its accuracy in several previous studies such as Darby et al. (2007); Rinaldi et al. (2004); Daporto et al. (2003); Simon et al. (2002); and Rinaldi and Casagli (1999). For the same reason, Slope/w software was used for simulating bank stability. In addition, Kean and Smith's (2006ab) method is applied to model fluvial erosion, by partitioning the total shear stress into skin friction and drag stress. Therefore, the details of methods and data parameters which are used to address the three sub-models are described in the following sub-sections.

3.1 The Mekong River[1]

The Mekong is the 12th longest river in the world, has a total length of 4880 km, draining a pan-shaped basin (795,000 km2) within the six countries of China, Myanmar, Lao PDR, Thailand, Cambodia and Viet Nam to the South China Sea (Figure 3.2). It is a globally significant river, with a monsoonal hydrological regime. Based on its mean annual discharge and suspended load, the Mekong is ranked as the 8th and 10th largest river in the world, respectively (Meade, 1996). In China, the Mekong River is known as the Lancang with the mountainous terrain, 0.0065 of gradient in steep V-shaped mountain valleys except for some wider river valleys between 3000m and 1000m. The river finally reaches an altitude of 310m at the river port of Simao. The terrain and the nature of the river remain similar until just a few kilometres upstream of Vientiane. The total vertical drop in the river within China is about 4500m. However the river drops only about 500m over the remaining 2600km to the South China Sea, giving an average slope of about 0.0002 for the whole system. The Upper Basin makes up 24% of the total area and contributes 15% to 20% of the water that flows into the Mekong River. Major tributary systems develop in the Lower Mekong Basin. These systems can be separated into two groups: tributaries that contribute to the major wet season flow, and tributaries that drain low relief regions of lower rainfall. The first group are left bank tributaries that drain the high-rainfall areas of Lao PDR. The second group are those on the right bank, mainly the Mun and Chi Rivers that drain a large part of Northeast Thailand.

[1] This section is heavily based on Carling (2009b) and MRC (2005).

Figure 3.2. Location of study sites within the Lower Mekong River Basin. Google Earth images show the local context for the study sites at Ang Nyay, Friendship Bridge and Pakse. The locations of bank material sampling sites (see text for latitudes and longitudes) are indicated by the open circles (Darby et al., 2010).

The climate of the Lower Mekong Basin (LMB) is dominated by the Southwest Monsoon, which generates wet and dry seasons of more or less equal length. The flood period in the LMB corresponds to the Southwest monsoon season which usually lasts from May until late September or early October. There are usually heavy rainfalls during one or two days in most parts of the basin. Later in the season, tropical cyclones occur over much of the area so that August, September and even October (in the delta) are the wettest months of the year. The Lower Mekong Basin is divided into six sub regions for the comparison of annual and monthly rainfalls and changes in space and time. Annual average rainfalls over the Cambodian floodplain and the Mekong delta are equally low and less than 1,500 mm. Elsewhere the highest rainfall is expected in the Central Highlands and within the mainstream valley at Pakse. Rainfall is less important in the more temperate northern regions around Chiang Rai. July, August and September are generally the months of highest rainfall, although there is evidence of a shift later in the season in Cambodia and in the delta where more rain falls in September and October. Tropical storms and cyclones have a strong effect on the climate of the basin. This effect shows up as a double peak in rainfall distribution over most of the Lower Mekong Basin during a wet period or season, and the concentration of maximum rainfalls during the last quarter of the year in Cambodia and Viet Nam. Tropical cyclones over central and southern Vietnam show that the occurrence of the cyclones is more frequent in the period September to November, causing higher rainfall during these months, which may generate flash floods in the tributaries.

The flooding of the Mekong River is a recurrent event caused by high water levels in the mainstream. Every year the Lower Mekong Basin (LMB) experiences flooding, which has the potential to adversely affect economic and human activities, often claiming lives and causing damage to important infrastructure, human settlements and essential services. The water level in flood may overflow lower sections of the embankment or local backwater may occur in ditches or small tributaries. Additionally, if there is heavy rainfall at the same time in areas where runoff is substantial (urban areas), there may be limited or no drainage. The flooding period is limited to the time the water level in the Mekong is at its highest, generally not more than one or two weeks. Flooding is seen as damaging as it may wash out infrastructure and houses. Casualties and loss of cattle are generally limited as the flood may be predicted easily by observing the water level of the Mekong, making preparedness easier. The limited duration of flooding does not have much effect on the rice production. Mitigation measures for limiting damage from such floods consist mainly of regulating land use, of limiting settlement and human activities in the risky areas, of diverting the flood to wetland areas where possible.

The flood in the Mekong Delta. The yearly flood is characterised by extended areas inundated by water from the Bassac River, the Mekong River and the numerous natural and artificial canals linking the two rivers that flow laterally to low lands. Sometimes, high water levels in the Bassac/Mekong systems may not drain easily to the sea due to tidal effect. This was the case during the severe 2000 flood in the downstream provinces of the Mekong Delta. Water level rises slowly for a long period. Every year there is substantial damage from these high water levels, primarily as a result of people drowning and from soil erosion damaging houses and infrastructure. Flooding is recognised as essential for soil fertility and biodiversity, but at the same time is perceived as an obstacle to the development of agricultural production and urbanisation. There is great pressure to protect land against floods by building dykes and backfilled areas. Land use planning and keeping the balance between socioeconomic and the environmental concerns remains a key issue for the future of the Mekong Delta.

3.2 Study sites

This eroded bank (left bank) is located at Ang Nyay. The total bank height is 13.2 m and bank materials consist of cohesive sediments.

Ban Hom (left bank), 12.5 m height with cohesive sediment materials.

Friendship Bridge (left bank) with 13.2 m bank height and bank materials consist of silty sand, silt and clay.

Ban Don (left bank), located 60 km downstream from Vientiane, 12m bank height and bank materials consist of cohesive sediments.

Pakse (right bank) consists of sandy silt and silty clay with 13.4m bank height.

Figure 3.3. Field reconnaissance along the Mekong

Figure 3.3 shows a field reconnaissance along the Mekong river (within Laos PDR). The bank heights are ranging from 12 to 14 m with bank materials compose of cohesive sediments. However, not all sites in this survey are conducted further research. The three sub-models in this research (Figure 3.1) require large amount of data such as: hydraulic data, hydrological data, bank geotechnical data, bank roughness data…Therefore, due to shortage data of some eroded sites (i.e no available aDCP data at Ban Don), there are three study sites were selected namely Ang Nyay (18°3´15.9´´N 102°19´5.5´´E), Friendship Bridge (17°52´59´´N 102°42´59´´E) and Pakse

(15°5´55´´N 105°47´58´´E). At all three sites, the channel type is single-thread or divided sinuous. The channel width at Friendship Bridge and Ang Nyay is about 1000 m with average channel gradient approximately 1.0×10^{-4} (Carling, 2009ab; Gupta and Liew, 2007). Pakse has a wider channel width of about 2 km and its gradient is 0.00006. Bank material at the study sites mostly is fine-grained, cohesive, sediment with bank heights typically higher than 10 m. There are commonly two climate seasons in the Mekong due to its monsoonal region location: the dry season (December to May) and the wet season (June and November) which exhibits a prolonged inundated flow hydrograph. Mean annual flow at Vientiane and Pakse is 4500 m^3/s and 9860 m^3/s, respectively.

3.3 Modelling seepage flow

Saturated and unsaturated flows in river banks are herein simulated by groundwater seepage analysis using Seep/w (Geo-Slope International, 2002). Seep/w is a software product that uses the finite element method to model the movement and pore-water pressure distribution within porous materials such as soil and rock. Its comprehensive formulation can analyse both simple and highly complex seepage problems. Seep/w is a seepage analysis program that models both saturated and unsaturated flow.

The inclusion of unsaturated flow in groundwater modelling is important for obtaining physically realistic results. In soils, the hydraulic conductivity and the water content, or water stored, changes as a function of pore-water pressure. Seep/w models these relationships as continuous functions. The software performs a two-dimensional, finite element seepage analysis using the governing equations of motion (Darcy's law) and mass conservation, the latter expressed here in a form extended to unsaturated conditions. The governing differential equation used in the formulation of Seep/w is:

$$\frac{\partial}{\partial x}(k_x \frac{\partial H}{\partial x}) + \frac{\partial}{\partial z}(k_z \frac{\partial H}{\partial z}) + Q = \frac{\partial \theta}{\partial t} \tag{3.1}$$

where H = total head (m), k_X = hydraulic conductivity in the horizontal x-direction (m/s), k_Z = hydraulic conductivity in the vertical z-direction (m/s), Q = unit flux passing in or out of an elementary cube (in this case an elementary square, given that the equation is in two-dimensions) (m^2/m^2s), θ = volumetric water content (m^3/m^3), and t = time (s).

To perform the groundwater flow modelling, each investigated riverbank was discretised into a series of finite elements, with regions of different materials being

defined to reproduce the observed bank stratigraphy. Application of the groundwater flow model requires a parameterization of the hydraulic and physical properties of these bank sediments. This process primarily involves the definition, for each type of sediment present at a specific bank location, of relations between hydraulic conductivity (k) and pore water pressure (u) (i.e. the hydraulic conductivity function or k-curve), and between the volumetric moisture content (θ) and pore water pressure (u) (i.e. the volumetric water content function or characteristic curve). The k-curves and characteristic curves of the different materials were estimated using empirical relations specific to each type of material that require the grain size distribution of each layer of sediment.

The groundwater flow model also requires the specification of boundary conditions along the borders of the finite element grid. The conditions including rainfall intensity and water stage, which are obtained in this study from observed data. These aspects are now discussed in the following parts.

3.3.1 Volumetric water content

One of the required input parameters for a transient analysis in the Seep/w model is the volumetric water content function. Because it can sometimes be difficult or time-consuming to obtain a volumetric water content function in a laboratory, it may be of benefit to develop an estimation of the volumetric water content function using either a closed-form solution that requires user-specified curve-fitting parameters, or to use a predictive method that uses a measured grain-size distribution curve. Seep/w has four built in methods available to estimate a volumetric water content function: Arya and Paris (1981); Modified Kovac (Aubertin et al., 2003); Fredlund and Xing (1994); and Van Genuchten (1980). The two latter methods are closed-form solutions that can be used to develop a volumetric water content function based on the user's knowledge of a group of three parameters: the 'a' parameter is the inflection point of the volumetric water content function; the 'n' parameter controls the slope of the volumetric water content function, and; the 'm' parameter controls the residual water content. Due to the lack of values for these parameters, these two methods Fredlund and Xing (1994); Van Genuchten (1980) are not used herein. The Arya and Paris (1981) and Modified Kovac (Aubertin et al., 2003) methods both use a grain-size distribution to estimate the volumetric water content so they were chosen for use in this study. The Arya and Paris (1981) method is used for sandy material, while the modified Kovac methods applied to silt and clay materials. The seep/w software has built-in functions for these methods, so the only input data required are grain-size data and the volumetric water content at saturated condition which were both measured in laboratory. Wet sieving is

used to analyse for part of sample larger than 64 microns while Coulter Counter is applied for the part less than 64 microns.

3.3.2 Hydraulic conductivity functions

Analysing saturated-unsaturated seepage processes requires establishing the hydraulic conductivity versus pore-water pressure relationship. In the seep/w software, several published and verified methods have been incorporated into the program to aid in the determination of these functions. There are three separate methods built into the model that can be used to predict unsaturated hydraulic conductivity functions based on the use of an estimated volumetric water content function and a specified value of the saturated hydraulic conductivity. These methods are due to Fredlund et al., (1994); Green and Corey (1971); and Van Genuchten (1980); moreover, all these predictive methods have been verified in the literature. These estimation methods generally predict the shape of the function relative to the saturated conductivity value in the Equation 3.2. The Green and Corey (1971) method was chosen to predict the conductivity function in this study as (1) when applying the model in data of environment, it offers the advantage of requiring only grain size data; and (2) it has applied successfully in previous research (Dapporto et al., 2001; Rinaldi et al. 2004; Darby et al. 2007).

Saturated conductivity can be estimated by particle size analysis of the sediment of interest, using empirical equations relating conductivity to some size property of the sediment. Numerous investigators have studied this relationship and several formulae have resulted based on experimental work. Kozeny (1927) proposed a formula which was then modified by Carman (1937, 1956) to become the Kozeny-Carman equation. Other attempts were made by Hazen (1892); Shepherd (1989); Alyamani and Sen (1993); and Terzaghi and Peck (1964). The applicability of these formulae depends on the type of soil for which hydraulic conductivity is to be estimated. In this study, the Kozeny-Carman's method is used as it is one of the most widely accepted equations:

$$K = \frac{g}{v} \times 8.3 \times 10^{-3} \left[\frac{n^3}{(1-n)^2} \right] d_{10}^2 \qquad (3.2)$$

where: g is gravity acceleration, v is kinematic viscosity, n is porosity and d_{10} represents the grain diameter for which 10% of the sample is finer. This method is used because the range of conditions for which this method has been calibrated matches the range of conditions found on the Mekong.

3.3.3 Hydrological data

The hydrological data which was available from the Mekong River Commissions were flow discharge and rainfall. The water stage data was converted from the discharge data through the rating equations which were obtained from the hydrometric stations on the Mekong mainstream (MRC, 2007). The Pakse study site uses data from the Pakse gauge while the Vientiane gauge supplies data for the Friendship Bridge study site and the Ang Nyay study site.

At the Pakse study site, the daily discharge data are available from 1923-2007, but rainfall data are only available for the period 1981-2007. The Friendship Bridge and the Ang Nyay study site have a longer series of data which last 94 years (1913-2007) for the daily discharge data and 56 years (1951-2007) for the rainfall data.

With a wide variety of hydrograph shapes representing the above observed data, it is very important to choose the hydrographs which represent a range of variability of the Mekong's monsoonal regimes. All hydrographs were classified into three categorise namely: (1) single peak hydrograph, (2) multiple peak hydrograph and (3) rapid fall hydrograph (see Fig 4.15, Fig 5.8 and Fig 6.8 for ranges of hydrographs). The statistical 'box and whiskers' method is used to select the representative events (Figure 3.4, Figure 3.5). In this study, the single peak hydrographs were employed as these occur at any river in any region. The multi-peak hydrographs are significant as the river banks are more likely to become unstable under the effect of a later peaks rather than the initial peak (Rinaldi et al., 2004) and because multi-peak hydrographs increase the incidence of wetting (Knighton, 1998). Rapid fall hydrograph was selected because bank mass failure often occurs during the rapid drawn down phase (Dapporto et al., 2003).

Four parameters are considered for each type of hydrograph including, rate of rise, rate of fall, Vrise/Vfall (volume of the rising part and falling part of the hydrograph) and peak magnitude (is expressed here through the use of a recurrence interval calculated by a probability method (m+1)/n). These parameters are significant in this study because they affect seepage flow within the river bank which in turn potentially affect bank stability. The peak magnitude is the most important value as the larger the flood, the more vulnerable the river bank.

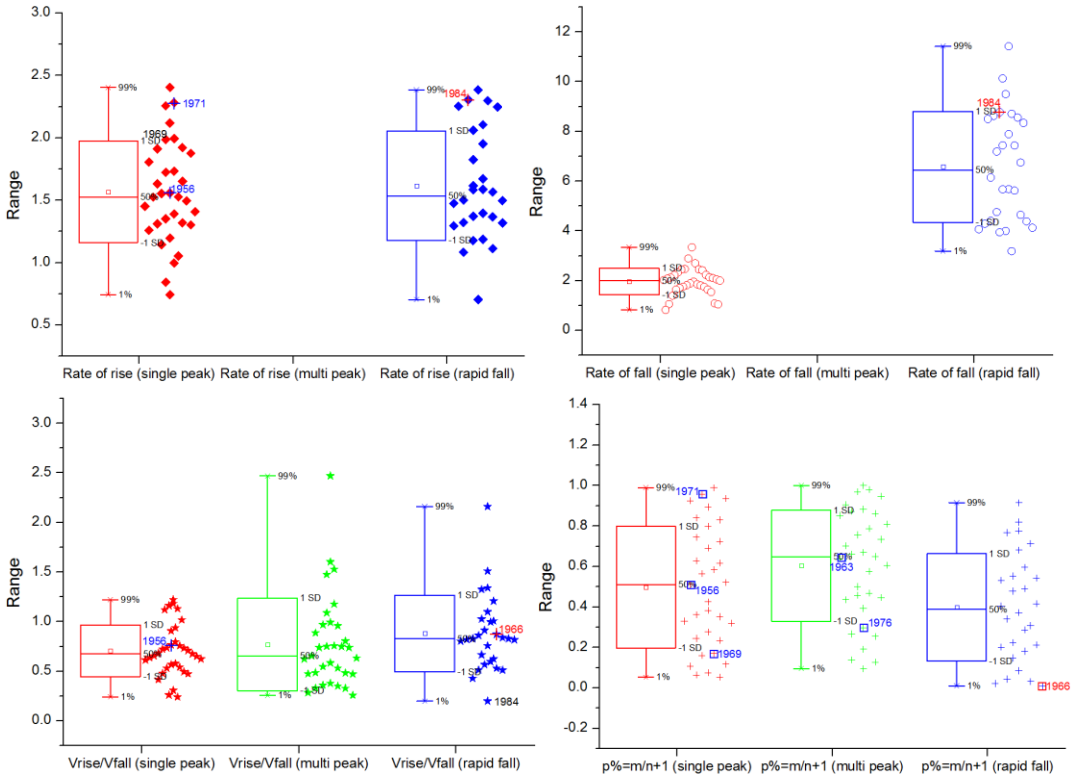

Figure 3.4. Statistical diagram of hydrographs at the Vientiane study site, with box on the left and data on the right on each diagram. Range of the box represents standard deviation; range of whisker is 1%-99%. Centre of the box expresses the mean value while the line in the box shows the median value. Red colour represents single peak hydrograph, green colour represents multi-peak hydrograph and blue colour is for rapid fall hydrograph. Different symbols express the statistical parameters (◆ is for Rate of rise, ○ is for Rate of fall, ★ is for Vrise/Vfall and + is for magnitude).

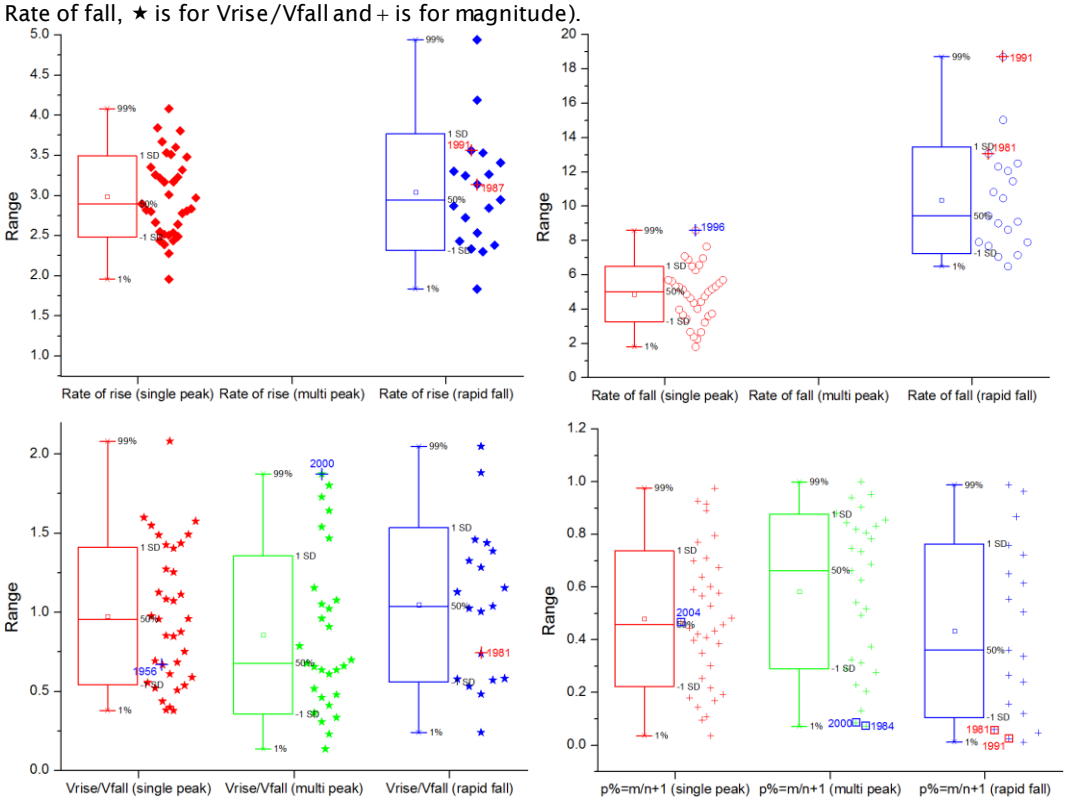

Figure 3.5. Statistical diagram of hydrographs at the Pakse study site (with similar caption in Figure 3.4)

All the data for the three types of hydrograph are plotted in Figure 3.4 and Figure 3.5. For each type of hydrograph, four parameters are calculated and expressed in box and whisker diagrams. Flow events which plot closest to the extreme value; the mean and median value; and to encompass one standard deviation are selected. Based on these criteria, these events which appear in more than once are picked i.e. at Vientiane, single hydrograph type, the 1946 event is an extreme value of parameter Vrise/Vfall, as well as coincidence with the mean and median value of the rate of rise parameter. The 1971 event is an extreme value in terms of the magnitude and rate of rise parameters.

For events which only appear once (i.e. at Vientiane, multi-peak hydrograph type), the magnitude parameter is preferable. However, because of the limited rainfall data (1981-2007 for Pakse; 1951-2007 for Vientiane), events outside of these periods are ignored. Therefore, the final flow events which are selected for river bank stability simulation on the Mekong are:

(1) at Vientiane: 1956, 1963, 1966, 1969, 1971, 1976, 1984 (for Friendship and Ang Nyay study sites).

(2) at Pakse: 1981, 1984, 1987, 1991, 1996, 2000, 2004 (for Pakse study site).

Of the above hydrographs, the 1966 event for Vientiane and the 2000 event for Pakse are paid special attention because they are historical floods for the rapid fall and multi-peak criteria, respectively.

3.3.4 Boundary conditions

Boundary conditions were defined as follows: (1) for the nodes along the bank profile, a total head versus time function was defined based on the observed hydrograph of the simulated flow event; (2) for the nodes at the top of the bank, a rainfall intensity versus time function was assigned, again using observed data; (3) for the lower horizontal boundary and for the right vertical boundary, a zero flux boundary function was assigned, these regions being always saturated.

3.4 Slope stability analysis

Bank stability analyses were performed using the Limit Equilibrium Method. For each time step of the hydrograph, the bank profile geometry (accounting for possible deformation calculated by the fluvial erosion model), and pore water pressure distribution (obtained by the groundwater flow model) were used to perform the stability analysis. Slope/w software (Geo-Slope International, 2002) was used for this purpose. In this software package, the Morgenstern-Price method was preferred to calculate FS, using the Mohr-Coulomb failure criterion in terms of effective stresses for the part of the bank with positive pore water pressures, and the Fredlund et al. (1978) criterion for the unsaturated portion of the bank, the latter being expressed as:

$$\tau = c' + (\sigma - u_a)\tan\phi' + (u_a - u)\tan\phi_b \qquad (3.3)$$

where τ - shear strength (kPa), c' - effective cohesion (kPa), σ - normal stress (kPa), u_a - pore air pressure (kPa), ϕ' - effective friction angle (º), u - pore water pressure (kPa) and ϕ_b - angle (º) expressing the rate of increase in strength relative to the matric suction ($u_a - u$). The bank stability analysis therefore requires the geotechnical properties (i.e. shear strength parameters and unit weight) of each layer of material present at each study site to be specified. These geotechnical properties were determined via direct measurement in situ using a Borehole Shear Test (BST) apparatus. Note that no adjustments were made to the measured geotechnical properties to account for the presence of vegetation on the surface on the bank (i.e. the effects of vegetation were not considered in the analysis). Besides the geotechnical properties, the slope/w model also requires the confining water level and pore water pressure results which are obtained from the seepage analysis.

Borehole shear test

The borehole shear test (BST) apparatus is a portable device which provides a convenient method to accurately measure the drained shear strength of soils in-situ. Tests typically require between 30 and 60 minutes, and the results are available immediately. The main components of the BST are a shear head, a pulling assembly and a console which contains the pressure gauge. The pulling assembly is hand-operated by turning a worm gear to provide a uniform rate of strain, which is monitored by a strain gauge (Figure 3.6). The tests were conducted by locating the shear head inside a borehole at the desired depth. A normal stress is then applied to push apart two serrated stainless steel plates, pressing them laterally against the sidewalls of the borehole. After allowing the soil to consolidate at the applied normal stress, usually about 15 to 20 minutes for the first test and 10 minutes for the

following tests, the shear head is pulled slowly upward by the pulling system until shearing occurs. The shearing force is progressively increased until the soil fails, then the point of failure is identified by noting the peak reading on the shear-stress meter. This maximum shear stress is then plotted with the corresponding normal stress to produce a point on the typical Mohr-Coulomb failure envelope. The same procedure typically is repeated four to five times at progressively higher normal stresses to obtain a series of different failure conditions. Then the cohesion and friction angle of the tested soil are obtained based on the relationship between shear stress and normal stress. Because the same soil is tested, the data usually can be fitted linearly with a coefficient of correlation of 0.90, or better.

Figure 3.6. BST shear head (left) and the control system (right)

3.5 Modelling of lateral erosion

The computational algorithm in Figure 3.1 shows that lateral erosion is one of the three sub-models simulated in this research. A new method (Kean and Smith, 2006ab) to partition the drag on bank roughness elements into form drag and skin drag components (the latter driving the fluvial erosion on river bank) is employed in this research:

$$\tau_T = \tau_{sf} + \tau_d \tag{3.4}$$

where τ_T is the total shear stress on the boundary of the channel, τ_{sf} is the skin drag component and τ_d is the form drag component.

Calculating the form drag component τ_d in Equation 3.4 is important due to the presence of large-scale topographic elements on the bank surface (Figure 3.7A). Kean and Smith (2006a) defined form drag (F) on an individual roughness element as:

$$F = \frac{1}{2}\rho C_D H B u_{ref}^2 \tag{3.5}$$

where ρ is the density of water, H is the protrusion height of the element, B is the length of the direction perpendicular to the x and z axes defined in Figure 3.7B, u_{ref} is a reference velocity, and C_D is the drag coefficient of the element.

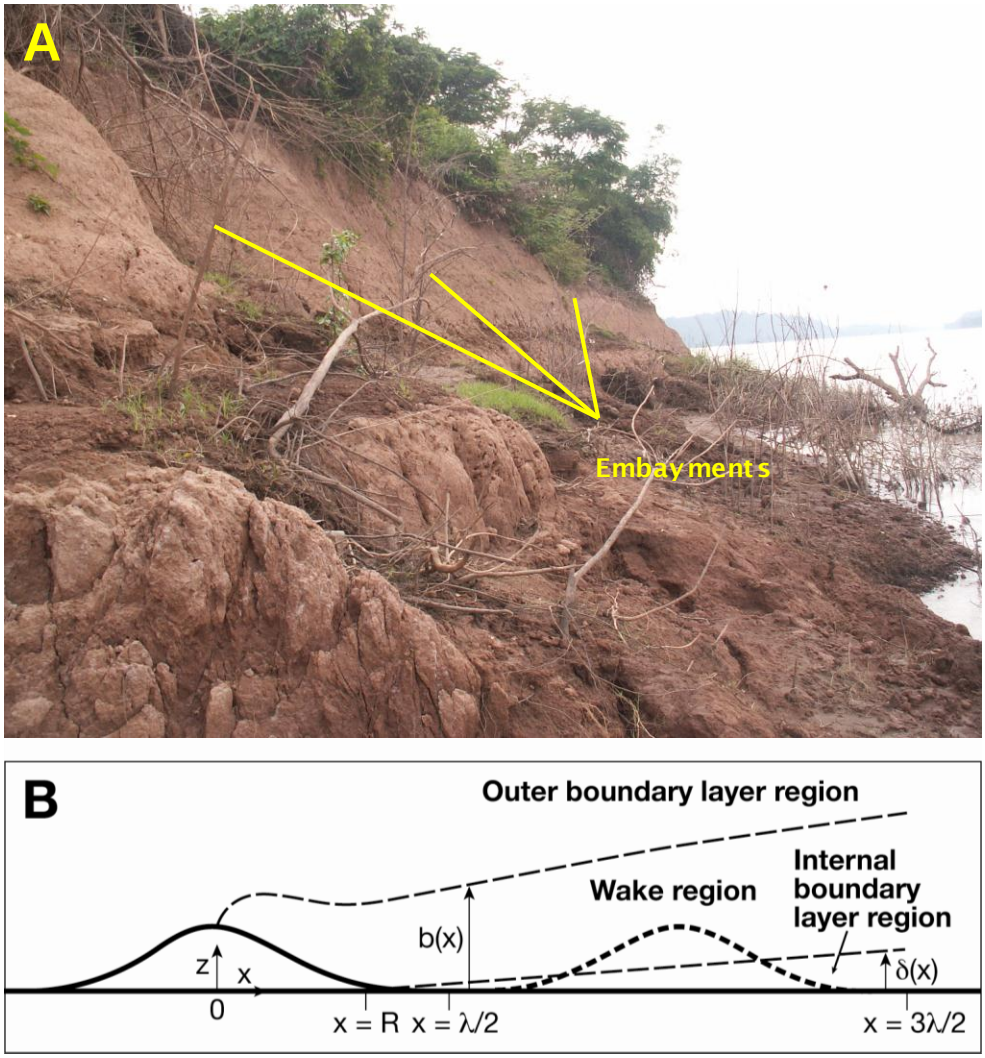

Figure 3.7. (A) Photograph of the river bank at the Pamong study site on the Lower Mekong River illustrating the bank protruding into the flow between embayments; (B) Overview of the Gaussian shaped plan view geometry of the modeled bank topographic roughness elements, along with the internal boundary layer, wake, and outer regions of the flow. The thick dashed line of the downstream element denotes that it is removed from the flow, with the u_{ref}^2 for this element being the average squared velocity over this area. The unit 'cell' from $\lambda/2$ to $3\lambda/2$ is the length over which the stresses are averaged (Darby et al. 2010). Panel (B) is reproduced from Kean and Smith (2006a).

This study follows Darby et al. (2010) (Appendix) which details about quantifying u_{ref}, in order to parameterise bank shear stress. Also parameterisation of bank roughness parameters, outer flow velocity and river bank erodibility parameters; all are described

in Darby et al. (2010). Results of that paper for Friendship Bridge, Pamong and Pakse study sites (below) are linked to river bank modelling which are illustrated in the following chapters (4, 5 and 6).

At Pakse: $\tau_{SF} = 0.4702 Ln(Q) - 3.1586$

At Ang Nyay: $\tau_{SF} = 0.2925\, Q^{0.1415}$

At Friendship Bridge: $\tau_{SF} = 0.0007\, Q^{0.775}$

Chapter 4 River Bank Stability Modelling at the Pakse Study Site

Based on the methods described in the last chapter, in this chapter the responses of the bank at the Pakse study site to a range of flow events are simulated. The input data used in the simulations (Table 4.1) are obtained from a combination of techniques involving in situ measurements, laboratory analysis and the use of empirically-derived functions, as detailed in Chapter 3. The results, presented below, show how the pore water pressure evolves and influences bank stability under a range of selected flow events, while the effects of fluvial erosion on the stability of the river bank are also evaluated.

Parameter	Symbol	Unit	Sediment layers		Note
			1	2	
			0 - 6 m	> 6 m	
Apparent cohesion	c_a	kPa	11..4	6.9	Data based on BST tests (see 3.3)
Effective friction angle	ϕ'	deg	33.4	35	Data based on BST tests (see 3.3)
Unit weight	γ	kN/m³	16.7 - 20.4	15.3 - 18.7	Data based on the samples which are taken from the site and analysed in the laboratory from dry to ambient condition
Porosity	n	%	35.7	41.0	Data based on the samples which are taken from the site and analysed in the laboratory
Saturated hydraulic conductivity	k_{sat}	m/s	1.32E-08	7.30E-09	Kozeny-Carman method based on grainsize data and porosity (see 3.2.2)
Critical shear stress	τ_c	Pa	1.02 ± 0.27	0.88 ± 0.47	Data based on CSM tests (Darby et al., 2010)
Erodibility Coefficient	k_d	m³/Ns	1.98E-07	2.13E-07	Hanson and Simon (2001)

Table 4.1. Geotechnical and hydraulic characteristics of bank material at Pakse (see Figure 4.2 for definition of sediment layers)

The river bank at Pakse is composed of two material layers with a total bank height of 13.4 m and a bank angle of 60° (Figure 4.1). The upper unit, which is some 6.0 m thick, is classified as a sandy silt with a porosity n=35.7% and a unit weight (under ambient conditions) of 20.4 kN/m³. The lower layer is a silty clay (thickness = 7.4 m) with a unit weight γ=18.7 and a porosity of 41%. The cohesion and friction angle of both layers were measured in situ using a borehole shear test apparatus, with values as illustrated in Table 4.1. The critical shear stress was also measured in situ using the cohesive strength meter jet-testing apparatus (see Section 3.3.1 and Darby et al. (2010) for a detailed description of BST and CSM sampling protocols, respectively).

Following previous studies (e.g. Dapporto et al., 2003; Rinaldi et al., 2004; Darby et al., 2007), the pore water pressure field within the bank was simulated via finite element

seepage analysis, with the bank discretised into a total of 21,300 quadrilateral elements. This mesh is finer than has been employed in previous bank stability investigations, with the typical cell size of the order of 0.1 m (Figure 4.2). This cell size is suitable for this study as it is sufficiently small to precisely update the bank profile following fluvial erosion; but it is not so small that the number of elements is increased to a point that requires excessive computational resource to run. Boundary conditions were defined at the bank top based on the observed rainfall intensity, while measured variations in water level (at the Pakse gauging station) were assigned to nodes along the river bank face. The remaining two vertical (left hand edge of model domain) and horizontal (bottom) boundaries were assigned as zero flux boundary conditions. With the assumption that the initial water table and river stage are in equilibrium, this initial ground water level is used to initialise estimates of pore water pressure assuming steady state conditions.

Figure 4.1. Pakse study site

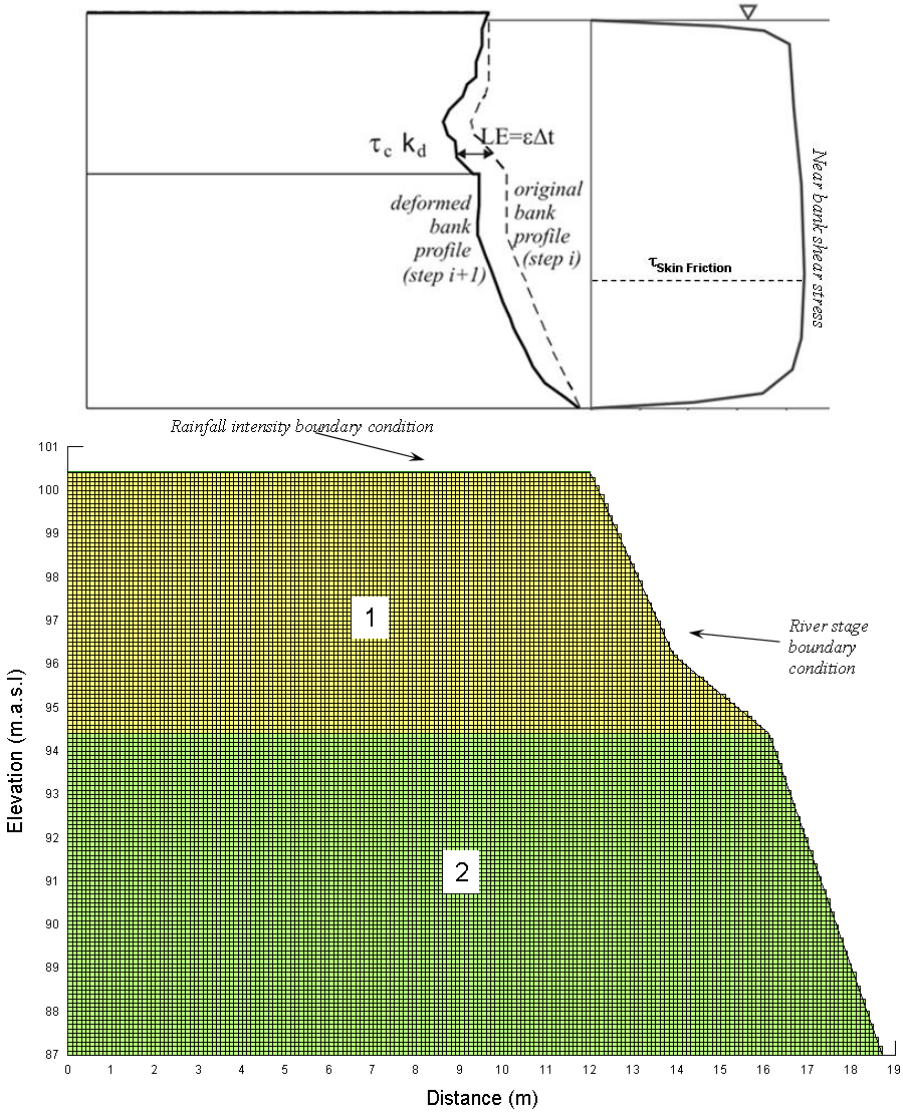

Figure 4.2. Overview of the seepage analysis and near bank shear stress distribution used to calculate fluvial erosion for the Pakse study site

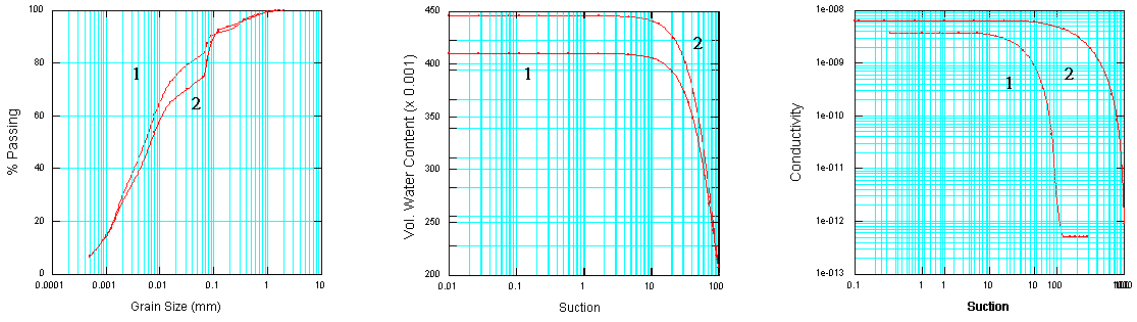

Figure 4.3. Bank material characteristics at the Pakse study site showing (a) the grainsize distribution; (b) soil water characteristic curves; and (c) hydraulic conductivity functions for the upper and lower layers of bank material

To model fluvial erosion during each simulated flow event, firstly, the shear stress which drives the hydraulic erosion τ_{SF} is obtained from Kean and Smith's (2006ab)

method for this study site (see Section 3.4). Then the Leutheusser (1963) approach is used to calculate the distribution of that shear stress along the full length of the bank profile. The Leutheusser distribution curve is applied to all nodes along the bank profile (Figure 4.2); the magnitude of the near-bank shear stress depends on the water level and skin friction shear stress at each time step.

Other input data for the seepage model are the hydraulic and physical properties of the bank materials. Figure 4.3 shows the relationships between hydraulic conductivity and pore water pressure (k-u) as well as volumetric water content and pore water pressure (θ-u). As discussed in Chapter 3, these functions were estimated based on the grain size distribution. Specifically, the Van Genuchten (1980) method was used to estimate the θ-u curve while the Green and Corey (1971) method was used to calculate the conductivity function.

Models were developed for a total of seven flow events (each of one calendar year duration), which were selected from the 87 years of flow records at Pakse (1923-2007) as discussed previously. Full details about these selected hydrographs are set out in Section 3.2.3 of the methodology chapter. Here is a summary of selected flows for Pakse: these flows were selected to represent annual hydrographs comprised of (i) a single peak hydrograph, (ii) a multiple peak hydrograph and (iii) rapid fall hydrographs. Due to the lack of rainfall data, which are only available for the period 1981-2000, simulated flows were selected from that period. The events observed in the years 2000 and 1981 represent the record flow and a large magnitude flow with recurrence probabilities of 2.38% and 8.33%, respectively. The 1987 event is the lowest flow year with an average daily discharge of only 7400 m^3/s. The 1996 and 2004 events are classified as single peak hydrographs, while the 2000 and 1984 events are multiple peaks hydrographs

Each hydrograph was discretised into 365 daily time steps. Table 4.2 summarises the flows selected for bank erosion modelling under the following three scenarios, which are designed to isolate the effects of fluvial erosion on bank stability. At the Pakse and Friendship Bridge study sites, two scenarios are applied but all three scenarios are applied at the Ang Nyay study site (see Chapter 5):

(1) There is no deformation of the bank geometry as no fluvial erosion is applied,

(2) There is no fluvial erosion but the bank profile is deformed by simulated mass wasting, and;

(3) The bank profile is allowed to freely deform in response to both simulated fluvial erosion and mass wasting.

	1981	1984	1987	1991	1996	2000	2004
Scenario 1	√	√	√	√	√	√	√
Scenario 2	n/a	n/a	n/a	n/a	n/a	n/a	n/a
Scenario 3	√	√	√	√	√	√	√

Table 4.2. Flow events and corresponding simulated scenarios at Pakse study site.

4.1 Results for the Year 2000 Hydrograph

In this section, results from the Pakse study site simulations for the flow year 2000 are analysed in detail while results for all the other flow events are summarised later, paying particular attention to the comparison between Scenarios 1 and 3 (Table 4.2). The year 2000 event hydrograph is characterised as a multiple peak hydrograph. The first peak, which is relatively small, begins its rise at 88.3 m a.s.l and reaches 92.2 m a.s.l at time step 144 (23 May 2000). After a slight draw down to 90 m a.s.l, it rises again to the second peak at 95 m a.s.l (time step 178, 26 June 2000). After decreasing to a flow stage of 93.9 m a.s.l, the river stage reaches a third peak at 98.2 m a.s.l, lagging the peak rainfall (step 198, 16 July 2000) by three days. A moderate draw down occurs after this as the water level goes down to a level of 94.9 m a.s.l (time step 235, 22 August 2000), but the flow then rises again to its highest peak at 99.8 m a.s.l at time step 259 (15 September 2000). It stays at the peak for only one day then decreases rapidly to 92.9 m a.s.l (step 295, 21 October 2000), prior to slowly declining until the end of the hydrograph.

4.1.1 Simulated fluvial erosion

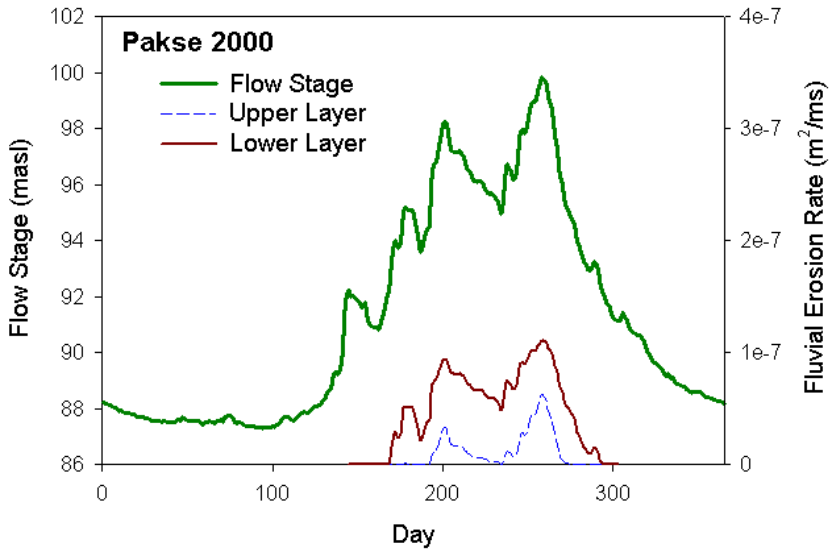

Figure 4.4. Simulated fluvial erosion for the year 2000 flow event at Pakse. Integrating the fluvial erosion curves across the duration of the hydrograph gives total bank eroded sediments of 0.89 and 4.90 m³/m for the upper (layer 1) and lower bank (layer 2) material layers, respectively.

Fluvial erosion is predicted to commence at time step 160 (8 June 2000), when the near bank shear stress exceeds the critical shear stress of the lower bank material. However, the erosion rate remains quite small until time step 192 (10 July 2000), after which point the bank profile begins to experience more significant deformation. The bank retreat at that time step is equal to the mesh size of 0.1 m. Erosion of the uppermost bank layer does not begin until time step 235 (22 August 2000) when the river stage begins to increase to its second peak. Figure 4.4 shows that the erosion rate of both the upper (layer 1) and lower (layer 2) layers increases and decreases in phase with the flow hydrograph. The rate of the fluvial erosion at the bank toe is double the rate at the bank top, due to the difference in erodibility (see Table 4.1). The duration of fluvial erosion at the bank top is from time step 167 (15 June 2000) to time step 265 (21 September 2000) (i.e., 98 days), which is much less than the duration of fluvial erosion at the bank toe (138 days). For these reasons the mean bank retreat integrated over the entire flow year at the bank toe and bank top due to hydraulic action is about 0.7 m and 0.2 m, respectively.

4.1.2 Pore water pressure

The seepage model provides spatially-distributed estimates of pore water pressure, to illustrate the evolution pore pressure. Figure 4.5 illustrates pore water pressure integrated along the whole failure surface Pw and along the saturated portion of failure surface Pw(+). Note that these parameters are selected here following Dapporto et al.

(2003) and Darby et al. (2007) because they are specifically relevant to quantifying the effect of pore water pressure on mass failure. By integrating the spatial field of simulated pore water pressure values along the failure surface, the parameters Pw(+) and Pw provide single estimates of the pore pressure field that are relevant to bank failure mechanics (see Darby et al., 2007). Both parameters are very important in controlling the bank failure mechanism, especially Pw(+), as apparently it affects the factor of safety computation through the weight of positive pore water pressure versus the weight of negative pore water pressure (the former being multiplied by $\tan\phi'$ and the latter by $\tan\phi_b$ (see Table 4.1)).

In general, Pw(+) follows the hydrograph but Pw has no clear trend, although it increases and decreases as the water level goes up and down. However, in both cases, the values simulated in scenario 3 are lower than that in scenario 1 when the hydrograph is on the rising limb, and the opposite is true on the falling limb of the hydrograph.

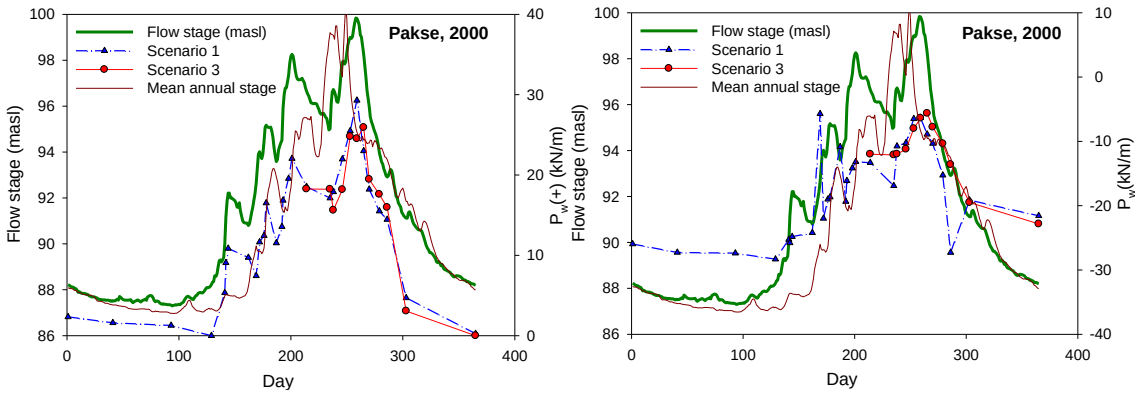

Figure 4.5. Evolution of average pore water pressure values integrated along the failure surface at the Pakse study site (event 2000) for scenario 1 (no bank deformation) and 3 (bank profile deformed by fluvial erosion): (Left) pore water pressure integral along the saturated portion of the failure surface and (Right) pore water pressure integral along the entire failure surface.

Further details of the pore water pressure distribution, in relation to the evolution of the event hydrograph and seepage flow characteristics (Figure 4.7 and Figure 4.8) are now described. Excluding time step 0, which is the initial condition when the water table and river stage are assumed to be in equilibrium, then the initial period of the simulation, which lasts between January and early April (time steps 1 to 93) involves a slight but progressive fall in water level from 88.2 m a.s.l to 87.3 m a.s.l as the dry season progresses. During this period, seepage flow is consistently directed from the bank towards the river, such that there is a seepage outflow at the intersection between the water table, the bank profile and the river stage, with a velocity of 7.33e-09 m/s (step 93, 2 April 2000). Note that this value is several orders of magnitude too small to cause seepage erosion. For example, Fox et al. (2007) shows average the

seepage erosion flow rate under low flow condition at Goodwin Creek is 0.05 l/min (approximately 2.08e-03 m/s). As such, the effect of seepage erosion can be discounted at this site at least during this period.

However, in the next phase of the simulation, from step 93 (2 April 2000) to step 129 (8 May 2000), there is a gradual rise in river stage (from 87.3 m a.s.l to 88.2 m a.s.l), most likely corresponding to the arrival of spring and snowmelt from the Tibetan headwaters. At step 129 (8 May 2000), when the river stage stays at the same level as the initial stage, the flow nearly stands at the intersection position where the water table, bank profile and river stage meet. Therefore, seepage flows are characterized by a change in the direction from the river to the bank during this period. The velocity at that intersection is 2.97e-09m/s. The water table lies below the potential failure surface so there is no appearance of positive pore water pressure. The average integrated pore water pressure Pw has a minimum value of -28.32 kN/m (step 129, 8 May 2000).

From step 129 (8 May 2000) to 162 (10 June 2000) there is a significant increase of flow stage as the water level rises to 92.2 m a.s.l (step 144, 23 May 2000), but this is still lower than the contact between the two sediment layers. It then declines a little to 90.8 m a.s.l (step 162, 10 June 2000). Positive pore water pressure occurs in the failure block with a Pw(+) value of 9.73 kN/m (step 162, 10 June 2000). The seepage flow is from the bank to the river, with the velocity at the intersection increasing to 8.4e-09 m/s. The matric suction near the bank top is reduced due to the effect of rainfall.

From step 162 (10 June 2000) to 187 (05 July 2000), the hydrograph exceeds the elevation of the contact between the two bank material layers, up to the level 95.2 m a.s.l (step 178, 26 June 2000), then drops to the stage 93.6 m a.s.l (step 187, 05 July 2000). A steep wetting front develops at the contact between the river and the bank profile. Rainfall occurs everyday due to the beginning of the wet season. The steep wetting front develops at the contact between the river and bank profile. The Pw(+) also increases to 16.52 kN/m and the seepage flow velocity also increases to 4.73e-08 m/s at the intersection (step 178, 26 June 2000).

The next phase of the simulation, from step 187 (05 July 2000) to 201 (19 July 2000), corresponds to a rapid rise in river stage to the first and minor peak (at 98.2 m a.s.l) in response to the onset of the monsoon. The river stage exceeds the contact between the two layers then rises to its peak. Rainfall occurs with a high intensity everyday. The highest daily amount of rainfall is measured at time step 198 (150 mm), three days

before the river stage rose to the second highest peak at time step 201. The wetting front has a very steep slope due to the low value of hydraulic conductivity. The pore water pressure distribution is illustrated within the higher regions at the top, close to the bank profile and lower area; while the lowest values occur in the middle. Pw(+) is calculated as 22.04 kN/m at time step 201 (19 July 2000). The seepage flow remains directed from the river into the bank, with a velocity of 1.58e-07 m/s at the intersection at the same time step.

From time step 201 (19 July 2000) to time step 235 (22 August 2000), this period witnesses the river stage decreasing to 94.9 m a.s.l, just above the contact between the two layers. The pore water pressure distribution shows that the minimum zone is reduced due to rainfall and river water infiltration, the value Pw(+) being reduced to 17.12 kN/m (step 235). With the onset of fluvial erosion, scenario 3 starts in this period (step 214, 01 August 2000) with a lower P(+) value in this time step but higher (18.23 kN/m) at step 235.

In the following phase of the simulation, from time steps 235 to 259 (which corresponds to the period between 22 August 2000 and 15 September 2000), the flow stage initially falls and then rises to the second and main peak (99.8 m a.s.l) due to a second pulse of monsoonal rainfall. The water level at the peak flow (step 259) is approximately at the bank full stage and high rainfall intensity occurs at this period leading to the significant change in pore water pressure distribution as the higher pore water pressure area increases. Pw(+) reaches its maximum value of 29.29 kN/m but the total average value of Pw is still less than 0. In scenario 3, all P(+) values in this period are less than that in scenario 1. The flow seepage remains directed into the bank with the velocity at the intersection being 3.33e-08 m/s.

From time step 259 (15 September 2000) to time step 279 (05 October 2000), the drawdown phase of the hydrograph starts. The river stage rapidly reaches a low in this period. The seepage flow still remains directed into the bank, but the velocity at the intersection is reduced to 3.39e-09 m/s. The minimum pore water pressure zone also is reduced; Pw(+) decreases to 15.5 kN/m (step 279). All P(+) values in scenario 3 of this period are higher than that in scenario 1 and the maximum Pw(+) of scenario 3 occurs at time step 265 (21 September 2000).

From time step 279 (05 October 2000) to time step 365 (31 December 2000), the river stage continues to draw down but at a smaller rate than in the preceding period. The seepage flow direction begins to reverse in the upper part of the water table from time step 303 (29 October 2000), but again with a very low velocity of 4.65e-09 m/s. For

the lower water table, the seepage flow is still directly into the river bank. Note that all the simulated results such as pore water pressure distribution, factor of safety, failure surface and erosion rate are illustrated by animations, which are stored in an accompanying CD.

4.1.3 Bank stability and sediment entrainment

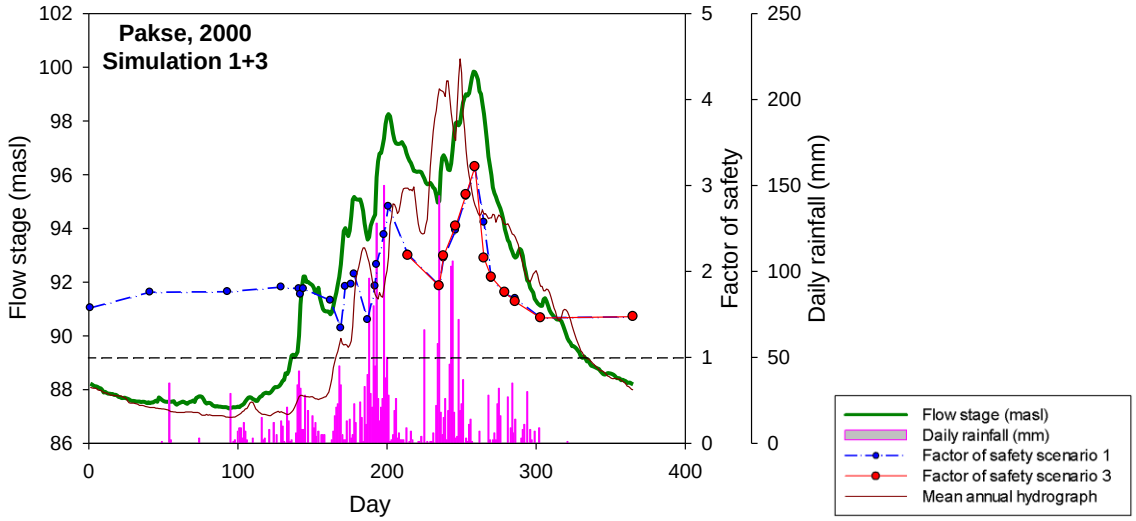

Figure 4.6. Hydrograph, rainfall intensity and simulated factors of safety of flow event 2000 for simulation scenario 1 (no fluvial erosion) and 3 (fluvial erosion) at the Pakse study site (for results for other events see Figure 4.15).

As illustrated in Figure 4.6 the factor of safety with respect to mass failure remains above the critical value of unity throughout the simulation period in both scenario 1 (no fluvial erosion) and 3 (with fluvial erosion), though considerable fluctuations in the value of the simulated factor of safety are evident throughout both simulations. In addition, and similarly to Darby et al. (2007), in both cases there is also a small net decline in stability by the end of the simulation period (for example the simulated factor of safety values exhibit a decrease of 0.104 and 0.101 for scenario 1 and 3, respectively, between the beginning and end of the simulation period). This reflects the destabilising (small in this example) effect of the elevated pore water pressures seen between the start and end of the simulation. There are only modest differences in the factor of safety values simulated under scenario 1 and 3 (except at time step 265, 21 September 2000), with factor of safety values for the latter scenario, as expected, being somewhat smaller (e.g. in time step 286 (12 October 2000), the FoS is 1.684 in scenario 1 and 1.647 in scenario 3) than the former scenario, indicating the net destabilising effect of fluvial erosion on mass stability.

Given the very small differences in the simulated factor of safety values for each simulation scenario, the simulated temporal variations in factor of safety in this case must be attributed to the varying values of pore water and confining pressure simulated during the course of each simulation. Thus, when the flow level is low (e.g. Figure 4.7, time step 129) the bank is dominated by negative (stabilising) pore-water pressures. In contrast, during peak flow, the immersion of the bank is sufficiently long to cause complete saturation and the generation of positive pore water pressures (Figure 4.7, time steps 235 to 259). When the river stage recedes on the falling limb, the water table also goes down along with the water level (Figure 4.7, time step 286), resulting in a significant reduction of hydrostatic confining pressure and thus factor of safety, but in this case the positive pore-water pressures generated by the prior flood are insufficient to trigger mass-failure.

Thus, it is apparent that, similar to Simon et al. (1999) and Darby et al. (2007), the dominating influence on bank stability is the hydrostatic confining pressure exerted by water in the channel, so that temporal trends of the factor of safety are strongly positively correlated with fluctuations in the flow hydrograph. For example, in scenario 1 (no fluvial erosion), the initial factor of safety is 1.575 but as flow stage increases the factor of safety also slightly increases to 1.758 by time step 41. When the river stage reaches the peaks observed at time steps 178, 201 and 259, the factor of safety also rises to 1.970, 2.755 and 3.206, respectively. By the end of the simulation, as flow stage decreases, the simulated factor of safety falls to its final value of 1.471.

As noted above, neither simulation scenario exhibits any mass wasting during the year 2000 flow event, even though fluvial erosion acts to reduce stability (scenario 3 simulation). The absence of mass wasting in scenario 3 can be explained by the fact that the magnitude and duration of simulated fluvial erosion during this event is rather small (see Section 4.1.1). For example, the bank profile only experiences deformation due to fluvial erosion from time step 214, and the overall magnitude of fluvial erosion at the bank toe (0.7 m) is rather small in relation to previous studies. Therefore, there is very little difference between the factor of safety in scenario 1 and 3. Unlike Darby et al. (2007) and Luppi et al. (2009), where the factor of safety in simulations with fluvial erosion (i.e., scenario 3) is always less than that in simulations without fluvial erosion (scenario 1), at Pakse the factor of safety in parts of the simulation scenario 3 is sometimes less than that in scenario 1 but in some time steps it is larger. At time step 214 (01 August 2000) and time step 235, the factor of safety at scenario 3 is less than scenario 1 (-0.6% and -0.3% respectively) but in the next four time steps, the factors of safety in scenario 3 are larger (1.2% (step 238, 25 August 2000); 2.0% (step 246, 02 September 2000); 0.7% (step 253, 09 September 2000) and 0.4% at step 259 (15

September 2000)). Overall, the differences between the factors of safety in both simulation scenarios are very small, typically around 1% except for time step 265 (21 September 2000), when a 16% difference is obtained.

Due to the absence of mass wasting failure in the year 2000, the volume of bank material entrained to the river is associated exclusively with that caused by fluvial erosion. The total unit volume of eroded sediment in this case is 5.79 m^3/m, with most (85%) of this being supplied from the lower unit of bank material due to the higher erosion rates that occur in this layer (Figure 4.4).

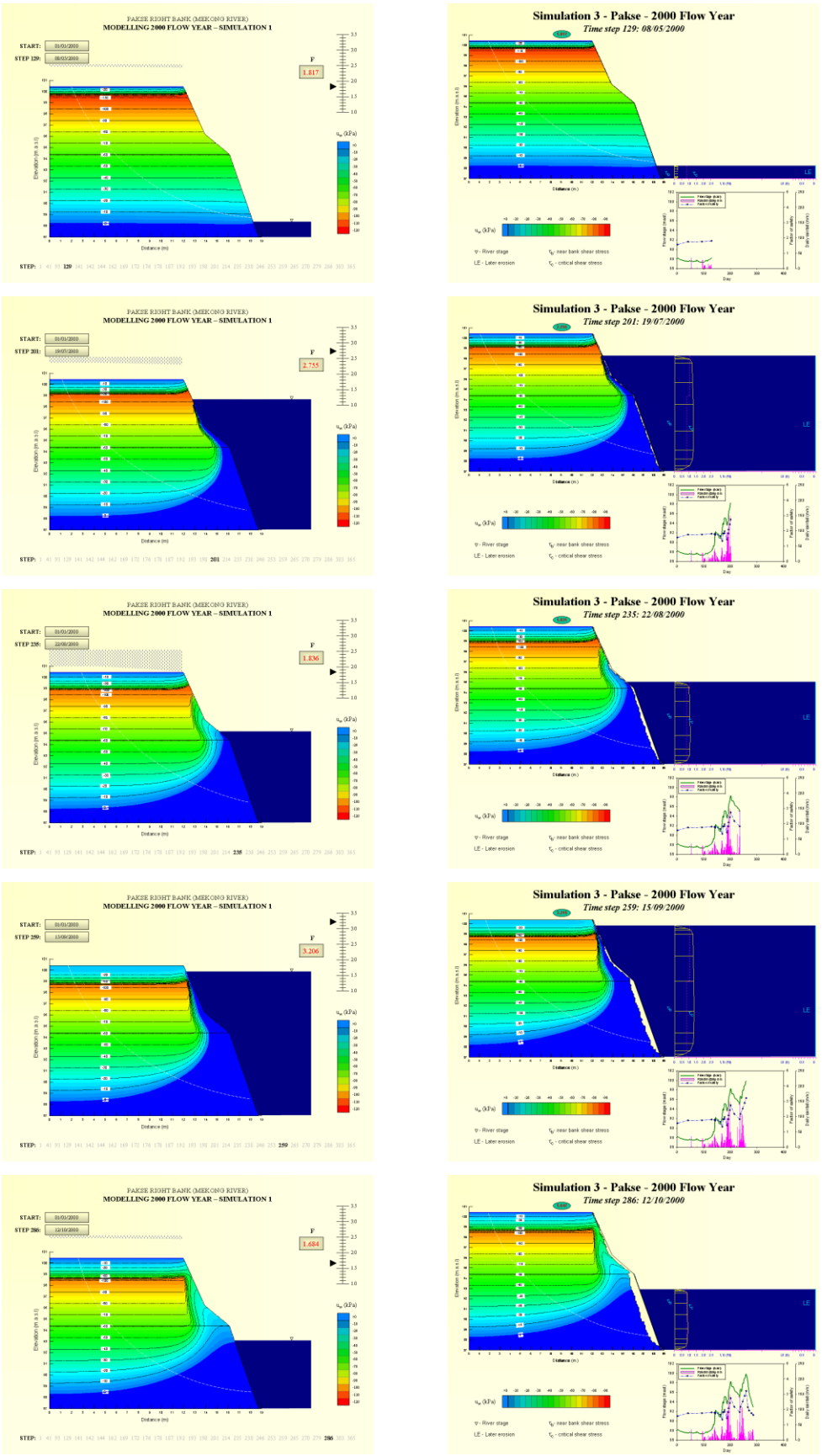

Figure 4.7. Simulated bank pore water pressure distribution for selected time steps at Pakse for scenario 1 (no bank deformation, left hand side) and 3 (bank profile is deformed by fluvial erosion, right hand side). Animations of the complete simulation sequence are available in the accompanying CD.

Step 93

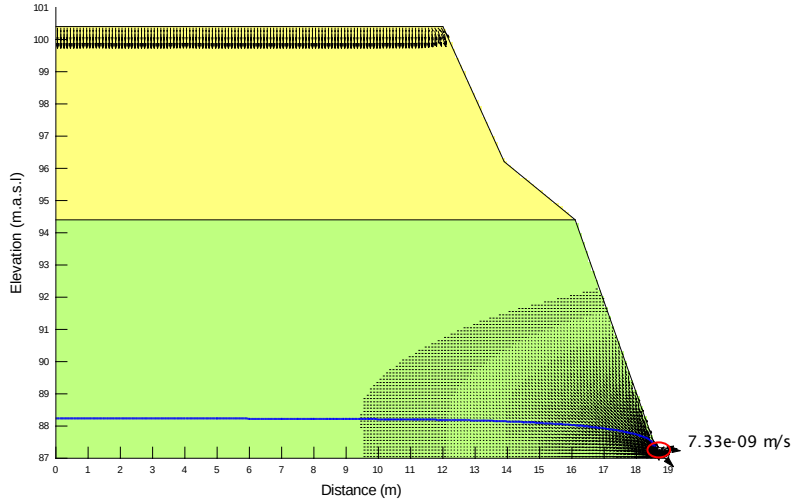

Step 259

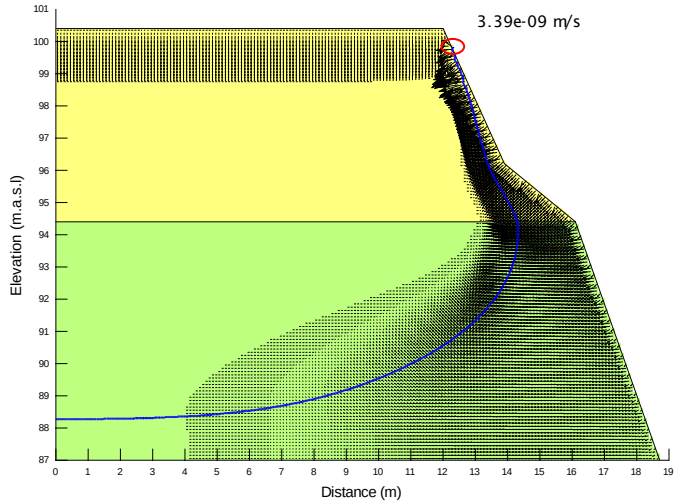

Step 303

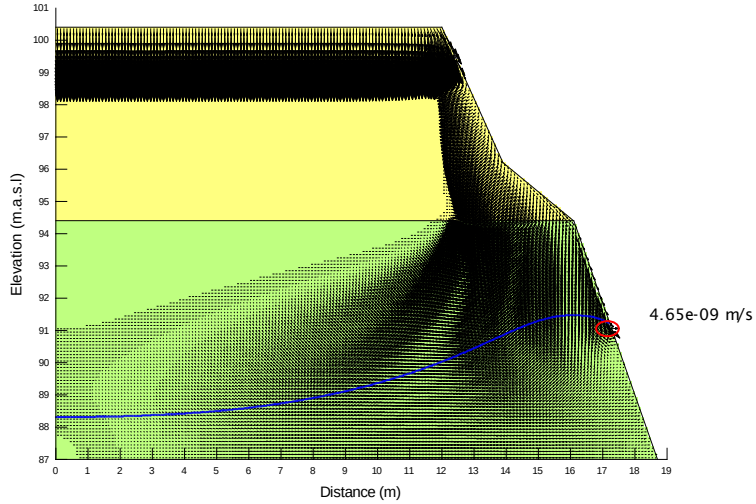

Figure 4.8. Simulated bank seepage flow for selected time steps at Pakse (scenario 1), green and yellow colour is river bank material, blue line is water table, and red circle is the intersection between bank surface, water table and river stage.

4.2 Results of other flow events

4.2.1 Results of 1981 flow event

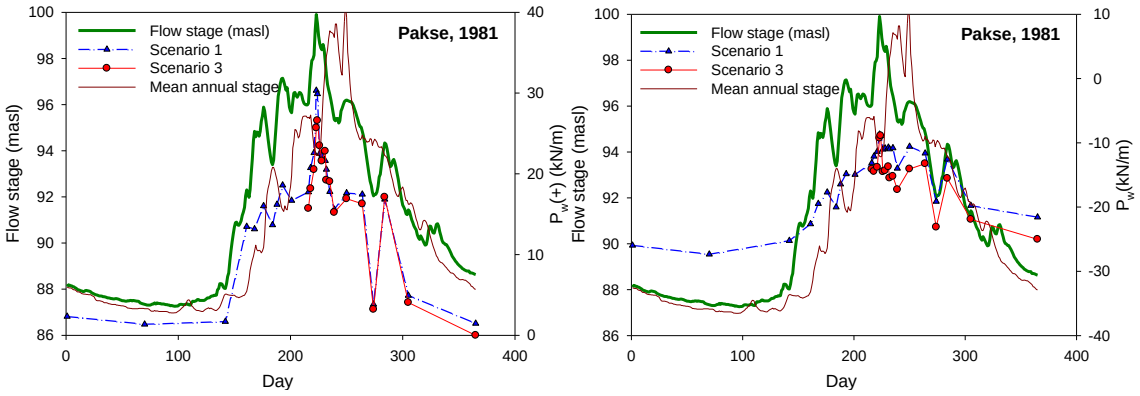

Figure 4.9. Evolution of average pore water pressure values integrated along the failure surface at the Pakse study site (event 1981) for scenario 1 (no bank deformation) and 3 (bank profile deformed by fluvial erosion): (left) pore water pressure integral along the saturated portion of the failure surface and (right) pore water pressure integral along the entire failure surface.

The 1981 flow hydrograph (Figure 4.9) is characterised as a typical single-peak hydrograph, with the peak discharge (Q_p = 45,500 cumecs) similar to the hydrograph of 2000, being a high flow event with a recurrence interval of 6.02%. The factors of safety, simulated for the 1981 event, follow in part the trend of the hydrograph. Similar to other events at Pakse, as well as Friendship Bridge and Ang Nyay (see Chapters 5 and 6), the FoS is greatest when the flow level is high; and indeed FoS > 1 at all times and for both simulation scenarios so the river bank remains stable with respect to mass failure throughout the 1981 event. The maximum factor of safety of 3.362 occurs in phase with the peak flow and the minimum factor of safety of 1.470 occurs at the end of the simulation, giving an overall range of simulated FoS of 1.892. The differences of factor of safety between the two simulation scenarios range between a minimum of 0.5% and a maximum of 6.5%. In the case of the 1981 flow event, pore water pressure values as integrated along the failure surface (i.e, the parameter Pw) remain negative throughout the whole of the simulation for both scenario 1 and scenario 3. Therefore, the fact that the pore water pressure has no effect on the stability (with respect to mass failure) of the river bank under this flow event is unsurprising, in that although there is a relatively high monsoonal flood, it fails to fully recharge the bank and elevate the pore water pressure field, most likely due to the relatively low hydraulic conductivity of the bank materials. Like other events at this study site, both the parameters Pw and Pw(+) exhibit clear trends which follow the hydrograph shape.

Rain occurs mostly everyday in the wet season of this year, so it keeps the discharge larger than the erosion threshold discharge and river stage is higher, leading to a long duration of fluvial erosion. The duration of fluvial erosion in this event is 138 days; only shorter than that in the event 2000. The total eroded volume is 4.962 m^3/m, of which ~90% is supplied from the lower layer.

4.2.2 Results of 1984 flow event

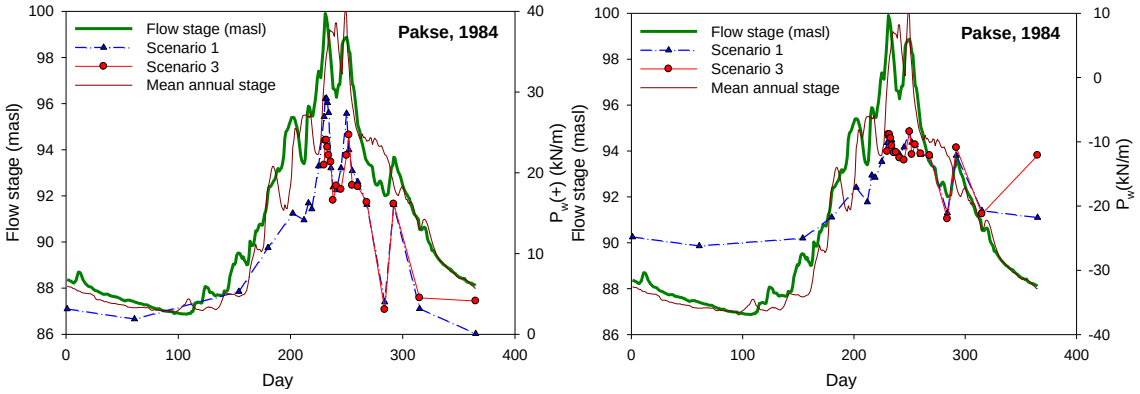

Figure 4.10. Evolution of average pore water pressure values integrated along the failure surface at the Pakse study site (event 1984) for scenario 1 (no bank deformation) and 3 (bank profile deformed by fluvial erosion): (left) pore water pressure integral along the saturated portion of the failure surface and (right) pore water pressure integral along the entire failure surface.

The 1984 flow hydrograph (Figure 4.10) is characterised as a multi-peak hydrograph with the second peak reached just after the rapid fall from the first peak. The magnitude of the peak discharge (Q_p = 45,500 cumecs) is quite high; as large as the hydrographs of 2000 and 1981, with a recurrence interval of 6.02%. The factors of safety simulated for the 1984 event follow mostly the trend of the hydrograph. The river bank remains stable with respect to mass failure throughout the 1984 flow event. The maximum factor of safety of 3.385 occurs in phase with the peak flow, and the minimum factor of safety of 1.480 occurs on the falling limb of hydrograph (step 315, 10 November 1984), giving an overall range of simulated FoS of 1.905. The differences of factor of safety between the two simulation scenarios range between a minimum of 0.3% and a maximum of 3.2%. In the case of the 1984 flow event, pore water pressure values, as integrated along the failure surface (i.e, the parameter Pw), remain negative throughout the whole of the simulation for both scenario 1 and scenario 3. Therefore, pore water pressure has no destabilising effect on the bank (with respect to mass failure) for this flow event. As noted previously this is most likely because of the low hydraulic conductivity of the bank materials.

The duration of fluvial erosion in this event is 124 days and the total eroded volume is 3.880 m^3/m, of which 87% is supplied from the lower layer.

4.2.3 Results of 1987 flow event

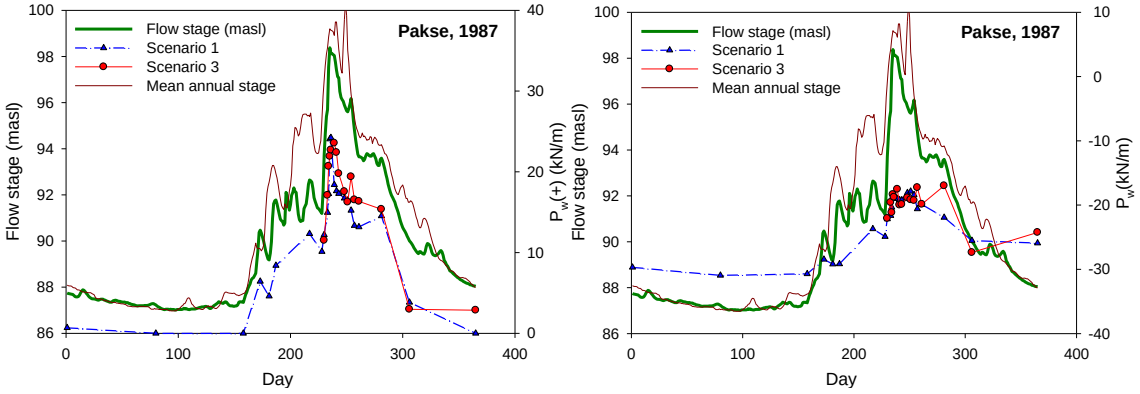

Figure 4.11. Evolution of average pore water pressure values integrated along the failure surface at the Pakse study site (event 1987) for scenario 1 (no bank deformation) and 3 (bank profile deformed by fluvial erosion): (left) pore water pressure integral along the saturated portion of the failure surface and (right) pore water pressure integral along the entire failure surface.

The 1987 flow hydrograph (Figure 4.11) is characterised as a typical single-peak hydrograph, with the peak flow (Q_p = 37,900 cumecs) being a relatively low flow event with a recurrence interval of 55.4%. Similar to other events, the FoS remains stable with respect to mass failure throughout the 1987 event. The maximum factor of safety of 2.965 occurs in phase with the peak flow and the minimum factor of safety of 1.543 occurs on the falling limb of the hydrograph (time step 306, 02 November 1987), giving an overall range of simulated FoS of 1.422. The differences of the factor of safety between the two simulation scenarios vary, ranging between a minimum of 0.0% and a maximum of 5.0%. In the case of the 1987 flow event, pore water pressure values, as integrated along the failure surface (i.e, the parameter Pw), remain negative throughout the whole of the simulation for both scenario 1 and scenario 3. Therefore, pore water pressure has no destabilising effect on the stability (with respect to mass failure) of the river bank for this flow event. Like other events at this study site, both the parameters Pw and Pw(+) exhibit clear trends which follow the hydrograph shape.

The duration of fluvial erosion in this event is only 93 days, the shortest of all the events simulated at Pakse, giving a total eroded volume of 4.108 m^3/m, of which 88% is supplied from the lower layer.

4.2.4 Results of 1991 flow event

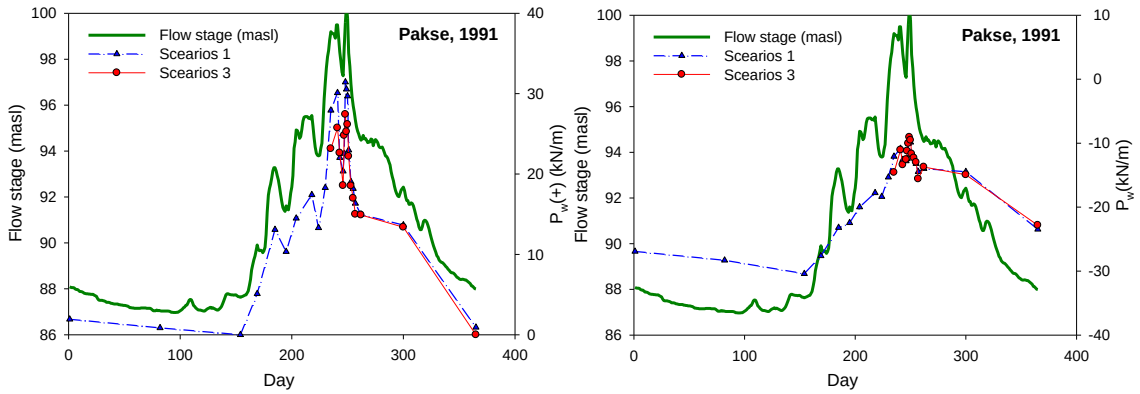

Figure 4.12. Evolution of average pore water pressure values integrated along the failure surface at the Pakse study site (event 1991) for scenario 1 (no bank deformation) and 3 (bank profile deformed by fluvial erosion): (left) pore water pressure integral along the saturated portion of the failure surface and (right) pore water pressure integral along the entire failure surface.

The 1991 flow hydrograph (Figure 4.12) is characterised as a multi-peak hydrograph, with the peak flow (Q_p = 47,600 cumecs) being the largest peak discharge of the selected simulation events (recurrence interval of 2.41%), but due to the rapid fall of the hydrograph and also is the mean annual hydrograph the duration of fluvial erosion is less and the least amount of erosion occurs in this year. The maximum factor of safety of 3.618 occurs in phase with the peak flow and the minimum factor of safety of 1.503 occurs at the end of the hydrograph (time step 365, 31 December 1991), giving an overall range of simulated FoS of 2.115.

4.2.5 Results of 1996 flow event

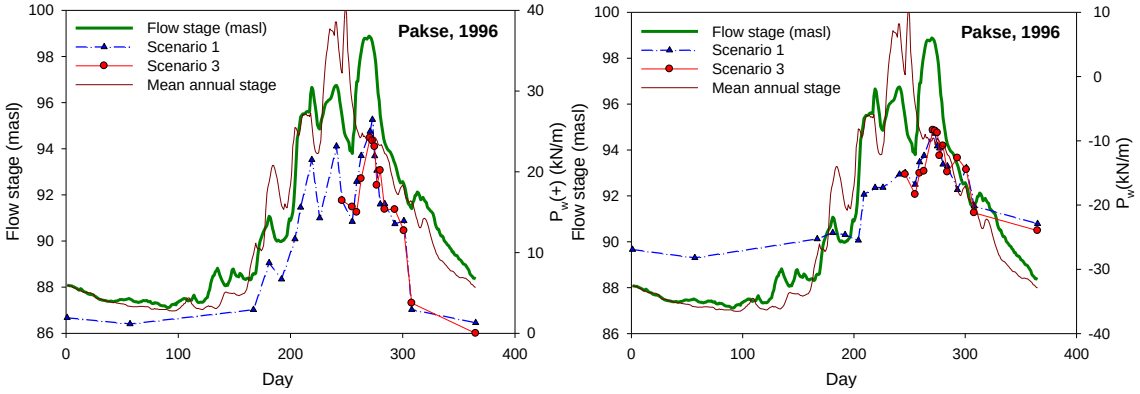

Figure 4.13. Evolution of average pore water pressure values integrated along the failure surface at the Pakse study site (event 1996) for scenario 1 (no bank deformation) and 3 (bank profile deformed by fluvial erosion): (left) pore water pressure integral along the saturated portion of the failure surface and (right) pore water pressure integral along the entire failure surface.

The 1996 flow hydrograph (Figure 4.13) is classified as a single peak hydrograph with the shortest days of fluvial erosion and average eroded volume of sediment entraining to the river, with the peak flow (Q_p = 40,300 cumecs) being a modest flow event (recurrence interval of the peak discharge of 30.12%). The factors of safety simulated for the 1996 event follows the trend of the hydrograph. Similar to all other events at Pakse, FoS is greatest when the flow level is high; and indeed FoS > 1 at all times and for both simulation scenarios: the river bank remains stable with respect to mass failure throughout the 1996 flow event. The maximum factor of safety of 3.000 occurs at time step 219 (06 August 1996), which is a minor peak before the main peak flow, and the minimum factor of safety of 1.492 occurs at the end of hydrograph, giving an overall range of simulated FoS of 1.508. In the case of the 1996 flow event, similar to other events at Pakse, pore water pressure values as integrated along the failure surface (i.e., the parameter Pw) remain negative throughout the whole of the simulations for both scenarios 1 and 3. Therefore, pore water pressure has no destabilising effect on the stability (with respect to mass failure) of the river bank for this flow event, for the same reason as noted previously. The duration of fluvial erosion in this event is only 110 days with a total eroded volume of 3.911 m^3/m, of which 89% is supplied from the lower layer.

4.2.6 Results of 2004 flow event

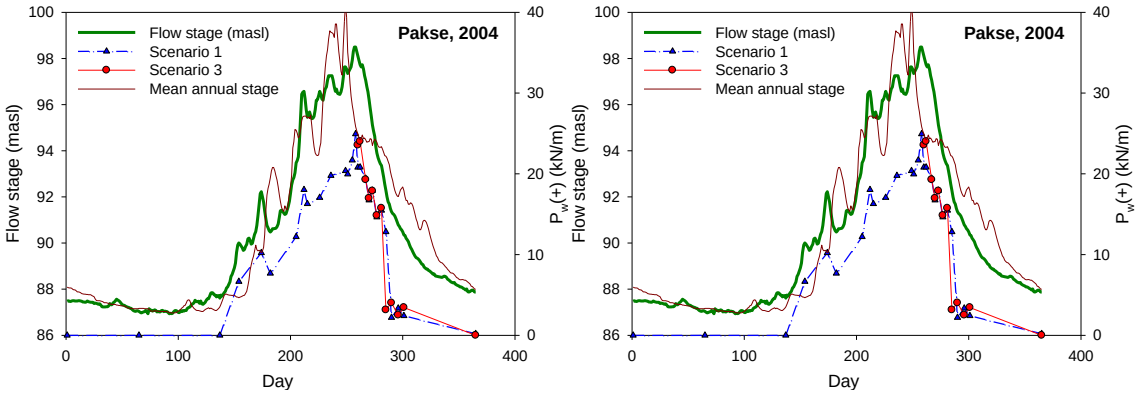

Figure 4.14. Evolution of average pore water pressure values integrated along the failure surface at the Pakse study site (event 2004) for scenario 1 (no bank deformation) and 3 (bank profile deformed by fluvial erosion): (left) pore water pressure integral along the saturated portion of the failure surface and (right) pore water pressure integral along the entire failure surface.

The 2004 flow hydrograph (Figure 4.14) is characterised as a typical single-peak hydrograph, with the peak flow (Q_p = 38,500 cumecs) being a modest flow with a recurrence interval of 46.99%. The maximum factor of safety of 3.206 occurs in phase with the peak flow and the minimum factor of safety of 1.557 occurs on the falling limb of hydrograph (time step 301, 27 October 2004), giving an overall range of simulated FoS of 1.649. In the case of the 2004 flow event, pore water pressure values, as integrated along the failure surface (i.e., the parameter Pw), again remain negative throughout the whole of the simulations for both scenario 1 and scenario 3. Therefore, pore water pressure has no effect on the stability (with respect to mass failure) of the river bank under this flow event which is unsurprising given the relatively low value of this monsoonal flood, but it fails to fully recharge the bank and elevate the pore water pressure field due to the low saturated conductivity of the bank materials. Like other events at this study site, both the parameter Pw and Pw(+) exhibit clear trends which follow the hydrograph shape. The duration of fluvial erosion in this event is only 112 days with a total eroded volume of 3.836 m^3/m, of which 88% is supplied from the lower layer.

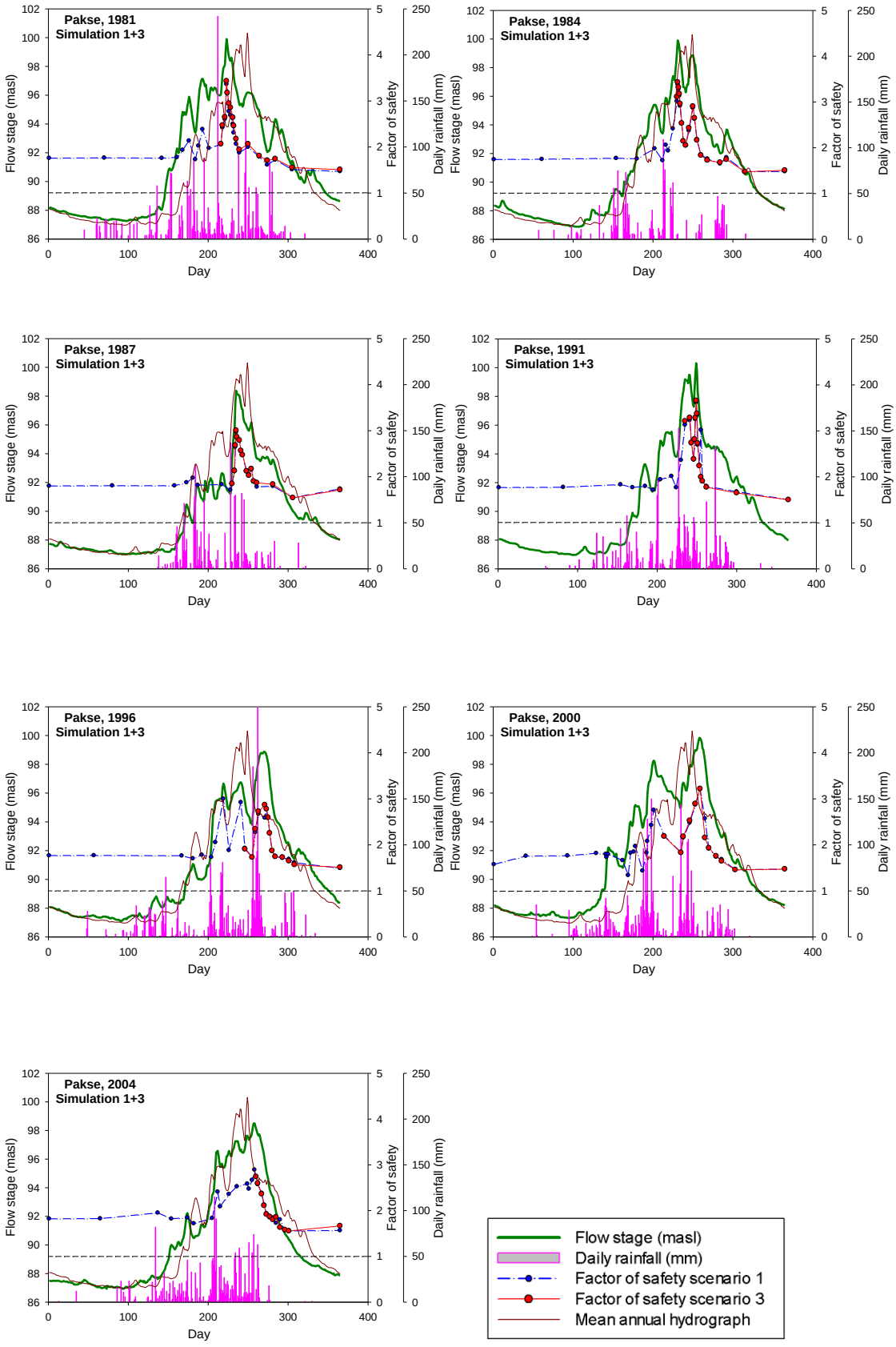

Figure 4.15. Hydrograph, rainfall intensity and simulated factors of safety for the selected flow events for simulation scenario 1 (no fluvial erosion) and 3 (fluvial erosion) at the Pakse study site.

4.3 Synthesised results at Pakse study site

In this section the principal findings from the simulations undertaken at the Pakse study site are discussed. The effects on pore water pressure distributions of variations in event hydrograph shape are explored first, because it has been shown that the pore pressure distribution, particularly as expressed by the parameters Pw and Pw(+), exerts an important control on the likelihood and timing of bank failure. Figure 4.16 shows the relationship between Pw, Pw(+) and the peak discharge (Q_{peak}) of each simulated flow event.

As can be seen from Figure 4.16A, as expected the peak pore water pressure Pw(+) max increases in proportion to the peak discharge (i.e. the largest flood event simulated (1991) generates the largest value of Pw(+), irrespective of the specific simulation scenarios (1 or 3)). The correlation of Pw(+) with Q_{peak} in scenario 1 has a very strong value of r^2=0.98, while the value of r^2=0.79 is somewhat less in scenario 3, the effect of fluvial erosion evidently introducing noise into the correlation. Note that the Pw(+) values for scenario 3 are always lower than those for scenario 1, with the difference increasing as Q_{peak} increases. Therefore, this is the reason why the riverbank is more stable in scenario 3: changes in bank geometry caused by fluvial erosion evidently act to reduce Pw(+) values, due to the change in seepage gradient between the eroding bank face and the incipient failure plane location.

Figure 4.16B shows that there is nearly an overlap between the line of regressions of maximum Pw in scenario 1 and 3 (red and green), with similar correlations of r^2=0.56 and 0.57, respectively. Similar to the regressions of maximum Pw(+), the trends of these two maximum Pw curves also increase along with the peak discharge. Clearly, Pw remains negative in both scenarios so there is no effect on the bank in terms of bank instability.

Because the correlation coefficients of above linear regressions are not high enough to indicate a strong relationship between peak discharge and pore water pressure, non-linear regressions have also been applied to the data (also in Figure 4.16B). Logarithmic trends are added but very little difference in the r^2 values appear. Polynomial trends, however give a much stronger correlation with r^2=0.95 for scenario 1 and r^2=0.94 for scenario 3. Although the polynomial fit gives very high r^2, it is difficult to think of physical explanation that this regression shows possible behaviours of the data. Therefore, linear fit is actually better for physical considerations. It is also worth noting that at the other study sites investigated in this research (Ang Nyay and

Friendship Bridge), polynomial fit gives very poor representation of behaviour. Therefore, for all these reasons, a linear regression is chosen.

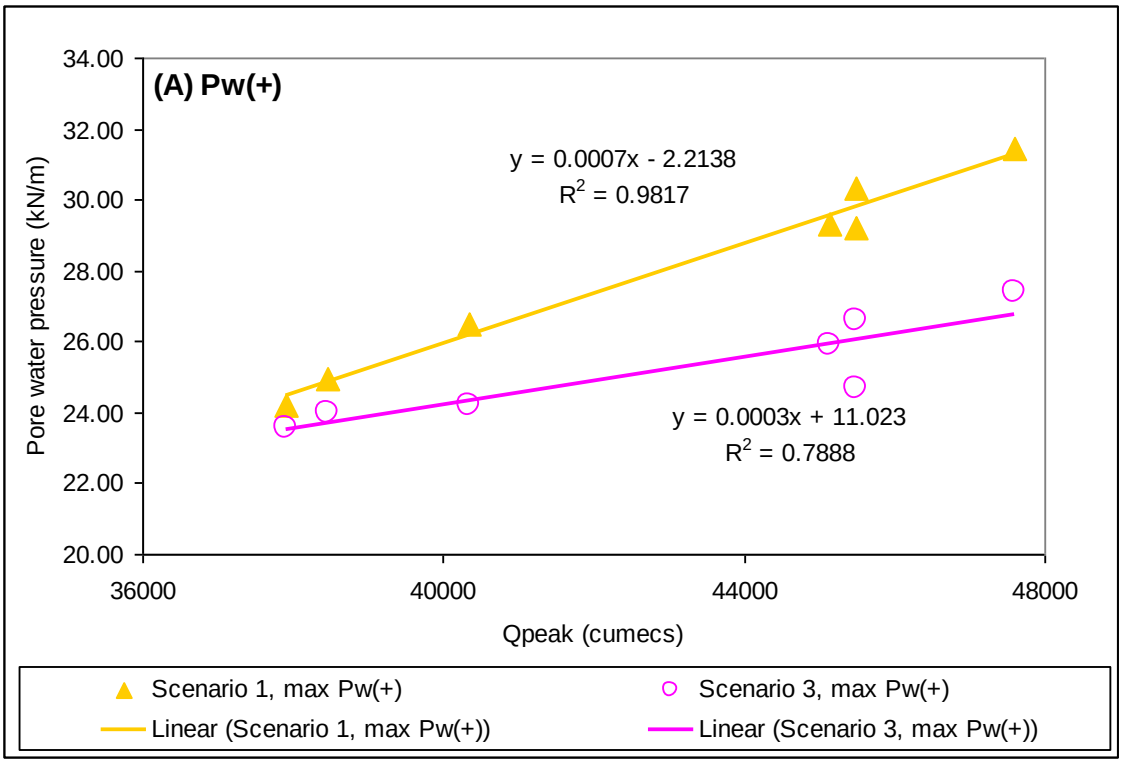

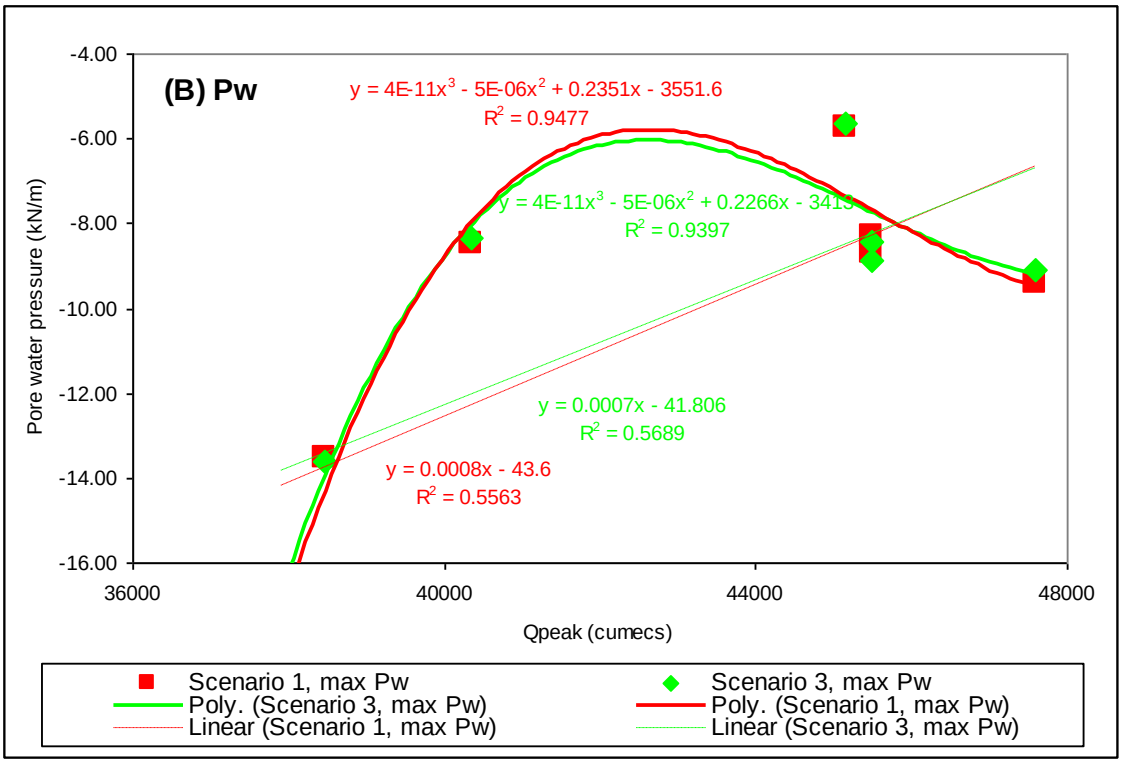

Figure 4.16. The maximum and minimum average pore water pressure integrated along the failure surface at the Pakse study site for simulation scenarios 1 and 3. Pw is the pore water pressure integral along the whole of the failure surface and Pw(+) is the pore water pressure integral along the saturated portion of the failure surface.

Following Luppi et al. (2009), Figure 4.17 presents a synthesis of the simulated factor of safety data results for Pakse, showing the relationship between bank stability and an index of the flood hydrology. Specifically, the simulation data are scaled to peak flow stage against total bank height D_{peak}/H_{bank} in order to facilitate comparison of results between Pakse, the Ang Nyay and Friendship Bridge study sites, as well as with other sites such as the Sieve River (Darby et al., 2007) and the Cecina River (Luppi et al., 2009). More details of this comparison will be described in Chapter 7.

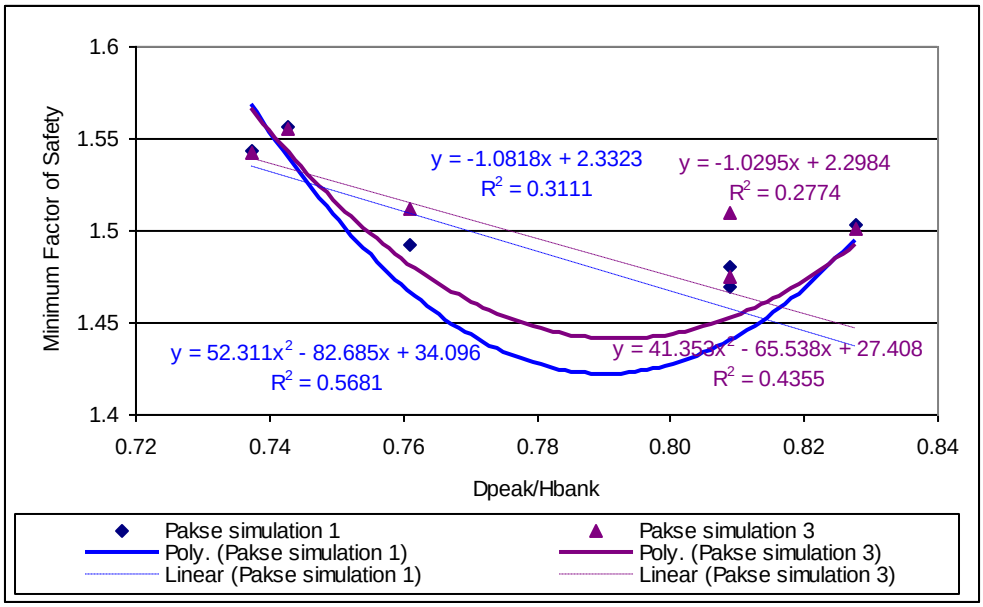

Figure 4.17. Minimum factor of safety for slide failures as a function of non-dimensionalised peak flow depth at Pakse study site, D_{peak}: peak flow depth; H_{bank}: bank height; D_{peak}/H_{bank}: non-dimensionalised peak flow depth.

In Figure 4.17 mostly the minimum factors of safety in scenario 3 are larger than those in scenario 1. However, weak regressions are acquired with $r^2 = 0.31$ in scenario 1 and $r^2 = 0.28$ for simulation 3. As expected, there is a declining trend in the factor of safety when the peak flow stage increases in both scenarios, meaning that stability reduces as D_{peak}/H_{bank} increases. This result is consistent with previous studies such as Rinaldi et al. (2004) and Luppi et al. (2009)'s observations that the higher the river stage, the more unfavourable the pore water pressures. However, unlike those studies, here the gap between the factors of safety in the two scenarios is very small; indicating there is only a small effect of fluvial erosion in this study site in terms of mass failure, presumably due to the low rates of simulated fluvial erosion. Moreover, the important point in Figure 4.17 is the minimum FoS for scenario 3 is typically higher than that for scenario 1. This result is not expected, and the relationship between fluvial erosion and seepage flow could be a factor driving that result. As analysed above (in Figure

4.16A) the Pw(+) values for scenario 3 are always lower than those for scenario 1, thereby leading to the river bank in scenario 3 being more stable than scenario 1. Similar to the analysis conducted in Figure 4.16B, non-linear regressions are also applied to these data. Correlation coefficients in these cases increase (r^2=0.57 for scenario 1 and r^2=0.44 for scenario 3) but it is still evident that bank stability and flood hydrology at Pakse are only weakly linked. These polynomial fits are not considered to be the best forms of the physical considerations, so linear regressions are chosen for the stability hydrology relationship.

Figure 4.18 shows the relationship between the total accumulated annual excess discharge (i.e. the total flow over threshold discharge) and the amount of sediment is eroded by fluvial erosion. Unlike Figure 4.16 and Figure 4.17 above, in which only the peak discharge is taken into account, here Σ(Q-Qc) is employed as the hydraulic action which causes the fluvial erosion occurs not only at the peak but also at other phases of the hydrograph. It may be seen in Figure 4.18 that for both material units fluvial erosion increases in proportion to Σ(Q-Qc). However, the regression correlations are not strong (i.e. the bank toe trend with r^2=0.49 and the bank top's correlation is even lower with the value of r^2=0.32). Moreover, the bank toe also produces much more sediment than the other layers, i.e. about 86% to 90% in all selected simulation events.

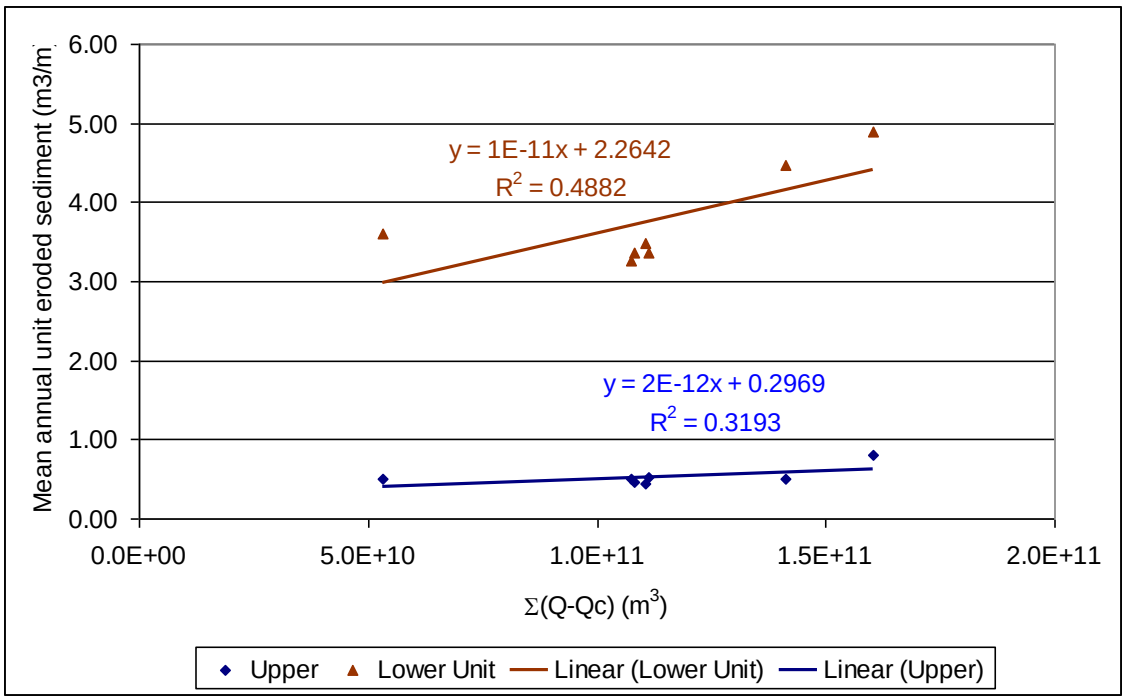

Figure 4.18. Total annual discharge over the threshold discharge Σ(Q-Qc) versus eroded volume at the bank top (blue) and at the bank toe (yellow) at the Pakse study site.

Chapter 5 River Bank Stability Modelling at the Ang Nyay Study Site

Similar to chapter 4, this chapter describes the river bank response to a range of simulated flow events at the Ang Nyay study site, which is located about 20 km upstream of Vientiane. In this chapter, the approach taken is similar to that in chapter 4, in which, the discussion focuses first detail on a simulation before comparing results with the Pakse and Friendship study site.

Parameter	Symbol	Unit	Sediment layers			Note
			1	2	3	
			0-1.4m	1.4-2.3m	>2.3m	
Apparent cohesion	c_a	kPa	9.2	7.4	13.5	Data based on BST tests (see 3.3)
Effective friction angle	ϕ'	deg	36	39	39	Data based on BST tests (see 3.3)
Unit weight	γ	kN/m^3	14.3-16.8	13.6-18.0	15.7-19.3	Data based on the samples which are taken from the site and analysed in the laboratory from dry to ambient condition
Porosity	n	%	44.9	47.7	39.5	Data based on the samples which are taken from the site and analysed in the laboratory
Saturated hydraulic conductivity	k_{sat}	m/s	1.51E-08	1.35E-08	1.22E-08	Kozeny-Carman method based on grainsize data and porosity (see 3.2.2)
Critical shear stress	τ_c	Pa	0.45±0.21	0.65±0.03	0.83±0.57	Data based on CSM tests (Darby et al., 2010)
Erodibility Coefficient	k_d	m^3/Ns	2.98E-07	2.48E-07	2.20E-07	Hanson and Simon (2001)

Table 5.1. Geotechnical and hydraulic characteristics of bank material at Ang Nyay, (see Figure 5.2 for definition of sediment layers).

The river bank at Ang Nyay is composed of three material layers, with a total bank height of 13.2 m and mean bank angle of 69° (Figure 5.1). The upper unit (Unit 1 in Table 5.1), which is 1.4 m thick, is classified as sand with a porosity n=44.9% and a unit weight (under ambient conditions) of 16.8 kN/m^3. The middle layer (Unit 2 in Table 5.1) is a clay (thickness = 0.9 m) with a unit weight γ=18.0 kN/m^3 and a porosity of 47.7%. The 10.9 m thick lower layer (Unit 3), which is mottled clay, has a porosity of 39.5% and the unit weight is γ=19.3 kN/m^3.

Figure 5.1. Ang Nyay study site.

Following the procedures adopted at the Pakse study site (see Chapter 5) and other previous studies (e.g. Dapporto et al., 2003; Rinaldi et al., 2004; Darby et al., 2007), the pore water pressure field within the bank at Ang Nyay was simulated using finite element seepage analysis, with the bank in this case being discretised into a total of 19,287 quadrilateral elements (Figure 5.2).

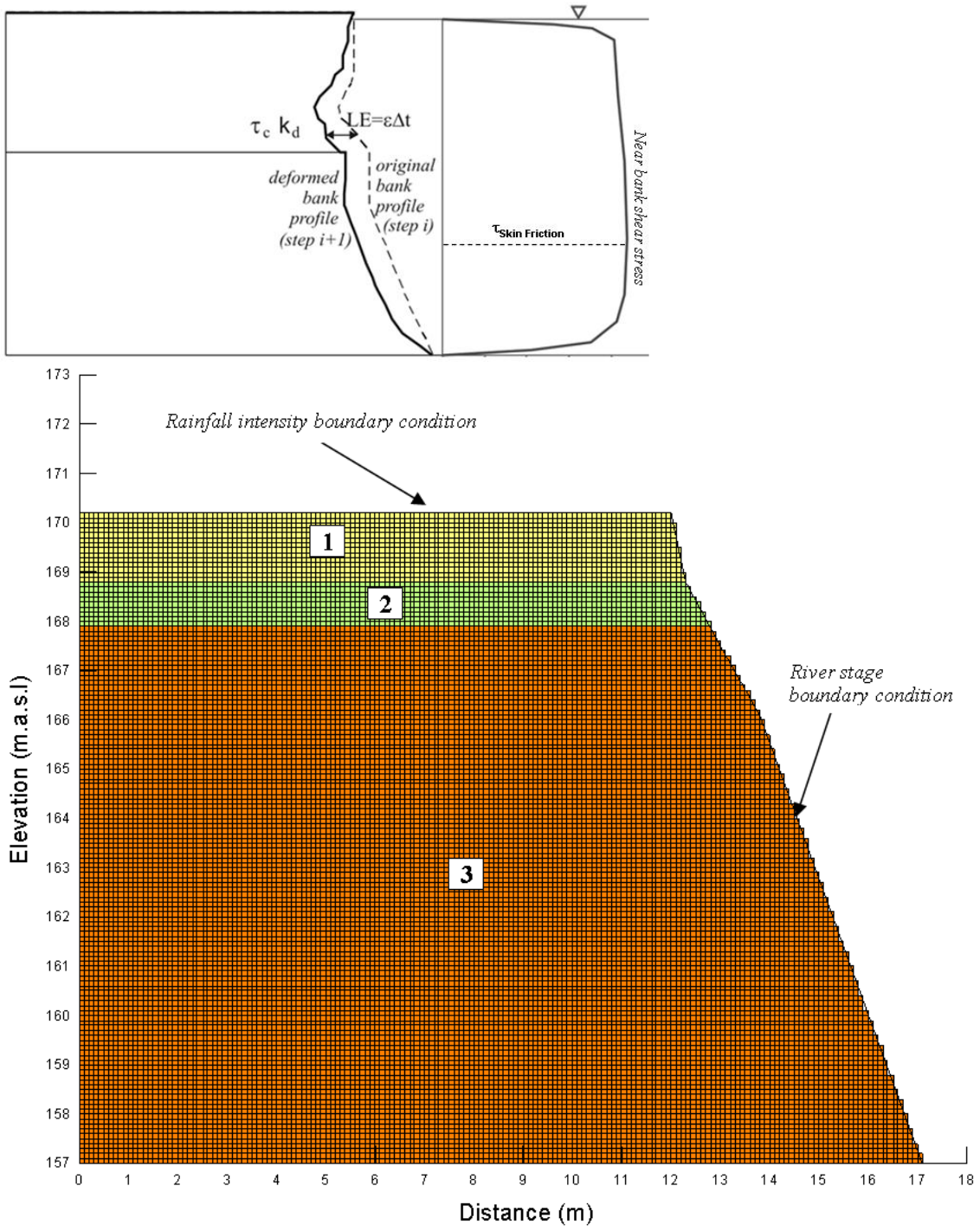

Figure 5.2. Overview of the seepage analysis and near bank shear stress distribution used to calculate fluvial erosion for the Ang Nyay study site.

The selection of flow events for simulation has been described in chapter 3, but at Ang Nyay special attention is paid to the 1966 event because it is the largest magnitude flood (in terms of available data) and its hydrograph characteristic is classified as rapid fall, which is likely to cause mass failure due to the possible imbalance between elevated pore water pressure inside river bank and loss of confining pressure under these flow conditions.

Scenarios 1 and 3 again were applied to all of the flow events at the Ang Nyay study site. However, for the 1966 flood, a mass failure is simulated during the course of scenario 1. Consequently an additional scenario (scenario 2) is applied to investigate the bank response to the flow event after the bank profile is changed to its new shape following mass failure. Table 5.2 below shows the flow events and their corresponding simulated scenarios at the Ang Nyay study site.

	1956	1963	1966	1969	1971	1976	1984
Scenario 1	√	√	√	√	√	√	√
Scenario 2	n/a	n/a	√	n/a	n/a	n/a	n/a
Scenario 3	√	√	√	√	√	√	√

Table 5.2. Flow events and corresponding simulated scenarios at Ang Nyay study site.

5.1 Results for the Year 1966 Hydrograph

Following the approach taken in the other results chapters reported in this thesis, detailed results are initially reported for only the 1966 flood, with summary data being provided subsequently for all the other flow events (1956, 1963, 1969, 1971, 1976, and 1984) simulated for this site. The 1966 hydrograph begins with a gradual decrease to a stage of 158.4 m a.s.l at time step 98 (08 April 1966), remaining around that base flow level for approximately one month (time step 130; 10 May 1966), after which there is a small increase to time step 144 (24 May 1966). A significant rise occurs during May and June (up to time step 181, 30 June 1966), with the flow fluctuating at that stage until time step 211 (30 July 1966), at which point it jumps to 169.2 m a.s.l at time step 219 (07 August 1966) before rising to another peak at 172.4 m a.s.l in the two week period from time steps 234 (22 August 1966) to 248 (05 September 1966). A sharp draw down then occurs to time step 277 (04 October 1966), and subsequently, at reduced rate, from step 283 (10 October 1966), before the flow tails off to the end of the year.

5.1.1 Simulated fluvial erosion

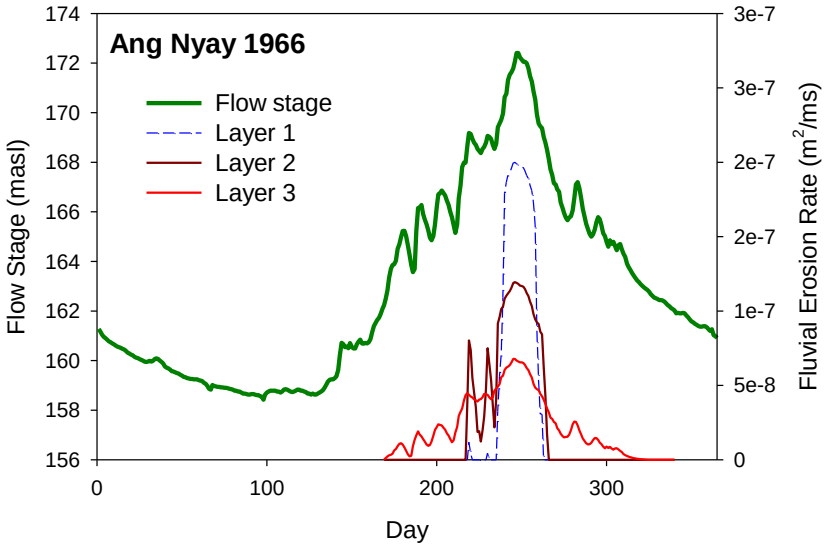

Figure 5.3. Simulated fluvial erosion for the year 1966 flow event at Ang Nyay. Integrating the fluvial erosion curves across the duration of the hydrograph gives total bank eroded sediments of 0.50, 0.29 and 3.62 m^3/m for the upper (layer 1), middle (layer 2) and lower bank (layer 3) material layers, respectively.

As indicated in Figure 5.3, fluvial erosion, as simulated using the approaches outlined previously (See Section 3.4), is predicted to commence at time step 169 (18 June 1966) at the bank toe, when the near bank shear stress exceeds the critical shear stress of the lower bank material (i.e. Unit 3). The erosion rate fluctuates and follows the hydrograph shape, with the maximum rate obtained in the upper layer (layer 1) of 6.8e-08 m/s occurring when hydrograph reaches the peak (time step 248; 05 September 1966). The bank retreat is calculated and, when it is larger or equal to the mesh size of 0.1 m, the bank profile is deformed. Erosion of the middle (Unit 2) and uppermost (Unit 1) bank layers does not begin until time step 218 (06 August 1966) and 219 (07 August 1966), respectively, when the river stage begins to increase. Like the lower layer (Unit 3), Figure 5.3 shows that the erosion rate of both Layers 1 and 2 increases and decreases in phase with the flow hydrograph. Unlike the Pakse study site, where the rate of fluvial erosion at the bank toe is double the rate at the bank top, at Ang Nyay the rate of bank top retreat is almost double the middle layer's (Layer 2) rate and is triple the lower layer's (Layer 3) rate, albeit for shorter durations. This finding can be explained by the differences in the values of the critical shear stress of each layer of bank material (see Table 5.1). However, as noted above, the duration of fluvial erosion at the bank top lasts only from time step 219 (07 August 1966) to time step 263 (20 September 1966) (i.e., 44 days), which is similar to the duration of erosion of the middle layer (Layer 2; 50 days), with both values being much less than the duration of fluvial erosion at the bank toe (156 days). For these reasons the mean bank retreat over the entire flow year (approximately 0.45 m) is similar across all three layers of material.

5.1.2 Pore water pressure

Figure 5.4 provides a summary of the results of the finite element seepage modelling for the 1966 flow event. As in preceding chapter this figure again presents data that focuses on the time-varying value of the pore water pressure integrated along the saturated portion of the failure surface (Pw(+), Figure 5.4a) and along the entire failure surface (Pw, Figure 5.4b), respectively. In general, the evolution of both Pw and Pw(+) follows the 1966 flood hydrograph.

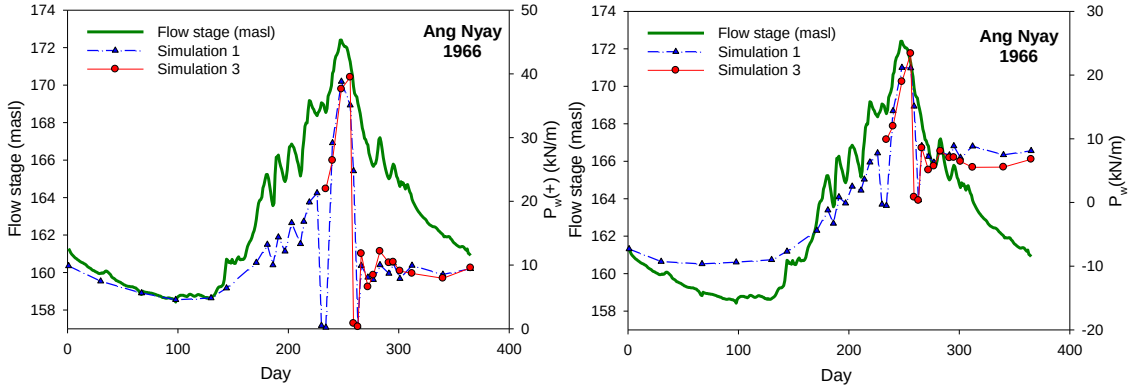

Figure 5.4. Evolution of average pore water pressure values integrated along the failure surface at the Ang Nyay study site (1966 flow event) for scenarios 1 (no bank deformation) and 3 (bank profile deformed by fluvial erosion and mass wasting): (Left) pore water pressure integral along the saturated portion of the failure surface and (Right) pore water pressure integral along the entire failure surface.

Further details of the pore water pressure distribution, in relation to the evolution of the event hydrograph and seepage flow characteristics (Figure 5.6 and Figure 5.7) are described now. Excluding time step 0, which is the initial condition when the water table and river stage are assumed to be in equilibrium, then in the initial period of the simulation, which lasts between January and early April (time steps 1 to 98), there is a slight but progressive fall in water level from 161.3 m a.s.l to 158.4 m a.s.l as the dry season progresses. During this period, seepage flow is consistently directed from the bank towards the river, that is there is a seepage outflow at the intersection between the water table, bank profile and river stage with the outflow velocity on the order of 1.10e-08 m/s (time step 98, 08 April 1966). As noted in the case of Pakse in Chapter 4, this value is far too small to cause seepage erosion.

The hydrograph subsequently fluctuates around its base level before beginning to rise, to a flow stage of 160.7 m.a.s.l at time step 144 (24 May 1966), most likely due to the arrival of spring melt from the Tibetan headwaters. At this point the seepage flows simulated previously change direction, such that the river flow is infiltrating into the bank, albeit at rather low flow velocities. For example, the infiltration velocity at the intersection between the water table, the face of the bank profile and the river stage is

1.15e-08m/s. The infiltration of this water begins to have an important impact on the pore water pressures simulated within the bank interior. In particular, the elevation of the water table becomes sufficiently high to intersect the potential failure surface, meaning positive pore water pressures appear for the first time in the simulation, even if the average integrated pore water pressure (Pw) has a modest negative value (i.e. stablising) of -7.69 kN/m.

In the subsequent time steps there is a significant rise in the flow hydrograph until it stabilises at a level of 165.2 m a.s.l at time step 181 (30 June 1966). The seepage flow continues to be directed from the river into the bank, with the velocity at the intersection rising an order of magnitude to 1.9e-07 m/s. This significant recharge is sufficiently high that the positive pore water pressure now nearly balances with the negative pore water pressure, with the average total integrated value of Pw rising to -1.21 kN/m at this point in time. In the next month of the simulation, that is from time step 181 (30 June 1966) to time step 211 (30 July 1966), the hydrograph fluctuates around a stage of 165.1 m a.s.l. The pore water pressure in this period therefore also fluctuates but the lag in the response of the pore water pressure field to the rising flow means that pore pressures continue to increase, and the value of Pw becomes positive for the first time in the simulation (i.e., Pw = 0.85 kN/m at time step 191 (10 July 1966)), while the seepage inflow velocity reduces to a value of 2.7e-08 m/s.

Over the course of the next three weeks of the flood, the hydrograph experiences a steep rise such that the flow stage exceeds the level of the contacts between Layers 2 and 3 and Layers 1 and 2 of the bank materials (time step 219 (07 August 1966), 169.2 m a.s.l). In response, a steep wetting front develops at the contact between the river and the bank profile, seepage inflow velocities at the intersection between the water table, the face of the bank profile and the river stage increase by an order of magnitude to a value of 1.1e-07 m/s, and the pore water pressure index value Pw rises to 6.32 kN/m. After slightly decreasing in the following two weeks, from time step 234 (22 August 1966), the hydrograph again rises and reaches its peak at a level of 172.4 m a.s.l by time step 248 (05 September 1966). Both Pw and Pw(+) attain their maximum values of 21.18 kN/m and 38.8 kN/m, respectively, at this point. These values are, in principle, sufficiently high to significantly destabilise the bank with respect to mass failure but, as discussed further below (see Section 5.1.3), the effect of the large confining pressure exerted by the flow is sufficiently high to ensure that the simulated factor of safety is also high at this time. However, by this point in time the accumulated erosion by the hydraulic action of the flow is also sufficient to deform the bank profile, such that scenario 3 is initiated at time step 234 (22 August 1966).

After the peak of the flood the water stage falls significantly (at a rate of 0.22 m/day) over the course of the next month, reaching a level of 165.7 m a.s.l by time step 277 (04 October 1966). In this period, the seepage flow in the upper part of the water table has reversed out of the bank and is directed to the river, but it is still flowing inwards, for the lower part under the water table. The seepage velocity at the contact between layer 2 and 3 of the upper part is 6.71e-09 m/s and at the intersection between the water table, the face of the bank profile and the river stage it is 4.75e-09 m/s. Also the value of Pw decreases to a value of 6.29 kN/m in this period. However, it is noteworthy that Pw remains positive in sign while the confining pressure of the flow is falling significantly, leading to a dramatic drop in the factor of safety (See Section 5.1.3). After this time, the hydrograph experiences another small peak when it rises 1.5m by time step 283 (10 October 1966) before dropping again to a lower level of 165.0 m a.s.l a week later. In this period the parameter Pw also rises to 7.90 kN/m before reducing to a value of 7.42 kN/m by time step 291 (18 October 1966). It is especially noteworthy that the net effect of this fluctuation in the flow hydrograph is that, following the fall after the secondary peak, the simulated value of Pw (7.42 kN/m) is *greater* than the value of 6.29 kN/m simulated at 04 October 1966, even though the corresponding flow stage (at 17 October 1966) is *lower*. This is consistent with one of the findings of Luppi et al. (2009) who worked on the Cecina River in central Italy, namely that flow hydrographs with multiple peaks tend to be more destabilizing (in terms of elevating the value of Pw) than single peak hydrographs, due to the 'pre-wetting' effect of a series of peaks. This point is returned to in Chapter 7.

Finally, after time step 295 (22 October 1966), the hydrograph continues to fall until the end of the simulation, reaching a minimum stage of 160.9 m.a.s.l. The pore water pressure Pw does not fall significantly in this period but instead fluctuates, ending with a value of 8.11 kN/m. There is a similar value of Pw(+) in both scenario 1 and scenario 3 but there is a significant difference in Pw between two scenarios. The value of Pw is 8.82 kN/m in scenario 1 but is 5.52 kN/m in scenario 3 (time step 312, 08 November 1966), so explain why bank mass failure occurs in this period under scenario 1 (see Section 5.1.3. The seepage flow at the end of hydrograph (time step 365, 31 December 1966) is directed from the bank to the river with the outflow velocity at the intersection between the water table, the face of the bank profile and the river stage being 1.06e-08 m/s.

5.1.3 Bank stability and sediment entrainment

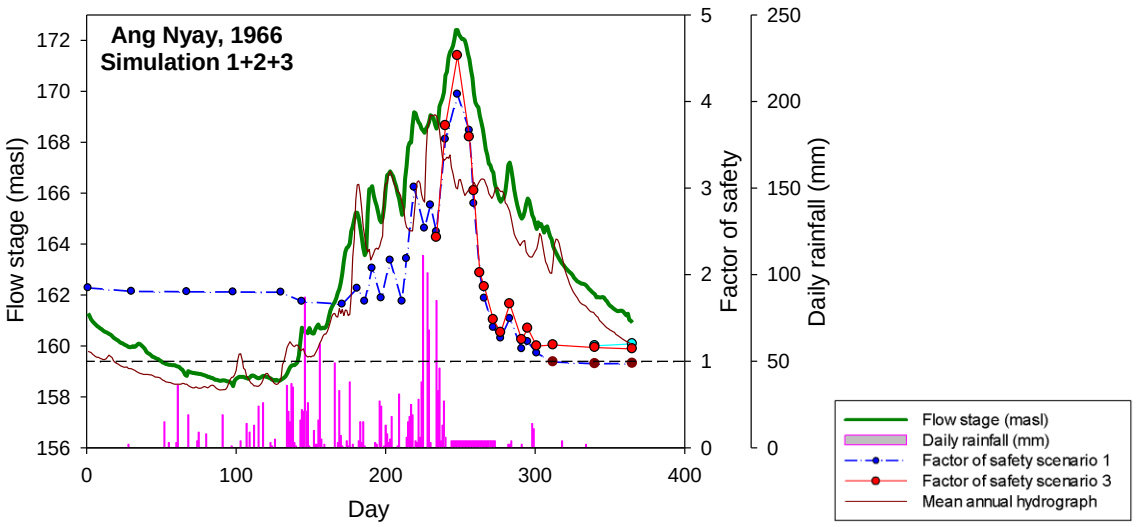

Figure 5.5. Hydrograph, rainfall intensity and simulated factors of safety of flow event 2000 for simulation scenario 1 (no fluvial erosion) and 3 (fluvial erosion) at the Ang Nyay study site (for results for other events see Figure 5.8).

As illustrated in Figure 5.5, the factor of safety (FoS) with respect to mass failure in scenario 1 remains above the critical value of unity until time step 312 (08 November 1966) when it attains a value of 0.991, meaning that a bank failure is simulated at this point. Scenario 2 is subsequently conducted from time step 312 (08 November 1966) based on the updated bank profile following the failure surface simulated in scenario 1. The bank in this scenario (2) remains stable throughout the remainder of the simulation. In scenario 3, where fluvial erosion is applied, the FoS remains above 1 throughout the simulation period. This point is returned to below. In addition, and similarly to Darby et al. (2007), in all three cases there is also a decline (though not a small one like the Pakse study site discussed in Chapter 4) in stability by the end of the simulation period (for example the simulated FoS values exhibit a decrease of 0.872, 0.647 and 0.705 for scenario 1, 2 and 3, respectively, between the beginning and end of the simulation period). This reflects the destabilising effect of the elevated pore water pressures seen between the start and end of the simulation (e.g. the integrated pore water pressure Pw at step 1 and step 365 is -7.30 kN/m and 8.11 kN/m, respectively in scenario 1). There are only modest differences in FoS values simulated under scenarios 1 and 3, with FoS for the latter scenario (again, like the Pakse study site) being somewhat larger than the former scenario (i.e. at step 240 (28 August 1966), the Fos is 3.562 in scenario 1 and in scenario 3 it is 3.721; at step 272 (29 September 1966), the Fos in scenario 1 is 1.390 and scenario 3 it is 1.480).

Given the differences in the simulated FoS values for each scenario, the temporal variations in FoS must be attributed to the varying values of pore water and confining pressure simulated during the course of each simulation. Thus, when the flow level is low (e.g. Figure 5.6, time step 130, 10 May 1966) the bank is dominated by negative (stabilising) pore-water pressures. In contrast, during peak flow, the immersion of the bank is sufficiently long to cause complete saturation and the generation of positive pore water pressures (Figure 5.6, time step 248, 05 September 1966). When the river stage recedes, the ground water table also goes down along with the water level (Figure 5.6, time step 312, 08 November 1966), resulting in a significant reduction of hydrostatic confining pressure and thus factor of safety, which ultimately triggers the mass failure noted in scenario 1. However, in scenarios 2 and 3, the positive pore-water pressures are insufficiently high to trigger mass-failure (e.g. the average integrated pore water pressure Pw in scenarios 1, 2 and 3 are 8.82 KN/m, 7.76 kN/m and 5.52 kN/m, respectively).

Thus, it is apparent that, similar to Simon et al. (1999), Darby et al. (2007) and the results from the Pakse study site reported in chapter 4, the dominating influence on bank stability is the hydrostatic confining pressure exerted by water in the channel, so that temporal trends of FoS are strongly positively correlated with fluctuations in the flow hydrograph. For example, in scenario 1 (no fluvial erosion), the initial factor of safety is 1.847, but as flow stage decreases the factor of safety also slightly decreases to 1.805 and 1.799 by time step 30 (30 January 1966) and 98 (08 April 1966), respectively. When the river stage reaches the peaks observed at time steps 181 (30 June 1966), 219 (07 August 1966) and 248 (05 September 1966), the factor of safety also rises to 1.841, 3.009 and 4.083, respectively. On the first half of the falling limb when the flow stage recedes rapidly from its peak then at step 256 (13 September 1966), 263 (20 September 1966) and 277 (04 October 1966), the simulated factor of safety also falls to values of 3.665, 2.015 and 1.265, respectively.

Scenario 3 incorporates the effects of fluvial erosion and, as such, it might initially be thought that this scenario would be associated with reduced FoS values. However, except for time steps 234 (22 August 1966) and 256 (13 September 1966), when the factor of safety in scenario 3 is 2.429 and 3.590, respectively, compared to values of 2.494 and 3.665 in scenario 1, scenario 3 in fact experiences larger factors of safety. Therefore, there is no mass wasting in scenario 3. The difference between the FoS values simulated in scenarios 1 and 3 range from approximately 0.2% to 20%, with the higher value occurring late in the simulation because of the mass failure in scenario 1. The mass wasting occurs at some time steps (312, 08 November 1966; 340, 06 December 1966 and 365, 31 December 1966) at the end of the hydrograph due to the

lack of confining pressure while the pore water pressure values are still high. The Pw in these cases are 8.82 kN/m, 7.47 kN/m and 8.11 kN/m while the corresponding FoS values are 0.991, 0.970 and 0.975, respectively. In contrast in scenario 3, due to the effects of fluvial erosion which change the bank geometry and water table gradient, the Pw values reduce to 5.52 kN/m, 5.55 kN/m and 6.78 kN/m so the corresponding FoS values increase to 1.187, 1.158 and 1.142, respectively. In addition to the reduction of positive pore water pressure associated with scenario 3, the fluvial erosion at Ang Nyay also stabilises the bank as the mean bank retreat at the bank top and the middle layer are as large as at the bank toe (see Section 5.1.1). The initial bank angle is 68°5' but after the bank profile is deformed by hydraulic action (at step 312, 08 November 1966), the new bank angle is slightly flattened to 67°5', leading to a change in the slip surface position that stabilises the bank with respect to mass failure.

Due to the absence of mass wasting in scenario 3, the volume of bank material entrained to the river is associated exclusively with fluvial erosion. The total unit volume of eroded sediment in this case is 4.4 m^3/m, with most (82%) being supplied from the lower unit of bank material, mainly due to its greater thickness, even though the mean erosion rates of each layer are similar.

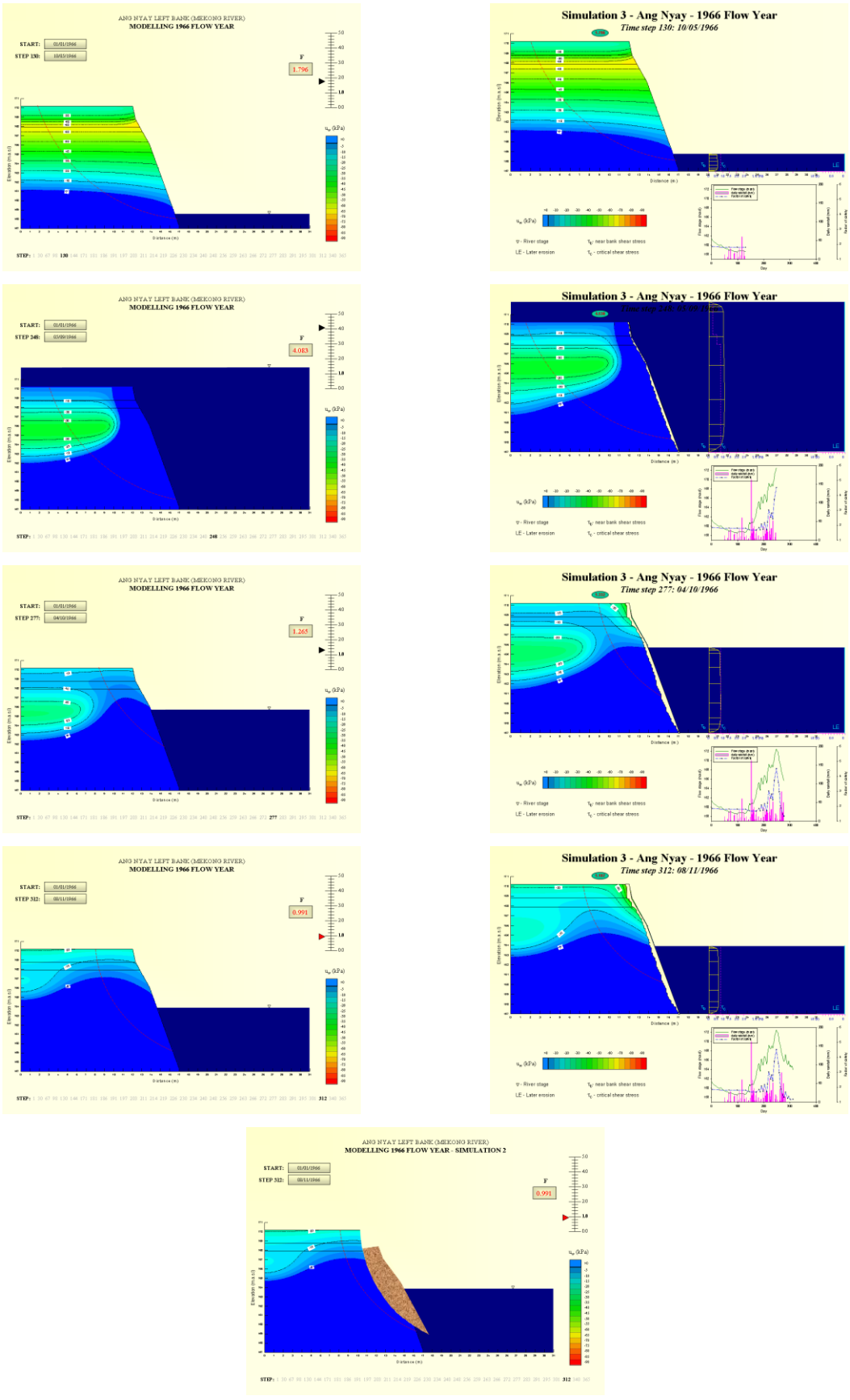

Figure 5.6. Simulated bank pore water pressure distributions for selected time steps at Ang Nyay for scenario 1 (no bank deformation, left hand side), scenario 2 (bank profile is deformed by mass wasting, middle column) and 3 (bank profile is deformed by both fluvial erosion and mass wasting, right hand side). Animations of the complete simulation sequence are available in the accompanying CD.

Step 130

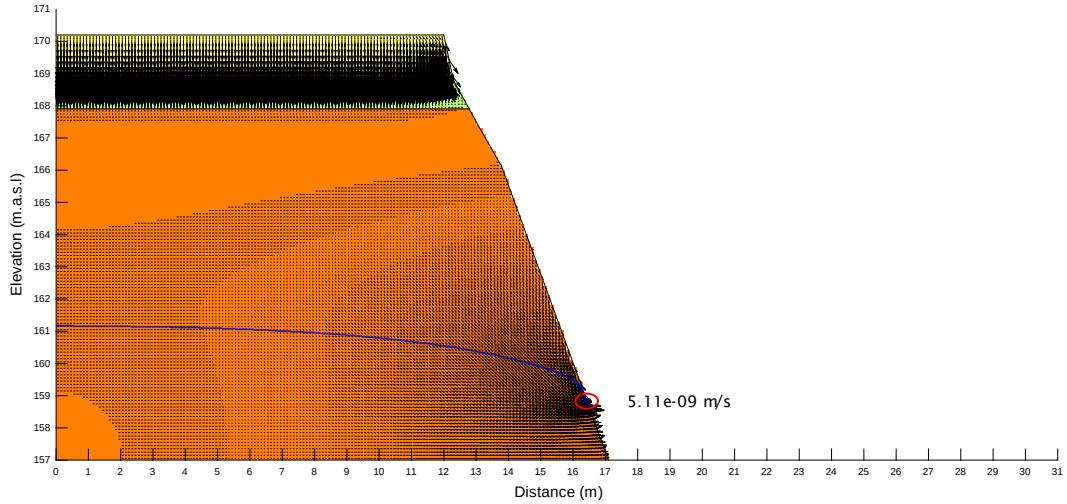

Step 277

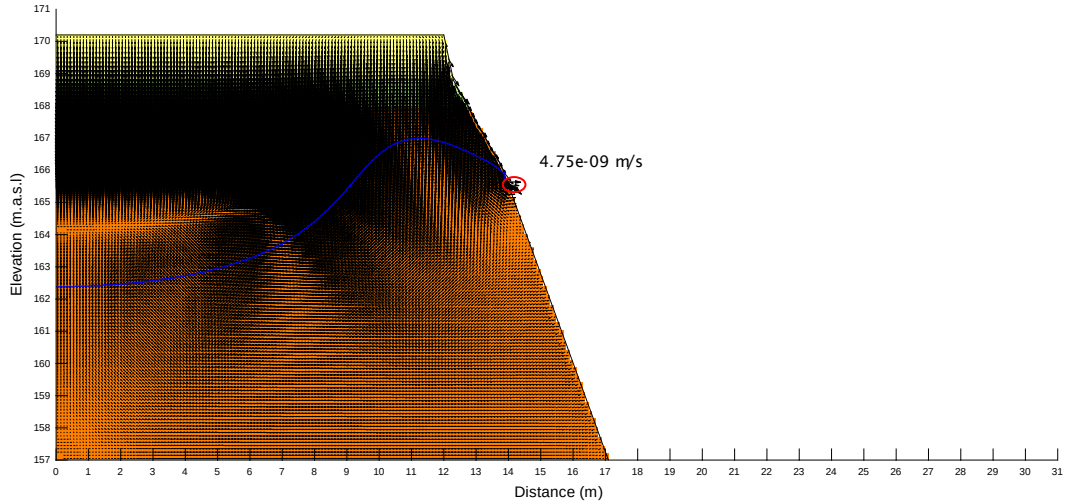

Step 365

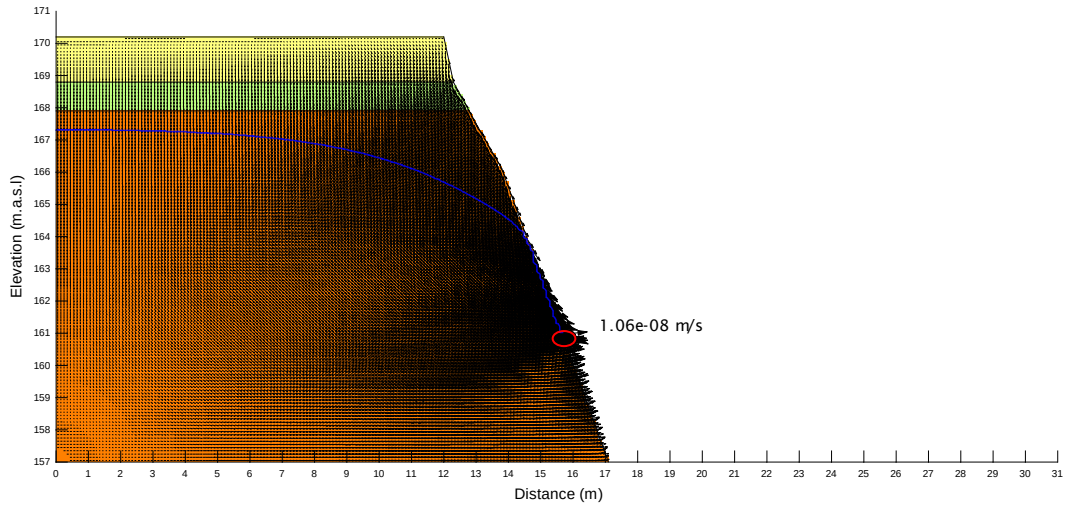

Figure 5.7. Simulated bank seepage flow for selected time steps at Ang Nyay (scenarios 1), green and yellow colour is river bank material, blue line is water table, and red circle is the intersection between bank surface, water table and river stage

5.2 Synthesised results at Ang Nyay study site

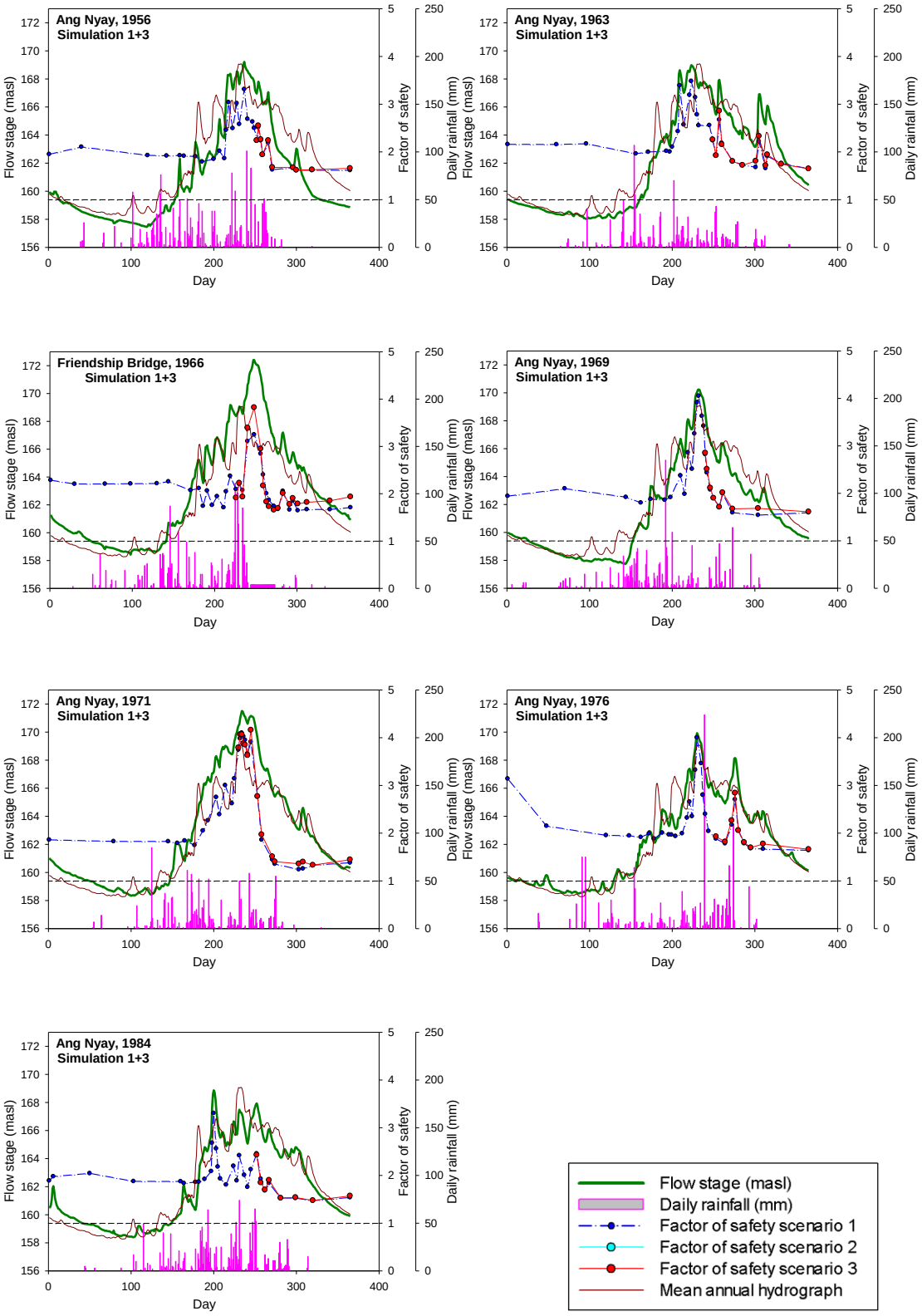

Figure 5.8. Hydrograph, rainfall intensity and simulated factors of safety for the selected flow events for simulation scenarios 1, 2 and 3 at the Ang Nyay study site.

As can be seen in Figure 5.8, the factors of safety follow in part the trend (1956) or mostly the trend (1963, 1969, 1971, 1976 and 1984) of the hydrograph, the FoS is greatest when the flow level is high; and indeed FoS remains above 1 at all times and for both simulation scenarios so the river bank at this site remains stable with respect to mass failure. The maximum factor of safety occurs in phase with the peak flow and the minimum factor of safety mostly occurs at the end of the simulation, giving an overall range of simulated FoS from 1.697 for a low flow event (i.e 1956) to 3.113 for a high flow event (i.e. 1966). Pore water pressure values, as integrated along the failure surface (i.e, the parameter Pw), remain negative mostly for the whole simulation in both scenario 1 and 3 (in case of low flow event i.e. 1956, 1963, 1984); remain positive for part of the high stage hydrograph (in case of a medium high flow event i.e. 1969, 1976); or remain positive through the whole simulation (high flow event i.e. 1971). However, even for the brief maxima the maximum value of Pw in all the above cases is still insufficient to trigger mass failure.

In this section the principal findings of the simulations undertaken for the full range of flow events investigated at the Ang Nyay study site are discussed. The effects on pore water pressure distributions of variations in event hydrograph shape are explored first, because it has been shown that the pore pressure distribution, particularly as expressed by the parameters Pw and Pw(+), exerts an important control on the likelihood and timing of bank failure. Figure 5.9 shows series of relationships between maximum and minimum values of both Pw, Pw(+) and the hydrograph peak Q_{peak}.

As can be seen from Figure 5.9A and Figure 5.9B, there is a good correlation between pore water pressure (maximum Pw and Pw(+) values) and peak discharge values in both scenarios 1 and 3. Their trends show that the peak pore water pressure increases in proportion to the peak discharge, i.e. the largest flood events simulated (1966 and 1971) generate the largest values of Pw, irrespective of the specific simulation scenarios (1, 2 or 3). The correlation of Pw(+) and Pw in scenario 1 has a similar value of r^2=0.90, a little stronger than those values in scenario 3 at r^2=0.87 and r^2=0.83, respectively. As with the Pakse site, the effect of fluvial erosion might be a reason for the reduced correlation in scenario 3.

The difference between the maximum Pw (+) and maximum Pw is about 20 kN/m and 15 kN/m for scenario 1 and 3, respectively. The reason might be the timing of the maximum values, i.e. in scenario 1, the maximum Pw(+) occurs at the time step corresponding with the peak of the hydrograph, while maximum Pw occurs at the flood peak (e.g. 1966 event), after the peak (e.g. 1969) and in the falling limb (e.g. 1976, 1984). However, in scenario 3, except for the 1971 event, the maximum Pw and Pw(+)

values occur at the same time step (e.g. step 254 (10 September 1956) in the 1956 event). This gap and others at Pakse and Friendship Bridge study site will be discussed in chapter 7.

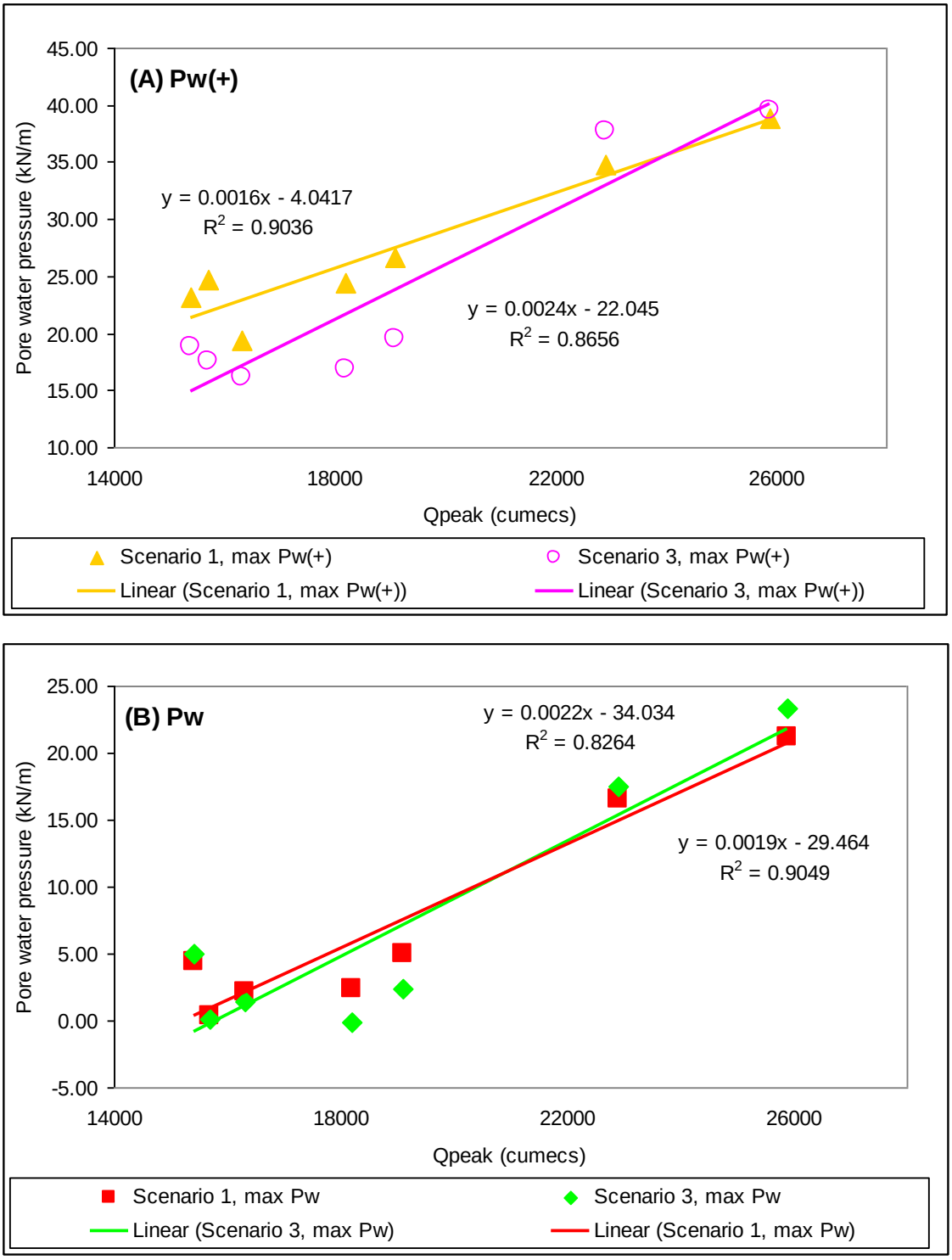

Figure 5.9. The maximum and minimum average pore water pressure integrated along the failure surface at the Ang Nyay study site for simulation scenarios 1 and 3. Pw is the pore water pressure integral along the whole of the failure surface and Pw(+) is the pore water pressure integral along the saturated portion of the failure surface.

Figure 5.10 illustrates the relationship between stability with respect to mass failure and the flow intensity. The data are again scaled to peak flow stage against total bank height D_{peak}/H_{bank}. In Figure 5.10 mostly the minimum factors of safety in scenario 3 are larger than those in scenario 1. However, a more robust regression is acquired in simulation 1 with $r^2 = 0.79$ and with a little lower $r^2 = 0.69$ for simulation 3. There is a declining trend in factor of safety as peak flow stage increases in both scenarios. This result is similar to the finding of Rinaldi et al. (2004) and Luppi et al. (2009)'s research in that the higher river stage, the more unfavorable pore water pressure it exhibits. However, unlike those studies, the gap between the factors of safety in the two scenarios increases along with the peak flow stage, indicating that for the high flow event, the effect of fluvial erosion at this study site is more significant in terms of its effect on mass failure.

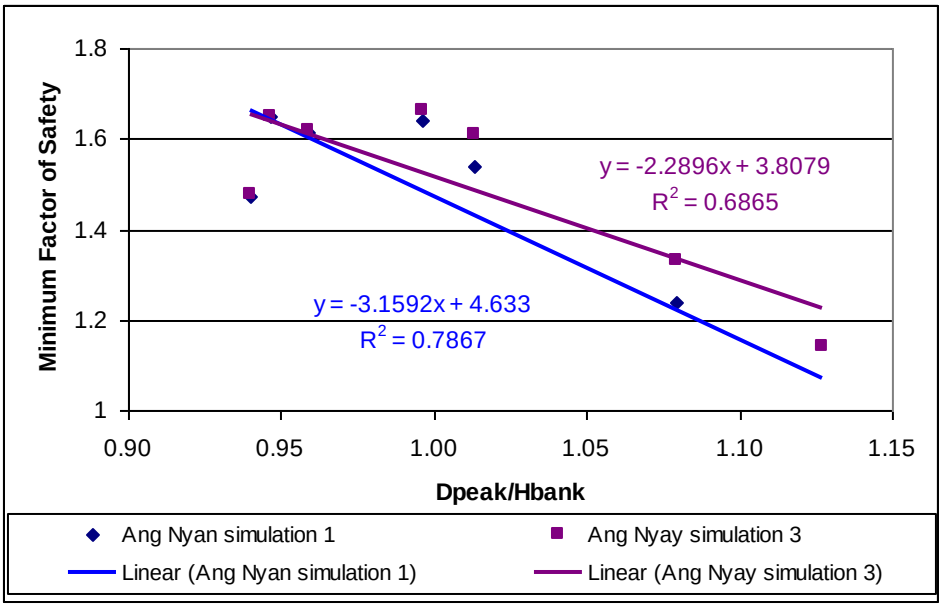

Figure 5.10. Minimum factor of safety for slide failures as a function of non-dimensionalised peak flow depth at Ang Nyay study site, D_{peak}: peak flow depth; H_{bank}: bank height; D_{peak}/H_{bank}: non-dimensionalised peak flow depth.

Figure 5.11 shows the relationship between total annual discharge over the threshold discharge and the total amount of sediment eroded by fluvial erosion. It can be seen in Figure 5.11 that all three material units erode in proportion to the Σ(Q-Qc) parameter. All have strong regression correlations, especially the bank toe trend with r^2=0.94, the bank top and the middle layer have similar correlations with the value of r^2=0.83. Moreover, the bank toe also produces much more sediment than the other layers, i.e. about 81% for high flow events (1966, 1971) and more than 99% for low flow events (1984).

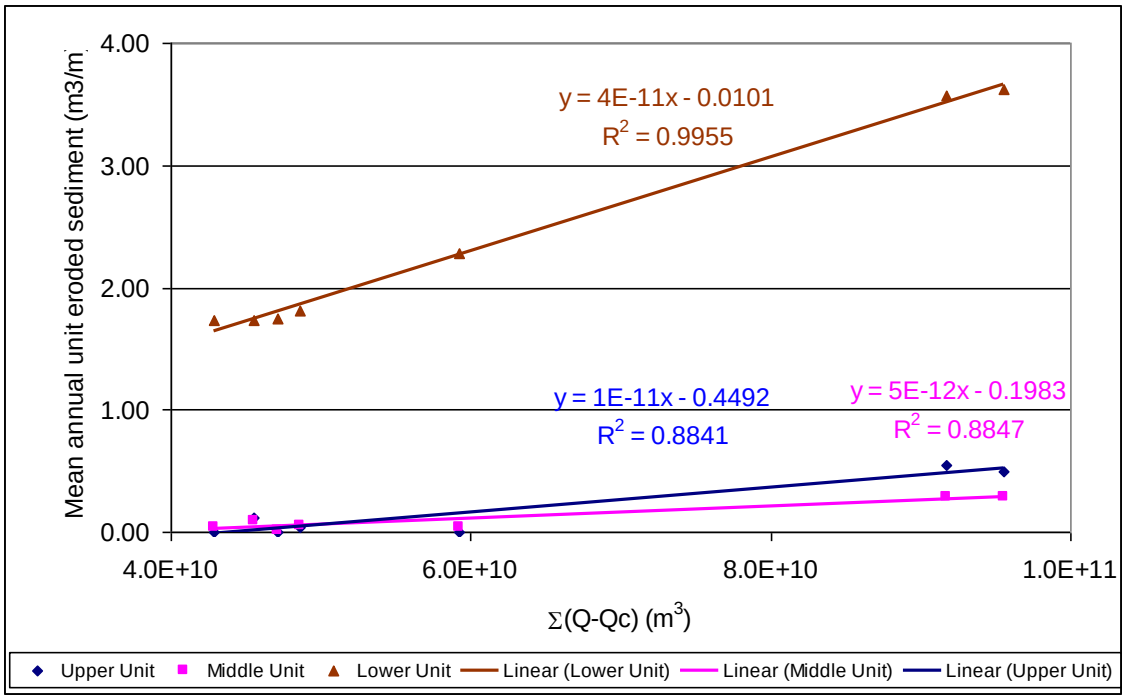

Figure 5.11. Total annual discharge over the threshold discharge Σ(Q-Qc) versus eroded volume at the bank top (purple), at the middle layer (blue) and at the bank toe (yellow) at the Ang Nyay study site.

Chapter 6 River Bank Stability Modelling at the Friendship Bridge Study Site

Similar to Chapter 4 and 5, this chapter will describe the river bank response to flow events at the Friendship Bridge study site. The Friendship Bridge study site is located at Vientiane and has been described in the methodology chapter (see Section 3.1).

Parameter	Symbol	Unit	Sediment layers			Note
			1	2	3	
			0-1.3m	1.3-3.2m	>3.2m	
Apparent cohesion	c_a	kPa	28.1	25.4	26.4	Data based on BST tests (see 3.3)
Effective friction angle	ϕ'	deg	36	36	36	Data based on BST tests (see 3.3)
Unit weight	γ	kN/m^3	11.3-12.1	15.0-16.8	16.2-17.6	Data based on the samples which are taken from the site and analysed in the laboratory from dry to ambient condition
Porosity	n	%	56.4	42.2	37.5	Data based on the samples which are taken from the site and analysed in the laboratory
Saturated hydraulic conductivity	k_{sat}	m/s	3.48E-08	8.89E-07	3.93E-07	Kozeny-Carman method based on grainsize data and porosity (see 3.2.2)
Critical shear stress	τ_c	Pa	0.50±0.20	1.03±0.36	0.50±0.24	Data based on CSM tests (Darby et al., 2010)
Erodibility Coefficient	k_d	m^3/Ns	2.82E-07	1.97E-07	2.82E-07	Hanson and Simon (2001)

Table 6.1. Geotechnical and hydraulic characteristics of bank material at Friendship Bridge, (see Figure 6.2 for definition of sediment layers).

The river bank at Friendship Bridge is composed of three material layers with a total bank height of 13.2 m and mean bank angle of 35° (Figure 6.1). The upper unit, which is 1.3 m thick, is classified as silty sand with a porosity n=56.4% and a unit weight (under ambient conditions) of 12.1 kN/m^3. The middle layer is a silt (thickness = 1.9 m) with a unit weight γ=16.8 kN/m^3 and a porosity of 42.2%. The 10.0 m thick lower layer, which is mottled clay, has a porosity of 37.5% and unit weight γ=17.6 kN/m^3.

Following previous studies (e.g. Dapporto et al., 2003; Rinaldi et al., 2004; Darby et al., 2007), the pore water pressure field within the bank was simulated via finite element seepage analysis, with the bank discretised into a total of 21,658 quadrilateral elements. Boundary conditions were defined at the bank top based on the observed rainfall intensity, while the measured variations in water level were assigned to nodes along the river bank face. The remaining two vertical (left hand edge of model domain) and horizontal (bottom) boundaries were assigned as zero flux boundary conditions. With the assumption that the initial water table and river stage is in equilibrium, the steady state is used to define the initial head.

Figure 6.1. Friendship Bridge study site.

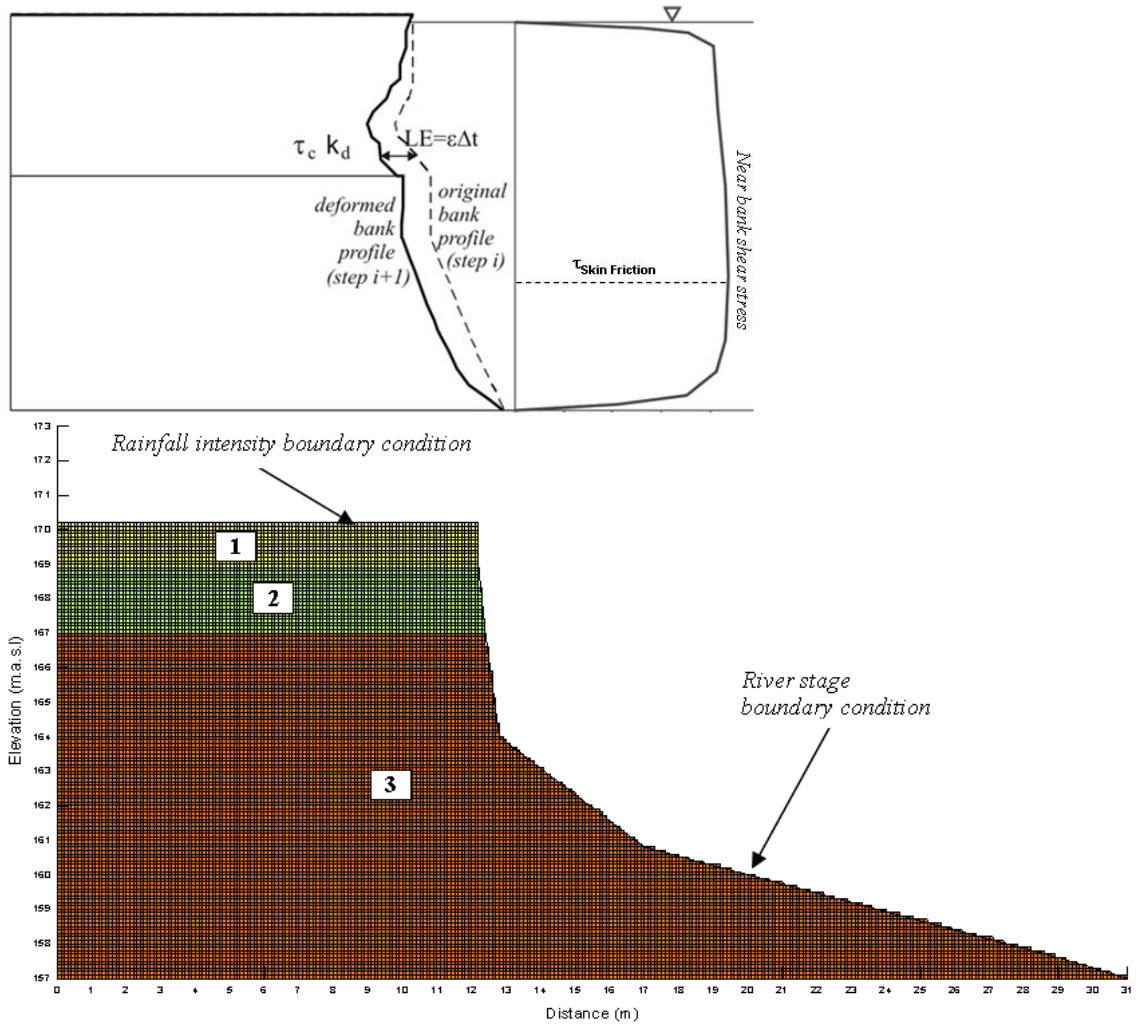

Figure 6.2. Overview of the seepage analysis and near bank shear stress distribution used to calculate fluvial erosion for the Friendship Bridge study site

Due to the location of Friendship Bridge at Viantiane city, the closet gauging station is Vientiane. Therefore, both Friendship Bridge and Ang Nyay study sites have the same hydrological data. As described in the previous chapter for Ang Nyay, the 1966 flow event is also selected for modelling in this part.

	1956	1963	1966	1969	1971	1984
Scenario 1	√	√	√	√	√	√
Scenario 2	n/a	n/a	n/a	n/a	n/a	n/a
Scenario 3	√	√	√	√	√	√

Table 6.2. Flow events and corresponding simulated scenarios at Friendship Bridge study site.

Similarly to the Pakse and Ang Nyay study sites, scenarios 1 and 3 again were applied to all of the flow events at the Friendship Bridge study site. Table 6.2 shows the flow events and the corresponding simulated scenarios at the Friendship Bridge study site.

6.1 Results for the Year 1966 Hydrograph

Following the approach taken in the other results chapters, detailed results are initially reported for only the 1966 flood, with summary data being provided subsequently for all the other flow events (1956, 1963, 1969, 1971, 1976, 1984) simulated for this site. The 1966 hydrograph begins with a gradual decrease to a stage of 158.4 m a.s.l at time step 98 (08 April 1966), remaining around that base flow level for approximately one month (time step 130; 10 May 1966), after which there is a small increase to time step 144 (24 May 1966). A significant rise occurs during May and June (up to time step 181, 30 June 1966), with the flow fluctuating at that stage until time step 211 (30 July 1966), at which point it rises to 169.2 m a.s.l at time step 219 (07 August 1966) before rising to another peak at 172.4 m a.s.l in the two week period from time steps 234 (22 August 1966) to 248 (05 September 1966). A sharp draw down then occurs to time step 277 (04 October 1966) and subsequently, at reduced rate, from step 283 (10 October 1966), before the flow tails off to the end of the year.

6.1.1 Simulated fluvial erosion

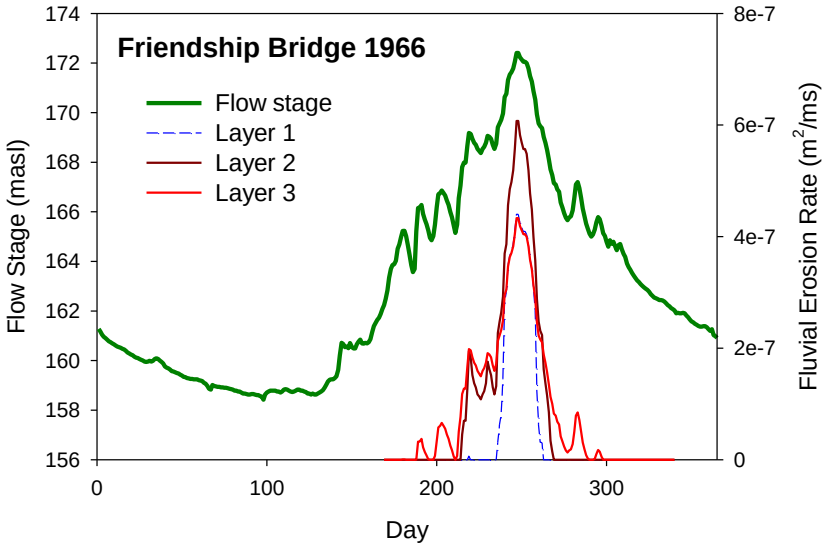

Figure 6.3. Simulated fluvial erosion for the year 1966 flow event at Friendship Bridge. Integrating the fluvial erosion curves across the duration of the hydrograph gives total bank eroded sediments of 0.93, 1.15 and 14.04 m^3/m for the upper, middle and lower bank material layers, respectively.

As indicated in Figure 6.3, fluvial erosion as simulated using the approaches outlined previously (See Section 3.4), is predicted to commence at time step 180 (29 June 1966) at the bank toe, when the near bank shear stress exceeds the critical shear stress of the lower bank material (i.e. Unit 3). The erosion rate fluctuates and follows the hydrograph shape, with the maximum rate obtained in the middle layer (layer 2) of 6.1e-07 m/s occurring at time step 248 (05 September 1966) on the day the hydrograph reaches the peak. The bank retreat is calculated and, when it is larger or equal to the mesh size of 0.1 m, the bank profile is deformed. Erosion of the middle (Unit 2) and uppermost (Unit 1) bank layers does not begin until time step 215 (03 August 1966) and 219 (07 August 1966), respectively, when the river stage begins to increase. Like the lower layer (Unit 3), Figure 6.3 shows that the erosion rate of both the Layers 1 and 2 increases and decreases in phase with the flow hydrograph. Unlike either the Pakse study site, where the rate of fluvial erosion at the bank toe is double the rate at the bank top, or at Ang Nyay, where the rate of bank top retreat is almost double the middle layer's (Layer 2) rate and is triple the lower layer's (Layer 3) rate, here at the Friendship Bridges study site, the rate due to hydraulic action on the bank top is similar to the bank toe and is two thirds of the middle layer's. This finding can be explained by the differences in the values of the critical shear stress of each layer of bank material (see Table 6.1). In addition, the duration of fluvial erosion at the bank top lasts from time step 219 (07 August 1966) to time step 263 (20 September 1966) (i.e. 44 days), which is similar to the duration of erosion of the middle layer (Layer 2; 50 days), with both values being much less than the duration of fluvial erosion at the bank toe (117 days). For these reasons the mean bank retreat over the entire flow year is similar across the bank top and the middle layer of material (approximately 0.7 m and 0.6 m, respectively) and for the bank toe, that value is about 1.4 m. These values are greater than Ang Nyay's with the same simulated flow event 1966. At Ang Nyay, the mean bank retreat over the 1966 event of about 0.45 m applied for all three bank layers.

6.1.2 Pore water pressure

Figure 6.4 provides a summary of the results of the finite element seepage modelling for the 1966 flow event. This figure again presents data that focus on the value of the pore water pressure, integrated along the saturated portion of the failure surface (Pw(+), Figure 6.4a) and along the entire the failure surface (Pw, Figure 6.4b), respectively. In general, the evolution of both Pw and Pw(+) follows the 1966 flood hydrograph.

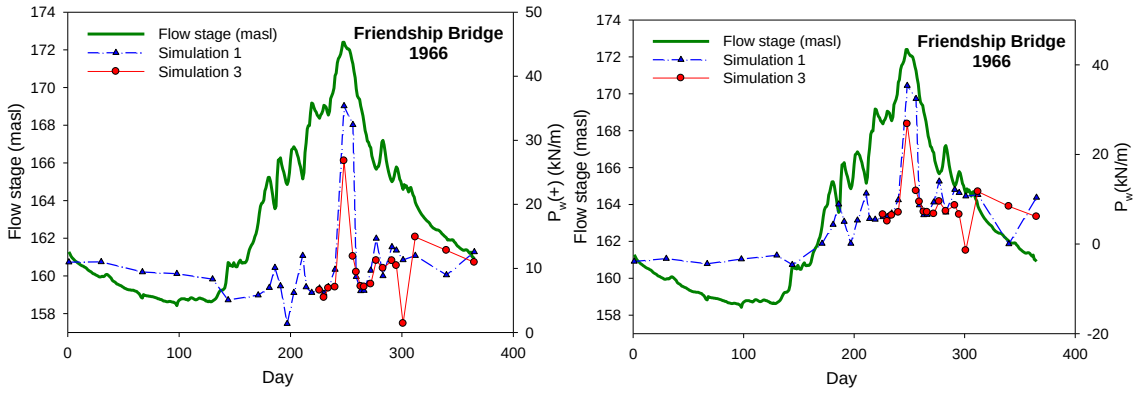

Figure 6.4. Evolution of average pore water pressure values integrated along the failure surface at the Friendship Bridge study site (1966 flow event) for scenarios 1 (no bank deformation) and 3 (bank profile deformed by fluvial erosion and mass wasting): (Left) pore water pressure integral along the saturated portion of the failure surface and (Right) pore water pressure integral along the entire failure surface.

Further details of the pore water pressure distribution, in relation to the evolution of the event hydrograph and seepage flow characteristics (Figure 6.6 and Figure 6.7) are now described. Excluding time step 0, which is the initial condition when the water table and river stage are assumed to be in equilibrium, then in the initial period of the simulation, which lasts between January and early April (time steps 1 to 98), there is a slight but progressive fall in water level from 161.3 m a.s.l to 158.4 m a.s.l as the dry season progresses. During this period, seepage flow is consistently directed from the bank towards the river, such that is there is a seepage outflow at the intersection between the water table, bank profile and river stage with an outflow velocity on the order of 2.6e-08 m/s (time step 98, 08 April 1966). However, it is noted that, unlike the Pakse and Ang Nyay study sites where the value of saturated hydraulic conductivity is low (see Table 5.1 and 6.1), here at Friendship Bridge, the saturated hydraulic conductivity is quite high especially within unit 2 and unit 3 with values of 8.89e-07 m/s and 3.93e-07m/s, respectively (see Table 6.1), so it will have crucial effects with respect of the seepage flow under actions of rainfall and confining river stage. Therefore, there is a seepage flow coming out of the unit 3 and most of unit 2 due to rainfall infiltration. The seepage velocity at the intersection between these two layers

and bank face is quite low with the value of 9.91e-09 m/s. As noted in the Pakse chapter (Chapter 4), this value is far too small to cause seepage erosion.

The hydrograph subsequently fluctuates around its base level before beginning to rise, to a flow stage of 160.7 m.a.s.l at time step 144 (24 May 1966), most likely due to the arrival of spring melt from the Tibetan headwaters. At this point, the seepage flows of unit 2 are still going out (velocity 3.94e-08 m/s at the intersection between unit 2, 3 and the bank face), but the seepage flows around the water table change direction, such that the river flow is infiltrating into the bank, albeit at rather low flow velocities. For example, the infiltration velocity at that intersection between the water table, the face of the bank profile and the river stage is 1.91e-08m/s. However, the infiltration of this water is too little to cause an impact on the pore water pressures simulated within the bank interior, so the average integrated pore water pressure (Pw) has a small negative value (i.e. stablising) of -4.61 kN/m.

In the subsequent time steps there is a significant rise in the flow hydrograph to a level of 162.8 m a.s.l at step 171 (20 June 1966) then until it stabilises at a level of 165.2 m a.s.l at time step 181 (30 June 1966). The seepage flow (around the water table) continues to be directed from the river into the bank, with the velocity at the intersection rising an order of magnitude to 7.29e-08 m/s. This significant recharge is sufficiently high that the positive pore water pressure now balances with negative pore water pressure and the value of Pw becomes positive for the first time in the simulations, with the average total integrated value of Pw being 0.11 kN/m at this time (step 171, 20 June 1966). At time step 181 (30 June 1966), inside the river bank, seepage flows which are infiltrating due to rainfall meet up with the seepage flows which are related to the rising water table, due to the river stage. The direction of the seepage flow is outwards at the intersection between the water table, the face of the bank profile and the river stage with a velocity of 3.73e-08m/s

In the next month of the simulation, that is from time step 181 (30 June 1966) to time step 211 (30 July 1966), the hydrograph fluctuates around a stage of 165.1 m a.s.l. The pore water pressure in this period therefore also fluctuates but increase to a value of Pw = 11.31 kN/m at time step 211 (30 July 1966). The seepage inflows inside unit 3 nearly stay constant, only seepage flow within unit 2 still is going out with a velocity of 6.76e-08 m/s.

Over the course of the next three weeks of the flood, the hydrograph experiences a steep rise such that the flow stage exceeds the level of the contacts between Layers 2 and 3 and Layers 1 and 2 of the bank materials (time step 219 (07 August 1966),

169.2 m a.s.l). Due to this high river stage, the seepage flows at this point directly and totally are going in to the bank. The velocity at the intersection between the water table, the face of the bank profile and the river stage decreases by an order of magnitude to a value of 1.11e-08 m/s and the pore water pressure index value Pw drops to 5.48 kN/m. After slightly decreasing in the following two weeks, from time step 234 (22 August 1966) the hydrograph again rises and reaches its peak at a level of 172.4 m a.s.l by time step 248 (05 September 1966). The seepage flows are going in at this time step. The average total integrated value of Pw attains its maximum value of 35.36 kN/m at this point. These values are, in principle, sufficiently high to significantly destabilise the bank with respect to mass failure, but as discussed further below (see Section 6.1.3), the effect of the large confining pressure exerted by the flow is sufficient to ensure that the simulated factor of safety is also high at this time. However, by this time the accumulated erosion by hydraulic action of the flow is also sufficient to deform the bank profile, such that scenario 3 is initiated at time step 226 (14 August 1966).

After the peak of the flood, the water stage falls significantly (at a rate of 0.22 m/day) over the course of the next month, reaching a level of 165.7 m a.s.l by time step 277 (04 October 1966). In this period, the seepage flows still go in when the river stage exceeds the bank top but they reverse out of the bank to the river when the hydrograph falls. The seepage velocity at the intersection between the water table, the face of the bank profile and the river stage is 5.09e-07 m/s (step 266, 23 September 1966). In addition, the value of Pw decreases to a value of 13.99 kN/m in this period. However, it is noteworthy that Pw remains positive in sign during this period when the confining pressure of the flow is falling significantly, leading to a dramatic drop in the factor of safety (see Section 6.1.3). After this time, the hydrograph experiences another small peak when it rises 1.5m by time step 283 (10 October 1966) before dropping again to a lower level of 165.0 m a.s.l a week later. In this period, the parameter Pw declines to 7.08 kN/m before rising to a value of 12.13 kN/m by time step 291 (18 October 1966).

Finally, after time step 295 (22 October 1966), the hydrograph continues to fall until the end of the simulation, reaching a minimum stage of 160.9 m.a.s.l. The pore water pressure Pw does not fall significantly fall in this period, but instead fluctuates, ending with a value of 10.39 kN/m. The seepage flow at the end of hydrograph (step 365, 31 December 1966) is directed from the bank to the river with the outflow velocity at the intersection between the water table, the face of the bank profile and the river stage being 2.81e-08 m/s.

6.1.3 Bank stability and sediment entrainment

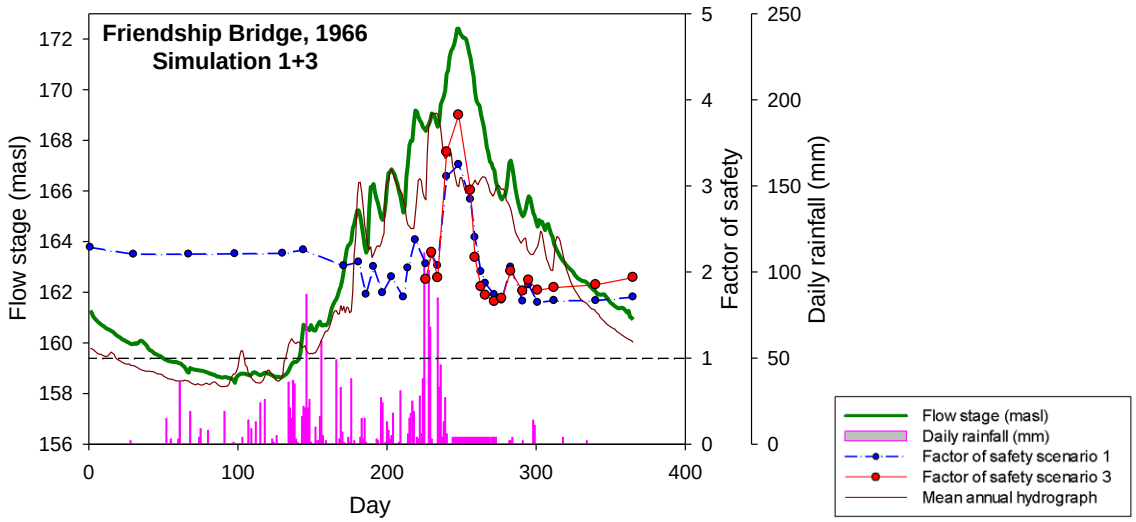

Figure 6.5. Hydrograph, rainfall intensity and simulated factors of safety of flow event 2000 for simulation scenario 1 (no fluvial erosion) and 3 (fluvial erosion) at the Friendship Bridge study site (for results for other events see Figure 6.8).

As illustrated in Figure 6.5, the factor of safety (FoS) with respect to mass failure in both scenario 1 and 3 remains above the critical value of unity so the bank is stable under the 1966 event conditions. In addition, and similarly to Darby et al. (2007), in both two cases there is also a decline (though not a small one like the Pakse study site discussed in Chapter 4) in stability by the end of the simulation period (for example the simulated FoS values exhibit a decrease of 0.576 and 0.349 for scenario 1 and 3, respectively, between the beginning and end of the simulation period). This reflects the destabilising effect of the elevated pore water pressures seen between the start and end of the simulation (e.g. the integrated pore water pressure Pw at step 1 and step 365 is -3.88 kN/m and 10.39 kN/m, respectively in scenario 1). There are only modest differences in FoS values simulated under scenarios 1 and 3, with FoS for the latter scenario, as expected, being both somewhat larger and smaller (unlike the Ang Nyay study site but similar to Pakse) than the former scenario (i.e. at step 234 (22 August 1966), the Fos is 2.072 in scenario 1, larger than that in scenario 3 (1.932); at step 291 (18 October 1966), the FoS in scenario 1 is 1.661 less than that in scenario 3 (1.778)).

Given the differences in the simulated FoS values for each simulation scenario, the simulated temporal variations in FoS must be attributed to the varying values of pore water and confining pressure simulated during the course of each simulation. Thus, when the flow level is low (e.g. Figure 6.6, time step 130, 10 May 1966) the bank is dominated by negative (stabilising) pore-water pressures. In contrast, during peak flow,

the immersion of the bank is sufficiently long to cause complete saturation and the generation of positive pore water pressures (Figure 6.6, time step 248, 05 September 1966). When the river stage recedes, the ground water table also goes down along with the water level (Figure 6.6, time step 312, 08 November 1966), resulting in a significant reduction of hydrostatic confining pressure. However, in both scenarios 1 and 3, the positive pore-water pressures are insufficiently high to trigger mass-failure (e.g. the average integrated pore water pressure Pw in scenarios 1 and 3 are 11.00 KN/m and 11.69 kN/m, respectively).

Thus, it is apparent that, similar to Simon et al. (1999), Darby et al. (2007) and the results from the Pakse and Ang Nyay study site reported in Chapter 5 and 6, the dominating influence on bank stability is the hydrostatic confining pressure exerted by water in the channel, so that temporal trends of FoS are strongly positively correlated with fluctuations in the flow hydrograph. For example, in scenario 1 (no fluvial erosion), the initial factor of safety is 2.285, but as flow stage decreases the factor of safety also slightly decreases to 2.210 by time step 98 (08 April 1966). When the river stage reaches the peaks observed at time steps 181 (30 June 1966), 219 (07 August 1966) and 248 (05 September 1966), the factor of safety also rises to 2.115, 2.373 and 3.248, respectively. On the first half of the falling limb when the flow stage recedes rapidly from its peak then at step 256 (13 September 1966), 263 (20 September 1966) and 277 (04 October 1966), the simulated factor of safety also falls to values of 2.844, 2.003 and 1.671, respectively.

Scenario 3 incorporates the effects of fluvial erosion and, as such, it initially might be thought that this scenario would be associated with reduced FoS values. However, similar to the Pakse study site, compared with values in scenario 1 and scenario 3 in fact scenario 3 experiences both larger and smaller factors of safety. The difference between the FoS values simulated in scenarios 1 and 3 range from approximately 1.2% to 13.3%. The differences in the factors of safety can be grouped into three periods: from step 230 (18 August 1966) to 256 (13 September 1966), step 259 (16 September 1966) to 283 (10 October 1966) and from step 291 (18 October 1966) to 365 (31 December 1966). In the first period, except for step 234, the larger factors of safety in scenario 3 are due to the smaller average integrated pore water pressure Pw (i.e. step 248 (05 September 1966), the factors of safety in scenarios 1 and 3 are 3.248 and 3.882, while the Pw for this step is 33.36 kN/m and 26.81 kN/m, respectively). The lower factors of safety in scenario 3 in the second period (except for step 277, 04 October 1966) are due to greater Pw values (except for step 272 (29 September 1966) and 277 (04 October 1966)), i.e. at step 266 (23 September 1966), the factors of safety in scenarios 1 and 3 are 1.868 and 1.729, while the Pw values in this step is 6.53

kN/m and 7.12 kN/m, respectively. In the last period, the factor of safety in scenario 3 again is larger than that in scenario 1 due to the lower value of Pw (except for step 312 (08 November 1966) and 340 (06 December 1966)), i.e. at step 295 (22 October 1966), the factors of safety in scenario 1 and 3 are 1.850 and 1.905, while the Pw values in this step are 11.45 kN/m and 6.60 kN/m, respectively.

Due to the absence of mass wasting in scenario 3, the volume of bank material entrained to the river is associated exclusively with fluvial erosion. The total unit volume of eroded sediment in this case is 16.1 m^3/m, four times larger than at the Ang Nyay study site (see Section 5.1.1), with most (87%) supplied from the lower unit of bank material (82% at Ang Nyay), mainly due to its greater thickness, even though the mean erosion rate of the bank toe is similar to the bank top and is two thirds of that of the middle layer (see Section 6.1.1).

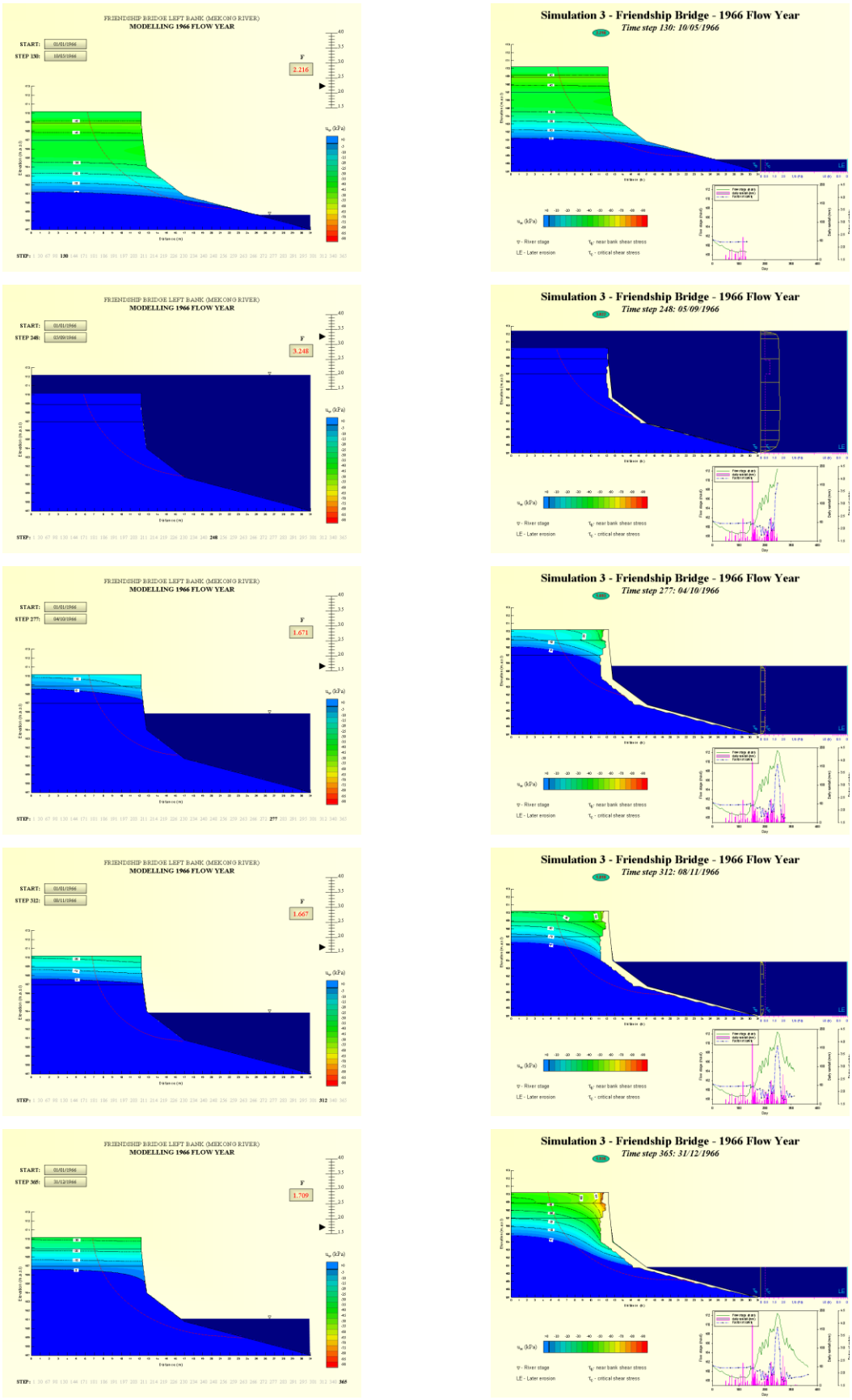

Figure 6.6. Simulated bank pore water pressure distributions for selected time steps at Friendship Bridge for scenario 1 (no bank deformation, left hand side), scenario 2 (bank profile is deformed by mass wasting, middle column) and 3 (bank profile is deformed by both fluvial erosion and mass wasting, right hand side). Animations of the complete simulation sequence are available in the accompanying CD.

Step 130

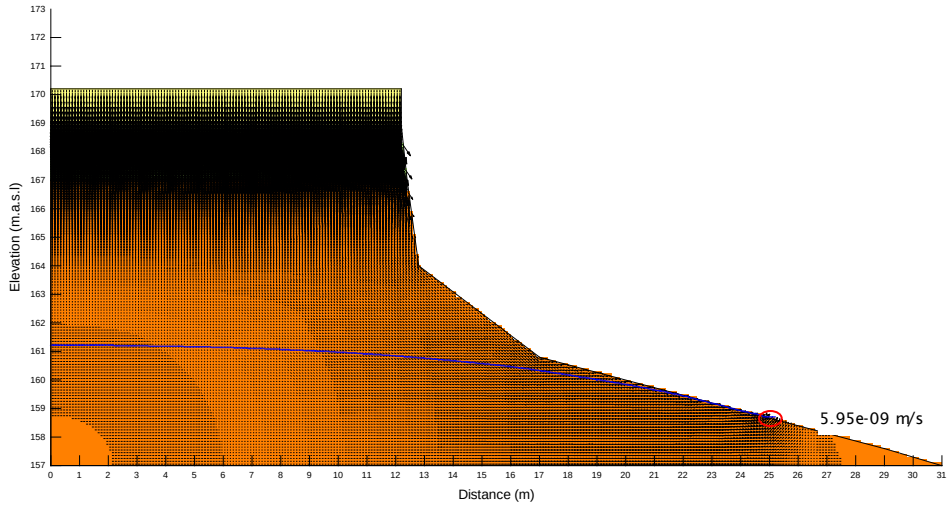

Step 277

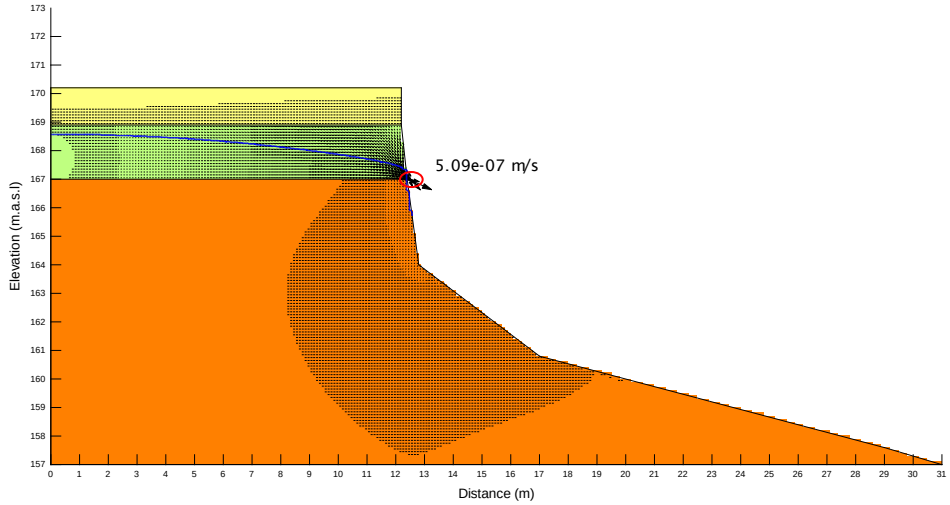

Step 365

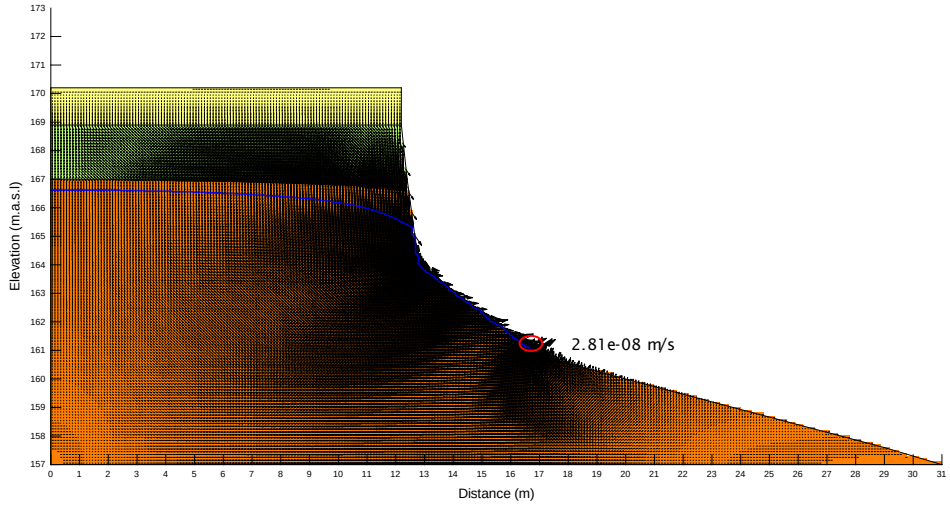

Figure 6.7. Simulated bank seepage flow for selected time steps at Ang Nyay (scenario 1), green and yellow colour is river bank material, blue line is water table, and red circle is the intersection between bank surface, water table and river stage

6.2 Synthesised results at the Friendship Bridge study site

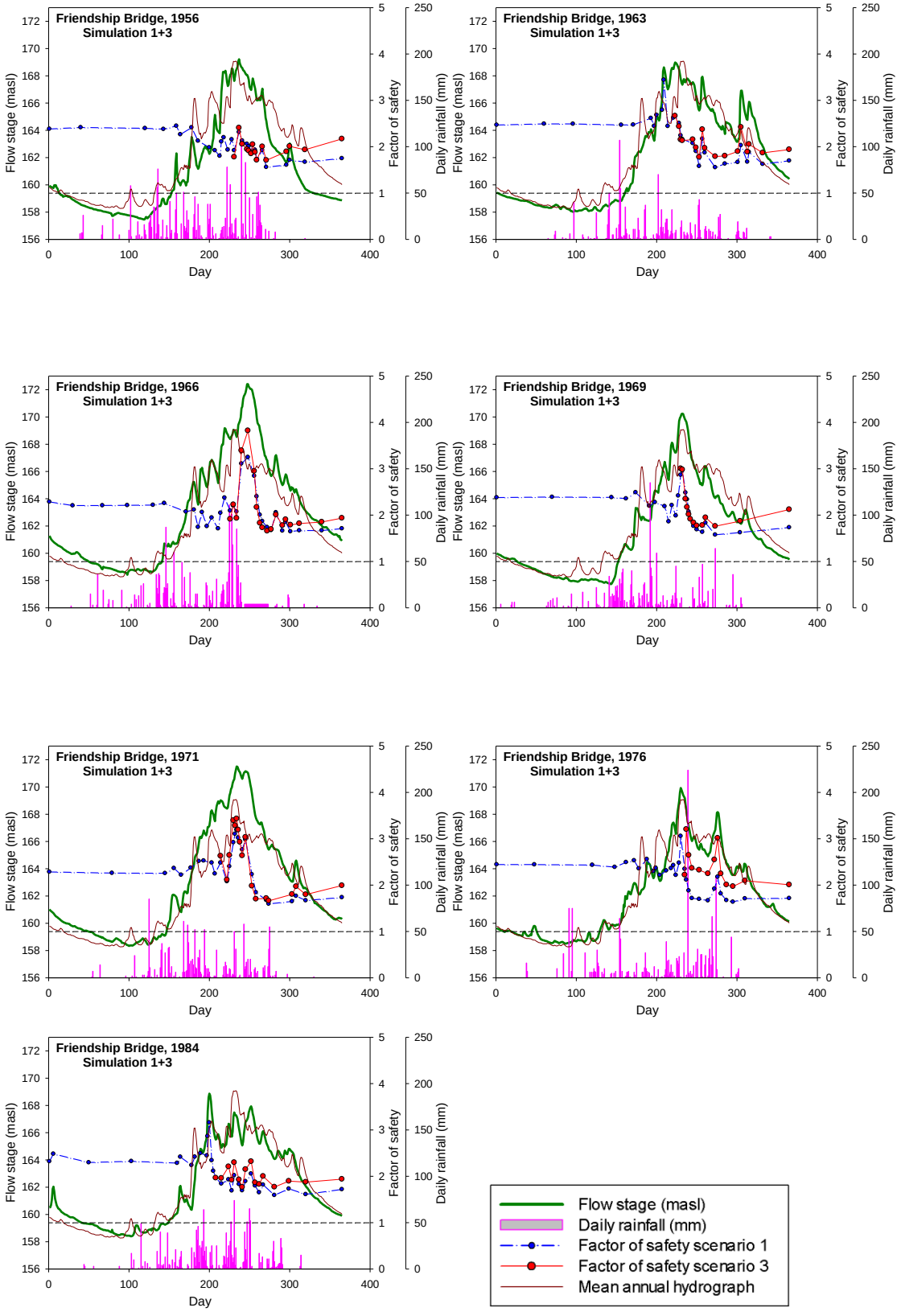

Figure 6.8. Hydrograph, rainfall intensity and simulated factors of safety for the selected flow events for simulation scenarios 1 and 3 at the Friendship Bridge study site

As can be seen in Figure 6.8, the factors of safety follow in part the trend (1956, 1969, and 1971) or mostly the trend (1963, 1976 and 1984) of the hydrograph, the FoS is greatest when the flow level is high; and indeed FoS remains above 1 at all times and for both simulation scenarios so the river bank remains stable with respect to mass failure. The maximum factor of safety occurs in phase with the peak flow and the minimum factor of safety mostly occurs at the end of the simulation, giving an overall range of simulated FoS from 0.889 for the low flow event (i.e 1956) to 1.603 for the high flow event (i.e. 1966). Pore water pressure values, as integrated along the failure surface (i.e, the parameter Pw), remain negative mostly for the whole simulation in both scenarios 1 and 3 (in case of low flow event i.e. 1956, 1963, 1984); remain positive in part of the high stage hydrograph (in case of medium high flow event i.e. 1969, 1976); or remain positive in the whole simulation (high flow event i.e. 1971). However, even for the brief maxima the maximum value of Pw in all the above cases is still insufficient to trigger mass failure. Therefore, the pore water pressure has relatively little effect on the stability (with respect to mass failure) of the river bank under all the above flow events.

As can be seen from Figure 6.9, the peak pore water pressure values increase in proportion to the peak discharge (i.e the largest flood events simulated (1966 and 1971) generate the largest values of Pw). The correlation of Pw and Pw(+) with Q_{peak} in scenario 1 has similar values of r^2=0.90 and r^2=0.87, respectively. In addition, note that the correlation is weaker than Ang Nyay study site, where the trends of Pw and Pw(+) in scenario 3 also have strong correlations, but here at Friendship Bridge these regressions have values of r^2=0.67 and r^2=0.77, respectively, though they also have increasing trends with hydrograph peak. In both cases of Pw and Pw(+), scenario 1 has a faster increasing rate than that for scenario 3, so the gap between the pore water pressure in the two scenarios becomes larger as flood magnitude increases.

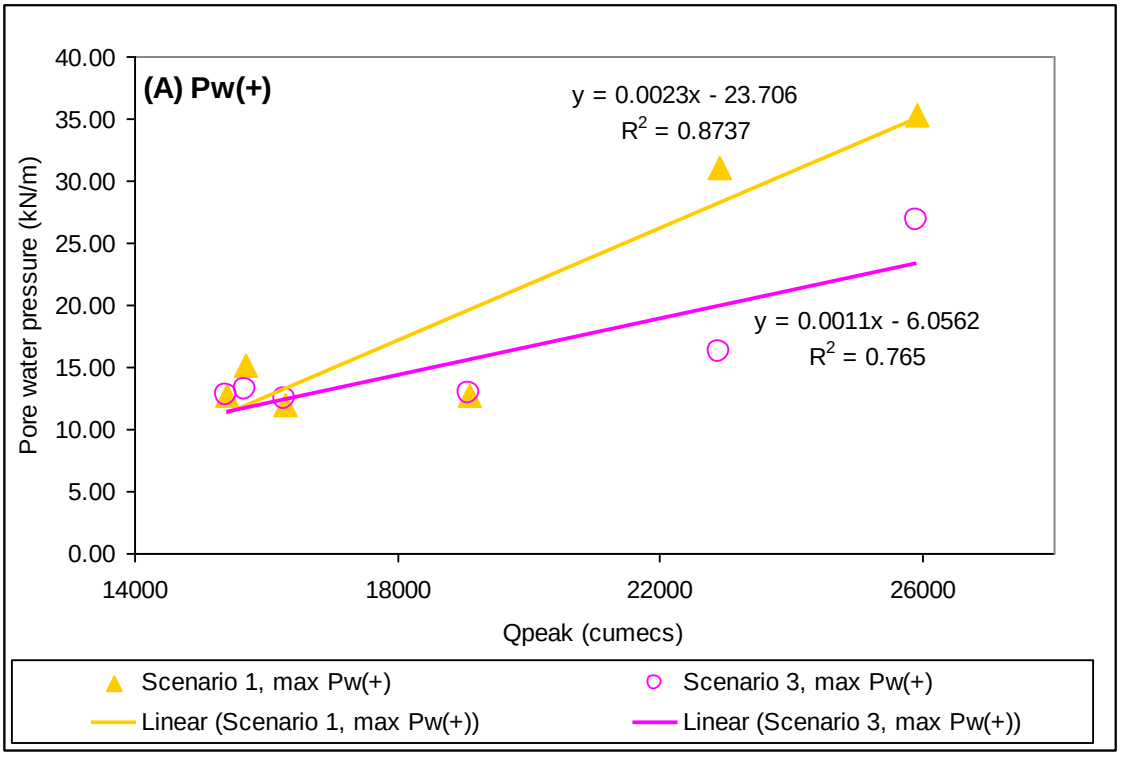

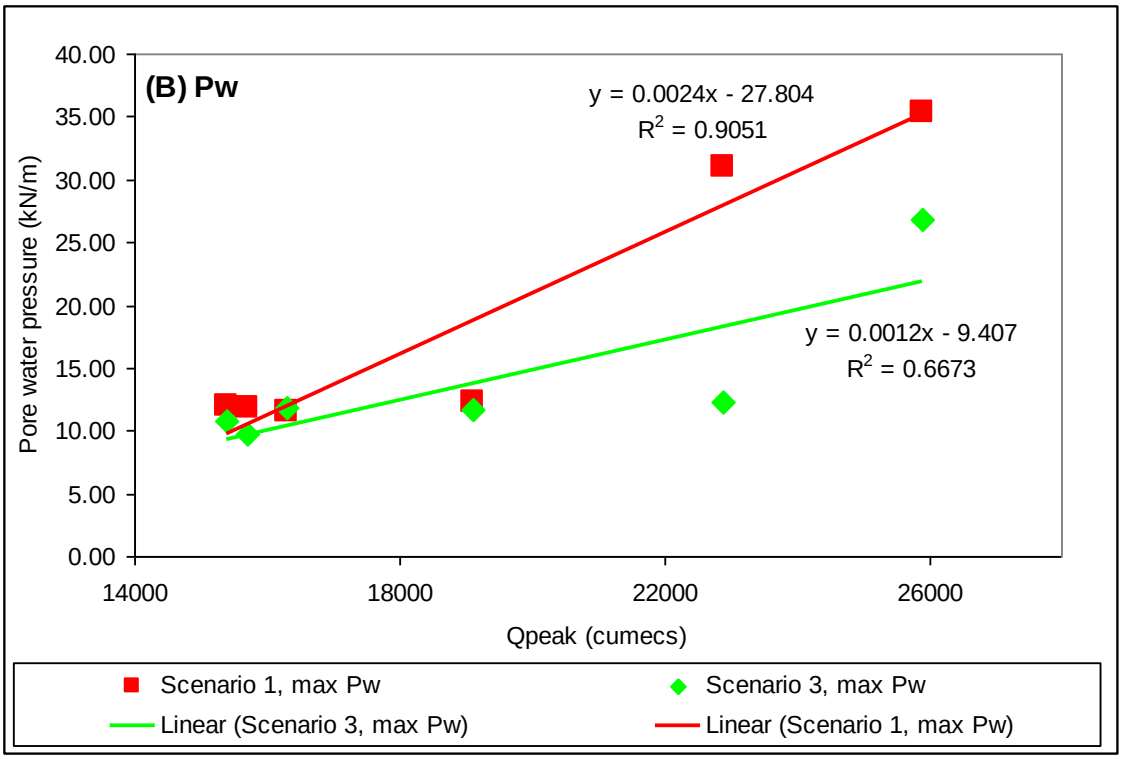

Figure 6.9. The maximum and minimum average pore water pressure integrated along the failure surface at the Friendship Bridge study site for simulation scenarios 1 and 3. Pw is the pore water pressure integral along the whole of the failure surface and Pw(+) is the pore water pressure integral along the saturated portion of the failure surface.

Following Luppi et al. (2009), Figure 6.10 illustrates the relationship between mass failure and flow intensity by plotting values of the minimum factor of safety and peak flow discharge. The data are scaled to peak flow stage against total bank height D_{peak}/H_{bank} in order to compare this study site (Friendship Bridge) with Pakse and Ang Nyay, as well as with other sites such as the Sieve river (Darby et al., 2007) and the Cecina river (Luppi et al., 2009).

In Figure 6.10 most of the minimum factors of safety in scenario 3 are larger than those in scenario 1, like the Ang Nyay study site. Moreover, fair regression correlation coefficients are acquired in both simulations with $r^2 = 0.67$ (scenario 1) and $r^2 = 0.70$ for simulation 3. There is a decline in the trend of the factor of safety when the peak flow stage increases in scenarios 3. This result is similar to Rinaldi et al. (2004) and Luppi et al. (2009)'s research wherein the higher river stage, the more unfavorable the pore water pressure. However, an increasing trend with peak flow stage occurs in scenario 1. In addition, unlike the Any Nyay study site, the gap between the factors of safety in the two scenarios is smaller along with the peak flow stage, indicating that in the high flow event, the effect of fluvial erosion at this study site is a disadvantage in terms of mass failure.

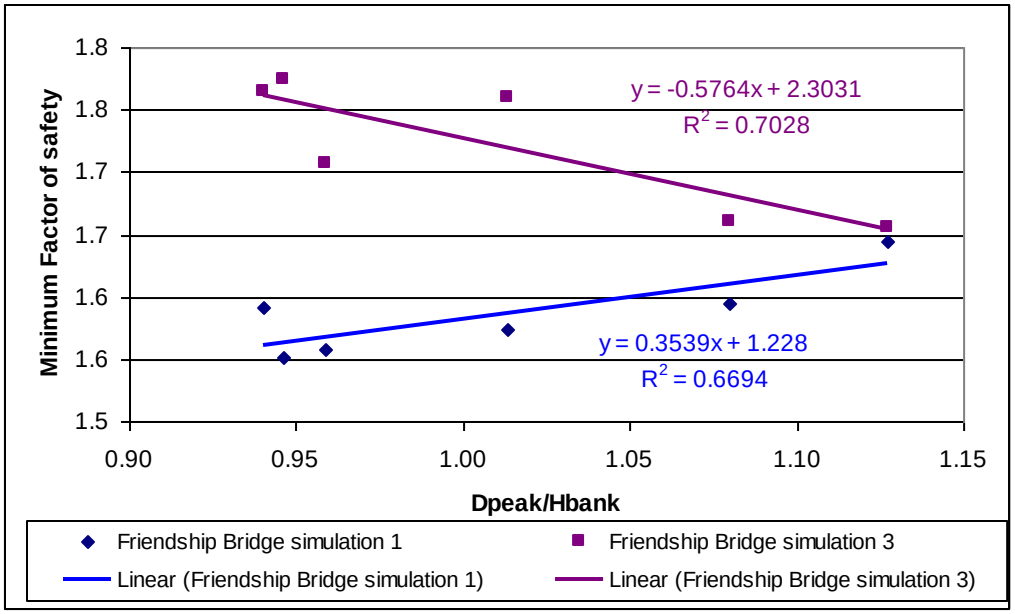

Figure 6.10. Minimum factor of safety for slide failures as a function of non-dimensionalised peak flow depth at Friendship Bridge study site, D_{peak}: peak flow depth; H_{bank}: bank height; D_{peak}/H_{bank}: non-dimensionalised peak flow depth.

Figure 6.11 shows the relationship between the annual discharge and the total amount of sediment eroded by fluvial erosion. Unlike Figure 6.9 and Figure 6.10 above where the peak discharge is taken into account, here the total annual discharge is employed as the hydraulic action which cause the fluvial erosion occurs not only at the peak but also at other phases of the hydrograph throughout the whole year simulation.

It can be seen in Figure 6.11 that all three material units exhibit an amount of sediment yield in proportion to the Σ(Q-Qc) discharge. All have very strong regressions with similar correlation coefficients for bank top, middle layer and bank toe is r^2=0.95, r^2=0.97 and r^2=1.00, respectively. Moreover, like the Pakse and the Ang Nyay studies, the bank toe also produces much more sediment than the other layers, i.e. about 87% for high flow events (1966, 1971) and more than 98% for low flow events (1984).

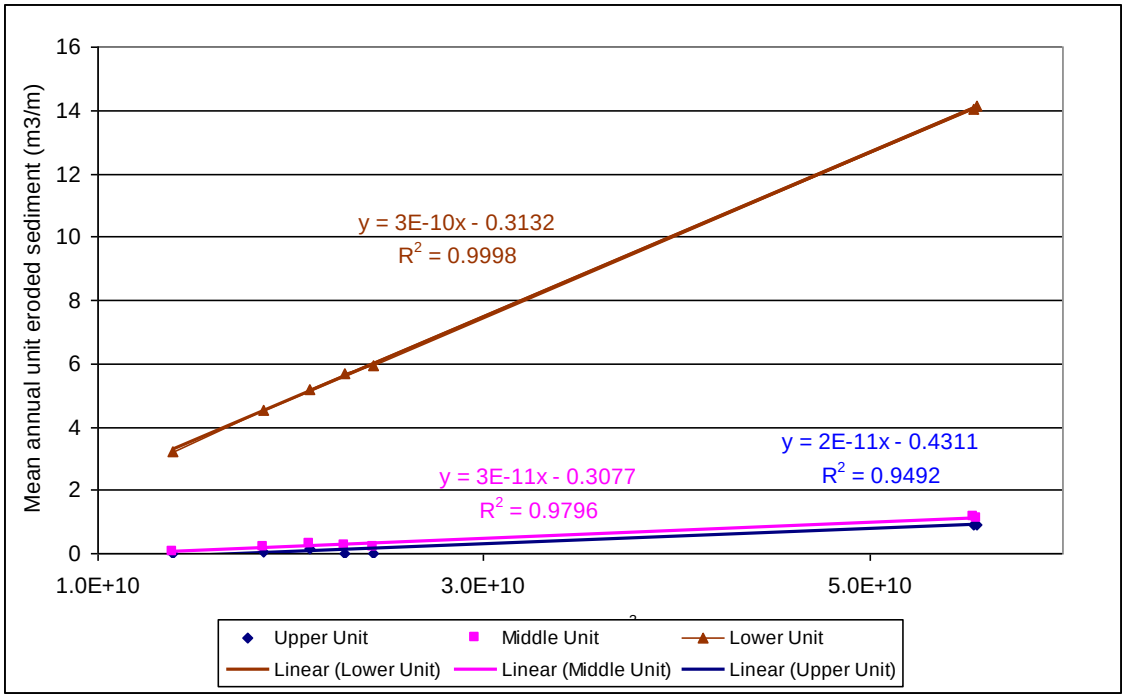

Figure 6.11. Total annual discharge over the threshold discharge Σ(Q-Qc) versus eroded volume at the bank top (purple), at the middle layer (blue) and at the bank toe (yellow) at the Friendship Bridge study site.

Chapter 7 Discussion and Conclusion

In the preceding chapters, the erosion processes along the Mekong have been analysed through simulations at three study sites: Friendship Bridge, Ang Nyay and Pakse. This chapter will discuss these erosion processes, specifically focusing on the issue of how the controlling factors affect the Mekong's river banks. In addition, results obtained from the Mekong will be compared with results from other rivers, to determine if the bank failure processes associated with this large, tropical, river system are distinctive.

7.1 Dominant processes

Similar to other research such as Dapporto et al. (2003); Darby et al. (2007); Rinaldi and Darby (2008); and Luppi et al. (2009), the bank erosion processes on the Mekong are affected by factors such as pore water pressure, flow discharge, river water level, bank material composition and bank geometry. The literature review chapter indicates the target of this research is to identify which of these factors have the most impact on river bank stability in the Mekong. Therefore, each of the factors which affect the factor of safety calculation is analysed in the sections below.

7.1.1 Pore water pressure

Arguably the most important factor in triggering bank failure, pore water pressure is discussed first. Similar to previous research, such as Rinaldi et al. (2004) or Darby et al. (2007), pore water pressure is identified as having a vital role on river bank stability at all three study sites. Negative pore water pressure is dominant in the initial time steps when the river stage is low. As the water level rises in the rainy season, positive pore water pressures develop. The positive pore water pressure obtains a maximum value mostly when the hydrograph reaches the peak (i.e Pakse in Section 4.1.2, Friendship Bridge in Section 6.1.2). When the hydrograph moves to the falling limb, the positive pore water pressure also decreases but at a lower rate. The river bank is therefore most vulnerable when the water level drops dramatically after the peak, because the positive pore water pressure can still remain high in the bank, leading to mass failure due to the lack of a confining water level (see Section 5.1.2 for Ang Nyay study site).

There are two parameters in this research which appear in the bank stability computation (factor of safety), namely the pore water pressure integrated along the saturated portion of the failure surface Pw(+) and along the whole failure surface Pw.

The Pw(+) has a more important effect than Pw as its value above the failure surface decides the value of the factor of safety. At all three study sites in the Mekong, peak pore water pressure Pw(+) increases in proportion to the magnitude of the peak discharge, meaning that large flow events exhibit greater values of Pw(+). Similar to Pw(+) at all three sites, the values of Pw also increase in proportion with peak flows.

7.1.2 Bank geometry

The bank height at all three sites exceeds 10m. At Friendship Bridge and Ang Nyay, the river banks are inundated during the highest flow events, for example the 1966 and 1971 floods. The fluvial erosion model applied in scenario 3 changes the bank profiles. For low flow events the bank angle increases due to the fluvial erosion of the lower bank unit, but the bank is stable as positive pore water pressure within the river bank is insufficient to cause mass failure. For high flow events, at Pakse and Ang Nyay, fluvial erosion causes the bank profile to flatten out, since the critical shear stress of the upper layers are less than those in the lower layers. Therefore the river banks at these two sites are stable. Note that this is unlike expectations compare with other rivers (Darby et al., 2007; Luppi et al., 2009). This could be a specific characteristic of the Mekong, where the high banks consolidate toe materials then make them more resistant.

7.1.3 Hydraulic conductivity

At Pakse, there is a very low hydraulic conductivity in both material layers, which are silt and clay, so the effect of rainfall is confined mainly to around the zone near the bank top. The combination of rainfall and water table effects occurs only when the river stage is high and within the upper material unit. The presence of low conductivity material also is a reason for the formation of steep wetting fronts.

At Friendship Bridge, there is a high conductivity (much more than Pakse), so the combination of rainfall and river stage leads to rapid changes in the water table and corresponding pore water pressures. The water table increases faster when the hydrograph rises in phase with high intensity rainfall i.e. time step 181 (30 June 1966), it also drops quickly on the falling limb (as well as in the dry season) when the amount of rainfall is limited.

At Ang Nyay, the conductivity is not as high as at Friendship Bridge but not as low as Pakse. When the river stage is low, rainfall infiltration causes a reduction of matric suction in the region near the bank top. When the flow stage increases, rainfall and

river stage induce a saturated wetting front and reduce the matric suction zone of the upper unit.

7.1.4 Rainfall intensity

The climate of the Lower Mekong Basin is dominated by the Southwest Monsoon, which generates wet and dry seasons of more or less equal length. Therefore, the flood period usually lasts from May until late September or early October. Heavy rain fall may persist for one or two days in most parts of the basin (MRC, 2005). Due to the modulating influence of the hydraulic conductivity, the role of rainfall is quite different for each site. In low conductivity bank material such as found at Pakse, the role of rainfall is very little as most of the rainfall becomes surface run-off and goes directly to the river. The saturated bank top portion expands slowly and meets the water table when flow stage is at a high level and at the zone near the bank surface. For a high conductivity river bank like Friendship Bridge, rainfall quickly infiltrates into the bank and becomes seepage flow.

7.1.5 Bank material

River banks on the Mekong are normally composed of fine-grained cohesive sediments. Bank material characteristics are also crucial in bank stability analysis, specifically the bank strength, hydraulic conductivity and material physical characteristics (i.e. critical shear stress; erodibility). As described above, the grain-size obtained from the bank material is used to estimate the hydraulic conductivity. Cohesion, friction angle and critical shear stress define material strength which affect the factor of safety and fluvial erosion calculations. At Friendship Bridge, the bank strength at the bank toe is high (see Section 6.1) which keeps the bank stable under any historical floods (i.e. 1966, 1971) and also the factor of safety at Friendship Bridge is generally higher than that at the other sites.

Critical shear stress has a close relationship with bank material, it is measured *in situ* by the CSM device at the bank face or from cores taken from boreholes. The higher the strength of the material, the higher the critical shear stress and the less sediment is eroded by fluvial erosion. At Ang Nyay, the bank top has a lower critical shear stress than the bank toe (noted above at Section 7.1.2), so the bank profile is flattened out.

7.1.6 Hydrograph

The Mekong River is located in the tropical monsoonal region, so its hydrographs have specific monsoonal characteristics such as a long duration of high water level, and prolonged rainfall in the wet season (MRC, 2007). While in temperate zone rivers, the flood pulses occur throughout the year albeit with seasonal bias. In the Mekong, peak flows and water levels are often such that the river banks are submerged for days or weeks (at Friendship Bridge and Ang Nyay) at a time.

As discussed in Chapter 3, in this study the hydrographs of the Mekong are divided into three types: single peak, multi-peak and rapid fall. In typical single peak hydrographs (i.e. Pakse 1956 or Friendship Bridge 1971), the effect of this type of hydrograph on river bank stability depends on its magnitude. The low and median flow hydrographs have less sediment, which is eroded by fluvial erosion into the river and the high flow discharge obviously has a higher erosion rate. The river bank under this type of hydrograph is normally stable because the water table and river stage are approximately is equilibrium.

For multi-peak hydrographs (most caused by tropical cyclones), there is an increase in unfavorable pore water pressure caused by the second peak because the river bank is already wetted by the preceding peak. However, those pore water pressures are still not large enough to trigger a mass failure. At Ang Nyay, both the 1963 and 1976 events are considered as low flow hydrographs so they cannot lift the elevated pore water pressure field to a high enough position which may cause bank mass failures.

Rapid fall hydrographs likely can cause bank mass wasting. At Ang Nay (1966), in the scenario 1, there is a failure of the river bank at the end of the falling limb due to a lack of confining pressure. For other rapid fall events on the Mekong, i.e at Pakse, 1981, 1991; although the factors of safety on the falling limb decrease quickly, they still remain larger than 1. The reason is the pore water pressure field is not high enough due to low conductivity of the bank materials. At Ang Nyay 1984, this event has a very impressive rate of fall but it is a relatively low flow flood, so the pore water pressure value is not sufficient to cause mass wasting. At Friendship Bridge (1966), the bank strength at this study site is so high that it is stable under any hydrological conditions.

7.1.7 Dominant processes for the Mekong

On the Mekong it has been shown there is little mass wasting and low rates of fluvial erosion. So mass wasting does not seem to be especially important on the Mekong. This is the case even when banks are submerged every year. One of the possible reasons is the great bank height, such that the bank material is more consolidated, stronger and the hydraulic conductivity is much lower than banks elsewhere (for example, saturated hydraulic conductivity of the bank top at Pakse, Ang Nyay and Friendship Bridge is 1.32e-08 m/s, 1.51e-08 m/s and 3.48e-08 m/s, respectively while that value at the bank top of Sieve river is 1.00e-4 m/s (Darby et al., 2007)). For this reason slow, gradual, fluvial erosion appears to be the dominant process.

7.2 Comparison of erosion processes on the Mekong versus other rivers

Based on the results obtained in Chapters 4, 5 and 6, this section will compare the erosion processes that occur on the Mekong with other rivers in the humid-temperate zone. Data used were from Rinaldi et al. (2004), Darby et al. (2007) and Luppi et al. (2009). However, this review will focus on the similarities and differences in scenario 3, so that the data which represents the dynamic simulations in Darby et al. (2007) and Luppi et al. (2009) will be utilised.

7.2.1 Mass wasting processes

Mekong data from all three study sites is here correlated together, while additional data from the Sieve river (Darby et al., 2007) and Cecina river (Luppi et al., 2009) is also included in the deliberation. As described in Luppi et al. (2009), the regression of relationship between mass failure and flow intensity (scenario 3) for the non-Mekong river has a regression r^2=0.54 while that regression obtained through all the Mekong data is not significant at all (r^2=0.01). One of the reasons why the correlation coefficient for the Mekong is so low is because Friendship Bridge and Ang Nyay have the same hydrological data (they are both located near Vientiane gauging station), so they have the same values of D_{peak}/H_{bank} but of course difference in values of factor of safety. Therefore, the data from the Mekong is evaluated separately for study site (Figure 7.1). It can be seen from Figure 7.1 that the trends are similar between all regressions for both Mekong and non-Mekong river banks as there is a decrease of factor of safety as a function of event magnitude. However, the Mekong sites start with higher stability values than the Italian river sites. For the Mekong sites, Pakse site is

mostly less stable than Ang Nyay, which in turn is less stable than Friendship Bridge. It can also be noted that the gradient of the curves in Figure 7.1 are similar for both Mekong and non-Mekong river banks with the exception of Ang Nyay, where the rate of decline in stability with event magnitude is very high. The reason for this difference is that although Ang Nyay and Pakse have the same flood hydrology index, bank strengths at Ang Nyay is weaker than that of Friendship Bridge.

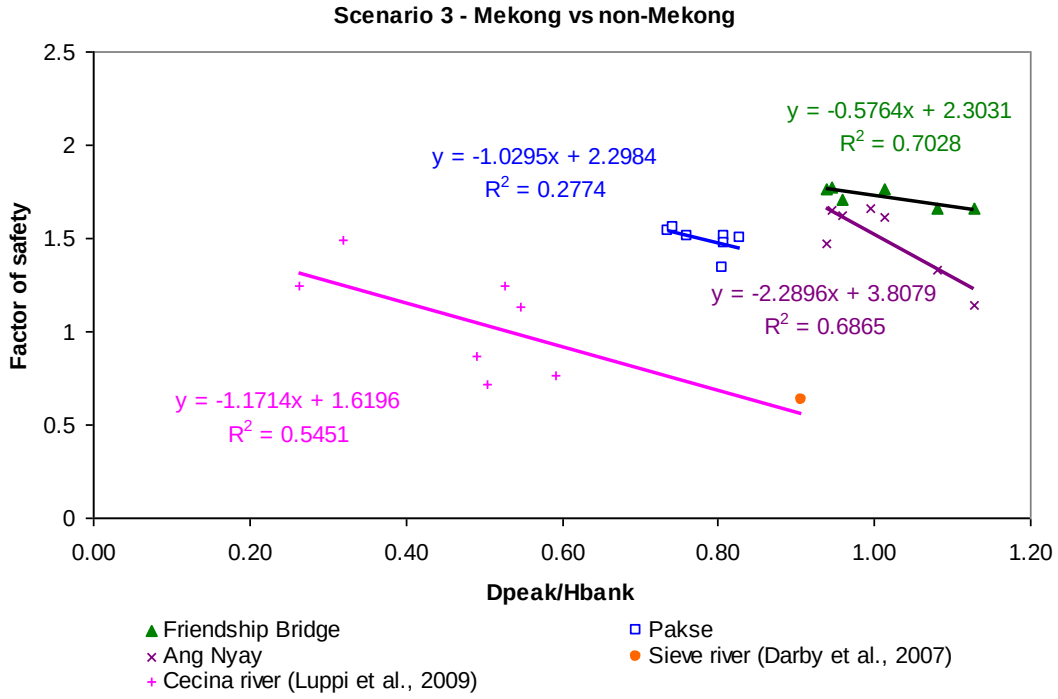

Figure 7.1. Minimum factor of safety for slide failures as a function of non-dimensionalised peak flow depth: comparison of results from this research (all three study sites) with results of other bank simulations. D_{peak}: peak flow depth; H_{bank}: bank height; D_{peak}/H_{bank}: non-dimensionalised peak flow depth.

Friendship Bridge and Ang Nyay have the highest values of D_{peak}/H_{bank}, while values of D_{peak}/H_{bank} at Pakse, though larger than that at Cecina, are less than the Sieve River. Although the discharge at Pakse is normally larger than flow discharge at Friendship Bridge and Ang Nyay, as Pakse is located downstream, river banks at Friendship Bridge and Ang Nyay often are inundated in the wet season so they have higher values of relation of peak flow depth and bank height.

It should also be noted that data for the Sieve River is single peak hydrograph, while at the Cecina River the data comprises both single peak and multi-peak hydrographs. Therefore, the data of these two types from Mekong are plotted and compare with the corresponding types for the Sieve and Cecina rivers (Figure 7.2). Because there are only two data points, the regression at Pakse for this type of hydrograph is ignored.

Similar to Figure 7.1 above, the trends of Italian rivers and the Mekong river all have negatives slopes. The value of the correlation coefficient for Italian rivers is good

(r^2=0.79) but a little bit less than that of Ang Nyay (r^2=0.82). However the correlation at Friendship Bridge is very low (r^2=0.26). Bank stability at Friendship Bridge is higher than that of Ang Nyay and both Mekong sites are more sable than those in Italian rivers. The reason, as analysed above (Section7.1), might be that the Mekong has greater bank heights and more consolidated bank materials.

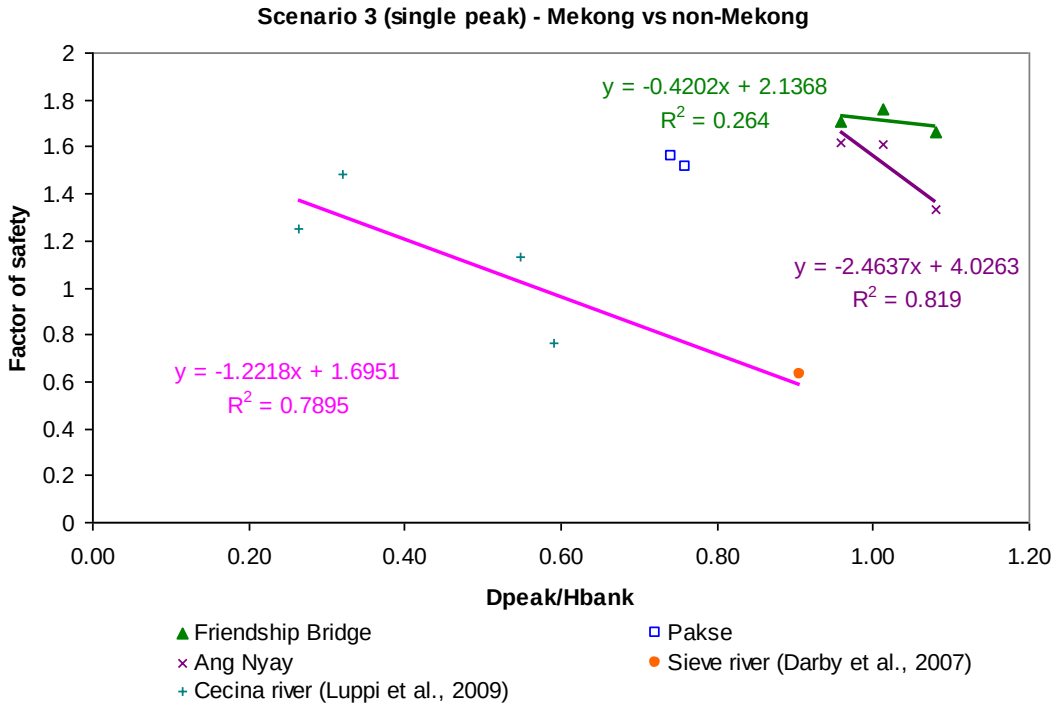

Figure 7.2. Minimum factor of safety for slide failures (for single peak hydrograph) as a function of non-dimensionalized peak flow depth: comparison of results from this research (all three study sites) with results of other bank simulations.

Figure 7.3 shows data for multi-peak hydrographs on the Mekong versus the Cecina river. Because there are only two data points for this kind of hydrograph at each Mekong study site, all data for the three sites are lumped together. The resulting Mekong data exhibit a very good correlation coefficient (r^2=0.75) and the regression trend increases with increases in peak river stage. The reason explains why on the Mekong, the stability increases with increasing event magnitude is as noted above, Pakse site is less stable than Ang Nyay and Friendship Bridge sites, also Ang Nyay and Friendship Bridge have higher values of hydrology index than that of Pakse.

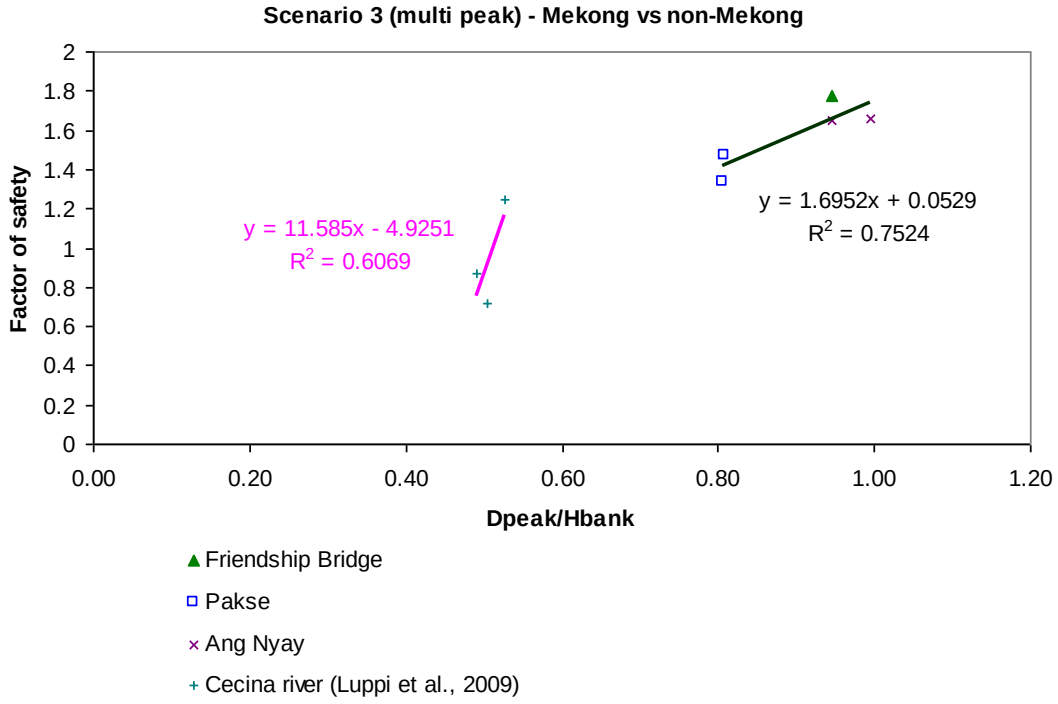

Figure 7.3. Minimum factor of safety for slide failures (for multi-peak hydrograph) as a function of non-dimensionalised peak flow depth: comparison of results from this research (all three study sites) with results of other bank simulations.

From the analysis above it can be concluded that similarities and differences exist between these two types of river as follows:

(i) The Italian rivers and the Mekong have similar regression trends such that the factors of safety decrease as the river stage increases (in general and for single peak hydrograph) or the factors of safety increase in proportion to the peak discharge (for multi-peak hydrograph).

(ii) The Mekong has a higher index of flood hydrology, ranging from 0.7 to 1.15 while that in the Italian cases range from 0.3 to 0.9.

(iii) The river banks of the Mekong have greater stability. The minimum factors of safety in the Mekong range from 1.4 to 1.8, while for the non-Mekong rivers, factors of safety range from 0.6 to 1.5.

7.2.2 Fluvial erosion and sediment entrainment

Unlike Darby et al. (2007), Rinaldi et al. (2008) and Luppi et al. (2009) where mass wasting is the dominant type of bank erosion process, in the Mekong there are no mass failures observed at the study sites, so the rate of erosion of the river bank is mainly due to fluvial erosion. The trend of the erosion rate for each sediment layer also

follows the hydrograph. The amount of sediment eroded from the bank toe is much larger than that from bank top.

Sections 4.1.1, 5.1.1 and 6.1.1 described fluvial erosion curves that follow the hydrographs. The reason for this behaviour is that the skin drag shear stress which drives fluvial erosion has a proportional relationship with the discharge (Figure 7.4, left), so that when the discharge goes to the peak, the skin drag shear stress has a maximum value, leading to the highest erosion rate. When the flood moves to the falling limb, the skin drag shear stress also decreases along with the river stage, so there is a decrease in erosion rate (Figure 7.4, right).

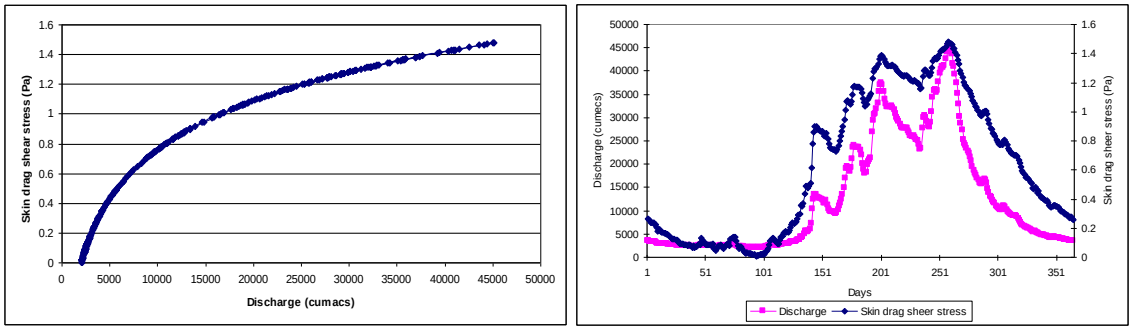

Figure 7.4. (Left) Discharge and skin drag relationship and (Right) discharge hydrograph and skin drag hydrograph at Pakse.

Fluvial erosion occurs in every event simulated in this research but at a gradual rate, even during large events. The erosion rate is quite small compared to previous research i.e. during the Pakse 2000 event: 0.2m and 0.7 m (layer 1 and 2); during the Ang Nyay 1966 event: approximately 0.45 m (all three layers) during the Friendship Bridge 1966 event: 0.7m, 0.6m and 1.4m (layer 1, 2 and 3).

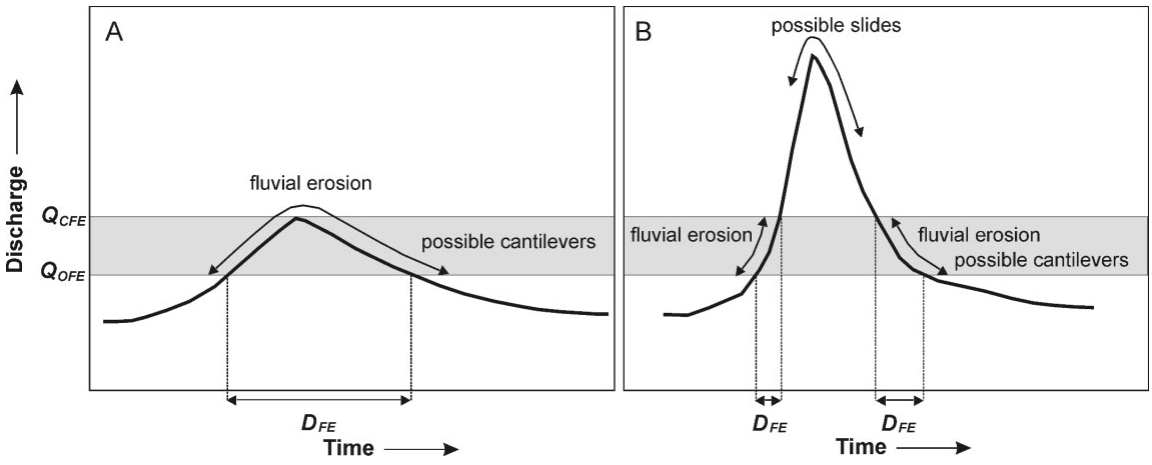

Figure 7.5. Schematic conceptual model of bank responses to hydrographs with different shapes and peak stages. (A) Hydrograph with lower peak discharge and relatively slow ascending and descending phases. (B) Hydrograph with higher peak discharge and relatively fast ascending and descending phases. Q_{OFE}, discharge

of onset for fluvial erosion; Q_{CFE}, discharge of cessation for fluvial erosion; D_{FE}, duration of fluvial erosion (Luppi et al., 2009)

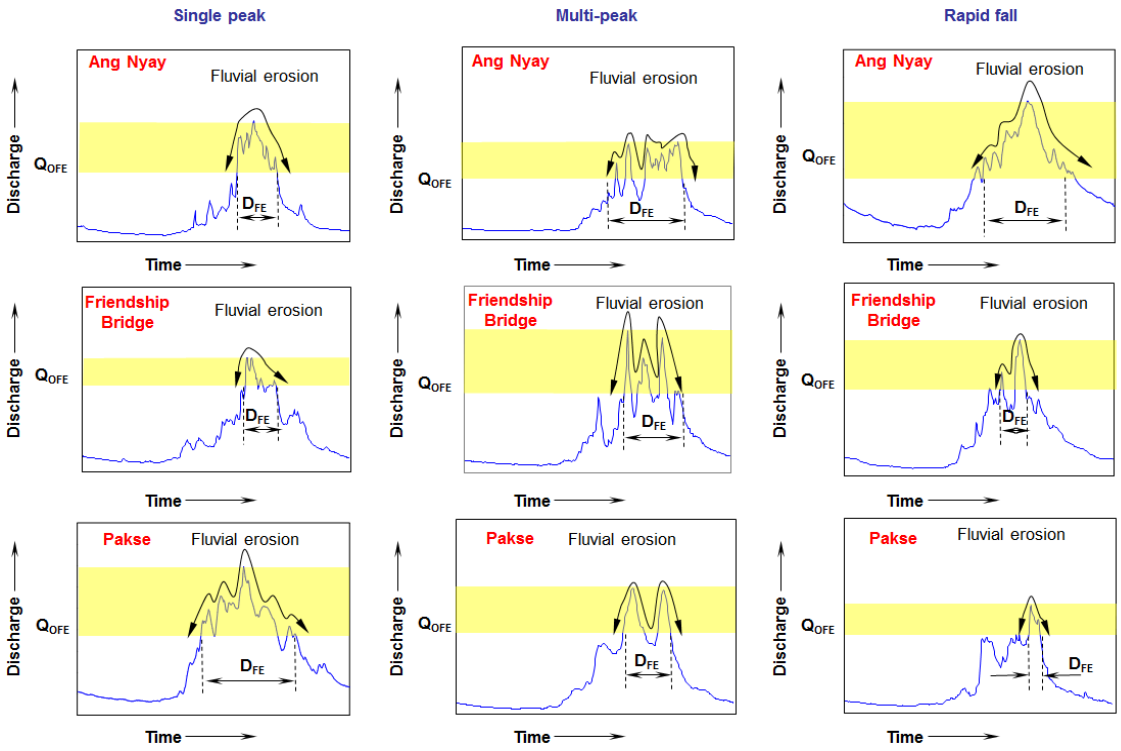

Figure 7.6. Schematic conceptual model of bank responses to hydrographs with different shapes and peak stage on the Mekong. Q_{OFE}- threshold discharge of onset for fluvial erosion, D_{FE} - duration of fluvial erosion. Yellow band shows range of fluvial erosion.

Following Luppi et al. (2009) (Figure 7.5), in this study, the results are synthesised as a conceptual model of bank response to different Mekong flood hydrographs, with three type of hydrograph and peak discharge. As illustrated in Figure 7.6, fluvial erosion at the three sites is distributed throughout the period of the hydrograph when the discharge exceeds Q_{OFE}. The duration period starts on the rising limb, continues through the peak and goes to the falling limb. In a large, high flow hydrograph, the duration of fluvial erosion is longer than that in the medium and low flow hydrograph. Also, in the case of similar magnitudes, the multi-peak hydrograph tends to produce a longer period of erosion than single and rapid fall hydrographs. As can be seen in Figure 7.6 the threshold discharges are different at the three Mekong study sites. The threshold discharge at Friendship Bridge is larger than that at Ang Nyay and Pakse, leading to the duration of fluvial erosion at Friendship Bridge being less than at the other two sites.

Bank material characteristics at all three sites influence the sediment yield by constraining the erosion with the greatest proportion (more than 80%) being derived from the lower unit. At Pakse, the volume of eroded sediment by fluvial action ranges

from 3.77 to 5.70 m^3/m; larger than that at Ang Nyay which values range from 1.75 to 4.4 m^3/m. The values at these sites are both a little less than that at Friendship Bridge; which ranges from 3.28 to 6.13 m^3/m (except for two highest events 1966 and 1971 when the eroded volumes are 16.11 and 16.15 m^3/m).

7.3 Conclusions for the Mekong

(1) The Mekong river banks are stable (in terms of mass wasting) under single peak flow events under any hydraulic and hydrological conditions. All factors of safety in all simulations of scenario 3, at all three study sites are larger than 1. Erosion processes on the Mekong are caused predominantly by fluvial erosion as there is no mass wasting in scenario 3 for any simulations.

(2) The pore water pressure, hydrograph and bank material characteristics are crucial factors in controlling bank failure mechanisms. Pore water pressure changes inside the river bank with different rates of channel water level. When water levels fall during a rapid recession period, the bank stability is at risk when pore water pressure is still high and it is more secure when pore water pressure decreases. The hydrograph has three types, and factor of safety follows the hydrograph shapes no matter what type of hydrograph shape selected. Bank materials characteristics affect the factor of safety calculation. The greater the strength of bank material, the more stable the river bank is.

(3) The fluvial erosion rate is small compared to other rivers. Application of the new novel model of computing fluvial erosion (Kean and Smith, 2006ab) leads to more accuracy in lateral erosion computations. Eroded sediment mostly is sourced from the lower bank unit. More than 80% of eroded material is calculated to derive from the bank toe at all three sites.

(4) There are some similar regression trends between Mekong and non-Mekong data. In the single peak hydrograph, the multi-peak hydrograph or all data comparisons, the trend of Mekong regressions are similar to the trends of Italian rivers.

(5) With stable river banks in terms of mass failure at the Mekong, flow discharge is regarded as the main control on river bank erosion. Therefore, with the reduction in the higher flows in the future due to Chinese dams, Lower Mekong Basin main stream and tributary dams, there is likely a trend of decrease on basin-scale bank erosion rate. However, if there is an increasing in high flows under future climate change, would potentially increase in bank erosion.

Appendix

Author's Publication: Darby, S.E., Trieu, H.Q., Carling, P.A., Sarkkula, J., Koponen, J., Kummu, M., Conlan, I. and Leyland, J., 2010, A physically based model to predict hydraulic erosion of Fine-Grained River Banks: The Role of Form Roughness in Limiting Erosion, *Journal of Geophysical Research*, 115.

My contributions in this paper are:

- Processing and analysing ADCP data.
- Conducting bank roughness surveys.
- Processing and analysing bank roughness data.
- Developing bank boundary shear stress as a function of flow discharge for Ang Nyay and Pakse.

A physically based model to predict hydraulic erosion of fine-grained riverbanks: The role of form roughness in limiting erosion

Stephen E. Darby,[1] Hai Q. Trieu,[1] Paul A. Carling,[1] Juha Sarkkula,[2] Jorma Koponen,[3] Matti Kummu,[4] Iwona Conlan,[5] and Julian Leyland[1]

Received 1 March 2010; revised 3 June 2010; accepted 21 June 2010; published 6 October 2010.

[1] Hydraulic erosion of bank toe materials is the dominant factor controlling the long-term rate of riverbank retreat. In principle, hydraulic bank erosion can be quantified using an excess shear stress model, but difficulties in estimating input parameters seriously inhibit the predictive accuracy of this approach. Herein a combination of analytical modeling and novel field measurement techniques is employed to improve the parameterization of an excess shear stress model as applied to the Lower Mekong River. Boundary shear stress is estimated using a model (Kean and Smith, 2006a, 2006b) for flow over the irregular bank topography that is characteristic of fine-grained riverbanks. Bank erodibility parameters were obtained using a cohesive strength meter (Tolhurst et al., 1999). The new model was used to estimate annual bank erosion rates via integration across the Mekong's annual flow regime. Importantly, the simulations represent the first predictions of hydraulic bank erosion that do not require recourse to calibration, thereby providing a stronger physical basis for the simulation of bank erosion. Model predictions, as evaluated by comparing simulated annual rates of bank toe retreat with estimates of bank retreat derived from analysis of aerial photographs and satellite imagery, indicate a tendency to overpredict erosion (root-mean-square error equals ±0.53 m/yr). Form roughness induced by bank topographic features is shown to be a major component (61%–85%) of the spatially averaged total shear stress, and as such it can be viewed as an important factor that self-limits bank erosion.

Citation: Darby, S. E., H. Q. Trieu, P. A. Carling, J. Sarkkula, J. Koponen, M. Kummu, I. Conlan, and J. Leyland (2010), A physically based model to predict hydraulic erosion of fine-grained riverbanks: The role of form roughness in limiting erosion, *J. Geophys. Res.*, *115*, F04003, doi:10.1029/2010JF001708.

1. Introduction

[2] The erosion of sediment from riverbanks is a key factor affecting a range of physical, ecological and management issues in the fluvial environment, with significant fractions of the total sediment load transported within alluvial sedimentary systems being sourced from river bank erosion [*Rinaldi and Darby*, 2007]. When rivers flow through densely populated regions, even modest rates of bank erosion can present a significant hazard to agriculture, built infrastructure and navigation. Furthermore, the sediments supplied from the process can be important in the establishment of river and floodplain morphology and their associated habitats [*Thorne and Lewin*, 1979; *Millar*, 2000; *Goodson et al.*, 2002; *Eaton et al.*, 2004], as well as contributing to the loss of channel conveyance [*Piégay et al.*, 2005] and nutrient or contaminant problems [e.g., *Marron*, 1992; *Reneau et al.*, 2004] downstream. For all these reasons an ability to predict bank erosion rates accurately is fundamentally important in fluvial geomorphology and hydraulic engineering.

[3] Given the importance of the topic, bank erosion has been the subject of a large body of research. Recent work has focused on developing models to predict the conditions under which riverbanks become susceptible to large-scale mass failure under gravity [e.g., *Osman and Thorne*, 1988; *Simon and Collison*, 2002; *Rinaldi and Casagli*, 1999; *Rinaldi et al.*, 2004], but fewer studies have been concerned with the process of hydraulic (also known as fluvial) erosion, which involves the removal of bank materials by the direct erosive action of the flow. This is a significant limitation because mass wasting is often triggered by hydraulically controlled bank toe erosion, and it is widely accepted that the long-term rate of bank retreat is, therefore, controlled by the rate of hydraulic erosion at the toe [*Thorne*, 1982;

[1]School of Geography, University of Southampton, Highfield, Southampton, UK.
[2]Finnish Environment Institute, Helsinki, Finland.
[3]Environmental Impact Assessment Centre of Finland Ltd, Espoo, Finland.
[4]Water and Development Research Group, Aalto University School of Science and Technology (TKK), Aalto University, Espoo, Finland.
[5]Department of Resource Management and Geography, University of Melbourne, Melbourne, Victoria, Australia.

0148-0227/10/2010JF001708

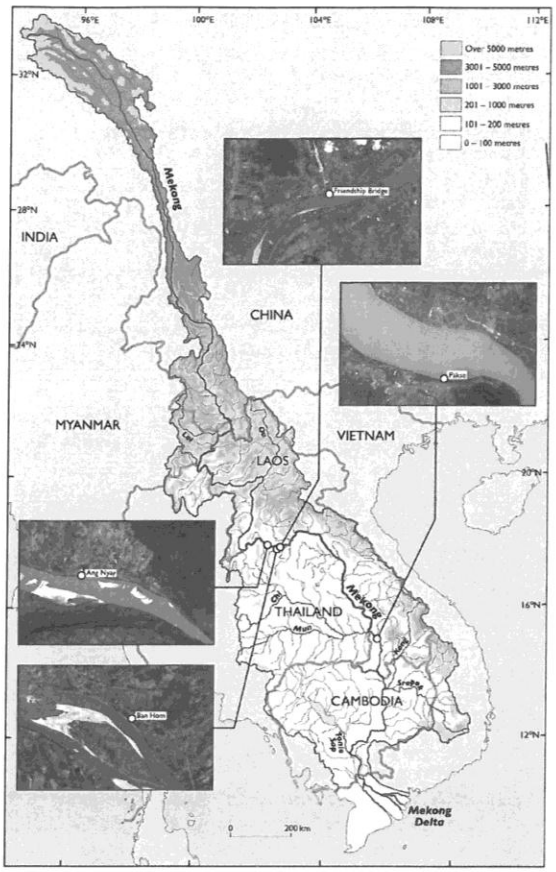

Figure 1. Location of study sites within the Lower Mekong River Basin. Google Earth images show the local context for the study sites at Ang Nyay, Ban Hom, Friendship Bridge, and Pakse. The locations of bank material sampling sites (see text for latitudes and longitudes) are indicated by the open circles. Google Earth imagery ©Google Inc. Used with permission.

Rinaldi and Darby, 2007]. Hydraulic bank erosion rates are most commonly quantified using an excess shear stress formula such as [*Partheniades*, 1965; *Arulanandan et al.*, 1980]

$$\varepsilon = k(\tau_{sf} - \tau_c)^a, \quad (1)$$

where ε (m/s) is the fluvial bank erosion rate per unit time and unit bank area, τ_{sf} (Pa) is the skin drag component of boundary shear stress, k (m^2 s/kg) and τ_c (Pa) are erodibility parameters (coefficient, k, and critical shear stress, τ_c) and a (dimensionless) is an empirically derived exponent, often assumed to take a value of 1 in bank erosion studies [*Rinaldi and Darby*, 2007].

[4] Excess shear stress models of this type have been used in a range of geomorphological applications [e.g., *Govers*, 1991; *Howard*, 1994; *Arulanandan et al.*, 1980]. These models have the great advantage of simplicity, but observed rates of bank erosion range over several orders of magnitude [*Hooke*, 1980] and bank erosion rates are predictable only to the extent that the controlling parameters can be estimated accurately. Unfortunately, characterizing these parameters accurately is challenging, due to the very high natural variability of bank materials [*Darby*, 1998; *Rinaldi and Darby*, 2007]. Moreover, an issue that has been overlooked frequently is the need to partition the boundary shear stress exerted on eroding riverbanks into skin drag and form drag components, the former being the stress available for bank erosion. The few empirical and numerical studies that have investigated near bank flows confirm the dominance of the form drag component [*Thorne and Furbish*, 1995; *McBride et al.*, 2007], but the inherent complexity of flow over the irregular topography characteristic of eroding riverbanks has until recently inhibited analytical solutions. For these several reasons, applications of excess shear stress models frequently involve predictive errors of up to an order of magnitude [*Darby*, 1998; *Mosselman*, 1998; *Julian and Torres*, 2006]. In light of this difficulty, researchers often simply estimate the erodibility parameter values in equation (1) by means of calibration, even though this diminishes the physical basis of the model [*Julian and Torres*, 2006; *Constantine et al.*, 2009].

[5] To address these issues, recent advances in measurement and modeling technologies are exploited herein in an attempt to improve the parameterization of the excess shear stress model. Specifically, a jet testing device is employed to characterize the erodibility of fine-grained bank sediments, while a hydraulic model is used to partition the skin drag and form drag components of boundary shear stress exerted on eroding banks. The analytical nature of this hydraulic model is significant, since the need for computationally intensive numerical simulation is avoided. Moreover, using these new techniques enables parameterization of the excess shear stress model without recourse to calibration, thereby providing a stronger physical basis for the simulation of bank erosion. Not only are all relevant input parameters readily measurable but, as shown below, they can be linked to flow discharge records commonly available at stream gauging stations, enabling convenient simulation of high-resolution, multidecadal, time series of bank erosion.

2. Study Site

[6] The Mekong River is a globally significant watercourse, ranking 27th in terms of its basin area (816,000 km^2) [*Kummu*, 2008] and, at approximately 4900 km [*Liu et al.*, 2007], it is the world's 12th longest river. The tropical monsoonal climate generates a mean annual runoff of 475 km^3 [*Mekong River Commission*, 2005] and a mean annual sediment load of 1.6×10^8 t [*Milliman and Meade*, 1983], values that rank 10th and 9th, respectively, among the world's rivers. Rising in Tibet and discharging into the South China Sea, the Mekong basin (Figure 1) can be divided into two units: (1) the Upper Mekong Basin, which lies within China, and (2) the Lower Mekong Basin (LMB) which lies to the south of the border between China and Laos. This division demarks the rapid broadening of basin form as it debouches from the confines of the Himalayas, prior to being joined by numerous, sizable tributaries [*Carling*, 2009a].

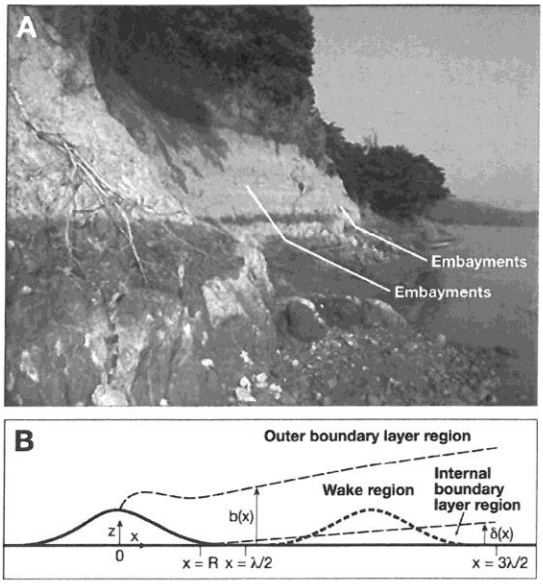

Figure 2. (a) Photograph of the riverbank at the Ban Hom study site on the Lower Mekong River illustrating the bank protruding into the flow between embayments. (b) Overview of the Gaussian-shaped plan view geometry of the modeled bank topographic roughness elements, along with the internal boundary layer, wake, and outer regions of the flow (flow direction is left to right). The thick dashed line of the downstream element denotes that it is removed from the flow, with the u_{ref}^2 for this element being the average squared velocity over this area. The unit "cell" from $\lambda/2$ to $3\lambda/2$ is the length over which the stresses are averaged. Figure 2b is reproduced from *Kean and Smith* [2006a, Figure 5].

[7] In this study we focus on four study sites on the Mekong main stem in Laos (Figure 1). Three of these, at Ang Nyay (18°3′15.9″N 102°19′5.5″E), Ban Hom (17°49′49″N 102°38′41″E) and Friendship Bridge (17°52′59″N 102°42′59″E), are located on the left bank within a reach that encompasses the gauging station at Vientiane. The fourth site is located further downstream, on the right bank close to the Pakse gauging station at 15°5′55″N 105°47′58″E. These sites are all located within single-thread or divided sinuous channels. The reach near Vientiane has an average gradient of about 1.0×10^{-4}, widths that range between 800 and 1300 m, and seasonal flow stage changes of around 13 m [*Carling*, 2009b; *Gupta and Liew*, 2007]. At Pakse, the channel is flatter (6.0×10^{-5}) and wider (typically ~2 km), with seasonal flow stage changes of about 14 m [*Carling*, 2009b; *Gupta and Liew*, 2007]. Much of the Mekong between Ang Nyay and Pakse is alluvial, with a fine sand bed and silty riverbanks that veneer patchy outcrops of bedrock. The presence of bedrock acts to constrain the lateral migration of the river, and alluvial bank erosion rates are typically rather low (~1 m/yr) [see *Kummu et al.*, 2008], despite the large scale of the river. A key feature of the river in this reach is its tendency to develop a divided channel (wandering) configuration, with large elongate islands. Thus, even if rates are low, it is clear that within the alluvial reaches the channel is actively migrating laterally via long-radius bends [*Carling*, 2009b].

[8] Prior studies of bank erosion have tended to be located within relatively small-scale upland or piedmont systems in humid temperate regions that often have low bank heights and coarse basal sediments (see *Rinaldi and Darby* [2007] for a review). In contrast, the riverbanks of the Mekong are high and, with the exception of isolated lenses of coarse material, composed of fine-grained, cohesive, sediments. For example, bank heights typically exceed 10 m, with sediments composed of reddish-brown sandy silts and/or gray clays. Furthermore, the LMB experiences a tropical monsoonal climate [*Mekong River Commission*, 2005]. River flows are therefore highly variable, with a prolonged annual flood (usually between June and November) and pronounced dry season (December to May) low flows. At Vientiane (mean annual flow of 4500 m^3/s), flow discharge varies between about 1000 m^3/s and a mean annual peak of 16,750 m^3/s. Further downstream, at Pakse, substantially increased flows range between about 1700 m^3/s to mean annual peaks of 37,700 m^3/s (mean annual flow is 9860 m^3/s). The hydrological context for this study is therefore relatively unusual in relation to prior studies, but the monsoonal flow regime is also convenient in the sense that it presents a relatively simple case in which it is feasible to model multi-decadal time series, each annual flood presenting a potentially erosive, but nevertheless individual, flow event.

3. Model Development

[9] In this paper two novel methods are applied to parameterize the terms in equation (1). Specifically, the *Kean and Smith* [2006a, 2006b] model is employed to estimate the skin drag component of bank boundary shear stress, while a jet testing device is used to estimate the erodibility of the riverbank materials. The use of these methods provides a means to obtain the very first predictions of hydraulic bank erosion rates that do not require recourse to calibration, thereby significantly enhancing the physical basis of the model relative to prior studies. Each of the two methods is now discussed.

3.1. Parameterization of Bank Shear Stress

[10] Near-bank flows are characterized by strong lateral shear and high form resistance induced by the topographic irregularities associated with eroding banks [e.g., *Thorne and Furbish*, 1995; *Kean and Smith*, 2006a]. In this paper *Kean and Smith*'s [2006a, 2006b] method of partitioning the drag on bank roughness elements into form and skin components is employed, in which

$$\tau_T = \tau_{sf} + \tau_d, \tag{2}$$

where τ_T is the total shear stress on the boundary of the channel, τ_{sf} is the skin drag component and τ_d is the form drag component induced as a result of pressure forces acting on the surfaces of large-scale topographic elements (Figure 2a) which protrude into the flow. Note that, from

equation (1), it is the skin drag component that is of interest in the context of bank erosion modeling. Because prior models of riverbank erosion do not adequately incorporate the form drag component, use of the Kean and Smith model represents a potentially significant advance.

[11] The form drag (F) on an individual roughness element is defined as [*Kean and Smith*, 2006a]

$$F = \frac{1}{2}\rho C_D H B u_{ref}^2, \tag{3}$$

where ρ is the density of water, H is the protrusion height of the element (this height being normal to the x axis in Figure 2b), B is the length of the direction perpendicular to the x and z axes defined in Figure 2b, u_{ref} is a reference velocity, and C_D is the drag coefficient of the element. In equation (3), the square of the reference velocity is defined by Kean and Smith as the average of the square of the velocity that would be present at the location of a roughness element if that element were removed from the flow. For each topographic element in a sequence of regularly spaced elements, the reference velocity is controlled by wakes shed from the element upstream [*Kean and Smith*, 2006a]. In addition, Figure 2b shows that u_{ref} is also affected by a growing internal boundary layer on the wall that begins at the reattachment point (R) of the separation zone on the upstream form. Consequently u_{ref} is affected by three interdependent regions: an internal boundary layer region, a wake region, and an outer boundary layer region and to calculate u_{ref}, the velocity field within each region must be determined.

[12] *Kean and Smith*'s [2006a] model follows *Smith and McLean* [1977] and *McLean and Smith* [1986] in describing the velocity field in each region separately, joining them together using matching conditions so that u_{ref} can be determined by spatially averaging the (matched) velocity field over the unit volume of the roughness element. This requires an assumption to be made about the element's geometry and, in Kean and Smith's analysis, the elements are approximated as Gaussian-shaped "bumps." *Kean and Smith* [2005, 2006b] provide data from small streams in the midwest and western United States to support this assumption, and the bank roughness elements at the Lower Mekong field sites in this study are also well described as Gaussian forms (see section 3.1.1). Regarding the methods employed to estimate the velocity field, within the internal boundary layer region the velocity is defined by the law of the wall [*Kean and Smith*, 2006a],

$$u = \frac{u_{*IBL}}{\kappa}\ln\frac{z}{z_{oSF}}, \tag{4}$$

where κ is von Karman's constant, z is the distance away from the boundary, z_{oSF} is the local roughness height of the boundary without topographic roughness elements (i.e., a skin roughness height, see below for details), and u_{*IBL} is the shear velocity within the internal boundary layer (equals $\sqrt{\tau_{sf}/\rho}$). The flow in the outer region similarly follows the law of the wall,

$$u = \frac{u_{*T}}{\kappa}\ln\frac{z}{z_{oT}}, \tag{5}$$

where $u_{*T} = \sqrt{\tau_T/\rho}$ and z_{oT} is the roughness height due to skin friction plus form drag. The wake region is modeled using *Schlichting*'s [1979] far-field wake solution,

$$u = u_b\left[1 - g(x)f\left(\frac{z-\eta}{b}\right)\right], \tag{6}$$

within which *Kean and Smith* [2006a] employ

$$g(x) = A_2\left(\frac{x+x_o}{C_D H}\right) \tag{7}$$

and

$$f\left(\frac{z-\eta}{b}\right) = \left[1 - \left(\frac{z-\eta}{b}\right)^{3/2}\right]^2, \tag{8}$$

where x is the distance downstream from the center of the element producing the wake, z is the distance away from the reference level of the roughness elements, $z = \eta$ is the surface of the boundary, u_b is the velocity at the top of the wake, x_o is the virtual origin, which Kean and Smith equate to zero, and the wake thickness, b (Figure 2), is given by [*Kean and Smith*, 2006a]

$$b = 2A_1 C_D H\left(\frac{x+x_o}{C_D H}\right)^{1/2}. \tag{9}$$

The constants A_1 and A_2 are set equal to $\sqrt{10\beta}$ and $\sqrt{20}/(18\beta)$, respectively, with β an empirically determined constant that sets the value of the eddy viscosity within the wake. *Kean and Smith* [2006a] used data from the flume experiments of *Hopson* [1999] to suggest

$$\beta = 0.226\left[1 - \exp\left(-0.353\frac{\lambda}{H}\right)\right], \tag{10}$$

where λ is the spacing of the roughness elements.

[13] A critical aspect of the Kean and Smith model lies in applying the velocity matching conditions between the internal boundary layer and wake, and between the wake and the outer flow region. Full details of both matching conditions are reported in *Kean and Smith* [2006a] and are not repeated here for reasons of space. Suffice to note that equations (4), (5) and (6), together with the corresponding velocity matching conditions, fully specify the velocity field, $u(x, z)$, that would be present if the roughness element were removed from the flow. This procedure enables the reference velocity in equation (2) to be defined using [*Kean and Smith*, 2006a]

$$u_{ref}^2 = \frac{1}{A}\int_A u^2(x,z)dA, \tag{11}$$

where A is the plan view area of the roughness element. For bank roughness elements that are Gaussian in shape, it follows that

$$A = H\sigma\sqrt{\pi/2}\left[erf\left(\frac{x_{dn}-x_c}{\sqrt{2\sigma}}\right) - erf\left(\frac{x_{up}-x_c}{\sqrt{2\sigma}}\right)\right], \tag{12}$$

where σ is the streamwise length of the element, x is the streamwise coordinate, and the subscripts *up*, *dn* and *c*

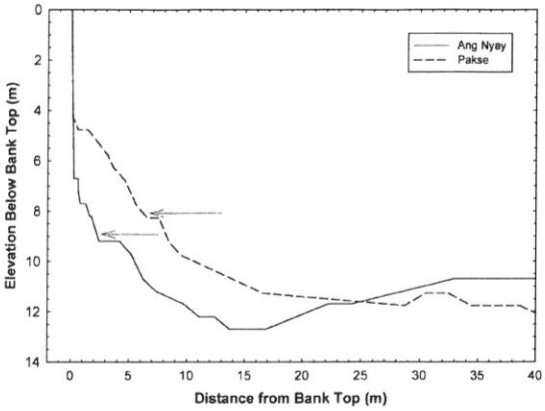

Figure 3. Examples of bank profiles at Ang Nyay and Pakse study sites, indicating that the longitudinal bank roughness profiles were collected from points (locations indicated by arrows) representative of the lower portion of the bank profile.

denote the upstream and downstream limits and crest of the roughness element.

[14] To close the model, a known value of velocity within the outer region of the flow must be specified (see below for details of how the outer region flow velocities are determined in this study), which then enables the total drag on the topographic elements to be related to properties of the outer flow via equation (1). Using (3), and recalling that the bank topographic roughness elements are assumed to be Gaussian in shape, the drag stress is calculated using

$$\tau_d = \frac{1}{2}\rho C_D \frac{H}{\lambda} u_{ref}^2, \tag{13}$$

By expressing the average skin friction stress in terms of the shear velocity in the internal boundary layer, the total stress on the boundary is written

$$\tau_T = \rho \langle u_{*IBL} \rangle^2 + \frac{1}{2}\rho C_D \frac{H}{\lambda} u_{ref}^2, \tag{14}$$

wherein *Kean and Smith* [2006a] estimate the drag coefficient using an empirical function derived from the experimental data of *Hopson* [1999],

$$C_D = 1.79 \exp\left(-0.77 \frac{\sigma}{H}\right). \tag{15}$$

[15] To solve (14), initial estimates of the total roughness height and shear velocity, z_{oT} and u_{*T}, in the outer flow are made that match the specified outer velocity, u_{out}. This estimation procedure then enables $< u_{*IBL} >$ and u_{ref} to be determined via the velocity matching conditions and (11), from which improved estimates of u_{*T} and z_{oT} are obtained from (14) and (5). This iterative sequence is repeated until the solution converges. Input data requirements include a set of parameters describing the geometrical characteristics of the bank roughness elements (H, σ, λ), an estimate of the roughness height associated with the skin drag component (z_{oSF}), and a specified flow velocity within the outer flow region, u_{out}, at a known distance from the boundary, z_{crit}. Details of how these parameters were estimated are provided below.

3.1.1. Parameterization of Bank Roughness Parameters

[16] At each study site, streamwise profiles of bank surface topography were obtained using a handheld Leica Disto A5 laser range finder (accuracy ±2 mm) to measure offsets at approximately periodic (0.5–1.0 m) intervals along survey transect lines positioned at constant elevations along the bank. Similar to the examples shown in *Kean and Smith* [2006a], the bank topographic features identified in this study are essentially two-dimensional; that is their shape does not significantly vary with elevation above the bed. At each site the longitudinal bank profiles were, therefore, positioned close to the base of the near-vertical face that is a ubiquitous feature of the Mekong's riverbanks (Figure 3). The survey transect is, therefore, in all cases representative of the lower portion of the bank, though the precise elevation of each transect above the bank toe varied in position between about 0.1 (Ang Nyay) and 0.5 (Pakse) of the bank height (Figure 3).

[17] For reasons of space, only one example (Figure 4) of the bank topographic profiles, from the Ang Nyay study site, is presented here. In all cases the length of an individual profile was sufficient to encompass a sequence of several bank roughness elements (see Table 1 for details). Following *Kean and Smith* [2005], each topographic profile initially was detrended to remove low-frequency undulations associated with channel curvature. The positions of higher-frequency undulations associated with individual roughness elements along the bank then were identified manually, prior to Gaussian curves being fitted to each of the individual "bumps" using Matlab's curve fitting toolbox. For all bumps in this study (126 bumps) statistically significant ($P < 0.001$) fits were obtained, with correlation coefficients ranging between 0.203 (with only five bumps having r^2 values less than 0.500) to 1.0 ($\mu = 0.833$, $\sigma = 0.142$). This indicates that the bank roughness elements are approximated well as Gaussian shapes, as has been found previously on a wide range of other riverbanks [*Kean and Smith*, 2006a, 2006b]. Note that, here and throughout this study, where parametric statistical tests are used, the data were scrutinized to ensure that underlying assumptions of the tests were not violated, and unless otherwise stated no such violations were found.

[18] Figure 4 is typical in that bank roughness elements are invariably irregularly shaped. *Kean and Smith* [2006b] show that the topography of irregular surfaces can be transformed into an equivalently rough surface of regularly spaced, identical, elements using the approximation

$$\begin{aligned} H_{reg} &= H_{88} \\ \sigma_{reg} &= \sigma_{88} \\ \lambda_{reg} &= 6H_{88} \end{aligned}, \tag{17}$$

where the subscripts indicate the percentile of the extracted (irregular) bank roughness parameter distributions used to represent the equivalent "regularized" surface. The skin roughness height parameter, z_{oSF}, also was estimated using the bank topographic profiles. *Kean and Smith* [2005] suggest that finer scales of bank roughness can be characterized by

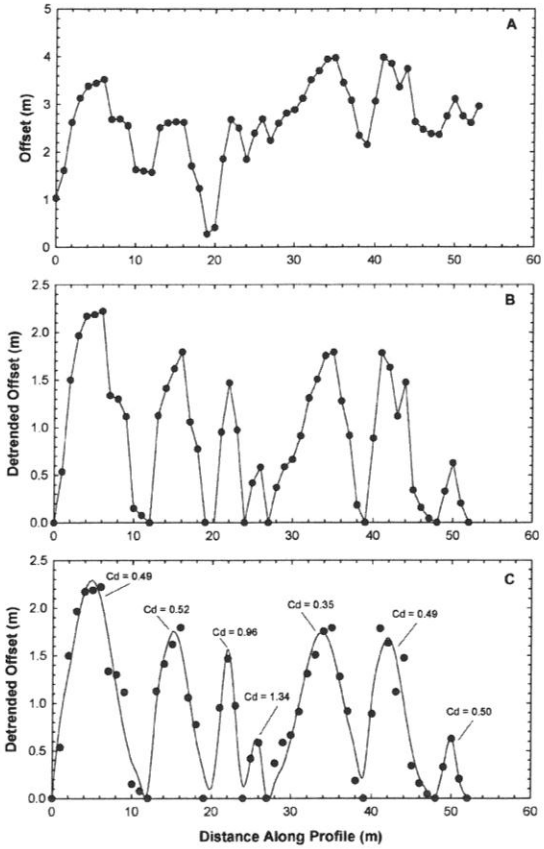

Figure 4. Measurements and analysis of part of the bank topographic profile from the Ang Nyay study site on the Lower Mekong River. (a) Original measurements with low-frequency undulations. (b) Detrended profile with low-frequency undulations removed. (c) Gaussian fits to the detrended sequence of topographic roughness elements. The drag coefficients (C_D) associated with each of the fitted bumps are also shown. Note change of vertical scale in Figure 4a relative to Figures 4b and 4c.

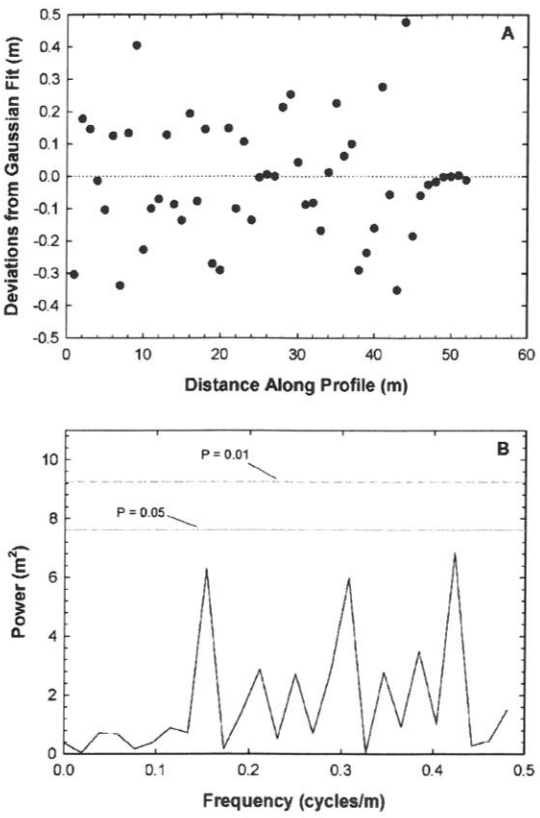

Figure 5. Characterization of the finer scale of bank roughness at the Ang Nyay study site on the Lower Mekong River. (a) Deviations from the Gaussian fits shown in Figure 3c. (b) Power spectrum of the deviations showing the lack of a statistically significant characteristic frequency, the 0.05 and 0.01 significance levels being illustrated by the solid and dashed gray horizontal lines, respectively.

analyzing the deviations from the Gaussian fits (Figure 5a). Specifically, Fourier analysis is used to identify any characteristic wavelengths associated with this secondary roughness and, if significant, it can be modeled as a series of Gaussian shapes approximating a sine wave of the characteristic frequency [*Kean*, 2003]. However, no such characteristic frequencies were found to be present at Ang Nyay (Figure 5b) or at any other sites in this study. This suggests that secondary scales of roughness are absent at the Mekong study sites, though this is discussed further below (section 5). Following *Kean and Smith* [2005], z_{oSF} is approximated by

Table 1. Bank Roughness Parameters Employed in This Study[a]

Sample Location	H_{reg} (m)	σ_{reg} (m)	λ_{reg} (m)	C_D	Number of Bank Roughness Elements	z_{osf} (m)
Ang Nyay	2.37	6.55	14.22	1.26	55	3.7×10^{-4}
Ban Hom	1.82	4.14	10.91	1.34	9	1.9×10^{-2}
Friendship Bridge	1.33	2.62	7.99	1.44	18	1.4×10^{-2}
Pakse	3.81	5.1	22.86	1.51	44	1.6×10^{-2}

[a] H_{reg} is the protrusion height of the bank roughness element, σ_{reg} is the streamwise length scale of the bank roughness element, λ_{reg} is the spacing of the bank roughness element, C_D is the drag coefficient, and z_{osf} is the skin friction roughness height. The subscript "reg" refers to the use of the 88th percentile of the distribution of each bank roughness parameter, this value being used to transform the effects of a sequence of irregularly shaped roughness elements into an equivalently rough surface of regularly spaced identical elements [see *Kean and Smith*, 2006b].

taking a tenth of the standard deviation of the residuals, by analogy to the relation $z_o = 0.1D_{84}$ often used for granular surfaces [e.g., *Whiting and Dietrich*, 1990; *Wiberg and Smith*, 1991]. Details of the bank topographic and skin roughness parameters estimated for the Lower Mekong study sites and used in subsequent computations are summarized in Table 1.

3.1.2. Parameterization of the Outer Flow Velocity

[19] In this study two separate approaches for the specification of the outer region flow velocity were employed, depending on data availability. At two study sites (Ang Nyay and Pakse) measurements of flow velocity were available from a campaign of acoustic Doppler current profiling (ADCP) undertaken as part of another study (I. Conlan, The geomorphology of deep pools on the Lower Mekong River: Controls on pool spacing and dimensions and processes of pool maintenance, manuscript in preparation, 2010). However, field data were not available at the Ban Hom or Friendship Bridge study sites, so Environmental Impact Assessment Centre of Finland (EIA) 3-D hydrodynamic model simulations, again available from a separate prior study [*Koponen et al.*, 2008], were employed instead. Importantly, in both cases estimates of the outer region flow velocity were obtained for a range of flow discharges, allowing τ_{sf} in equation (1) to be related to flow discharge (see section 4.1). In turn, this enables time series of bank erosion rates to be computed using the multidecadal historical flow discharge records that are available at gauging stations located close to the study sites.

[20] Acoustic Doppler current profiler (ADCP) measurements were obtained using a 600 kHz Workhorse Rio Grande ADCP manufactured by RD Instruments mounted approximately 0.35 m below the water surface on a stainless steel frame attached to the side of a survey vessel. Single ensembles were recorded at a ping rate of 1–3 s, depending on flow and depth conditions encountered in each survey. The horizontal position of the boat at each ping was recorded using a Trimble SPS550 Differential GPS at a rate of 2 Hz. Real-time differential corrections were received from the subscription-based Omnistar XP satellite signal, giving submeter position accuracy. Between three and six crossings were made at each cross section during each survey period.

[21] At Ang Nyay, 10 separate surveys at discharges ranging between 1070 m^3/s and 13,940 m^3/s were undertaken between the end of the dry seasons in May 2006 and April 2007. This range represents the mean annual hydrograph for the nearby Vientiane gauge well, while the maximum discharge recorded in the field surveys is also close to the mean annual peak discharge (1913–2006) of 16,750 m^3/s at Vientiane. At Pakse, 11 separate survey missions were undertaken between May 2006 and March 2007 encompassing 17 separate flow discharges ranging from 1930 m^3/s and 28,090 m^3/s. These flows again bracket the mean annual hydrograph very well, but the largest flow falls below the mean annual peak discharge (37,700 m^3/s; 1960–2003) for the Pakse gauge.

[22] To determine the outer region flow velocities, ADCP data were used to quantify transverse variations in depth-averaged flow velocity via nonlinear regression (Figure 6). *Kean and Smith* [2006a] note that the outer region flow velocity must lie at a point (termed the critical distance, z_{crit}) beyond the region of the flow affected by wakes shed by bank roughness elements. However, no observations on the lateral extent of the wake zone were made during the ADCP surveys. In this study z_{crit} was, therefore, defined as being equal to three times the bank height (H_b), which is assumed to be at a location sufficiently distant from the bank to be safely outside the zone affected by wakes, while not being so distant that the local shear stresses are influenced unduly by transverse variations in channel depth. Note that, because the bank roughness parameters are derived from bank profiles that extend along the study reach, all available ADCP data (i.e., from each cross section and from the multiple traverses at each cross section) were employed in the regressions, thereby accounting for within-reach variability in flow hydraulics. The regression equations were then used to estimate the depth-averaged outer region flow velocity (u_{out}) for the specified value of z_{crit}.

[23] Values of u_{out} and z_{crit} derived in this way and employed in subsequent computations are listed in Table 2. Note that in some cases (e.g., Figures 6a and 6b; see bold text in Table 2 for full list) no clear transverse velocity profile was evident and, in these instances, the outer region flow velocity was estimated simply by averaging all ADCP velocity returns within ±1 m of the z_{crit} location. These instances, particularly at Pakse, correspond to relatively low flows (<4200 and 6600 m^3/s for Ang Nyay and Pakse, respectively), and it is likely that flow diversion around midchannel bars and/or islands upstream is responsible for the lack of a well developed transverse flow structure. However, it is later shown (Table 4) that, at Pakse, affected flows are below the threshold for the onset of bank erosion, so any errors introduced do not affect predictions of bank erosion at this location.

[24] At the Ban Hom and Friendship Bridge study sites the EIA 3-D hydrodynamic model was used to simulate the outer region flow velocities across a wide range (5000–15,000 m^3/s) of flow discharges. The EIA 3-D model can be classified as a three-dimensional baroclinic multilayer model [*Simons*, 1980; *Virtanen et al.*, 1986; *Koponen et al.*, 1992] and is based on solving simplified Navier Stokes equations on a rectangular model grid. Model simulations (Figure 7) were undertaken using a 50 m horizontal resolution computational mesh that had 10 vertical layers, of which the 9 uppermost layers were 1 m thick and the tenth varied according to the water depth. Both the vertical and horizontal velocities were simulated at the two above mentioned study sites. Vertical velocities are obtained as averages over each grid cell from the continuity equation, so the actual vertical velocities may be significantly higher than the averaged ones.

[25] Outer region flow velocities were estimated using simulated flow velocity data extracted from a 3 × 3 matrix of grid cells surrounding the precise location of the study site. This matrix comprised three grid cells at locations downstream, at, and upstream of the study site, with a further three grid cells extending to a distance of 150 m away from the bank at each of these locations. To provide a representative transverse profile of simulated flow velocity the three estimates of flow velocity within each of the cells in each of the three streamwise-aligned rows were initially averaged. Because the velocity components are calculated in the center of the grid cells (i.e., at distances of 25 m, 75 m and 125 m from the bank), the outer region flow velocity at $z_{crit} = 3H_b$ was then estimated by interpolation (see Table 2 for outer region flow velocities).

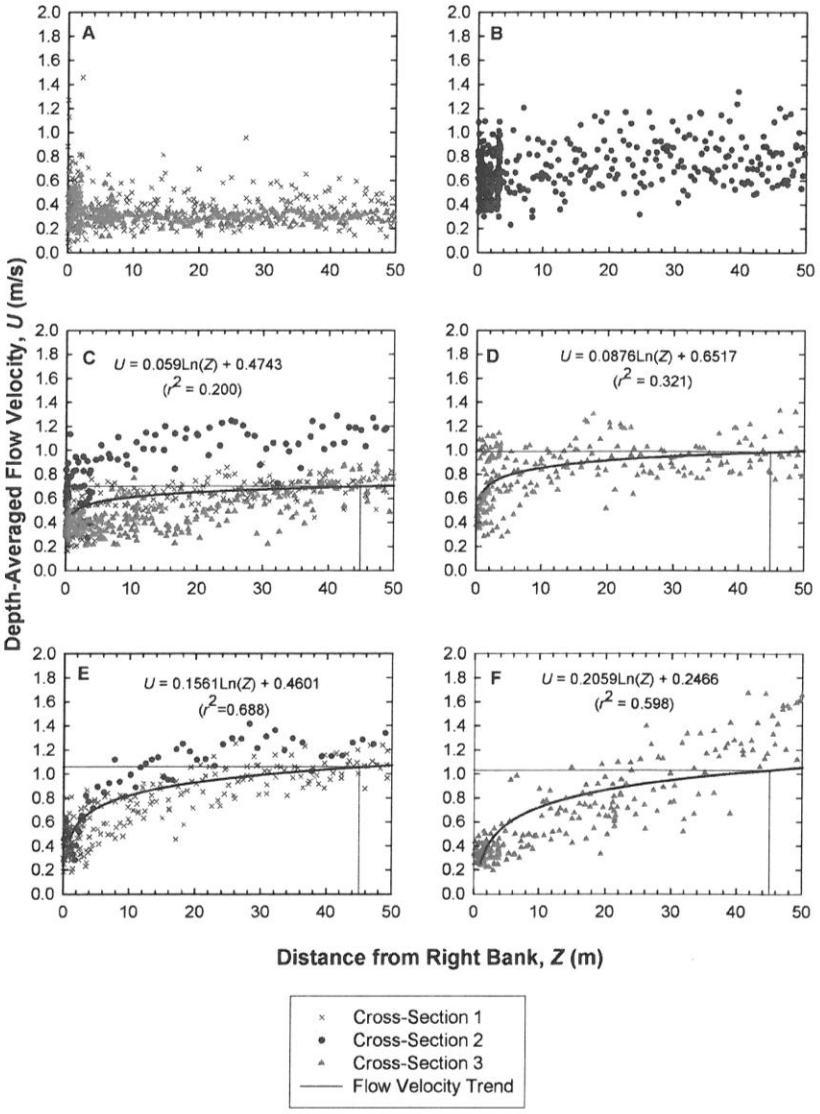

Figure 6. Transverse profiles of depth-averaged flow velocities acquired via acoustic Doppler current profiler (ADCP) measurements at the Pakse study site, for a range of flow discharges (Q). The symbols indicate individual ADCP measurements, whereas the solid lines indicate the fitted trends (regression relationships shown) through these data. The position of the outer flow region (z_{crit}, indicated by the thin vertical line) is equated to $z = 45.0$ m, which is equal to three times the bank height at Pakse. The outer region flow velocity (thin horizontal line) is then estimated based by substituting the value of z_{crit} into the fitted transverse flow velocity profile functions. (a) Flow velocity profile for Q = 2220 m^3/s; (b) flow velocity profile for Q = 6590 m^3/s; (c) flow velocity profile for Q = 11,420 m^3/s; (d) flow velocity profile for Q = 15,130 m^3/s; (e) flow velocity profile for Q = 21,560 m^3/s; and (f) flow velocity profile for Q = 28,090 m^3/s. Note that cross sections 1, 2, and 3 are spaced at 700 m intervals (approximately 0.4 channel widths at this study site).

3.2. Riverbank Erodibility Parameters (τ_c and k)

[26] Estimating the critical shear stress for the fine-grained, cohesive, materials that are the subject of this study is a challenging problem. Unlike granular sediments, the entrainment threshold depends not only on the weight of the grain but additional factors that are difficult to parameterize, including clay and organic content, as well as grain

Table 2. Outer Flow Region Velocities at Specified Distance From the Bank for a Range of Flow Discharge Values at Study Sites Used in This Study[a]

Site	Q (m^3/s)	u_{out} (m/s)	z_{crit} (m)
Ang Nyay	1070	1.00	36.0
	1350	1.08	36.0
	2270	**1.25**	**36.0**
	3240	0.95	36.0
	4190	**0.93**	**36.0**
	5420	1.29	36.0
	6360	1.63	36.0
	8860	1.24	36.0
	9070	1.30	36.0
	13940	1.25	36.0
Ban Hom	5000	0.79	42.0
	10000	0.89	42.0
	15000	0.99	42.0
Friendship Bridge	5000	0.55	40.0
	10000	0.74	40.0
	15000	0.84	40.0
Pakse	**1930**	**0.28**	**45.0**
	2220	**0.46**	**45.0**
	2280	**0.40**	**45.0**
	4800	**0.51**	**45.0**
	5430	**0.57**	**45.0**
	6590	**0.69**	**45.0**
	11420	0.92	45.0
	15130	1.06	45.0
	15530	0.92	45.0
	20700	1.30	45.0
	21110	1.17	45.0
	21560	1.11	45.0
	22210	1.20	45.0
	25970	1.25	45.0
	27050	1.15	45.0
	27210	1.31	45.0
	28090	1.29	45.0

[a]Outer flow region velocities, u_{out}; distance from the bank, z_{crit}; and flow discharge values, Q. The outer region flow velocities at the Ang Nyay and Pakse study sites are estimated from ADCP measurements, whereas the outer region flow velocities at Ban Hom and Friendship Bridge are derived from hydrodynamic modeling. Bold text indicates data points at Ang Nyay and Pakse for which no clear transverse velocity gradient was identified from the ADCP data (see section 3.1.2 for details).

mineralogy and the chemical composition of interstitial fluids [*Arulanandan et al.*, 1980; *Grissinger*, 1982]. Thus methods of predicting the erodibility of cohesive bank materials remain poor [*Rinaldi and Darby*, 2007].

[27] An alternative to prediction is to deploy jet testing devices [e.g., *Hanson*, 1990; *Hanson and Simon*, 2001; *Clark and Wynn*, 2007; *Thoman and Niezgoda*, 2008] to obtain direct measurements of bank erodibility in situ. These devices operate by directing jets of water with known, progressively increasing, hydraulic properties at the bank materials. Eventually the jet becomes sufficiently strong to initiate erosion, the depth of the resulting scour hole being measured periodically with a mechanical point gauge, until an equilibrium scour depth is attained. The measured erosion rate, scour depth and known hydraulic properties are then used to back-calculate the erodibility parameters. The development and use of jet testers of this type represents an important advance in that both (τ_c and k) erodibility parameters are directly measured in situ, while the small scale of the impinging jet means that scale problems associated with the larger sampling footprint of devices such as portable flumes [*Tolhurst et al.*, 2000; *Aberle et al.*, 2006; *Widdows et al.*, 2007] are eliminated. However, the large size and weight of the equipment, and the need for peripherals such as a pump and hoses, make the deployment of established jet testing devices unwieldy, particularly in remote locations. In addition, on resistant surfaces, errors involved in mechanically inserting the point gauge into the base of the scour hole can be similar in magnitude to the scour depth itself, while erodible materials generate scour depths that can exceed the extent of the gauge. Moreover, it is recognized that natural cohesive materials are highly variable [e.g., *Arulanandan et al.*, 1980; *Grissinger*, 1982; *Thorne*, 1982; *Samadi et al.*, 2009], which necessitates repeat sampling. Because individual tests are time consuming (~0.5 h), it is difficult to obtain the replicate samples needed to characterize the inherent variability of fine-grained bank materials.

[28] Alternative instruments such as the cohesive strength meter (CSM) [*Tolhurst et al.*, 1999], which have been

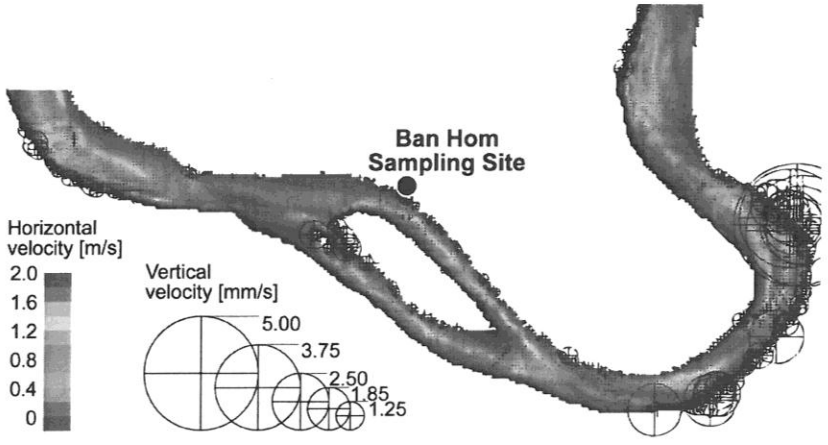

Figure 7. Example of simulated horizontal (colors) and vertical (crosses and circles) flow velocities from the EIA 3-D model for a reach of the Lower Mekong River encompassing the Ban Hom (location shown on the diagram) study site for a flow discharge of 12,000 m^3/s.

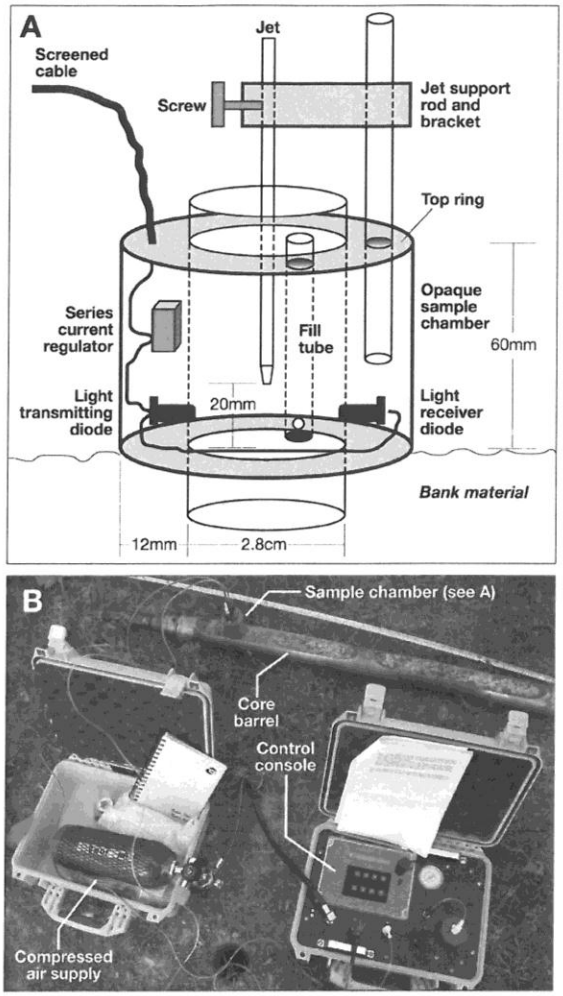

Figure 8. Diagram illustrating the cohesive strength meter apparatus employed in this study. (a) Detailed view of the sampling chamber [after *Tolhurst et al.*, 1999]. (b) Method of deploying the sampling chamber into bank toe sediments extracted using the core barrel.

widely employed in studies of intertidal flat sediments [*Paterson*, 1989; *Tolhurst et al.*, 1999; *Tolhurst et al.*, 2000], but have not been used yet for studies of fine-grained riverbank erosion, appear to offer some advantages over conventional jet testing devices. The CSM operates in similar fashion, firing submerged jets of increasing intensity at the target surface. However, the CSM detects the onset of erosion by monitoring optical transmission within an opaque test chamber that houses the brass jet nozzle (1 mm internal diameter) and infrared transmitter and receiver diodes (Figure 8a). An onboard data logger records the jet pressure and optical transmission values at and after each pulse. The moment of erosion is detected via drops in optical transmission induced by the suspension of eroded sediment, with the jet properties at that threshold used to define the critical stress. The test chamber consists of two concentrically located plastic cylinders, the outer one (external diameter 5.6 cm, internal diameter 2.8 cm) encasing the diodes and filling tubes (Figure 8a), and the inner one (internal diameter 2.8 cm, external diameter 3.0 cm), enclosing a sediment sampling footprint of 6.6 cm^2 [*Tolhurst et al.*, 1999]. Before a test, the chamber is inserted carefully into the sediment by pushing it flush to the surface prior to being gently (so as to avoid disturbing the sediment surface) filled with water via a syringe directed into a tube set within the test chamber wall. Tests are both automated and rapid (typically less than 3 min in the configurations employed in this study) so large numbers of samples can readily be obtained, while its relatively small size (Figure 8b) and weight (13 kg) enable operatives to deploy the CSM in remote locations and on steep riverbanks that would otherwise be difficult to access.

[29] In this study the CSM was used to determine the erodibility of bank toe materials. A focus on bank toe material is appropriate because long-term rates of bank erosion are known to be controlled by toe erosion [*Thorne*, 1982; *Rinaldi and Darby*, 2007]. Note that the bank "toe" in this context refers to the lower part of the bank profile, that is accordant with the location of the bank roughness profiles described previously. Where possible, samples were accessed by climbing down to the exposed toe and inserting the CSM test chamber directly into the bank face. More commonly, the bank toe was not accessible. In these cases bank toe materials were extracted by means of an open core barrel driven by means of a percussion corer into a vertical borehole located on the floodplain surface close to the bank edge. After removing the core from the borehole, the outer disturbed portion of the core was cleaned using a sharp knife. The CSM test chamber was then inserted directly into the materials exposed in the open barrel (Figure 8b).

[30] At the Pakse study site bank toe materials were sampled both by direct access and by coring. A simple t test indicates that there is no significant difference (at 99.9% confidence) between the two types of samples, providing some degree of confidence that the sampling method does not adversely affect the results. The CSM enables users to select from an array of test sequences that control test parameters such as the pulse duration, optical transmission logging parameters, initial and final pulse strength and pulse increments. In all cases reported here the test sequence used an initial pulse pressure of 3.45 kPa, incremented at 3.45 kPa intervals to a maximum value of 137.90 kPa. Pulse duration was 1 s and optical transmission values were logged for 3 s at 0.1 s intervals after each pulse, with the jet nozzle deployed at a height of 2.0 cm above the sediment surface.

[31] Post processing involved plotting optical transmission, averaged in the period between 0.2 and 1.2 s after each pulse [*Black and Tolhurst*, 2000], versus jet pressure for each of the individual tests undertaken at each site (Figure 9). Outliers were inspected carefully to evaluate whether blunders had been made during testing and, where necessary, such few instances (not shown here) were removed from further analysis. It is important to note that outliers were only removed if there was clear evidence that human error (usually associated with the inadvertent presence of sediment on the optical transmission diodes) had been made. Thus, while Tests 17, 18 and 25 at Ban Hom (Figure 9b), and Test 36 at

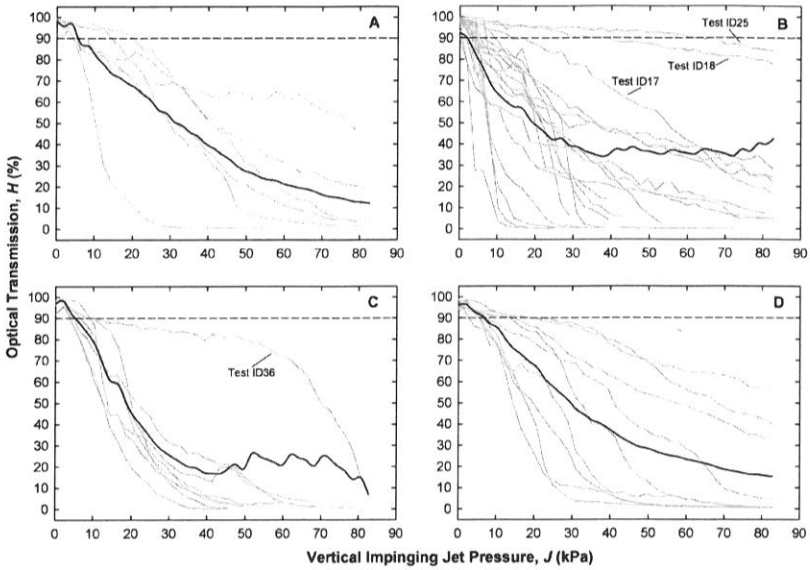

Figure 9. Curves of optical transmission (H) (measured in percent) versus vertical jet pressure (J) (measured in kilopascals) for the CSM test results obtained at the (a) Ang Nyay, (b) Ban Hom, (c) Friendship Bridge, and (d) Pakse study sites. Individual tests results are illustrated by the thin gray curves; the solid black curves indicate the mean of each ensemble. The horizontal dashed lines indicate the critical optimal transmission value (90%) used to define the onset of erosion.

Friendship Bridge (Figure 9c), all appear to follow different trajectories relative to other tests in their respective ensembles, no evidence of any sampling errors was noted and therefore all were included in subsequent analysis. The inclusion of Test 36 at Friendship Bridge has no significant effect on the derived bank erodibility statistics, because divergence from the other tests in the ensemble only occurs after the threshold for onset of erosion has been attained.

[32] Regarding this threshold condition, a standard criterion for the vertical jet pressure at the onset of erosion was defined as the point at which the optical transmission drops below 90% of its initial value [*Black and Tolhurst*, 2000]. The vertical jet pressure at the onset of erosion (J, in kPa) is calibrated to an equivalent horizontal critical shear stress (i.e., τ_c) using [*Tolhurst et al.*, 1999],

$$\tau_c = 66.6734(1 - \exp(-J/310.09433)) - 195.27552(1 - \exp(-J/1622.56738)), \quad (18)$$

with equation (18) being developed by subjecting unimodal quartz particles to both (1) CSM tests and (2) laboratory flume investigations to calculate the critical shear stress (see *Tolhurst et al.* [1999] for details). Unlike conventional jet testing devices, which provide estimates of both τ_c and k, the CSM provides only the critical shear stress. Advantage is therefore taken of the strong inverse relationship between τ_c and k [*Arulanandan et al.*, 1980; *Hanson and Simon*, 2001], with k being calculated using an empirical relationship ($n = 83$; $r^2 = 0.64$) derived from jet testing data obtained by *Hanson and Simon* [2001] (modified here for the units employed in this study):

$$k = 2.0 \times 10^{-7}(\tau_c^{-0.5}). \quad (19)$$

The τ_c and k values so obtained are listed in Table 3.

4. Results

4.1. Applying the Model

[33] The preceding analyses were used to provide estimates of bank erosion rate as follows.

[34] 1. The bank roughness (Table 1) and outer region flow velocity data (Table 2) were initially employed to calculate

Table 3. Erodibility Parameters of Bank Toe Materials Investigated in This Study

Sample Location	Bank Toe Material	Sampling Method	τ_c[a] (Pa)	k (m^2 s/kg)	Number of Samples
Ang Nyay	silt (D_{50} = 19 μm)	core	0.83 ± 0.57	2.20×10^{-7}	6
Ban Hom	silt (D_{50} = 36 μm)	exposed toe material	0.84 ± 1.16	2.18×10^{-7}	19
Friendship Bridge	very fine sand (D_{50} = 82 μm)	exposed toe material	0.56 ± 0.20	2.67×10^{-7}	8
Pakse	fine silt (D_{50} = 9 μm)	exposed toe material	0.88 ± 0.47	2.13×10^{-7}	9

[a]Critical shear stress (τ_c) values listed here are the mean ±1 standard deviation.

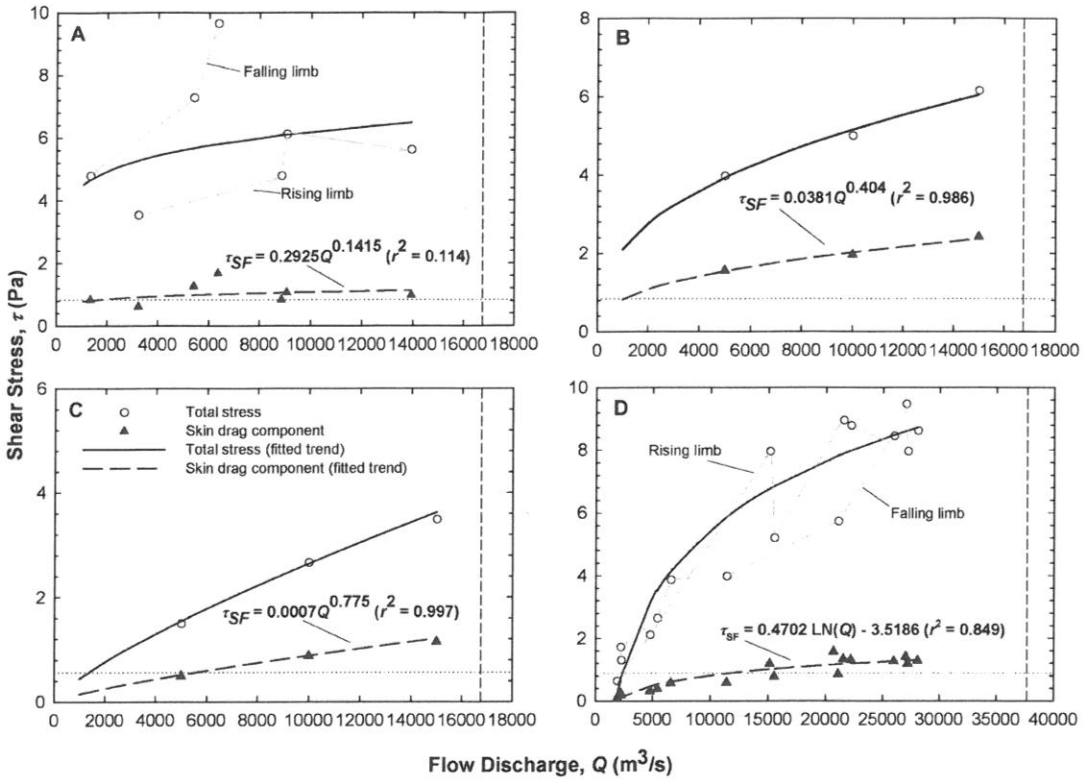

Figure 10. Simulated bank boundary shear stresses as a function of flow discharge for study sites at (a) Ang Nyay, (b) Ban Hom, (c) Friendship Bridge, and (d) Pakse. The horizontal lines indicate the mean critical shear stress values estimated from CSM measurements in this study. Vertical lines indicate the mean peak discharge observed at the gauging stations at Vientiane (for the Ang Nyay, Ban Hom, and Friendship Bridge study sites) and Pakse (for the Pakse study site). The regression relationships linking the total stress (solid lines) and skin drag component (dashed lines) of bank boundary shear stress to the flow discharge at each study site, with the latter being used in the bank erosion modeling, are also shown. At Ang Nyay and Pakse the temporal sequence of sampled flow events across the rising and falling limbs of the flood hydrograph is indicated by the gray arrows (shown for the total bank boundary shear stress only).

the bank boundary shear stress components, using the Kean and Smith model as described above. An Interactive Data Language (IDL) script written by Jason Kean was used for this purpose. Note that the availability of outer region flow velocity data for a range of flow discharges enabled multiple simulations to be undertaken, thereby obtaining total, form and skin drag components of boundary shear stress across a wide range of flow discharges.

[35] 2. The simulated boundary shear stress components obtained in Step 1 were then linked to flow discharge using bivariate regression (Figure 10). In all cases significant ($P < 0.001$) regression relationships were obtained. A wide range of models (logarithmic, power, etc) were explored, with the selected relationships initially chosen simply on the basis of those that provided the best fit. However, at Pakse the best fit ($r^2 = 0.951$) initially was obtained using a second-order polynomial. This model was rejected on the basis that a decline in applied boundary shear stress at flow discharges higher than the function's local maximum ($Q \approx 45000$ m^3/s) is physically unrealistic. The favored logarithmic curve (Figure 10d) still provides a very good fit ($r^2 = 0.918$), but ensures that simulated boundary shear stresses monotonically increase with flow discharge. At one study site (Ang Nyay, Figure 10a) there is evidently hysteresis in the relationship between the flow discharge and simulated bank boundary shear stress, this being caused by hysteresis in the relationship between discharge and the outer region flow velocity. The cause and implications of this hysteresis are discussed further below (section 6).

[36] 3. The fitted relationships between bank shear stress and flow discharge were next used to reconstruct daily variations in applied shear stress using mean daily discharge records from the Vientiane and Pakse flow gages. Note that, for the highest flow discharges in the record (25,900 m^3/s in 1966 at Vientiane; 56,000 m^3/s in 1978 at Pakse), the fitted relationships (Figure 10) must be extrapolated beyond the

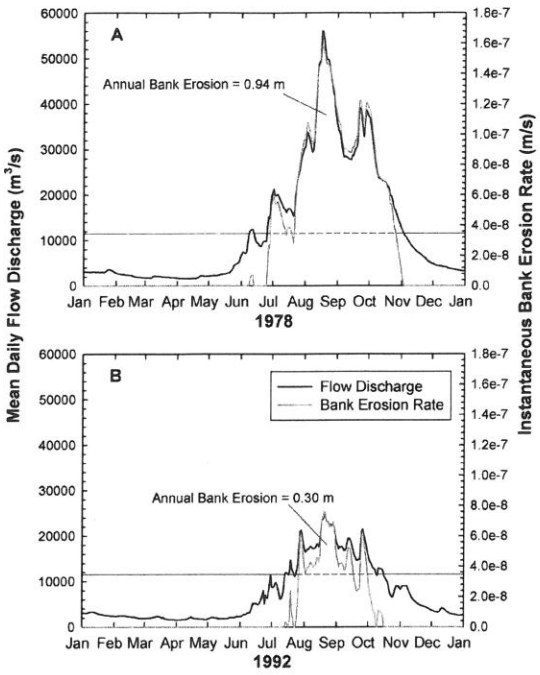

Figure 11. Time series of instantaneous simulated bank erosion rates (gray lines) at the Pakse study site induced by selected annual flood hydrographs (black lines): (a) 1978, a high flow year (the peak discharge of 56,000 m^3/s being the highest on record) that forces the highest annually integrated rate of bank erosion (0.94 m) in the simulation period 1961–2007; and (b) 1992, a low flow year with the corresponding lowest annually integrated rate of bank erosion (0.30 m) during 1961–2007. Note that all the plots are scaled identically and that the mean annual bank erosion rate during 1961–2007 is 0.61 m/yr. The horizontal lines indicate the threshold flow discharge (Q_c = 11,555 m^3/s) for the initiation and cessation of bank erosion, where the solid portion indicates periods when the flow is below the threshold (no erosion) and the dashed portion indicates periods when the flow exceeds the threshold. The volume of runoff contained between the dashed line and the solid curve of the annual hydrograph therefore effectively determines the annual erosion rate.

range of data used to construct them. This procedure is potentially problematic in that the simulated shear stress values within the extrapolated domain induce the highest instantaneous simulated bank erosion rates, but the relatively low duration of these flows must also be recognized. For example, exceedance probabilities of flows within the extrapolated range are less than 3.4% (Q > 13,940 m^3/s) at Ang Nyay, and less than 2.1% (Q > 15,000 m^3/s) at Ban Hom and Friendship Bridge. However, extrapolated flows have a slightly larger exceedance probability of 7.8% (Q > 28,090 m^3/s) at Pakse. Although the gauging stations have records dating from 1913 and 1923, respectively, simulations in this study were initialized either at 1959 (Ang Nyay and Pakse) or 1961 (Ban Hom and Friendship Bridge), to coincide with the availability of data used in the model validation (see section 4.2).

[37] 4. The reconstructed daily shear stress time series were then used in equation (1), together with the values of τ_c and k derived from the CSM measurements (Table 3), to develop time series of simulated instantaneous bank erosion rates at daily time steps. Simulations were repeated for scenarios in which erodibility parameters were set using (1) the mean critical shear stress values (Figure 11 and Table 4) plus (2 and 3) a range of erodibility parameters with limits corresponding to plus or minus one standard deviation about the mean critical stress (Table 4).

[38] Two illustrative examples of model outputs obtained by following the above procedure are shown in Figure 11 for the Pakse study site. It is worth reiterating that, to the best of our knowledge, these simulations represent the first simulations of hydraulic bank erosion that are obtained without recourse to calibration. Furthermore, in addition to the strong physical basis of the model, the availability of the regression relationships linking simulated bank boundary shear stress and flow discharge (Figure 10) provides a means to obtain simple bank erosion rate predictions that are linked directly to the controlling flow discharge regime. In fact, Figure 11 shows that it is the accumulated volume of runoff above the threshold discharge required to initiate bank erosion, $\Sigma(Q - Q_c)$, which is the key hydrological control on bank erosion. For the LMR at Pakse, variations in $\Sigma(Q - Q_c)$ are induced primarily as a result of interannual variability in the magnitude of the annual flood. Thus, during the period 1923–2009 the highest (0.94 m) and lowest (0.30) annual rates of bank erosion occurred in years with the highest (56,000 m^3/s, in 1978) and lowest (24,600 m^3/s, in 1992) peak flow discharges (Figures 11a and 11b). Peak flows are controlled primarily by the intensity of the monsoon (more specifically, the volume of monsoonal rainfall falling in the Mekong catchment), but any simple link between monsoon intensity and bank erosion is masked by the fact

Table 4. Computed Bank Erosion Statistics for the Various Study Sites[a]

Study Site	Simulation Period	Threshold Flow Discharge for Onset of Bank Erosion, Q_c (m^3/s)	Cumulative Simulated Bank Toe Erosion (m)	Mean Annual Rate of Simulated Bank Toe Erosion (m/yr)
Ang Nyay	1961–2007	1590 (0–63,920)	32.6 (0.0–391.6)	0.68 (0.0–8.2)
Ban Hom	1961–2005	2115 (0–18,100)	77.9 (0.1–2020.4)	1.76 (0.0–45.6)
Friendship Bridge	1961–2005	5570 (3150–8260)	32.2 (12.7–78.2)	0.73 (0.3–1.8)
Pakse	1961–2007	11,555 (4250–31,390)	29.3 (0.8–137.7)	0.61 (0.0–2.9)

[a]Values in parentheses indicate the range of values induced by using critical shear stress values of ±1 standard deviation from the mean.

Table 5. Summary of Data Sets Used to Determine Bankline Positions at the Various Study Sites

Study Site	Data Sets Employed	Error	Erosion Epoch Used in Analysis	Cumulative Error
Ang Nyay	1959 aerial imagery	±20.4 m	1959–2000 (41 years)	±35.4 m (±0.86 m/yr)
	Landsat satellite image (1/4/2000)	±15 m		
Ban Hom	1961 Hydrographic Atlas	±1.4 m	1961–1992 (31 years)	±4.0 m (±0.13 m/yr)
	1992 Hydrographic Atlas	±2.6 m	1992–2005 (13.33 years)	±5.1 m (±0.38 m/yr)
	SPOT5 satellite image (28/4/2005)	±2.5 m		
Friendship Bridge	1961 Hydrographic Atlas	±1.4 m	1961–1992 (31 years)	±4.0 m (±0.13 m/yr)
	1992 Hydrographic Atlas	±2.6 m	1992–2005 (13.33 years)	±5.1 m (±0.38 m/yr)
	SPOT5 satellite image (28/4/2005)	±2.5 m		
Pakse	1959 aerial imagery	±4.5 m	1959–2009 (50 years)	±5.0 m (±0.1 m/yr)
	GeoEye satellite image (10/4/2009)	±0.5 m		

that $\Sigma(Q - Q_c)$ depends also on interannual variations in the duration of flows above the threshold. The latter is a complex function of variations in the timing of the onset and cessation of the monsoon, as well as variations in the contribution to summer base flows of glacier and snowmelt from Tibetan source regions. Detailed analysis of the effects of hydroclimatological variability and change on bank erosion is beyond the scope of this paper, but the ability of the new model to obtain a simple, but physically based, link between flow discharge and simulated bank erosion rates means that it is well suited for such investigations. In practice it is necessary to have confidence in the model's predictions, so attention is now turned to evaluating the performance of the new model.

4.2. Model Evaluation

[39] Model predictions were evaluated by comparing simulated bank erosion rates with those estimated by analysis of map data and remotely sensed imagery. In the case of the Ban Hom and Friendship Bridge study sites, observed rates of erosion were determined in a study by *Kummu et al.* [2008]. In summary, *Kummu et al.* [2008] employed three main spatial data sets:

[40] 1. The 1:20,000 scale Hydrographic Atlas of 1961 [*Mekong River Commission*, 1961], which is based on field surveys and aerial photographs recorded between 1959 and 1961. Images from the atlas were scanned and geo-referenced to an average root-mean-square error (RMSE) of ±1.4 m (see *Kummu et al.* [2008] for full details), prior to the banklines being digitized and converted into a shape file for use in GIS analysis.

[41] 2. The 1:20,000 scale Hydrographic Atlas of 1992 [*Mekong River Commission*, 1992], which is based on aerial photos acquired in 1991/1992. This atlas is already available in digital format, so scanning was not necessary, but the images were in this case geo-referenced to an average RMSE of ±2.6 m (see *Kummu et al.* [2008] for full details).

[42] 3. A rectified SPOT5 satellite image acquired on 28 April 2005 and with a resolution of 2.5 m was used to map the bank locations in 2005 [*Kummu et al.*, 2008].

[43] The 1961 Hydrographic Atlas provides aerial photos of the entire Lower Mekong River and the original 1959 aerial photos used in the derivation of the Atlas were therefore employed at the Ang Nyay and Pakse study sites. The 1959 images were supplemented with more recent ones. At Pakse a rectified 0.5 m resolution GeoEye satellite image, acquired on 10 April 2009, was used. Control points visible on the 2009 satellite image and on the 1959 aerial images were used to geo-reference the 1959 images to the 2009 image (RMSE equals ±4.5 m), using a total of 12 control points. At Ang Nyay recent high-resolution imagery was not available, so a 15 m resolution Landsat image, acquired on 1 April 2000, was used instead. The 1959 images were georeferenced to the Landsat image, in this case using a total of 7 control points (RMSE equals ±20.4 m). The bankline positions on each image were then digitized and the Digital Shoreline Analysis System (DSAS) of *Thieler et al.* [2009] was used to cast transects across the banklines and thus determine the amount of bank top retreat during the measurement interval at the two sites. These various data sets provide a total of 6 epochs of observed bankline shift, with identified errors, across the four study sites (Table 5).

[44] A comparison of simulated versus observed data is shown in Figure 12. It is emphasized that observed rates of bank erosion strictly correspond to shifts in the position of the bank top identified from the satellite images/aerial photographs, whereas model simulations correspond to rates of bank toe erosion. The assumption that long-term rates of bank retreat are forced by rates of bank toe erosion (see section 6) is, therefore, pertinent. Note that predictive uncertainty (associated with scenarios 2 and 3 outlined in section 4.1 (step 4), and illustrated by the horizontal error bars on the plot) are large, reflecting the high natural variability of bank material erodibility (Table 3). Consequently, the predictive uncertainty bands overlap the line of perfect agreement for four of the six data points presented on Figure 12 (the exceptions being the 1959–1992 and 1992–2005 epochs at Friendship Bridge). The measurement errors are smaller than the predictive uncertainty bands (measurement errors range from 0.10 to 0.86 m/yr (see Table 5) and are illustrated by the vertical error bars on the plot), so only two data points to overlap the line of perfect agreement. That is, four to five of the six available data points plot sufficiently close to the line of perfect agreement to intersect it, within the bounds of the (albeit large) uncertainty inherent in the analysis.

[45] A linear regression equation of the form $\varepsilon_{obs} = c + m\ \varepsilon_{pred}$ was used to compare observed and simulated erosion rates quantitatively. Note that due to the low number of data points, the regression was undertaken using a nonparametric [*Theil*, 1950; *Sen*, 1968] regression estimator. The values of the gradient (m = 0.303) and intercept (c = 0.374) obtained via Theil-Sen regression indicate the general tendency of the model to overpredict (RMSE equals ±0.53 m/yr), though the low value of the coefficient of

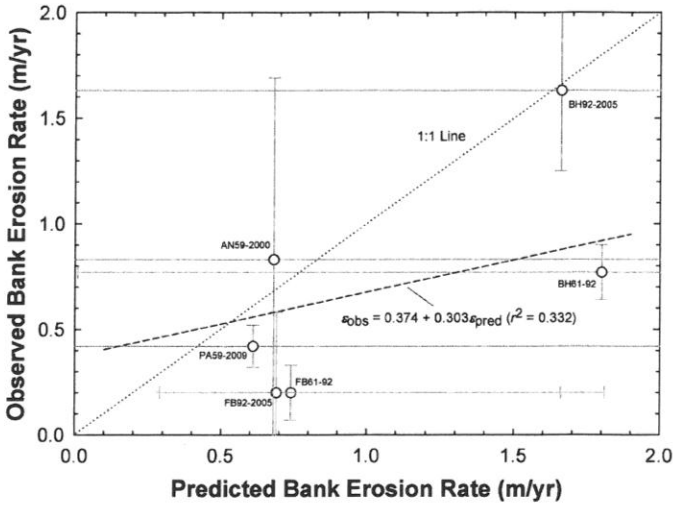

Figure 12. Comparison of predicted and observed bank erosion rates at the study sites on the Lower Mekong River. The vertical error bars indicate image analysis errors (see Table 5 for details), whereas the horizontal error bars reflect prediction uncertainty associated with a ±1 standard deviation range in the critical shear stress values employed in the analysis. Data points are labeled as follows: AN59-2000 for the Ang Nyay study site; PA59-2009 for the Pakse study site; FB61-92 and FB92-2005 denote the Friendship Bridge study site for the 1961–1992 and 1992–2005 epochs, respectively, and; BH61-92 and BH92-2005 denote the Ban Hom study site for the 1961–1992 and 1992–2005 epochs, respectively. The line of perfect agreement (dotted) and the Theil-Sen regression line (dashed) through the data points are also shown.

determination of the regression (r^2 = 0.332) highlights the considerable scatter in the limited data set employed here.

[46] It is stressed that the number of data points (6) employed in this analysis is clearly less than would be ideal for a comprehensive analysis of model performance. However, the logistical difficulties involved in collecting the data necessary to parameterize, and particularly to validate, the model should be recognized. A key limiting factor concerns the lack of available satellite imagery or aerial photographs of sufficiently high resolution and at frequent temporal intervals. As such the validation presented in Figure 12 provides only a tentative indication of model performance and further work is required to assess model capability across a wider range of river contexts than has been possible herein. As such, it is appropriate to consider the nature of likely model error from first principles (section 5) and as informed by model sensitivity analysis.

4.3. Sensitivity Analysis

[47] To investigate the relative importance of the different factors controlling simulated rates of bank erosion, and to better understand how predictive uncertainties might be generated by errors in the parameterization of these factors, a series of model sensitivity analyses were undertaken. In these sensitivity analyses the roughness, flow and bank erodibility input data for the Pakse study site (see Tables 1–3) were used as baseline parameters. Simulations were undertaken using the mean annual hydrograph as determined from hydrological records at the Pakse gauge for the period 1923–2007, 1923 being the earliest date for which data are available. With these input parameters a mean annual rate of hydraulic erosion of 0.60 m/yr is obtained. Note that this differs very slightly from the mean annual rate of erosion (0.61 m/yr) simulated previously, the difference being caused by the use of a mean annual hydrograph for the monitoring period 1961–2007 in the prior simulations. Individual sensitivity tests were undertaken for the six model input parameters that represent different aspects of the bank roughness (H, σ, λ, z_{oSF}), outer region flow (u_{out}) and bank material erodibility (τ_c). In each case sensitivity tests were undertaken by systematically perturbing these input parameters across an arbitrarily selected range of ±25% relative to its baseline state, while holding all the other parameters at their baseline values.

[48] Results of the sensitivity analyses are illustrated in Figure 13. It is immediately clear that model response to changes in input parameters is highly sensitive. Variations in all six input parameters induce relative increases in simulated bank erosion rates (ranging from a factor of about 0.8 (for z_{oSF}) to a factor of 3.6 for u_{out}) that are much greater than the ±25% perturbation in each input parameter. It should also be noted that the nonlinear response of bank erosion rate to perturbations in many of the input parameters suggests that the extent to which model response is sensitive is likely to be site specific. For example, model response to the bank roughness parameters is more sensitive on smoother banks (low H, σ and z_{oSF} values), whereas model sensitivity is dampened on rougher banks. In the extreme case of banks that

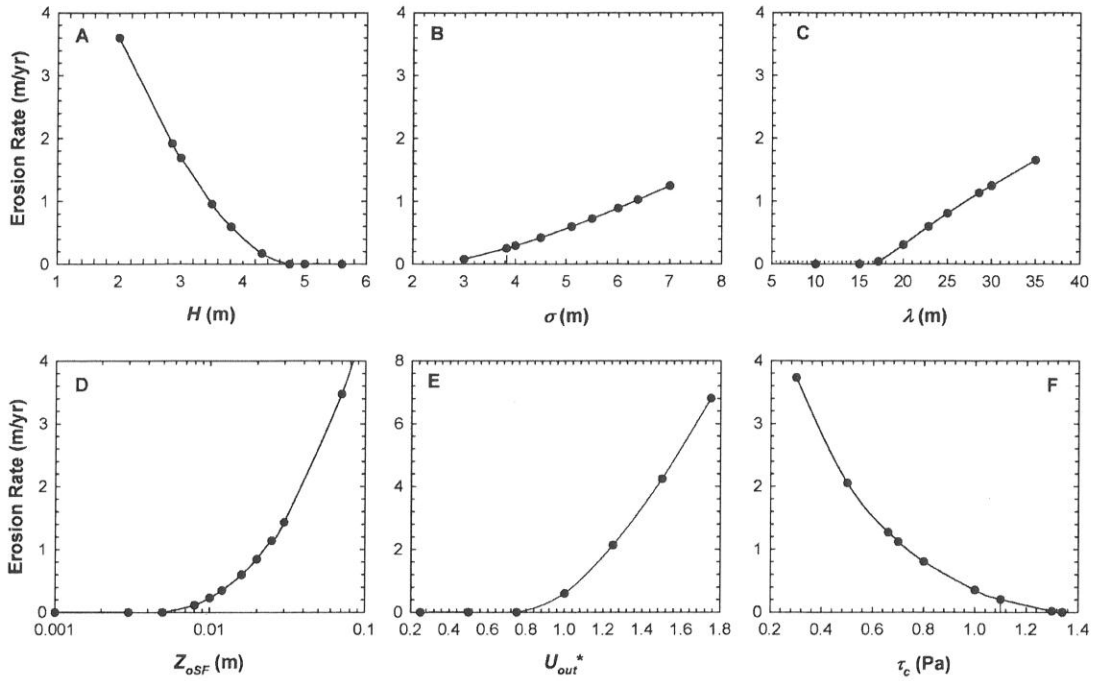

Figure 13. Sensitivity of simulated annual rates of bank erosion to variations in model input data parameters: (a) bump protrusion height (H, in meters); (b) Bump length (σ, in meters); (c) bump spacing (λ, in meters); (d) skin roughness height (Z_{oSF}, in meters); (e) nondimensional outer region flow velocity (u_{out}*, in meters per second); and (f) critical shear stress (τ_c, in pascals). Annual erosion rates are calculated based on the mean annual hydrograph (1923–2005) for Pakse. Note the change in the vertical scale in Figure 13e.

are so rough that the applied skin drag component of fluid stress is insufficient to surpass the critical shear stress, simulated erosion rates and hence sensitivity of erosion rate to variations in input parameters, both fall to zero. This observation emphasizes the importance of accurate estimation of all the input parameters employed in the model, but with particular emphasis on characterizing the outer region flow and the macro-scale bank roughness. The significance of this latter point is discussed further below (section 5).

4.4. Influence of Form Roughness on Boundary Shear Stress and Bank Erosion

[49] It is noteworthy that the bank shear stress values obtained are rather small (<10 Pa), even at flow discharges that exceed 25,000 m^3/s. This result is not unreasonable given the low channel gradients encountered on this large river. Moreover, the significance of the form drag component in the shear stress partitioning is also evident, this component accounting for between 61% (Ban Hom) and 85% (Pakse) of the total stress imparted on the banks. The large form drag component has the effect of reducing the skin drag component to values similar to the estimated critical shear stresses, the latter being indicated by the horizontal dashed lines in Figure 10. Assuming that the CSM data provide a reliable representation of these erosion thresholds, the large magnitude of the form drag components of boundary shear stress therefore suggests that approaches which fail to account for the form drag (i.e., which assume $\tau_d = 0$) would result in gross overestimates of bank erosion.

[50] This is illustrated by comparing annual bank erosion rates (during 1961–2007) simulated at each of the Ang Nyay (0.68 m/yr versus 30.8 m/yr), Ban Hom (1.76 m/yr versus 12.46 m/yr), Friendship Bridge (0.73 m/yr versus 6.62 m/yr) and Pakse (0.61 m/yr versus 21.0 m/yr) study sites for scenarios with (first quoted figures) and without (second quoted figures) the form drag component (i.e., using the total drag and skin drag curves in Figure 10, respectively). Thus simulated rates of bank erosion as obtained assuming zero bank roughness are greater than the rates obtained when including the bank form drag by factors that vary between about 7.1 (Ban Hom) and 45.3 (Ang Nyay). As such, the presence of high bank form roughness, induced by the presence of irregular bank topography, can be viewed as an important factor that self-limits the rate of bank erosion.

5. Discussion: Potential Sources of Model Error

[51] Assuming that the data presented in Figure 12 reflect a true tendency for the model to overpredict bank erosion rates, it follows that the source of error must either lie in

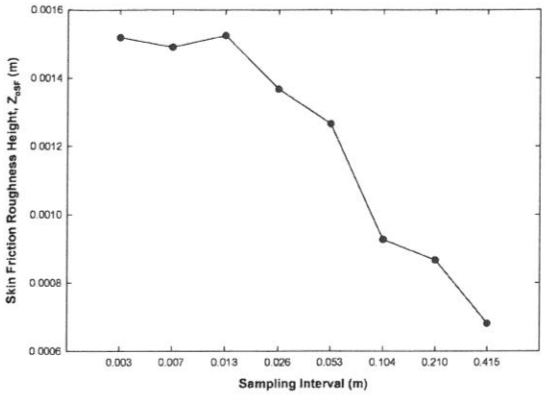

Figure 14. Influence of the spatial resolution of bank topographic profiles on estimates of skin friction roughness height (z_{oSF}) as derived from a 2008 laser scan survey of a riverbank on the Cecina River, Italy.

overestimation of computed values of τ_{sf}, or underestimation of τ_c (and therefore k), or both. In fact, systematic under-estimation of τ_c is consistent with recent work [*Vardy et al.*, 2007] which has suggested that the CSM calibration relationship (equation 18) should be expressed in terms of the jet pressure exerted on the sediment surface, not the jet pressure at the nozzle exit as in equation 18, with formulations based on the latter underestimating the true critical stress [*Vardy et al.*, 2007]. Unfortunately, revised calibrations for the CSM model (Mark IV) used in this study are not yet available.

[52] Inaccurate estimation of τ_{sf} could be induced via inaccurate parameterization of any or all of the outer region flow velocity (u_{out}), bank macro-scale roughness (H_{reg}, σ_{reg}, λ_{reg}) or skin friction roughness height (z_{oSF}) parameters. The sensitivity analyses (Figure 13) indicate that small errors in u_{out} can have a large affect on τ_{sf} and thus bank erosion rates, but misparameterization of u_{out} is unlikely responsible for overprediction of bank erosion in this study. This is because Figure 6 shows that, if anything, the value of u_{out} is underestimated, which would lead to underestimation (not overestimation) of τ_{sf}. Significant error in the values of H_{reg}, σ_{reg}, λ_{reg} also appears unlikely given the high quality of the Gaussian fits achieved with the bank topographic data in this study.

[53] An alternative explanation for possible overestimation of τ_{sf} is that, although the 0.50 m sampling interval used to survey bank topographic profiles may be sufficient to capture adequately the macro-scale bank roughness, the sampling interval may be too coarse to determine z_{oSF} accurately. Moreover, in some rivers, bank roughness is characterized by a hierarchy of different sized topographic features, with the total stress being partitioned between the skin-friction grain roughness, as well as the form roughness on meso- and macro-scale bank form roughness elements (e.g., Rio Puerco bank roughness discussed by *Kean and Smith* [2006b]). The coarse sampling interval employed in this study opens the possibility of there being unresolved form drag producing secondary roughness at the meso-scale, which would reduce τ_{sf} and predicted erosion rates.

[54] The extent to which unresolved micro- and meso-scale roughness may be significant on the banks of the Mekong remains unknown, but to demonstrate how the coarse sampling interval employed in this study may affect the estimation of z_{oSF} a series (5, distributed at equidistant vertical intervals) of longitudinal bank roughness profiles were extracted from a mean 3 mm resolution TIN model constructed from a high-resolution (mean point density ~57,000 pts/m^2) topographic survey, the latter being acquired through terrestrial laser scanning (TLS). The scan was undertaken in September 2008 at a riverbank on the Cecina River in Italy (see *Luppi et al.* [2009] for a description of this study site). Bank roughness profiles extracted from the TIN were systematically decimated so as to simulate the effects of varying sampling interval on the resulting estimate of z_{oSF}. As expected, the results (Figure 14) show z_{oSF} systematically decreases as survey resolution is increased, with convergence to a scale-independent value at sampling intervals of less than ~0.01 m. It follows that z_{oSF} has been systematically underestimated for the Mekong riverbanks (since our sampling interval was 0.50 m). However, the prior sensitivity analyses (Figure 13d) show that bank erosion rate is likely unaffected by this error, due to the relatively insensitive response across the specific range of z_{oSF} values that are relevant in this case. The availability of historical (2005 and 2006) photogrammetric surveys from the Cecina study site also provides an opportunity to undertake a preliminary test of one of the key model assumptions (see section 6); namely that, at the scale of the reach, the derived bank roughness parameters remain time invariant, even when the bank is actively retreating. The data partially support this assumption. Statistical tests (ANOVA) reveal that the bump spacing (λ) values obtained for each survey date (2005, 2006, 2008) do not differ significantly ($P = 0.346$), but the estimated bump protrusion lengths, H, are significantly different ($P < 0.001$). The results for the streamwise length scale (σ) of each bump also provide some evidence of difference, even if the P value obtained (0.068) is not less than 0.05.

[55] The above discussion suggests that the most likely sources of error contributing to the evident overprediction of bank erosion rate in this study is either (1) systematic underestimation of the bank material erodibility parameters as obtained from the CSM, or (2) systematic overprediction of τ_{sf} due to the omission of secondary scales of bank form roughness. A final possibility is that the value of the exponent a in equation (1) is not equal to unity in this case. Further work is necessary to demonstrate whether either, or both, of a revised CSM calibration or the routine characterization of bank topography at finer spatial resolution would indeed lead to improved model fit.

6. Conclusion

[56] In this study a combination of analytical modeling and novel field measurement techniques is employed to parameterize an excess shear stress model of riverbank erosion, with the new model being applied to the fine-grained, cohesive, riverbanks of the Lower Mekong River.

Bank boundary shear stress is estimated using a model [*Kean and Smith*, 2006a, 2006b] of flow over the irregular bank topography that is characteristic of fine-grained riverbanks. The Kean and Smith model provides a means to partition the form and skin drag components of bank boundary shear stress and thus determine the extent to which form drag influences bank erosion rates. In addition, the use of the CSM enables bank material erodibility parameters to be estimated directly. The use of these two methods in tandem has enabled this study to present the very first predictions of hydraulic bank erosion rates that do not require recourse to calibration. This, together with the point that the form drag component of bank boundary shear stress has typically been neglected hitherto, significantly enhances the physical basis of the bank erosion model presented herein relative to prior studies.

[57] The main finding of this study concerns the dominance of the form drag component in the bank boundary shear stress partitioning. Specifically, form drag was found to accounts for between 61% (Ban Hom) and 85% (Pakse) of the total stress imparted on the riverbanks investigated in this study. This dominant form drag component has the effect of reducing the skin drag that actually drives bank erosion to values similar to the estimated critical shear stresses. As such, the presence of high bank form roughness, induced by the presence of irregular bank topography, can be viewed as a key factor that self-limits the rate of bank erosion.

[58] Preliminary results that suggest that the new model has a tendency to overpredict bank erosion rates notwithstanding, a lack of suitable data inhibited comprehensive model validation in this study. It is therefore appropriate to conclude by highlighting some of the key assumptions employed in the model's derivation.

[59] 1. The model does not directly consider how mass wasting, common along the high banks of the Mekong, influences bank top retreat. Rather, consistent with the concept of basal endpoint control [*Carson and Kirkby*, 1972; *Thorne*, 1982], it is assumed that parallel bank retreat occurs at a rate that is controlled by the rate of hydraulically forced bank toe erosion. The veracity of this assumption has been tested by undertaking trial simulations (not reported here) that follow *Rinaldi et al.* [2008] in coupling fluvial erosion (as simulated here), mass wasting and finite element seepage analyses, for a range of flow hydrographs. In these simulations rates of bank top retreat are virtually identical to rates of bank toe retreat at both Ang Nyay and Pakse.

[60] 2. In applying equation (1) it is assumed that the threshold shear stresses associated with the onset and cessation of hydraulic erosion are identical. Temporal variations in bank material erodibility associated with the effects of weathering and/or seasonal wetting/drying cycles have been documented in prior studies [*Prosser et al.*, 2000; *Couper and Maddock*, 2001; *Couper*, 2004; *Wynn et al.*, 2008], but are excluded from consideration here. Given the LMB's tropical climate, there is no doubt significant potential for effective subaerial weathering on exposed bank faces. Nevertheless, the focus in this study is on bank toe materials located at, near, or below the dry season waterline. It is therefore speculated that bank toe materials are less likely to experience the variations in thermal or moisture conditions that are necessary to induce significant time variations in erodibility.

[61] 3. It is assumed that any hysteresis in the relationship between flow discharge and outer region flow velocity, and thus in the relationship between flow discharge and boundary shear stress, is sufficiently small that there is no significant difference in the functions linking τ_{sf} to Q on the falling and rising limbs of the flow hydrograph. The presence or absence of hysteresis can only be explored at the Ang Nyay and Pakse study sites, where ADCP data are available. There is no evidence of hysteresis at Pakse (Figure 10d), but at Ang Nyay boundary shear stress values are significantly higher on the falling limb of the hydrograph (Figure 10a). This hysteresis is evidently forced by u_{out} values being higher on falling limb flows, probably due to the influence on the flow field of an island immediately upstream of the study site. Whatever the precise cause of the hysteresis at Ang Nyay, a lack of data at this site inhibits derivation of separate τ_{sf} versus Q relations (for use in equation 1) to better characterize rising limb and falling limb flows. For this reason the single function shown on Figure 10a is preferred for use in this study, noting that the consequent likely overprediction of instantaneous daily erosion rates on rising limb flows is probably offset by underprediction of instantaneous daily erosion rates on falling limb flows. Net errors in long-term erosion rates are, therefore, likely most pronounced in years when the flow hydrograph shape is distinctly asymmetric.

[62] 4. It is assumed that the relationship between flow discharge and outer region flow velocity, as might for example be caused by long-term morphological adjustments, remains invariant throughout the duration of model simulations.

[63] 5. It is assumed that bank roughness parameters remain time invariant. At any specific point on the bank profile this is clearly unlikely to be the case, as the process of bank erosion by definition must alter the bank morphology and thereby affect the local roughness. However, it remains unclear whether ongoing hydraulic erosion of a *sequence* of bumps would lead to systematic variations, random changes, or no changes at all, in the statistical properties (H_{reg}, σ_{reg}, λ_{reg}) of that sequence, the latter being the key data that are employed in the model simulations.

[64] These limitations notwithstanding, the new model developed here presents some clear practical advantages beyond its enhanced physical basis. Specifically, the excess shear stress model used to simulate bank erosion is very simple and can, by the simple expedient of establishing a relationship between flow discharge and bank boundary shear stress, be driven using estimates of flow discharge. Consequently, the new model offers the means to construct multidecadal time series of simulated bank erosion rates using readily available flow discharge records, which is useful for the purpose of examining hydro-climatological controls on bank erosion.

[65] **Acknowledgments.** Hai Quang Trieu is supported by a bursary from the Mekong River Commission and the School of Geography, University of Southampton. Jason Kean (USGS) very kindly provided us with a copy of his IDL code used to undertake the flow modeling, while Laura Nardi and Rosaria Scozzafava (University of Florence, Italy) developed Matlab scripts that we used in the bank roughness analysis. We were fortunate, by chance, to meet Mark Schmeeckle (Arizona State University) while undertaking fieldwork near Vientiane. We enjoyed his company and assistance while carrying out CSM measurements at the Ban Hom study site. Last, but by no means least, we are very grateful to Jason Kean, Jim Pizzuto,

and Tess Wynn for their very helpful, thoughtful, and constructive reviews, which have contributed greatly to enhancing the clarity of the manuscript.

References

Aberle, J., V. Nikora, and R. Walters (2006), Data interpretation for in situ measurements of cohesive sediment erosion, *J. Hydraul. Eng.*, *132*, 581–588, doi:10.1061/(ASCE)0733-9429(2006)132:6(581).

Arulanandan, K., E. Gillogley, and R. Tully (1980), Development of a quantitative method to predict critical shear stress and rate of erosion of natural undisturbed cohesive soils, *Tech. Rep. GL-80-5*, U. S. Army Corps of Eng. Waterw. Exp. Stn., Vicksburg, Miss.

Black, K. S., and T. J. Tolhurst (2000), The Mk 4 60psi cohesive strength meter (CSM), user manual, Sediment Serv., Horsham, U. K.

Carling, P. A. (2009a), The geology of the Lower Mekong River, in *The Mekong: Biophysical Environment of an International River Basin*, pp. 13–28, edited by I. Campbell, Academic, New York.

Carling, P. A. (2009b), Geomorphology and sedimentology of the Lower Mekong River, in *The Mekong: Biophysical Environment of an International River Basin*, edited by I. Campbell, pp. 77–111, Academic, New York.

Carson, M. A., and M. J. Kirkby (1972), *Hillslope Form and Process*, Cambridge Univ. Press, Cambridge, U. K.

Clark, L. A., and T. M. Wynn (2007), Methods for determining streambank critical shear stress and soil erodibility: Implications for erosion rate predictions, *Trans. ASABE*, *50*, 95–106.

Constantine, C. R., T. Dunne, and G. J. Hanson (2009), Examining the physical meaning of the bank erosion coefficient used in meander migration modeling, *Geomorphology*, *106*, 242–252, doi:10.1016/j.geomorph.2008.11.002.

Couper, P. (2004), Space and time in river bank erosion research: A review, *Area*, *36*, 387–403, doi:10.1111/j.0004-0894.2004.00239.x.

Couper, P., and I. P. Maddock (2001), Subaerial river bank erosion processes and their interaction with other bank erosion mechanisms on the River Arrow, Warwickshire, UK, *Earth Surf. Processes Landforms*, *26*, 631–646, doi:10.1002/esp.212.

Darby, S. E. (1998), River width adjustment II: Modeling, *J. Hydraul. Eng.*, *124*, 903–917.

Eaton, B. C., M. Church, and R. G. Millar (2004), Rational regime model of alluvial channel morphology and response, *Earth Surf. Processes Landforms*, *29*, 511–529, doi:10.1002/esp.1062.

Goodson, J. M., A. M. Gurnell, P. G. Angold, and I. P. Morrissey (2002), Riparian seed banks along the lower River Dove, UK: Their structure and ecological implications, *Geomorphology*, *47*, 45–60, doi:10.1016/S0169-555X(02)00140-X.

Govers, G. (1991), Rill erosion on arable land in central Belgium: Rates, controls and predictability, *Catena*, *18*, 133–155, doi:10.1016/0341-8162(91)90013-N.

Grissinger, E. H. (1982), Bank erosion of cohesive materials, in *Gravel-Bed Rivers*, edited by R. D. Hey, J. C. Bathurst, and C. R. Thorne, pp. 273–287, John Wiley, Chichester, U. K.

Gupta, A., and S. C. Liew (2007), The Mekong from satellite imagery: A quick look at a large river, *Geomorphology*, *85*, 259–274, doi:10.1016/j.geomorph.2006.03.036.

Hanson, G. J. (1990), Surface erodibility of earthen channels at high stresses. Part II: Developing an in situ testing device, *Trans. ASAE*, *33*, 132–137.

Hanson, G. J., and A. Simon (2001), Erodibility of cohesive streambeds in the loess area of the midwestern USA, *Hydrol. Processes*, *15*, 23–38, doi:10.1002/hyp.149.

Hooke, J. M. (1980), Magnitude and distribution of rates of river bank erosion, *Earth Surf. Processes Landforms*, *5*, 143–157.

Hopson, T. M. (1999), The form drag of large natural vegetation along the banks of open channels, M. S. thesis, 114 pp., Univ of Colo., Boulder.

Howard, A. D. (1994), Badlands, in *Geomorphology of Desert Environments*, edited by A. D. Abrahams and A. J. Parsons, pp. 213–242, Chapman and Hall, London.

Julian, J. P., and R. Torres (2006), Hydraulic erosion of cohesive riverbanks, *Geomorphology*, *76*, 193–206, doi:10.1016/j.geomorph.2005.11.003.

Kean, J. W. (2003), Computation of flow and boundary shear stress near the banks of streams and rivers, Ph.D. thesis, Univ of Colo., Boulder.

Kean, J. W., and J. D. Smith (2005), Generation and verification of theoretical rating curves in the Whitewater River basin, Kansas, *J. Geophys. Res.*, *110*, F04012, doi:10.1029/2004JF000250.

Kean, J. W., and J. D. Smith (2006a), Form drag in rivers due to small-scale natural topographic features: 1. Regular sequences, *J. Geophys. Res.*, *111*, F04009, doi:10.1029/2006JF000467.

Kean, J. W., and J. D. Smith (2006b), Form drag in rivers due to small-scale natural topographic features: 2. Irregular sequences, *J. Geophys. Res.*, *111*, F04010, doi:10.1029/2006JF000490.

Koponen, J., E. Alasaarela, K. Lehtinen, J. Sarkkula, P. Simbierowicz, H. Vepsä, and M. Virtanen (1992), Modelling the dynamics of a large sea area: Bothnian Bay Research Project 1988–90, *Publ. Water Environ. Res. Inst.*, *7*, 1–91.

Koponen, J., et al. (2008), Hydrological, environmental and socio-economic modelling tools for the Lower Mekong Basin impact assessment, *WUP-FIN Phase II Model Rep.*, 413 pp., Mekong River Comm., Vientiane, Laos. (Available at http://www.eia.fi/wup-fin/wup-fin2/publications.htm)

Kummu, M. (2008), Spatio-temporal scales of hydrological impact assessment in large river basins: The Mekong case, Ph.D. thesis, Water Resour. Res. Unit, Helsinki Univ. of Technol., Espoo, Finland. (Available at http://lib.tkk.fi/Diss/2008/isbn9789512296668/)

Kummu, M., X. X. Lu, A. Rasphone, J. Sarkkula, and J. Koponen (2008), Riverbank changes along the Mekong River: Remote sensing detection in the Vientiane-Nong Khai area, *Quaternary Int.*, *186*, 100–112, doi:10.1016/j.quaint.2007.10.015.

Liu, S., P. Lu, D. Liu, and P. Jin (2007), Pinpointing source of Mekong and measuring its length through analysis of satellite imagery and field investigations, *Geo-Spatial Inf. Sci.*, *10*(1), 51–56, doi:10.1007/s11806-007-0011-6.

Luppi, L., M. Rinaldi, L. B. Teruggi, S. E. Darby, and L. Nardi (2009), Monitoring and numerical modelling of riverbank erosion processes: A case study along the Cecina River (central Italy), *Earth Surf. Processes Landforms*, *34*, 530–546, doi:10.1002/esp.1754.

Marron, D. C. (1992), Floodplain storage of mine tailings in the Belle Fourche River, *Earth Surf. Processes Landforms*, *17*, 675–685, doi:10.1002/esp.3290170704.

McBride, M., W. C. Hession, D. M. Rizzo, and D. M. Thompson (2007), The influence of riparian vegetation on near-bank turbulence: A flume experiment, *Earth Surf. Processes Landforms*, *32*, 2019–2037, doi:10.1002/esp.1513.

McLean, S. R., and J. D. Smith (1986), A model for flow over two-dimensional bed forms, *J. Hydraul. Eng.*, *112*, 300–317, doi:10.1061/(ASCE)0733-9429(1986)112:4(300).

Mekong River Commission (1961), Hydrographic atlas of 1961 for the Mekong. surveyed in 1959–1961, Vientiane, Laos.

Mekong River Commission (1992), Hydrographic atlas of 1992 for the Mekong. surveyed in 1989–1992, Vientiane, Laos.

Mekong River Commission (2005), Overview of the hydrology of the Mekong River basin, Vientiane, Laos.

Millar, R. G. (2000), Influence of bank vegetation on alluvial channel patterns, *Water Resour. Res.*, *36*, 1109–1118, doi:10.1029/1999WR900346.

Milliman, J. D., and R. H. Meade (1983), World-wide delivery of river sediments to the oceans, *J. Geol.*, *91*, 1–21, doi:10.1086/628741.

Mosselman, E. (1998), Morphological modeling of rivers with erodible banks, *Hydrol. Processes*, *12*, 1357–1370, doi:10.1002/(SICI)1099-1085(19980630)12:8<1357::AID-HYP619>3.0.CO;2-7.

Osman, A. M., and C. R. Thorne (1988), Riverbank stability analysis. I: Theory, *J. Hydraul. Eng.*, *114*, 134–150, doi:10.1061/(ASCE)0733-9429(1988)114:2(134).

Partheniades, E. (1965), Erosion and deposition of cohesive soils, *J. Hydraul. Div. Am. Soc. Civ. Eng.*, *91*, 105–138.

Paterson, D. M. (1989), Short term changes in the erodibility of intertidal cohesive sediments related to the migratory behaviour of epipelic diatoms, *Limnol. Oceanogr.*, *34*(1), 223–234, doi:10.4319/lo.1989.34.1.0223.

Piégay, H., S. E. Darby, E. Mosselman, and N. Surian (2005), A review of techniques available for delimiting the erodible river corridor: A sustainable approach to managing bank erosion, *River Res. Appl.*, *21*, 773–789, doi:10.1002/rra.881.

Prosser, I. P., A. O. Hughes, and I. D. Rutherfurd (2000), Bank erosion of an incised upland channel by subaerial processes: Tasmania, Australia, *Earth Surf. Processes Landforms*, *25*, 1085–1101, doi:10.1002/1096-9837(200009)25:10<1085::AID-ESP118>3.0.CO;2-K.

Reneau, S. L., P. G. Drakos, D. Katzman, D. V. Malmon, E. V. McDonald, and R. T. Ryti (2004), Geomorphic controls on contaminant distribution along an ephemeral stream, *Earth Surf. Processes Landforms*, *29*, 1209–1223, doi:10.1002/esp.1085.

Rinaldi, M., and N. Casagli (1999), Stability of streambanks formed in partially saturated soils and effects of negative pore water pressures: The Sieve River (Italy), *Geomorphology*, *26*, 253–277, doi:10.1016/S0169-555X(98)00069-5.

Rinaldi, M., and S. E. Darby (2007), Modelling river-bank-erosion processes and mass failure mechanisms: Progress towards fully coupled simulations, in *Gravel-Bed Rivers 6: From Process Understanding to River Restoration*, *Dev. Earth Surf. Processes*, vol. 11, edited by H. Habersack, H. Piégay, and M. Rinaldi, pp. 213–239, Elsevier, Amsterdam, doi:10.1016/S0928-2025(07)11126-3.

Rinaldi, M., N. Casagli, S. Dapporto, and A. Gargini (2004), Monitoring and modeling of pore water pressure changes and riverbank stability during flow events, *Earth Surf. Processes Landforms*, *29*, 237–254, doi:10.1002/esp.1042.

Rinaldi, M., B. Mengoni, L. Luppi, S. E. Darby, and E. Mosselman (2008), Numerical simulation of hydrodynamics and bank erosion in a river bend, *Water Resour. Res.*, *44*, W09428, doi:10.1029/2008WR007008.

Samadi, A., E. Amiri-Tokaldany, and S. E. Darby (2009), Identifying the effects of parameter uncertainty on the reliability of riverbank stability modelling, *Geomorphology*, *106*, 219–230, doi:10.1016/j.geomorph.2008.10.019.

Schlichting, H. (1979), *Boundary-Layer Theory*, 817 pp., McGraw-Hill, New York.

Sen, P. K. (1968), Estimate of the regression coefficient based on Kendall's tau, *J. Am. Stat. Assoc.*, *63*, 1379–1389, doi:10.2307/2285891.

Simon, A., and A. J. Collison (2002), Quantifying the mechanical and hydrological effects of vegetation on streambank stability, *Earth Surf. Processes Landforms*, *27*, 527–546, doi:10.1002/esp.325.

Simons, T. J. (1980), Circulation models of lakes and inland seas, *Can. Bull. Fish. Aquat. Sci.*, *203*, 1–146.

Smith, J. D., and S. R. McLean (1977), Spatially averaged flow over a wavy surface, *J. Geophys. Res.*, *82*, 1735–1746, doi:10.1029/JC082i012p01735.

Theil, H. (1950), A rank-invariant method of linear and polynomial regression analysis, *Indagationes Math.*, *12*, 85–91.

Thieler, E. R., E. A. Himmelstoss, J. L. Zichichi, and A. Ergul (2009), Digital Shoreline Analysis System (DSAS) version 4.0—An ArcGIS extension for calculating shoreline change, *U. S. Geol. Surv. Open File Rep. 2008–1278*. (Available at http://pubs.usgs.gov/of/2008/1278/)

Thoman, R. W., and S. L. Niezgoda (2008), Determining erodibility, critical shear stress, and allowable discharge estimates for cohesive channels: Case study in the Powder River basin of Wyoming, *J. Hydrol. Eng.*, *134*, 1677–1687, doi:10.1061/(ASCE)0733-9429(2008)134:12(1677).

Thorne, C. R. (1982), Processes and mechanisms of river bank erosion, in *Gravel-Bed Rivers: Fluvial Processes, Engineering, and Management*, edited by R. D. Hey, J. C. Bathurst, and C. R. Thorne, pp. 227–271, John Wiley, Chichester, U. K.

Thorne, S. D., and D. J. Furbish (1995), Influences of coarse bank roughness on flow within a sharply curved river bend, *Geomorphology*, *12*, 241–257, doi:10.1016/0169-555X(95)00007-R.

Thorne, C. R., and J. Lewin (1979), Bank processes, bed-material movement and planform development in a meandering river, in *Adjustment of the Fluvial System*, edited by D. D. Rhodes and G. P. Williams, pp. 117–137, Kendall Hunt, Dubuque, Iowa.

Tolhurst, T. J., K. S. Black, S. A. Shayler, S. Mather, I. Black, K. Baker, and D. M. Paterson (1999), Measuring the in situ erosion shear stress of intertidal sediments with the cohesive strength meter (CSM), *Estuarine Coastal Shelf Sci.*, *49*, 281–294, doi:10.1006/ecss.1999.0512.

Tolhurst, T. J., K. S. Black, D. M. Paterson, H. J. Mitchener, G. R. Termaat, and S. A. Shayler (2000), A comparison and measurement standardization of four in situ devices for determining the erosion shear stress of intertidal sediments, *Cont. Shelf Res.*, *20*, 1397–1418, doi:10.1016/S0278-4343(00)00029-7.

Vardy, S., J. E. Saunders, T. J. Tolhurst, P. A. Davies, and D. M. Paterson (2007), Calibration of the high-pressure cohesive strength meter (CSM), *Cont. Shelf Res.*, *27*, 1190–1199, doi:10.1016/j.csr.2006.01.022.

Virtanen, M., J. Koponen, K. Dahlbo, and J. Sarkkula (1986), Three-dimensional water-quality–transport model compared with field observations, *Ecol. Modell.*, *31*, 185–199, doi:10.1016/0304-3800(86)90063-3.

Whiting, P. J., and W. E. Dietrich (1990), Boundary shear stress and roughness over mobile alluvial beds, *J. Hydraul. Eng.*, *116*, 1495–1511, doi:10.1061/(ASCE)0733-9429(1990)116:12(1495).

Wiberg, P. L., and J. D. Smith (1991), Velocity distribution and bed roughness in steep streams, *Water Resour. Res.*, *27*, 825–838, doi:10.1029/90WR02770.

Widdows, J., P. L. Friend, A. J. Bale, M. D. Brinsley, N. D. Pope, and C. E. L. Thompson (2007), Inter-comparison between five devices for determining erodibility of intertidal sediments, *Cont. Shelf Res.*, *27*, 1174–1189, doi:10.1016/j.csr.2005.10.006.

Wynn, T. M., M. B. Henderson, and D. H. Vaughan (2008), Changes in streambank erodibility and critical shear stress due to subaerial processes along a headwater stream, southwestern Virginia, USA, *Geomorphology*, *97*, 260–273, doi:10.1016/j.geomorph.2007.08.010.

P. A. Carling, S. E. Darby, J. Leyland, and H. Q. Trieu, School of Geography, University of Southampton, Highfield, Southampton SO17 1BJ, UK. (s.e.darby@soton.ac.uk)

I. Conlan, Department of Resource Management and Geography, University of Melbourne, Melbourne, Vic 2010, Australia.

J. Koponen, Environmental Impact Assessment Centre of Finland Ltd, Tekniikantie 21b, Espoo FI-02150, Finland.

M. Kummu, Water and Development Research Group, Aalto University School of Science and Technology (TKK), Aalto University, Espoo FIN-02015, Finland.

J. Sarkkula, Finnish Environment Institute, P.O. Box 140, Helsinki FI-00251, Finland.

References

Abernethy, B. and Rutherfurd, I.D., 1998, Where along a rivers length will vegetation most effectively stabilise stream banks? *Geomorphology*, 23, 55-75.

Abernethy, B. and Rutherfurd, I.D., 2000, The effect of riparian tree roots on the mass-stability of riverbanks. Earth Surface Process and Landforms. 25: 921-937.

Akkerman G.J., Mosselman E., Schiereck G.J., Pham A. T. and Pham D., 2006, Bank Erosion Mitigation Red River Vietnam, Towards an Anticipating River Training Strategy, *Proceedings Third International Conference on Scour and Erosion*, November 1-3, Amsterdam, The Netherlands

Alonso, C. V., and Combs, S. T., 1990, Streambank erosion due to bed degradation – A model concept, *Transactions of ASAE, 33(4)*, 1239-1248.

Alyamani, M. S., and Sen, Z., 1993, Determination of Hydraulic Conductivity from Grain-Size Distribution Curves, *Ground Water, 31*,551-555.

Arulanandan, K., Gillogley, E. and Tully, R., 1980, Development of a quantitative method to predict critical shear stress and rate of erosion of natural undisturbed cohesive soils: Report GL-80-5, *U.S. Army Engineers*, Waterways Experiment Station, Vicksburg, Mississippi.

Arya, L.M., and Paris, J.F., 1981, A Physico-empirical Model to Predict the Soil Moisture Characteristic from Particle-size Distribution and Bulk Density Data. *Soil Science Society of America Journal*, 45:1023-1030.

ASCE Task Committee on Sedimentation, 1966, Sediment Transportation Mechanics: Initiation of Motion, *Journal of the Hydraulics Division*, American Society of Civil Engineers, 92(2), 291-314.

ASCE Task Committee on Hydraulics., B. M. a. M. o. R. W. A., 1998a, River Width Adjustment, I: Processes and Mechanisms, *Journal of Hydraulic Engineering,* 124(9), 881-902.

Ashworth, P. J., and Ferguson R. I., 1989, Size-selective entrainment of bed load in gravel bed streams, *Water Resources Research*, 25(4), 627–634, doi:10.1029/WR025i004p00627

Aubertin, M., Mbonimpa, M., Bussière, B. and Chapuis, R.P., 2003, A model to predict the water retention curve from basic geotechnical properties, *Canadian Geotechnical Journal*, 40(6): 1104-1122.

Bishop, A. W., 1955, The use of the slip circle in the stability analysis of slopes, *Geotechnique,* 5, 7-17.

Bishop, A. W., and Morgenstern., N., 1960, *Stability Coefficients for Earth Slopes*, *Geotechnique*, 10(4), 129-150.

Carling, P. A., 2009a, The geology of the Lower Mekong River, In: I. Campbell (Ed), *The Mekong: Biophysical Environment of an International River Basin*, Elsevier, Netherlands.

Carling, P. A., 2009b, Geomorphology and sedimentology of the Lower Mekong River, In: I. Campbell (Ed), *The Mekong: Biophysical Environment of an International River Basin*, Elsevier, Netherlands.

Carman, P. C., 1937, Fluid Flow through Granular Beds, *Trans.Inst.Chem. Eng*, 15,150.

Carman, P.C., 1956, *Flow of Gases through Porous Media*, Butterworths Scientific Publications, London.

Casagli, N., Curini, A., Gargini, A., Rinaldi, M. and Simon, A., 1997, Effects of pore pressure on the stability of streambanks: preliminary results from the Sieve River, Italy, in Wang, S. S. Y., Langendoen, E. J. and Shields, F. D. Jr. (Eds), *Management of Landscapes Disturbed by Channel Incision, Stabilization, Rehabilitation, Restoration*, Center for Computational Hydroscience and Engineering, University of Mississii, 243-248.

Casagli, N., Rinaldi, M., Gargini, A. and Curini, A., 1999, Pore water pressure and streambank stability: results from monitoring site on the Sieve river, Italy, *Earth Surface Processes and Landforms,* 24, 1095-1114.

Chow, V.T., 1959, *Open-Channel Hydraulics*, McGraw-Hill, New York, 680.

Corey, J.C., 1957, Measurement of water and air permeability in unsaturated soil, *Soil Science of America*, Vol. 21.

Culmann, K., 1866, *Die Graphische Statik*, Von Meyer & Zeller, Zurich, Switzerland, 547–56.

Dapporto, S., 2001, Non-vertical jet testing of cohesive streambank toe material: School of Geography, University of Nottingham, in collaboration with USDA-ARS National Sedimentation Laboratory, Oxford, Mississippi, *Internal Report*.

Dapporto, S., Rinaldi, M. and Casag, N., 2001, Failure mechanisms and pore water pressure conditions- analysis of a riverbank along the Arno River, Central Italy. *Engineering Geology*, 61, 221-242.

Dapporto, S., Rinaldi, M., Casagli, N. and Vannocci, P., 2003, Mechanisms of riverbank failure along the Arno River, Central Italy, *Earth Surface Processes and Landforms,* 28(12), 1303-1323.

Darby, S. E., Gessler, D., and Thorne, C. R., 2000, Computer program for stability analysis of steep, cohesive riverbanks, *Earth Surface Processes and Landforms*, 25, 175-190.

Darby, S. E., Rinaldi, M., and Dapporto, S., 2007, Coupled simulations of fluvial erosion and mass wasting for cohesive river banks, *Journal of geophysical research*, 112.

Darby, S. E. and Thorne, C.R., 1996a, Development and Testing of Riverbank: Stability Analysis, Stability analysis for steep, eroding, cohesive river banks, *Journal of Hydraulic Engineering,* 122(8), 443-454.

Darby, S.E. and Thorne, C.R., 1996b, Bank stability analysis for the Upper Missouri River. Report *Prepared for the U.S. Army engineers Waterways Experiment Station*, Vicksburg, Missouri.

Darby, S.E. and Thorne, C.R., 1994, Prediction of tension crack location and riverbank erosion hazards along destabilized channels, *Earth Surface Processes Landforms, 19*: 233-245.

Darby, S.E., Trieu, H.Q., Carling, P.A., Sarkkula, J., Koponen, J., Kummu, M., Conlan, I. and Leyland, J., 2010, A physically based model to predict hydraulic erosion of Fine-Grained River Banks: The Role of Form Roughness in Limiting Erosion, *Journal of Geophysical Research*, 115.

Dunn, I.S., 1959, Tractive resistance of cohesive channels, *Journal of the Soil Mechanics and Foundations Division*, ASCE 85 (SM 3), 1– 24.

Esty, D.C., Levy, A.L., Srebotnjak, T. and de Sherbinin, A. , 2005, Environmental Sustainability Index: Benchmarking National Environmental Stewardship, *Yale Center for Environmental Law and Policy*, New Haven.

Ferguson, R. I., 1994, Critical discharge for entrainment of poorly sorted gravel, *Earth Surface processes and Landforms*, 19, 179-186.

Flintham, T.P. and Carling, P.A, 1988, The prediction of mean bed and wall boundary shear in uniform and compositely rough channels. In: W.R. White (Ed), *International Conference on River Regime,* Wiley and Sons, Chichester, UK, 267–287.

Fox, G.A., G.V. Wilson, A. Simon, E.J. Langendoen, O. Akay and J.W. Fuchs, 2007, Measuring streambank erosion due to ground water seepage: Correlation to bank pore water pressure, precipitation and stream stage, *Earth Surface Processes Landforms*, 32, 1558-1573.

Fredlund, D. G. and Rahardjo, H., 1993, *Soil Mechanics for Unsaturated Soils*, John Wiley & Sons, New York, New York.

Fredlund, D. G., and Xing A., 1994, Equations for the soil-water characteristic curve, *Canadian Geotechnical Journal,* 31, 521-532.

Fredlund, D. G., Morgenstern, N.R. and Widger, R.A., 1978, The shear strength of unsaturated soils, *Canadian Geotechnical Journal,* 15, 312-321.

Fredlund, D.G., Xing, A. and Huang, S., 1994, Predicting the permeability function for unsaturated soils using the soil-water characteristic curve, *Canadian Geotechnical Journal*, 31, 533-546.

Geo-Slope International Ltd, 2002, *Users Guide for Seep/W, Version 5,* Geo-Slope International Ltd., Calgary, Alta.

Gray, D.H. and Barker, D., 2004, Root-soil mechanics and interaction. In: Bennett, S.J., Simon, A. (Eds), *Riparian Vegetation and Fluvial Geomorphology*, American Geophysical Union, Washington, DC, 113-124.

Gray, D.H., 1978, Role of woody vegetation in reinforcing soils and stabilising slopes, *Proc.Symp.Soil Reinforcing and Stabilising Techniques*, Sydney, Australia, 253-306.

Green, R.E. and Corey, J.C., 1971, Calculation of Hydraulic Conductivity: A Further Evaluation of Some Predictive Methods, *Soil Science Society of America Proceedings,* 35, 3-8.

Grissinger, E. H., 1982, Bank erosion of cohesive materials, in R. D. Hey, J. C. Bathurst and C. R. Thorne (Eds) *Gravel-Bed Rivers*, John Wiley, Chichester, 273-287.

Gupta, A., and S. C. Liew, 2007, The Mekong from satellite imagery: A quick look at a large river, *Geomorphology*, 85, 259–274, doi:10.1016/ j.geomorph.2006.03.036.

GWSP Digital Water Atlas, 2008, Map 38: Mean annual surface runoff 1950–2000, (V1.0).

Hanson, G. J. and Simon, A., 2001, Erodibility of cohesive streambeds in the loess area of the midwestern USA, *Hydrological Processes,* 15, 23-38.

Hanson, G.J., 1990, Surface erodibility of earthen channels at high stresses. Part II-developing an *in situ* testing device, *Transactions of the American Society of Agricultural Engineers*, 33(1), 132–137.

Hanson, G.J., 1991, Development of a jet index to characterize erosion resistance of soils in earthen spillways, *Transactions of the American Society of Agricultural Engineers*, 36(5), 2015–2352.

Hazen, A., 1892, Some Physical Properties of Sands and Gravels, with Special Reference to their Use in Filtration. 24th Annual Report, *Massachusetts State Board of Health, Pub.Doc.* No.34, 539-556.

Hemphill, R.W. and Bramley, M.E., 1989, *Protection of river and canal banks,* CIRIA, London.

Hooke, J. M., 1979, An analysis of the processes of river bank erosion, *Journal of Hydrology*, 42, 39-62.

Hooke, J. M., 1980, Magnitude and distribution of rates of river bank erosion, *Earth Surface Processes and Landforms*, 5, 143-157.

Hough, P., 2004, *Understanding global security*, Routledge, New York.

Huang, Y.H., 1983, *Stability Analysis of Earth Slopes*, Van Nostrand Reinhold, New York.

Jia, D., Shao, X., Wang, H. and Zhou, G., 2010, Three-dimensional modeling of bank erosion and morphological changes in the Shishou bend of the middle Yangtze River, *Advances in Water Resources,* 33(3), 348-360.

Julian, J.P. and Torres R., 2006, Hydraulic erosion of cohesive riverbanks, *Geomorphology*, 76, 193–206.

Kean, J. W., and J. D. Smith, 2006a, Form drag in rivers due to small-scale natural topographic features: 1. Regular sequences, *Journal of Geophysical Research*, 111, F04009, doi:10.1029/2006JF000467.

Kean, J. W., and J. D. Smith, 2006b, Form drag in rivers due to small-scale natural topographic features: 2. Irregular sequences, *Journal of Geophysical Research* , 111(F04010), doi:10.1029/2006JF000490, 2006.

Knight, D.W., 1981, Boundary shear in smooth and rough channels, *Journal of Hydraulic Division, ASCE,* 107(7), 839-85.

Knight, D.W., Demetriou, J.D. and Hamed, M., 1984, Boundary shear stress in smooth rectangular channels, ASCE, *Journal of Hydraulic Engineering*, 110(4) April, 405-422.

Knighton, A. D., 1973, Riverbank erosion in relation to streamflow conditions, River Bollin-Dean, Cheshire. E. Midlands, *East Midland Geographer*, 5, 416-426.

Knighton, D., 1998, *Fluvial forms and processes: a new perspective,* Arnold.

Kozeny, J., 1927, Uber Kapillare Leitung Des Wassers in Boden, *Sitzungsber Akad. Wiss.Wien Math.Naturwiss.Kl.,* Abt.2a, 136, 271-306 (In German).

Kummu, M., Lu, X.X., Wang, J.J. and Varis, O, 2010, Basin-wide sediment trapping efficiency of emerging reservoirs along the Mekong, *Geomorphology*, 119 (3–4), 181–197.

Lane, E. W., 1955, Design of stable channels, *Transactions of the American Society of Civil Engineers*, 120, 1-34.

Lawler, D. M., 1986, River bank erosion and the influence of frost: a statistical examination, *Transactions of the Institute of British Geographers*, 11, 227-242.

Lawler, D. M., 1992, Process dominance in bank erosion systems. In P. A. Carling, Petts, G.E. (Eds.), *Lowland Floodplain Rivers: Geomorphological Perspective* John Wiley, Chichester, 117-143.

Lawler, D. M., Thorne, C. R., and Hooke, J. M., 1997, Bank erosion and instability, in C. R. Thorne, R. D. Hey and M. D. Newson (Eds), *Alied Fluvial Geomorphology for River Engineering and Management*, John Wiley, Chichester, 137-172.

Le M. H., Hitoshi T., Nguyen T. T. and Nguyen T. V., 2006, Prediction of River Bank Erosion in the Lower Mekong River Delta, *Japan Estuary Workshop*, August 22nd - 24th, Hanoi, Vietnam.

Leutheusser, H. J., 1963, Turbulent flow in rectangular ducts, *Proceedings of the American Society of Civil Engineers*, 89, HY3.

Lohnes, R. and Handy, R.L., 1968, Slope angles in friable loess, *Journal of Geology*, 76, 247–258.

Luppi, L., Rinaldi, M., Teruggi, L.B., Darby, S.E., and Nardi, L., 2009, Monitoring and numerical modelling of riverbank erosion processes: A case study along the Cecina River (Central Italy), *Earth Surface Processes Landforms*, 34, 530-546.

Meade. R. H., 1996, River-sediment input to major deltas. In J.D Milliman & B. U. haq: (Eds.), *Sea-level Rise and Coastal Subsidence: Causes, Consequences and Strategies*, Kluwer, Dordrecht, The Netherlands, 63-85.

Millar, R. G. and Quick, M.C., 1993, Effect of bank stability on geometry of gravel rivers, *Journal of Hydraulic Engineering*, 119, 1343-1363.

Millar, R. G., 2000, Influence of bank vegetation on alluvial channel patterns, *Water Resourses Research*, 36, 1109-1118.

Millar, R. G., Quick, M.C., 1997, Discussion of 'Development and Testing of Riverbank-Stability Analysis' by Stephen Darby and Colin Thorne, *Journal of Hydraulic Engineering*, 123(11), 1051.

Morgenstern, N. R., and Price, V. E., 1965, The analysis of the stability of general slip surfaces, *Geotechnique*, 15, 79-93.

Morgestern, N.R., 1963, Stability charts for earth slopes during rapid drawdown, *Geotechnique*, 13(2), 121–131.

MRC, 2005, Overview of the Hydrology of the Mekong Basin, *Mekong River Commission Report*, Vientiane, November 2005, 73.

MRC, 2007, *Annual Mekong flood report 2006*, Flood Management and Mitigation Programme, Vientiane, Lao PDR.

Nanson, G. C. and Hickin, E.J., 1986, A statistical analysis of bank erosion and channel migration in western Canada, *Geological Society of America Bulletin*, 97, 49-54.

NAPA National Adaptation Programme of Action, 2005, *Final Report,* Ministry of Environment and Forest Government of the Peoples Republic of Bangladesh.

NHC Northwest Hydraulics Consultants, 2006, River Flooding and Erosion in Northeast India, *Background Paper No. 4*, Edmonton, Alberta, Canada.

Osman, A. M. and Thorne, C.R., 1988, River bank stability analysis. I: Theory, *Journal of Hydraulic Engineering*, 114(2), 134-150.

Partheniades, E., 1965, Erosion and deposition of cohesive soils, *Journal of Hydraulics Division of the American Society of Civil Engineers*, 91, 105-139.

Pollen N., 2006, Temporal and spatial variability of root reinforcement of streambanks: accounting for soil shear strength and moisture, *Catena*, 69, 197–205.

Pollen, N. and Simon A., 2005, Estimating the mechanical effects of riparian vegetation on streambank stability using a fiber bundle model, *Water Resources Research* 41, W07025. DOI: 10.1029/2004WR003801

Ponce, V.M., 1978, Generalized Stability Analysis of Channel Banks, *Journal of the Irrigation and Drainage Division*, 104(4), 343-350.

Raudkivi, A. J., 1998, *Loose Boundary Hydraulics,* A. A. Balkema, Rotterdam.

Richard, K. S. and Lorriman, N.R., 1987, Basal erosion and mass movement. In M. G. Anderson, Richards, K.S. (Eds.), *Slope Stability*, 331-357, John Wiley, Chichester.

Rinaldi M. and Darby S.E., 2008, Modelling river-bank-erosion processes and mass failure mechanisms: progress towards fully coupled simulations. In: Habersack H., Piégay H. & Rinaldi M. (Eds), *Gravel-Bed Rivers 6 - From Process Understanding to River Restoration*. Series Developments in Earth Surface Processes, 11, Elsevier, Netherlands, 213-239.

Rinaldi M., Casagli N., Dapporto S. and Gargini A., 2004, Monitoring and modelling of pore water pressure changes and riverbank stability during flow events, *Earth Surface Processes and Landforms*, 29 (2), 237-254.

Rinaldi, M. and Darby S. E., 2008, Advances in modelling river bank erosion processes. In P. E. H. Habersack, T. Hoey, H. Piégay and M. Rinaldi (Eds.), *Gravel-Bed Rivers 6: From Process Understanding to River Restoration*. Elsevier, Netherlands: Series Developments in Earth Surface Processes.

Rinaldi, M. and N. Casagli, 1999, Stability of streambanks formed in partially saturated soils and effects of negative pore water pressures: The Sieve River (Italy), *Geomorphology*, 26, 253-277.

Selby, M.J., 1982, *Hillslope Materials and Processes*, Oxford University Press, Oxford, UK.

Shepherd, R. G., 1989, Correlations of Permeability and Grain Size, *Groundwater*, 27(5), 663-638.

Simon, A. and Collison, A., 2002, Quantifying the mechanical and hydrologic effects of riparian vegetation on streambank stability, *Earth Surface Processes and Landforms*, 27, 527-546.

Simon, A., Curini, A., Darby, S.E. and Langendoen, E.J., 1999, Streambank mechanics and the role of bank and near-bank processes in incised channels. In S. E. Darby, Simon, A. (Eds.), *Incised River Channels: Processes, Forms, Engineering and Management*, John Wiley, Chichester, 123-152.

Simon, A., Curini, A., Darby, S.E. and Langendoen, E.J., 2000, Bank and near-bank processes in an incised channel, *Geomorphology*, 35, 193-217.

Simon, A., Thomas, R. E., Curini, A., and Shields, F. D., Jr. 2002, Case study: Channel stability of the Missouri River, Eastern Montana, *Journal Hydraulic Engineering*, 128 (10), 880–890.

Simon, A., Langendoen, E.J., Collison, A. and Layzell, A., 2003, *Incorporating bank-toe erosion by hydraulic shear into a bank-stability model: Missouri River, Eastern Montana*, Proceedings, EWRL-ASCE, World Water and Environmental Resources Congress, CD-Rom, 11.

Simon, A., Wolfe, W.J. and Molinas, A., 1991, *Mass-wasting algorithms in an alluvial channel model*, Proceedings of the 5th Federal Interagency Sedimentation Conference, Las Vegas, Nevada, 2, 8-22 to 8-29.

Simon., A., Thomas, R.E., Curini A. and Shields, F.D., 2002, Case study: channel stability of the Missouri River, Eastern Montana, *Journal of Hydraulic Engineering*, 128(10), 880–890.

Taylor, D. W., 1948, *Fundamentals of soil mechanics*, John Wiley, New York, N.Y.

Terzaghi, K., and Peck, R. B., 1964, *Soil Mechanics in Engineering Practice,* Wiley, New York.

Thorne, C. R. and Osman, A.M., 1988, The influence of bank stability on regime geometry of natural channels. In W. R. White (Ed.), *River Regime* John Wiley, Chichester (135-147).

Thorne, C. R. and Tovey, N.K., 1981, Stability of composite river banks, *Earth Surface Processes and Landforms*, 6, 469-484.

Thorne, C. R., 1982, Processes and mechanisms of river bank erosion. In R. D. Hey, Bathurst, J.C., Thorne, C.R. (Eds.), *Gravel-bed rivers* John Wiley, Chichester, 227-271.

Thorne, C.R. and Tovey, N.K., 1979, Discussion on 'Generalized stability analysis of channel banks' by V.M. Ponce, Journal of the Irrigation and Drainage Division, *American Society of Civil Engineers*, 105(IR4), 436-437.

Thorne, C.R., Murphey, J.B. and Little, W.C., 1981, Stream Channel Stability Appendix D: Bank Stability and Bank Material Properties in the Bluffline Streams of Northwest Mississippi, *USDA Sedimentation Laboratory*, Oxford, Mississippi.

Tolhurst, T. J., Black, K.S., Shayler, S.A., Mather, .S., Black, I., Baker, K. and Paterson D.M., 1999, Measuring the in situ erosion shear strength of intertidal sediments with the Cohesive Strength Meter (CSM), *Estuarine, Coastal and Shelf Science*, Estuarine, Coastal and Shelf Science, 49.

Twidale, C. R., 1964, Erosion of an alluvial bank at Birdwood, South Australia. Z., *Geomorphology.*, 8, 189-211.

Van De Wiel, M. J., 2003, Numerical modeling of channel adjustment in alluvial meandering rivers with riparian vegetation, *PhD Thesis*, University of Southampton, Southampton, UK.

Van De Wiel, M.J. and Darby, S.E., 2007, A new model to analyse the impact of woody riparian vegetation on the geotechnical stability of riverbanks, *Earth Surface Processes and Landforms*, 32, 2185-2198.

Van Genuchten, M. T., 1980, A closed-form equation for predicting the hydraulic conductivity of unsaturated soils, *J. Soil. Sci. Soc. Am.*, 44, 892-898.

Vanoni, A. V., 1977, *Sedimentation Engineering.* ASCE Manuals and Reports on Engineering Practice No. 54, ASCE, New York.

Varis, O., Kummu, M. and Salmivaara, A., Ten major rivers in monsoon Asia-Pacific: An assessment of vulnerability, 2012, *Alied Geography*, 32(2), 441-454. In press, available online 22 July 2011, doi:10.1016/j.apgeog.2011.05.003.

Wolman, M. G., 1959, Factors influencing the erosion of cohesive river banks, *American Journal of Science*, 257, 204-216.

World Bank, 2008, *World development indicators 2008*, The World Bank, Washington D.C.

Wu, T.H., McKinnell, W.P. and Swanston, D.N., 1979, Strength of tree roots and landslides on Prince of Wales Island, Alaska, *Canadian Geotechnical Journal*, 16 (1), 19-33.

Yuen, K.W.H., 1989, A study of boundary shear stress, flow resistance and momentum transfer in open channel with simple compound trapezoidal cross sections. *PhD Thesis,* The University of Birmingham, Birmingham.